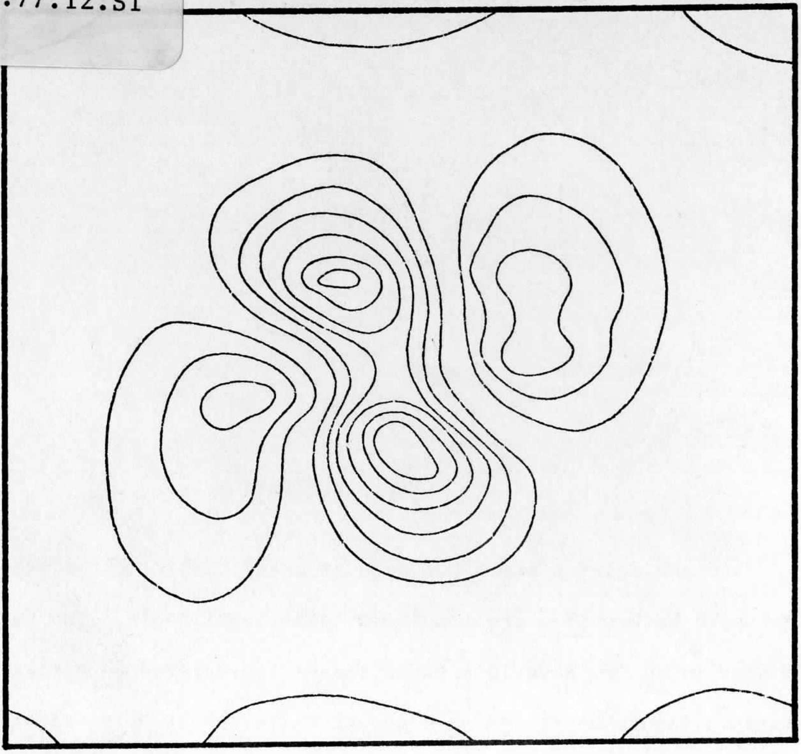

STUDIES OF THE ATMOSPHERE USING AEROSPACE PROBES

Annual Scientific Report - 1976
NOAA Grant 04-3-158-61
Space Science and Engineering Center
University of Wisconsin - Madison
December 1977

COVER ILLUSTRATION

Art and Science are often seen as antagonistic, but since both seek to interpret Nature they are sometimes indistinguishable. The pattern found on page 94 in Dr. Reynold's paper can be appreciated as easily as a vibrant abstract figure as it can as a quantitative result of a scientific study. We like to see it both ways.

STUDIES OF THE ATMOSPHERE
USING AEROSPACE PROBES

STUDIES OF THE ATMOSPHERE
USING AEROSPACE PROBES
1976

Annual Report, NOAA Grant 04-3-158-61

The research reported in this document has been supported by the National Oceanographic and Atmospheric Administration.

December 1977

Published for the
Space Science and Engineering Center
by the
University of Wisconsin Press

Published 1977
The University of Wisconsin Press
Box 1379, Madison, Wisconsin 53701

The University of Wisconsin Press, Ltd.
70 Great Russell Street, London

First Printing

Printed in the United States of America

ISBN 0-299-97060-4

This work is a result of research sponsored by the NOAA National Environmental Satellite Service, Department of Commerce, under Grant No. 04-3-158-61. The U.S. Government is authorized to produce and distribute reprints for governmental purposes notwithstanding any copyright notation that may appear hereon.

Correspondence concerning editorial matters should be addressed to:

Space Science and Engineering Center
University of Wisconsin
1225 West Dayton Street
Madison, Wisconsin 53706

Orders for copies of this report should be addressed to:

The University of Wisconsin Press

Principal Investigator:	Verner E. Suomi
Contributors:	Doron Nof Nathaniel D. Reynolds Alfred J. Stamm
	University of Wisconsin

CONTENTS

Technical Articles

Page

PREFACE

Take a straw and throw it up into the air--you may see by that which way the wind is.

John Selden 1689.

The authors of the three papers in this report are deeply concerned with finding "which way the wind is." Each throws a different straw, and each learns from the experience. Dr. Stamm compares the world created by a model with the real world and finds it simpler but useful. Dr. Nof casts his theoretical straw into two models and finds that the results compare well with laboratory tests. Dr. Reynolds throws his straw into the jet stream and follows it with two models to learn that the differences in the results are significant. We applaud these competent young scientists for their accomplishments, and we admire the patience and enthusiasm with which they have conducted their research. We are deeply grateful to our sponsors at the National Environmental Satellite Service, NOAA for their continuing support.

John A. Young　　　　　Verner E. Suomi

ON STEADY ADJUSTMENT IN CHANNELED DIFFLUENT FLOWS: THEORY AND LABORATORY EXPERIMENTS

Doron Nof

ABSTRACT

This work examines the dynamics of diffluent flows on the synoptic scale. Emphasis is given to the steady-state advective adjustment processes; to accomplish this, the dynamics of steady outflows when a confining channel suddenly widens are examined through two simplified frictionless models whose primary motions are not constrained to be quasi-geostrophic. Generalizations of the potential vorticity equation and the Bernoulli integral are solved for one- and two-layer models, using approximate analytical methods and asymptotic expansions. Some of the models' predictions are tested in the laboratory.

The single layer model predicts that an outflow from a channel with uniform velocity distribution deflects to the right or left depending on the depth of the basin into which it debouches. There is a "critical" Rossby number, below which the flow separates from one of the basin banks. When a non-uniform velocity is introduced upstream, the direction of deflection may differ substantially from the upstream uniform flow case.

The two-layer model predicts that an outflow from a channel with a uniform flow deflects to the right, but an outflow from a channel with a negative relative vorticity, approximately equal to the coriolis parameter, deflects to the left. As in the one-layer model, there is also a "critical" Rossby number, below which the current separates from the basin bank. In both models the parameters of the problem combine to show that rotation is important whenever the ratio of depth variation to Rossby number is not negligible.

Three experimental systems consisting of a rotating channel with an abrupt cross-sectional variation were used in the laboratory to test the theory described above. Deflections resulting from "super-critical" conditions in one- and two-layer systems were tested qualitatively with favorable results.

NOMENCLATURE

A = Velocity shear

A_n = Coefficients of Fourier Series

a = Half the basin width

B = Function of x^* and y^*

b = Half the channel width

c = Width ratio, a/b

D = Deflection variable, function of depth variation and Ro

d = Location of asymptotic separation line

$F;\tilde{F}$ = Froude number, $V_o^2/g\,H_o$; $\tilde{V}^2/g\tilde{H}$

F_1 = Internal Froude number, $V_o^2/g'H_o$

f = The Coriolis parameter

G = Function of the transport function ψ

g = Gravity

g' = "Reduced" gravity

$H_o;H_1$ = Depths of fluid in the channel and basin (constants)

$\tilde{H}$ = Average depth

$h(x,y)$ = Total depth of fluid column

h_B = Deviation of the bottom from a perfect flatness

h_i = Upstream depth of the upper layer

K = Functions of the transport function ψ

$\tilde{L}$ = Length scale of the exterior flow

P = Pressure

Ro = Rossby number, $V_o/2fb$

Ro_c = Critical Rossby number

r = Distance from experimental axis of rotation

S = Non-dimensional inverse shear, $2V_o/bA$

t = Time

V_o = Average velocity upstream

$\tilde{V}$ = Velocity scale of the exterior flow

u, v, w = Velocity components in the x, y, and z directions

x = Coordinate normal to the basin axis

y = Coordinate along the basin

z = Vertical coordinate

α, β = Coordinates in the complex plane

ΔH = Step parameter

δ = Location at which the particular solution vanishes

∇_H = Del operator

∇ = Non-dimensional del operator

ε = Small parameter

$\eta(x,y)$ = Surface displacement

η_i = Upstream surface displacement

λ = Rossby deformation radius, $\sqrt{g\tilde{H}}/f$

λ' = Internal Rossby deformation radius, $\sqrt{g'\tilde{H}}/f$

$\xi(x,y)$ = Interface displacement

ρ = Fluid density

$\Delta\rho$ = Density difference between the layers

Φ = Complex plane

ϕ = Integration variable

ψ = Volume transport function

$\psi^{(o)}$ = Basic state transport function

$\psi^{(1)}$ = Perturbation transport function

$\tilde{\psi}$ = Function

θ = on the order of

$\bar{\psi}$ = Particular solution far downstream

Ω = Rotation rate about vertical axis

Stars (*) denote non-dimensional variables. The subscripts "BC" and "SC" denote that the variable is associated with a "subcritical" and "supercritical" Rossby number, respectively. The subscripts "DSC" and "USC" denote that the variable is associated with a step down (DSC) or up (USC) with supercritical Rossby number. The subscripts "P" and "H" denote "particular" and "homogeneous" respectively; "i" denotes "initial", "u" denotes "upper layer" and "ℓ" denotes "lower layer."

1. INTRODUCTION

Motivation for research

Diffluent flow in the atmosphere is important because it is often accompanied by the development of spectacular weather events on smaller scales. The regions of strongest diffluence are found on the smaller synoptic scales, and appear to involve motions which depart significantly from a state of geostrophic balance. A good example is typically found in the "exit" region of upper level jet streams, where inertial (advective) accelerations are large.

These accelerations would occur even in a steadily propagating jet core; hence, the idealization of the problem to a steady state (in moving coordinates) is acceptable in a first attempt.

In a similar way, the dynamics of low level air currents which are channeled by topographic features can be studied as a steady→state problem. In fact, the results are also significant in the more general context of geophysical fluid dynamics. For example, the flows through sea straits and estuaries bear a resemblance to the idealizations used in this work.

This study is concerned with the interaction of a concentrated steady flow with a larger region of fluid into which it debouches. The problem consists of an initial balance flow in a channel and a subsequent spreading process subject to the influence of the earth's rotation. In the channel, the boundaries restrict the streamlines to be straight and parallel; removal of the boundaries, at a point, causes the current to enter into an adjustment process in which it becomes diffluent and eventually approaches a new state of geostrophic balance.

Background

As noted above, the problem of interest may be posed as an initial flow in a rotating channel, and a subsequent spreading process. It is related to the classical problem of adjustment toward a geostrophic balance (Rossby, 1938)[1] when a constraint (i.e., the channel boundary) is removed. Previous investigations related to the two types of flow are discussed below.

A) Flow in a rotating channel:

Although there is an appreciable amount of literature on "Open Channel Hydraulics" (Chow, 1959), the subject which we may call "Rotating Channel Hydraulics" has received very little attention. In textbooks on oceanography one finds that discussions about sea straits are usually limited to conservation-of-mass requirements. Using the non-rotating hydraulic principle of maximum transport in flow over a weir, Whitehead, Leetmaa and Knox (1974) investigated the effect of a geometrical restriction on the rotating flow in the lower layer. Stern (1972) studied the effect of a contraction on the formation of hydraulic jumps in a rotating channel.

B) Spreading of the flow:

Most of the investigations to date have been confined to small scale non-rotating plumes. These studies usually involve simplifications of the governing equations, using the assumption of similarity and the assumption that the flow has some of the characteristics of a symmetrical jet structure. See Koh (1970) and Stolzenbach and Harleman (1971).

Waldrop and Farmer (1974) studied the interaction between the initial flow and a cross-flow, using a three dimensional numerical model whose motions were not constrained to be similar. Paul and Lick (1974) studied river discharge into a lake, using a numerical model which included the Coriolis parameter. Their results are symmetrical and deflection of the flow is not noticed. However, the model does not include buoyancy near the outlet, which results in a limited rotational effect.

Takano (1954,1955) investigated a slow-moving frictional discharge. Neglecting the inertia terms, he showed analytically that as a result of the earth's rotation, the viscous plume deflects to the right in the Northern Hemisphere.

These solutions are of limited significance to the problem posed in this study, where accelerations and mass adjustments cause an evolution toward a new geostrophically balanced flow.

---

[1] Rossby's problem described the mass and velocity changes required to "adjust" an initially unbalanced current to a state of geostrophic balance. A complementary problem is the adjustment of initially unbalanced hydrostatic mass field toward a final geostrophic flow state.

Purpose of the present study

The goal of this study is to discuss the dynamics of forced outflows and the motion changes, associated with them. No attempt will be made to predict the distribution of thermodynamical properties, nor to produce detailed models of particular situations. This study will attempt to draw some general conclusions about the dynamical behaviour of rotational outflows and their induced circulation.

Some of the specific questions we wish to answer are:

i) What initial values of channel width, velocity, depth and density will exert a significant influence of rotation on the outflow?

ii) When do rotating plumes create longshore currents? What physical properties and parameters control their direction?

iii) What is the response to the current created by the plume?

It is assumed that such questions can be best answered by first considering simplified models that include only some of the physical processes. Therefore, we shall study first a one layer model of steady flow in which bottom topography, inertia, rotation and pressure are included, but in which buoyancy, friction, diffusion, entrainment and pre-existing cross-flows are excluded. The next step will be the study of a two layer non-linear model which includes buoyancy as well as bottom topography, inertia, rotation and pressure. The neglect of friction and diffusion is justified for the cases where the length scale of the adjustment is much smaller in comparison to that required for penetration of the ambient fluid into the core of the plume.

Methods and further simplifications

The geometry of the theoretical models has been adopted in such a way as to simplify the boundary conditions and to ensure that the problem is well posed. The hydrostatic and the rigid lid approximations are invoked, but the motions are not constrained to be quasi-geostrophic. Generalizations of the potential vorticity equation and the Bernoulli integral yield, for the one layer theory, a linear second-order partial differential equation of the elliptic type which is solved by means of conformal mapping, the Fourier integral and a Fourier series. The results are presented and discussed in Section 2.

For the two-layer theory (Section 3), the potential vorticity equation and the Bernoulli integral yield a pair of non-linear second order partial differential equations which are solved by means of asymptotic expansions in powers of the Froude number.

Laboratory experiments for both the one- and two-layer systems were performed on a rotating table to assess the validity and weaknesses of the mathematical solutions. The results are presented in Section 4, and appear to be in qualitative agreement with the theory. Section 5 discusses likely extensions of this work.

2. ONE LAYER MATHEMATICAL MODEL

Generalizations of the potential vorticity equation and the Bernoulli integral for a layer of variable depth

This section presents the derivation of the general equations which will be used throughout this study. Consider a homogeneous layer of fluid of constant density as shown in Figure 1. For steady flows subject to constant external pressure, the hydrostatic assumption is valid as long as $\frac{U^2H}{g\,L^2} \ll 1$, where U, H, L are typical velocity, depth and length scales, respectively, and g is the gravitational acceleration. For hydrostatic motions the pressure is a linear function of z, and the horizontal pressure gradients depend on x and y alone. Therefore, it is reasonable to assume that the horizontal velocity components are also independent of z. For such conditions, the steady frictionless equations of motion are:

$$u\frac{\partial u}{\partial x} + v\frac{\partial u}{\partial y} - fv = -g\frac{\partial \eta}{\partial x} \qquad (2.1)$$

$$u\frac{\partial v}{\partial x} + v\frac{\partial v}{\partial y} + fu = -g\frac{\partial \eta}{\partial y} \qquad (2.2)$$

$$\frac{\partial u}{\partial x} + \frac{\partial v}{\partial y} + \frac{\partial w}{\partial z} = 0$$

where u, v, and w are the x, y and z velocity components, f the Coriolis parameter and η the surface displacement. Integration of the incompressible continuity equation from the bottom of the layer to its top yields:

$$\frac{\partial}{\partial x}(hu) + \frac{\partial}{\partial y}(hv) = 0$$

where h is the depth of the layer and the boundary condition w (top) - w (bottom) = Dh/Dt, has been used. Therefore, one may define a transport function, ψ, such that:

$$-uh = \frac{\partial \psi}{\partial y}\ ;\ vh = \frac{\partial \psi}{\partial x}, \qquad (2.3)$$

with the condition that $\psi = 0$ at $x = -b$. Multiplication of (2.1) by uh and (2.2) by vh, addition of the equations obtained, and consideration of (2.3) gives the equation

$$\frac{\partial}{\partial(x,y)}\left[\psi\ ;\left(\frac{u^2+v^2}{2}+g\eta\right)\right]=0 \qquad (2.4)$$

By virtue of the known property of the Jacobian, the latter equation yields the Bernoulli integral

$$\frac{1}{2}\left(\frac{\nabla_H\psi}{h}\right)^2+g\eta=G(\psi) \qquad (2.5)$$

where $G(\psi)$, the Bernoulli ("energy") constant for each streamline, is to be determined from the boundary conditions. The potential vorticity equation is obtained by subtracting the derivative of (2.5) with respect to y from (2.2)

$$\nabla_H\cdot\left(\frac{\nabla_H\psi}{h}\right)+f=h\,K(\psi) \qquad (2.6)$$

where $K(\psi) = dG(\psi)/d\psi$, is the potential vorticity for each streamline, which depends (as does $G(\psi)$) on the boundary conditions.

The set (2.5) and (2.6) has been used by Charney (1955) to study certain features of the Gulf Stream, and by Gutman (1972) to study the effect of surface irregularities on atmospheric flows.

Outflow from a channel with uniform velocity distribution

Consider the model shown in Figure 1. To simplify the upstream boundary condition, it is assumed that the bottom has a transversal slope[1] of $\frac{dz_B}{dx} = fV_o/g$, where z_B is the bottom height, and $V_o = g\frac{\partial\eta}{\partial x}/f = \frac{\partial\psi}{\partial x}/H_o$ is the geostrophically balanced velocity in the channel. Under such conditions the column depth in the channel, H_o, is independent of cross-stream direction x.

Substitution of the upstream boundary condition into (2.5) and (2.6) yields $G(\psi) = \frac{1}{2}V_o^{\,2} + \frac{f\psi}{H_o} - fV_ob$ and $K(\psi) = f/H_o$, which, from (2.6) and (2.5), yield the governing equations

---

[1] It will become clear later that, due to the rigid lid approximation, this assumption can be avoided.

$$\nabla_H \cdot \left(\frac{\nabla_H \psi}{h}\right) = f(h-H_o)/H_o \tag{2.7}$$

$$\frac{1}{2}\left(\frac{\nabla_H \psi}{h}\right)^2 + g\eta = \frac{1}{2} V_o^2 + \frac{f\psi}{H_o} - fV_o b \tag{2.8}$$

These equations hold for all streamlines that originate in the channel. In the subsequent analysis, the following non-dimensional scaled variables are used

$$\left.\begin{array}{lll} \psi^* = \psi/(2V_o H_o b) & ; x^* = x/b & ; y^* = y/b \\ \eta^* = \eta/H_o & ; \Delta H^* = \Delta H/H_o & ; H_1^* = H_1/H_o \\ h^* = h/H_o & ; v^* = v/V_o & ; u^* = u/V_o \\ F = V_o^2/gH_o & ; \nabla = \nabla_H b & \\ Ro = V_o/2fb & & \end{array}\right\} \tag{2.9}$$

The non-dimensional equations in the basin ($y^*>0$) are:

$$\nabla \cdot \left(\frac{\nabla\psi^*}{1 + \Delta H^* + \eta^*}\right) = (\Delta H^* + \eta^*)/4Ro \tag{2.10}$$

$$2\eta^* + 4F\left(\frac{\nabla\psi^*}{1 + \Delta H^* + \eta^*}\right)^2 = F + \frac{F}{Ro}(2\psi^*-1) \tag{2.11}$$

For small η^*, (2.11) reduces to

$$\eta^* \simeq \frac{F}{2}\,[1 + (2\psi^* - 1)Ro^{-1} - 4(\nabla\psi^*)^2(1 + \Delta H^*)^{-2}]\left[1 - \frac{4F(\nabla\psi^*)^2}{(1 + \Delta H^*)^3}\right]^{-1} + \theta(\eta^*)^2 + \ldots$$

Therefore, assuming $(1 + \Delta H^*) \sim \theta(1)$, one may consider the surface as a flat rigid lid ($|\eta^*| << |\Delta H^*|$) as long as:

$$F << |\Delta H^*| \; ; \; \frac{F}{Ro} << |\Delta H^*| . \tag{2.12}$$

For such cases equation (2.10) can be approximated by the Poisson equation

$$\nabla^2\psi^* = \Delta H^*(1 + \Delta H^*)/4Ro \tag{2.13}$$

This equation corresponds to constant relative vorticity along each streamline.

Equation (2.13) holds for "rigid lid" motions which are not necessarily near geostrophic balance. Its scaling shows that $4Ro \gtrsim \theta(\Delta H^*)$. Since the quasi-geostrophic theory holds for $Ro \ll 1$, its scaling is valid for $|\Delta H^*| \ll 1$ and (2.13) reduces to the form

$$\nabla^2 \psi^* = \Delta H^*/4Ro \tag{2.14}$$

(It should be noted that the quasi-geostrophic theory is also valid in cases where the rigid lid approximation is <u>not</u> valid.) The above discussion shows that quasi-geostrophic theory yields approximately the same governing equation as (2.13), but is more restrictive.

To simplify the boundary conditions, it is assumed that the channel flow remains uniform until the outlet is reached ($y \lesssim o$); in reality, some modification is expected at a distance $\theta(b)$ upstream from the outlet. It will become clear later that this approximation has a minor effect on the flow downstream from the outlet, although the initial adjustment details will be altered. The boundary conditions are:

$$\left.\begin{array}{lllll}
\psi^* = o & ; & x^* = -c & ; & o<y^*<\infty \quad (a)\\
\psi^* = o & ; & -c<x^*<-1 & ; & y^* = o \quad (b)\\
\psi^* = \frac{1}{2}(1+x^*) & ; & -1\leq x^* \leq 1 & ; & y^* = o \quad (c)\\
\psi^* = 1 & ; & 1<x^*<c & ; & y^* = o \quad (d)\\
\psi^* = 1 & ; & x^* = c & ; & o<y^*<\infty \quad (e)\\
\dfrac{\partial\psi^*}{\partial y^*} = o & ; & -c\leq x^* \leq c & ; & y^* \to \infty \quad (f)
\end{array}\right\} \tag{2.18}$$

where $c = a/b$. Conditions (a), (b), (d) and (e) state that the basin walls are streamlines; (c) is the uniform flow assumption at the mouth; and (f) reflects the completed nature of the adjustment far downstream.

The general solution of (2.13) consists of a homogeneous part that satisfies (2.18), and a particular solution that satisfies the following homogeneous conditions:

$$\left.\begin{array}{lllll}
\psi_P = 0 & ; & x^* = -c & ; & o<y^*<\infty\\
\psi_P = 0 & ; & -c<x^*<c & ; & y^* = 0\\
\psi_P = 0 & ; & x^* = c & ; & o<y^*<\infty\\
\partial\psi_P/\partial y^* = 0 & ; & -c\leq x^* \leq c & ; & y^* \to \infty
\end{array}\right\} \tag{2.19}$$

A) <u>The homogeneous solution</u>

We shall find the homogeneous solution by transforming the interior of the basin into the upper half of the complex plane. Such mapping is done by a straight-forward Schwartz Christoffel transformation of the form

$$\Phi = \alpha + \beta i = \mathrm{Sin}[\pi(x^* + iy^*)/2c] \tag{2.20}$$

where Φ denotes the complex plane and

$$\left.\begin{aligned} \alpha &= \mathrm{Sin}(\tfrac{\pi x^*}{2c})\cosh(\tfrac{\pi y^*}{2c}), \\ \beta &= \cos(\tfrac{\pi x^*}{2c})\sinh(\tfrac{\pi y^*}{2c}) \text{ and} \\ c &= a/b. \end{aligned}\right\} \tag{2.21}$$

In the complex plane the boundary conditions are:

$$\left.\begin{aligned} \psi_H(\alpha,0) &= 0 && ;\ -\infty<\alpha<-\mathrm{Sin}\ \pi/2c \\ \psi_H(\alpha,0) &= \frac{1}{2}(1 + \frac{2c}{\pi}\,\mathrm{Sin}^{-1}\alpha) && ;\ -\mathrm{Sin}\ \frac{\pi}{2c} \leq \alpha < +\ \mathrm{Sin}\ \pi/2c \\ \psi_H(\alpha,0) &= 1 && ;\ \mathrm{Sin}\ \frac{\pi}{2c} < \alpha < \infty \end{aligned}\right\} \tag{2.22}$$

and the solution is given by the Fourier integral (Pearson, 1974),

$$\psi_H = \frac{1}{\pi}\int_{-\infty}^{\infty} \frac{\beta G(\phi)\,d\phi}{\beta^2 + (\alpha-\phi)^2}$$

where

$$G(\phi) = \psi_H(\alpha,0)$$

This integral yields

$$\left.\begin{aligned} \psi_H = 1/2 &+ \left(\frac{c\alpha}{\pi^2} + \frac{1}{2\pi}\right)\tan^{-1}\left(\frac{\alpha + \frac{\pi}{2c}}{\beta}\right) - \left(\frac{c\alpha}{\pi^2} - \frac{1}{2\pi}\right)\tan^{-1}\left(\frac{\alpha - \frac{\pi}{2c}}{\beta}\right) \\ &+ \frac{\beta c}{\pi^2}\ln\frac{\beta^2 + (\alpha - \pi/2c)^2}{\beta^2 + (\alpha + \pi/2c)^2} + \theta(\pi/24c^2) \end{aligned}\right\} \tag{2.23}$$

where $\alpha(x^*, y^*)$ and $\beta(x^*, y^*)$ are given by (2.21); we have used the approximation $\mathrm{Sin}\alpha \simeq \alpha$ for $\alpha<<1$ in calculating the integral from $-\mathrm{Sin}(\frac{\pi}{2c})$ to $+\mathrm{Sin}(\frac{\pi}{2c})$.

Note that

$$\lim_{y\to\infty} \psi_H = \frac{x^* + c}{2c} \tag{2.24}$$

For c = 1, (no channel widening), ψ_H is given by $\frac{x^* + 1}{2}$. The homogeneous solution for c = 4 is shown in Figure 2. This corresponds to irrotational potential flow.

B) The particular solution, ψ_P

Given the geometry of the problem, it is reasonable to assume that, far downstream, the particular solution, ψ_P, is independent of y*. This assumption is supported by the idea of geostrophic adjustment, since one expects the flow to be in geostrophic balance far downstream. This then requires that the flow also be one dimensional. Therefore, one may assume that ψ_P consists of

$$\psi_P = \tilde{\psi}(x^*, y^*) + \bar{\psi}(x^*) \tag{2.25}$$

where $\lim_{y^*\to\infty} \tilde{\psi}(x^*, y^*) = 0$

i) The particular solution far downstream

From (2.13) and (2.19) one obtains

$$\bar{\psi} = D[(x^*)^2 - c^2] \tag{2.26}$$

where $D = \Delta H^*(1 + \Delta H^*)/8Ro$ (2.27)

The velocity far downstream is

$$v^* = \frac{2}{H_1^*}\left[\lim_{y^*\to\infty}\left(\frac{\partial \psi_H}{\partial x^*}\right) + \frac{\partial \bar{\psi}}{\partial x^*}\right] = c^{-1}(1 + \Delta H^*)^{-1} + \frac{\Delta H^* x^*}{2Ro} \tag{2.28}$$

Since both ΔH* and x* are either positive or negative, the velocity according to (2.28) may become negative for sufficiently small Ro. It can be shown, however, that such a situation is impossible. A negative v* corresponds to parcels which have originitated at $y^*\to\infty$ and so have not passed across the step; therefore, the right hand side of (2.10) and the left of (2.11) are altered in such regions, and the negative v* flow found in (2.28) does not obey the proper equations. One concludes that the solution (2.28) is valid as long as v*>0. If v* (as determined by 2.28) is negative, separation occurs and $\bar{\psi}$ can no longer satisfy, simultaneously, the two conditions $\bar{\psi} = 0$ at $x^* = \pm c$.

One of these conditions should be replaced by a new condition, which will be determined from the location of the separation line (where $\psi^* = 0$ or unity in the interior of the basin). There is a certain difficulty in locating the separation line; the following logic is employed to find it.

Consider a case with a step down ($\Delta H^*>0$) as shown in Figure 3. The "critical" Rossby number, Ro_c, is defined as the one which first causes separation. For larger-than-critical Rossby numbers the velocity is always positive in the field. If the Rossby number is decreased (e.g., rotation rate is increased) to a critical value, the velocity vanishes at the left bank. If the Rossby number is further decreased, the flow may detach either from the left bank or from the right bank. These two possible distributions are marked by (a) and (b), respectively. At the point of detachment from the right bank (case (b)), the shear near the bank becomes infinite. A real fluid can not support such a shear and, therefore, situation (a)--in which there is no velocity discontinuity at the point of detachment--is more likely to occur.

The critical Rossby number is determined from the conditions:

$$v^* = 0 \; ; \; x^* = -c \quad \text{for a step down, } \Delta H^*>0$$

$$v^* = 0 \; ; \; x^* = c \quad \text{for a step up, } \quad \Delta H^*<0$$

Substitution of the above conditions into (2.28) yields the single relation:

$$Ro_c = c^2 |\Delta H^*| (1 + \Delta H^*)/2 \qquad (2.29)$$

which is shown in Figure 4. Note that the critical Rossby number is relatively small for the step up; in contrast, for a step down, there always exists a step size that can cause separation for any Rossby number and value of c. The critical Rossby number increases dramatically as basin width increases.

We shall consider now the separated solution for a step down. Separation occurs if $Ro<Ro_c$; the new boundary conditions at $y^*\to\infty$, equivalent to a zero value of $\bar{\psi}(x^*)$ at $x^* = \pm c$, are

$$\bar{\psi} = 0 \; ; \; x^* = c \; ; \; x^* = -\delta_{DSC}. \qquad (2.30)$$

The subscript "DSC" denotes that the variable in question is associated with a step down and a supercritical Rossby number. δ_{DSC} is the location at which the particular solution vanishes.

At the asymptotic separation line ($x^* = d_{DSC}$) for a step down ($D>0$),

$$\left.\begin{aligned} \psi^* &= \lim_{y^*\to\infty} \psi_H + \bar{\psi} = 0 \\ &\text{and} \\ v^* &= \frac{2}{H_1^*}\left[\frac{\partial}{\partial x^*}\left(\lim_{y^*\to 0} \psi_H\right) + \frac{\partial \bar{\psi}}{\partial x^*}\right] = 0 \end{aligned}\right\} \qquad (2.31)$$

where $\bar{\psi}(x^*)$ has the new form:

$$\bar{\psi}(x^*)_{DSC} = D(x^* - c)(x^* + \delta_{DSC}) \qquad (2.32)$$

The latter expression in (2.31) seems to be the only logical condition[1] on v^* at the separation line. Substitution of (2.32) and (2.24) into (2.31) yields a pair of algebraic equations with two unknowns: δ_{DSC} and the location of the separation line, d_{DSC}. Two solutions exist, but the physically relevant solution is:

$$\delta_{DSC} = -c + \frac{2}{\sqrt{|D|}} - \frac{1}{2c|D|} \qquad (2.33)$$

and

$$d_{DSC} = -\frac{1}{\sqrt{|D|}} + c \qquad (2.34)$$

Similarly, the new boundary conditions for $\bar{\psi}$ with a step up ($D<0$) and a supercritical Rossby number are:

$$\bar{\psi}(x^*) = 0 \;;\; x^* = -c \;;\; x^* = \delta_{USC} \qquad (2.35)$$

where the subscript "USC" denotes that the variable in question is associated with a step up and a supercritical Rossby number. At the separation line ($x^* = d_{USC}$),

---

[1] Note that for $Ro<Ro_c$, an assumption for v^* at the separation line is required; otherwise, the problem is not uniquely defined.

$$\left.\begin{aligned} \psi^* &= \lim_{y^*\to\infty}\psi_H + \bar{\psi} = 1 \\ \text{and}\qquad v^* &= \frac{2}{H_1^*}\left[\frac{\partial}{\partial x^*}\left(\lim_{y^*\to\infty}\psi_H\right) + \frac{\partial\bar{\psi}}{\partial x^*}\right] = 0 \end{aligned}\right\} \qquad (2.36)$$

where $$\bar{\psi}(x^*) = D(x^* + c)(x^* - \delta_{USC}) \qquad (2.37)$$

By substitution of (2.24) and (2.37) into (2.36), one obtains (as before) two algebraic equations. Their solution is $d_{USC} = \frac{1}{\sqrt{|D|}} - c$; $\delta_{USC} = \delta_{DSC}$. Thus the current width is simply $|D|^{-1/2}$ for steps up or down. The dependence of D upon ΔH^* indicates that the width will be smaller for a step down; the dependence upon Ro shows the confining effect of the earth's rotation.

ii) <u>The function $\tilde{\psi}(x^*, y^*)$</u>

The relation between $\tilde{\psi}$ and $\bar{\psi}$ is given by (2.25). It can be easily verified that the function

$$\tilde{\psi} = \sum_{n=1}^{\infty} A_n \exp\left(\frac{-n\pi y^*}{2c}\right) \operatorname{Sin} \frac{n\pi(x^* + c)}{2c} \qquad (2.38)$$

satisfies the Laplace equation and the homogeneous boundary conditions at all boundaries except at $y^* = 0$. However, one may express the coefficients A_n such that at $y^* = 0$, the total particular solution (the sum of $\tilde{\psi}$ and $\bar{\psi}$) will satisfy the complete homogeneous boundary conditions

$$\sum_{n=1}^{\infty} A_n \operatorname{Sin} \frac{n\pi(x^* + c)}{2c} = -\bar{\psi}(x^*) \qquad (2.39)$$

which yields

$$A_n = -\frac{1}{c}\int_{-c}^{c} \bar{\psi} \operatorname{Sin} \frac{n\pi(x^* + c)}{2c}\, dx^* \qquad (2.40)$$

We shall first construct $\tilde{\psi}_{bc}$, the subcritical flow for which $Ro > Ro_c$. Substitution of (2.26) into (2.40) and consideration of (2.38) gives

$$\tilde{\psi}_{bc} = -16c^2 D \sum_{n=1}^{\infty} \left(\frac{\cos n\pi - 1}{n^3\pi^3}\right) \exp\left(-\frac{n\pi y^*}{2c}\right) \operatorname{Sin} \frac{n\pi(x^* + c)}{2c} \qquad (2.41)$$

Under "supercritical" ($Ro<Ro_c$) conditions, a further connection is necessary. For a step down with $Ro<Ro_c$, one seeks an additional function that at $y^* = 0$ cancels the contribution of the difference between $\bar{\psi}_{DSC}$ given by (2.32) and $\bar{\psi}$ given by (2.26). This function is linear in x^* and vanishes at $x^* = +c$. In view of these considerations one finds

$$\tilde{\psi}_{DSC} = \tilde{\psi}_{bc} + 16CD(C - \delta_{DSC})\sum_{n=1}^{\infty} \frac{\mathrm{Sin}\,\frac{n\pi}{2}}{n^2\pi^2} \exp\left(\frac{-n\pi y^*}{4c}\right) \mathrm{Sin}\,\frac{n\pi(x^* - c)}{4c} \tag{2.42}$$

where δ_{DSC} is given by (2.33) and D by (2.27). For a step up with $Ro<Ro_c$, one seeks a function which at $y^* = 0$ cancels the contribution of the difference between $\bar{\psi}_{USC}$ given by (2.37) and $\bar{\psi}$ given by (2.26). Thus

$$\tilde{\psi}_{USC} = \tilde{\psi}_{bc} + 16CD(\delta_{USC} - C)\sum_{n=1}^{\infty} \frac{\mathrm{Sin}\,\frac{n\pi}{2}}{n^2\pi^2} \exp\left(\frac{-n\pi y^*}{4c}\right) \mathrm{Sin}\,\frac{n\pi(x^* + c)}{4c} \tag{2.43}$$

Typical total solutions from (2.23), (2.26), (2.32), (2.37), (2.41), (2.42), and (2.43) are shown in Figures 5,6,7 and 8. These figures illustrate subcritical and supercritical conditions and sensitivity to basin width, Rossby number and step size. It should be noted that the dependence on Ro and ΔH^* is linked, since for a given c, the solution depends only upon D.

Figure 5 shows non-separating flows for steps up and down. The center streamline deflects to the right (left) for parcels which have experienced a cyclonic (anti-cyclonic) vorticity in crossing the step. Figure 6 shows corresponding separating flows for the same basin width as shown in Fig. 5. When compared with Fig. 6(B), Fig. 7(A) shows the effect of changing only the basin width (or, equivalently, the inlet width for a fixed basin). Comparison of Fig. 7(B) with Fig. 6(B) shows the effect of changing only the Rossby number to a more extreme "supercritical" value. Fig. 8 shows how separation can occur even when there is no spreading effect. Note that due to the separation of the flow, (2.42) and (2.43) do not allow the boundary conditions $\psi^* = 0$ at $x^* = -c$ and $\psi^* = 1$; $x^* = +c$, to be respectively satisfied as should be the case.

It is difficult to determine analytically whether the functions evaluated above, together with the other functions that constitute the solution, produce a continuous separation line that intersects with the proper boundary. About forty numerical calculations of ψ from (2.23), (2.26), (2.32), (2.37), (2.41), (2.42) and (2.43) were performed, with $3\leq c\leq 18$;$0.05\leq Ro\leq 0.2$ and $-0.3\leq \Delta H^*\leq 0.3$; they showed a continuous separation line that intersects with the proper boundary in all cases. However, for the range: $c = 1$; $\Delta H^* = 0.3$ and $Ro<0.1$, the separation line did not intersect with the proper boundary and the solution presented in this section is not valid. This finding may be related to the assumption that $v^* = 0$ on the dividing streamline at $y^* \to \infty$, or to the uniform flow assumption at the mouth. However, the limitation mentioned above does not seem to be a severe restriction, since it occurs only for a very limited parameters range.

C) The exterior flow

In the exterior region (i.e., across the separation line) the fluid again obeys the basic laws (2.5) and (2.6), but $\Delta H^* = 0$ since these parcels have not passed the step. The domain is long and, except near the mouth, the flow is nearly one-dimensional; therefore, it is reasonable to assume that the exterior flow can be approximately described by the quasi-geostrophic theory. For this layer of fluid (confined between a flat rigid bottom and a free surface) the potential vorticity equation in the basin is,

$$\frac{D}{Dt}\left[(v_x - u_y + f)/[H_1 + \eta\,(x,y)]\right] = 0 \qquad (2.45)$$

For $\eta<<H_1$ and $\tilde{Ro} = \frac{\tilde{V}}{f\tilde{L}} <<1$, where $\tilde{V}$ and $\tilde{L}$ are typical velocity and length scales of the exterior flow, (2.45) can be approximated by

$$\frac{D}{Dt}\left[\frac{v_x - u_y}{H_1} - f\eta/H_1^{\,2}\right] = 0 \qquad (2.46)$$

where terms of fractional error of $\Theta(\tilde{Ro})$ and of $\Theta(\frac{f\tilde{U}\tilde{L}}{g\tilde{H}})$ have been neglected. To the same order of error, the velocity field is geostrophic, so (2.46) can be written in the form

$$\frac{D}{Dt}\left[\nabla_H^2\psi - \psi/\lambda^2\right] = 0$$

or

$$\nabla_H^2\psi - \psi/\lambda^2 = K(\psi)$$

where $K(\psi)$ (proportional to the quasi-geostrophic potential vorticity) is to be determined. Here ψ may be interpreted as a geostrophic stream function, $g\eta/f\tilde{H}$. The velocity distribution far downstream is unknown and one is unable to determine $K(\psi)$ without additonal information. The latter can be provided by assuming that, since there is no mechanism by which potential vorticity can be transferred from the interior to the exterior, there is no potential vorticity in the isolated exterior region. This condition yields $K(\psi) = 0$, which implies

$$\nabla_H^2\psi - \psi/\lambda^2 = 0 \tag{2.46a}$$

In view of the geometry of the exterior, one may approximate the latter equation by

$$\frac{\partial^2\psi}{\partial x^2} - \frac{\psi}{\lambda^2} = 0 \quad \text{for large } y.$$

The boundary conditions are that ψ vanishes at two parallel lines. It follows that in the exterior, $\psi = 0$ at large y, and by virtue of the known property of the elliptic equation (2.46a) (see for example Forsythe and Wasow, 1960), $\psi = 0$ in the entire exterior domain. We conclude that there is no motion in the whole exterior domain.

The above discussion has the following weakness. A basic assumption was that the exterior can be described by the quasi-geostrophic theory. This theory requires that a line of constant η will also be a line of constant ψ, while numerical calculations (based on the solution to the interior) show that η is not necessarily constant along the separation line; that is, the quasi-geostrophic theory satisfies only one of the two matching conditions.

Therefore, it can be applied to the exterior only if the motions which are caused by η variations along the separation line are negligible in comparison to motions in the interior. It is reasonable to assume that variations along the separation line can cause motions in the exterior which are comparable to the velocities in the interior along the separation line. Numerical calculations (for the cases mentioned in the earlier discussion of ψ_P) showed that the velocities along the separation line are small in comparison to the main interior motions only when the width of the interior is not very small in comparison to the basin width.

In the cases where the width of the separated current is small in comparison to the basin width, one would expect a stagnant region far downstream but a cyclonic or anticyclonic circulation near the outlet. This can be demonstrated by the following example. Figure 7 shows that the width of the interior at say $y^* = 10$ is about one third of the interior width at $y^* \to \infty$. Since the shear in the two locations must be almost the same, one concludes that at $y^* = 10$, the velocity in the interior at the separation line is of the same order as the velocity near the left wall. Therefore, in such extreme cases one expects to find, in the exterior near the basin inlet, a flow (which cannot be described by the quasi-geostrophic theory) with velocities of the same order of the velocities in the interior. A detailed solution of this field is beyond the scope of this study.

Outflow from a channel with a linear velocity distribution

In this section we consider a different version of the step problem. Assume that in the channel the velocity is

$$V = V_o + AX$$

where A is a positive or negative constant shear parameter. Using the rigid-lid approximation, the function $K(\psi)$ is found from the upstream boundary condition and (2.6) to be

$$K(\psi) = \frac{A + f}{H_o}$$

which implies

$$\nabla_H^2\psi = (AH_1 + f\Delta H)H_1/H_o \tag{2.47}$$

which is a generalization of (2.7) for the interior flow in the basin. In non-dimensional variables the latter equation is

$$\nabla^2\psi^* = (1 + \Delta H^*)[Ro^{-1}\Delta H^* + 4S^{-1}(1 + \Delta H^*)]/4 \tag{2.48}$$

where the non-dimensional shear parameter $S = \frac{2V_o}{bA}$ is either positive or negative. Equation (2.48) is identical in structure to (2.13), but the boundary condition at the outlet (i.e., $-1 \leq x^* \leq 1$; $y^* = 0$) is somewhat different than the one considered in the previous section. At the outlet, ψ^* is no longer given by $\frac{1 + x^*}{2}$ only; it has the additional term $\frac{S^{-1}}{2}[(x^*)^2 - 1]$. However, this outlet condition enters the problem through the homogeneous solution only, and any changes in the distribution of ψ^* at the outlet can be considered as imaginary sources and sinks whose net transport is zero. Therefore, the influence of such changes is confined to the immediate vicinity of the outlet, and one concludes that downstream, solutions of (2.48) are identical in structure to solutions of (2.13). That is, the current ultimately deflects to the right if the right side of (2.48) is positive, and to the left if it is negative.

The separation conditions and width of the final current are now dependent upon both ΔH^* and S. To demonstrate this, we shall consider the special case where $S^{-1} = 1/2$ and $Ro^{-1}\Delta H^* + 4S^{-1}(1 + \Delta H^*) = 0$, corresponding to cancellation of the initial vorticity by the step. At the outlet the boundary condition is $\psi^* = (x^* + 1)^2/4$. Using the Schwartz Christoffel transformation and the Fourier integral:

$$\psi^* \simeq \frac{\beta}{2\pi} \int_{-\pi/2c}^{\pi/2c} \frac{\left(\frac{2c^2\phi^2}{\pi^2} + \frac{2c\phi}{\pi} + \frac{1}{2}\right)d\phi}{\beta^2 + (\alpha - \phi)^2} + \frac{\beta}{\pi} \int_{\pi/2c}^{\infty} \frac{d\phi}{\beta^2 + (\alpha - \phi)^2}$$

which, as shown earlier, yields,

$$\left.\begin{aligned} \psi^* &= \frac{1}{2} + \frac{1}{\pi}\tan^{-1}\left(\frac{\alpha - \frac{\pi}{2c}}{\beta}\right) + \frac{1}{\pi}\left[\frac{1}{4} + \frac{c\alpha}{\pi} + \frac{c^2(\alpha^2 - \beta^2)}{\pi^2}\right] \\ &\text{times} \left[\tan^{-1}\left(\frac{\alpha + \pi/2c}{\beta}\right) - \tan^{-1}\left(\frac{\alpha - \pi/2c}{\beta}\right)\right] + \frac{c\beta}{\pi^2} + \\ &+ \frac{\beta c}{\pi^2}\left(\frac{1}{2} + \frac{\alpha c}{\pi}\right)\ln\frac{\beta^2 + (\alpha - \pi/2c)^2}{\beta^2 + (\alpha + \pi/2c)^2} + \theta\left(\frac{\pi}{24c^2}\right) \end{aligned}\right\} \qquad (2.49)$$

This relationship is shown in Fig. 9. Without the initial shear, the current would have deflected to the left, but due to the initial channel vorticity, the flow has a slight deformation near the outlet, but has no net deflection downstream.

3. TWO LAYER MATHEMATICAL MODEL

Outflow from a channel with a uniform flow

In this section we consider the model shown in Figure 10(A). We consider the cases in which the channel consists of two layers, since it appears to be the most common situation in nature. The two flows are often in opposite directions, but to simplify the model the lower layer is assumed to be deep and motionless. The flow in the upper layer near the outlet is assumed to be in geostrophic balance;

$V_o = g \frac{\partial \eta}{\partial x} / f = g \frac{\Delta\rho}{\rho} \frac{\partial \xi}{\partial x} / f$ where ξ is the interface displacement, ρ the density and $\Delta\rho$ the density difference between the layers.

As in the one layer model the hydrostatic and the rigid-lid approximations are invoked. The rigid-lid approximation is valid for this model, as long as $\frac{\Delta\rho}{\rho} \ll 1$, since then $|\eta| \ll |\xi|$. Equations (2.5) and (2.6) can be used for the two layer model since they have been derived for any layer of variable depth. The depth of the upper layer in the channel, h_i, can be approximated by

$$h_i = H_o + \xi_i = H_o + fV_o x/g' \quad \text{where} \tag{3.1}$$

g' is the "reduced gravity", defined as $g' = g \frac{\Delta\rho}{\rho}$; the index "i" denotes that the variable in reference is in its "initial" state (i.e., in the channel). The transport function, ψ, is a single valued function of x:

$$\psi = \int_{-b}^{x} V_o h_i dx = H_o V_o (x + b) + \frac{fV_o^2}{2g'} (x^2 - b^2) \tag{3.2}$$

Note that ψ is not linear in x even though the velocity is uniform. Eliminating x between (3.1) and (3.2),

$$h_i(\psi) = \left[H_o^2 \left(1 - \frac{F_1}{2Ro}\right)^2 + 2f\psi/g' \right]^{1/2} \tag{3.3}$$

where F_1 is the internal Froude number, given by $F_1 = F \frac{\rho}{\Delta\rho}$. The functions $K(\psi)$ and $G(\psi)$ are obtained by substitution of the upstream boundary conditions into (2.5) and (2.6).

$$G(\psi) = \frac{V_o^2}{2} + g'(h_i(\psi) - H_o) \tag{3.4}$$

$$K(\psi) = \frac{dG(\psi)}{d\psi} = f/h_i(\psi) \tag{3.5}$$

Inserting (3.4) and (3.5) into (2.6) and (2.5) yields the governing equations:

$$\nabla_H \cdot \left(\frac{\nabla_H \psi}{h}\right) + f = hf/h_i(\psi) \tag{3.6}$$

$$\frac{1}{2}\left(\frac{\nabla_H \psi}{h}\right)^2 + g'\xi = \frac{V_o^2}{2} + g'(h_i(\psi) - H_o) \tag{3.7}$$

In terms of the non-dimensional variables defined in (2.9) the governing equations are:

$$4Ro\nabla\cdot\left(\frac{\nabla\psi^*}{h^*}\right) + 1 = h^*\left[\left(1 - \frac{F_1}{2Ro}\right)^2 + \frac{2F_1\psi^*}{Ro}\right]^{-1/2} \tag{3.8}$$

$$F_1\left[2\left(\frac{\nabla\psi^*}{h^*}\right)^2 - \frac{1}{2}\right] + h^* = \left[\left(1 - \frac{F_1}{2Ro}\right)^2 + \frac{2F_1\psi^*}{Ro}\right]^{1/2} \tag{3.9}$$

The last two equations can be combined to form the single non-linear equation

$$\nabla\cdot\left(\frac{\nabla\psi^*}{h^*}\right) = \frac{F_1}{4Ro}\left[\frac{1}{2} - 2\left(\frac{\nabla\psi^*}{h^*}\right)^2\right]\left[\left(1 - \frac{F_1}{2Ro}\right)^2 + \frac{2F_1\psi^*}{Ro}\right]^{1/2} \tag{3.10}$$

The boundary conditions are:

$$\left.\begin{array}{lll}
\psi^* = 0 & ; \quad x^* = -c & 0 \le y^* < \infty \\
\psi^* = 0 & ; \quad -c < x^* < -1 & y^* = 0 \\
\psi^* = \frac{1}{2}(1 + x^*) - \frac{F_1}{8Ro}[1 - (x^*)^2] & ; \quad -1 \le x^* \le 1 & y^* = 0 \\
\psi^* = 1 & ; \quad 1 < x^* < c & y^* = 0 \\
\psi^* = 1 & ; \quad x^* = c & 0 \le y^* < \infty \\
\frac{\partial\psi^*}{\partial y^*} = 0 & ; \quad -c \le x^* \le c & y^* \to \infty
\end{array}\right\} \tag{3.11}$$

It is further assumed that the transport function and the layer depth possess asymptotic expansions in the form:

$$\left.\begin{array}{l}
\psi^* = \psi^{(o)} + F_1\psi^{(1)} + \ldots \\
h^* = h^{(o)} + F_1 h^{(1)} + \ldots
\end{array}\right\} \tag{3.12}$$

where F_1 is smaller than unity. The expansion is uniformly valid if $\psi^{(o)} > F_1\psi^{(1)}$ in the whole field. We consider Ro to be a fixed parameter which is not asymptotically small: $(F_1/Ro) << 1$. By substituting (3.12) into (3.9) and (3.10) and equating like powers of F_1, one obtains the zeroth order equations:

$$\left.\begin{array}{l} \nabla^2\psi^{(o)} = 0 \\ \\ h^{(o)} = 0 \end{array}\right\} \qquad (3.13)$$

and the first order equations:

$$h^{(1)} = \frac{1}{2} - 2(\nabla\psi^{(o)})^2 + (\psi^{(o)} - 1/2)/Ro \qquad (3.14)$$

$$\nabla^2\psi^{(1)} = \frac{1}{4Ro}\left[\frac{1}{2} + 2(\nabla\psi^{(o)})^2\right] - 2\nabla\psi^{(o)} \cdot \nabla\left[(\nabla\psi^{(o)})^2\right] \qquad (3.15)$$

It will be seen shortly that the last term in (3.15) is negligible for the cases of interest where $c >> 1$. The boundary conditions are obtained by inserting (3.12) into (3.11) and equating like powers of F_1.

One finds that the boundary conditions for $\psi^{(o)}$ are the same as those given by (2.18) and for $\psi^{(1)}$ the same as (2.19), except at the outlet where:

$$\psi^{(1)} = [(x^*)^2 - 1]/8Ro \qquad (3.16)$$

A) Solution of the zeroth and first order questions

The solution of (3.13) subject to its boundary conditions has been found earlier and is given completely by (2.23).

The last term on the right hand side of (3.15) is a function of the zeroth order solution only; it vanishes far downstream since the velocity is constant there. The following argument shows that it vanishes also in the vicinity of the outlet provided that $c^2 >> 1$.

For a very wide basin the solution in the vicinity of the outlet, except to a distance of $\Theta(b)$, is given by $\lim_{c\to\infty}\psi^{(o)} = \lim_{c\to\infty}\psi_H$, where ψ_H is given by (2.23). This yields

$$\psi^{(o)} = \frac{1}{2} + \frac{1}{\pi}\tan^{-1}(x^*/y^*); \; |x^*|, \; y^*>1$$

for which the term $\nabla\psi^{(o)} \cdot \nabla[(\nabla\psi^{(o)})^2]$ is identically zero. Therefore (3.15) can be approximated over most of the domain by:

$$\nabla^2\psi^{(1)} \simeq \frac{1}{4Ro}\left[\frac{1}{2} + 2(\nabla\psi^{(o)})^2\right] \tag{3.16a}$$

provided that $c>>1$.

We now consider the first order problem. We define $\psi^{(1)} = \psi_H^{(1)}/Ro + \psi_p^{(1)}$. Noting the similarity of the problem (3.16a) to the step down case (2.13) one finds using (3.13) that the non-separating particular solution is:

$$\psi_p^{(1)} = (\psi^{(o)})^2/4Ro + \frac{1}{16Ro}[(x^*)^2 - c^2] + \frac{\tilde{\psi}}{Ro}(x^*, y^*) \tag{3.17}$$

where $\tilde{\psi}$ is defined by

$$\tilde{\psi}(x^*, 0) + \frac{1}{16}[(x^*)^2 - c^2] = 0$$

$$\lim_{y^*\to\infty}\tilde{\psi}(x^*, y^*) = 0; \; \nabla^2\tilde{\psi}(x^*, y^*) = 0$$

Note that $\psi_p^{(1)}$ does not satisfy homogeneous boundary conditions with this definition, in contrast to the particular solution discussed in section 2. The function $\tilde{\psi}$ has been found earlier, and is given by (2.41) with $D = 1/16$.

To simplify the boundary conditions for $\psi_H^{(1)}$ one may add $-\psi^{(o)}/4Ro$ to the right hand side of (3.17); the latter cancels the contribution of $(\psi^{(o)})^2/4Ro$ along the solid boundaries. The revised $\psi_H^{(1)}$ obeys non-homogeneous boundary conditions at the mouth; the complete boundary conditions for $\psi_H^{(1)}$ are:

$$\left.\begin{array}{rlll}
\psi_H^{(1)} & = 0 & x^* = -c & 0\leq y^*<\infty \\
\psi_H^{(1)} & = 0 & -c<x^*<-1 & y^* = 0 \\
\psi_H^{(1)} & = \dfrac{(x^*)^2 - 1}{16} & -1\leq x^*\leq 1 & y^* = 0 \\
\psi_H^{(1)} & = 0 & 1<x^*<c & y^* = 0 \\
\psi_H^{(1)} & = 0 & x^* = c & 0\leq y^*<\infty \\
\partial\psi_H^{(1)}/\partial y^* & = 0 & -c\leq x^*\leq c & y^*\to\infty
\end{array}\right\} \quad (3.18)$$

The function $\psi_H^{(1)}$ is found by the Schwartz Christoffel transformation and the Fourier integral to be:

$$\psi_H^{(1)} = \frac{\beta}{16\pi}\int_{-\pi/2c}^{+\pi/2c} \frac{\left[\left(\frac{2c}{\pi}\right)^2\phi^2 - 1\right]d\phi}{\beta^2 + (\alpha - \phi)^2} + \theta\left(\frac{\pi}{24c^2}\right)$$

which yields

$$\left.\begin{array}{l}
\psi_H^{(1)} \simeq \dfrac{c^2}{4}\,\dfrac{\beta\alpha}{\pi^3}\ln\dfrac{\beta^2 + (\alpha - \pi/2c)^2}{\beta^2 + (\alpha + \pi/2c)^2} + \dfrac{c\beta}{4\pi^2} \\
+ \dfrac{1}{16\pi}\left[1 + \dfrac{4c^2(\beta^2 - \alpha^2)}{\pi^2}\right]\left[\tan^{-1}\left(\dfrac{\alpha - \pi/2c}{\beta}\right) - \tan^{-1}\left(\dfrac{\alpha + \pi/2c}{\beta}\right)\right]
\end{array}\right\} \quad (3.19)$$

where $\alpha(x^*, y^*)$ and $\beta(x^*,y^*)$ are given by (2.21). This function $\psi_H^{(1)}$ vanishes far from the outlet. The complete solution is

$$\psi^*\simeq\psi^{(o)} + \frac{F_1}{Ro}\left[\psi_H^{(1)} - \psi^{(o)}/4 + \left(\psi^{(o)}\right)^2/4 + \tilde{\psi}\,(x^*, y^*) + \frac{(x^*)^2 - c^2}{16}\right] + \Delta \quad (3.20)$$

where $\psi^{(o)}$ is given by (2.23), $\psi_H^{(1)}$ by (3.19) and $\tilde{\psi}(x^*, y^*)$ by (2.41) with $D = 1/16$. The error, Δ, in (3.20) is $\Delta \sim \theta(F_1/Ro)^2 + \theta(\frac{\pi}{24c^2})$. Note that, to this order, the solution depends only upon F_1/Ro and c.

A typical non-separating solution of (3.20) is given in Figure 11(A), which shows that the streamlines are displaced to the right. The latter result could be expected; as the flow spreads, the velocity decreases and the Bernoulli principle implies that an equivalent step down of as much as $V_o^2/2g'H_o$ is actually created by the flow.

To investigate the possibility of separation, we examine the limit of ψ^* from (3.20) as $y^* \to \infty$.

$$\lim_{y^*\to\infty}\psi^* = \frac{x^*+c}{2c} + \frac{F_1}{Ro}\left[-\left(\frac{x^*+c}{8c}\right) + \frac{(x^*+c)^2}{16c^2} + \frac{(x^*)^2 - c^2}{16}\right] \tag{3.21}$$

which implies

$$\lim_{y^*\to\infty}\frac{\partial\psi^*}{\partial x^*} = \left(1 - \frac{F_1}{4Ro}\right)\frac{1}{2c} + \frac{F_1}{8Ro}\left(\frac{x^*+c}{c^2}\right) + \frac{F_1 x^*}{8Ro} \tag{3.22}$$

One observes that for negative x^* and a sufficiently small Rossby number, the velocity may become negative. But, as has been previously explained, such a situation is impossible. Thus, separation does occur and the critical Rossby number is given by the condition that the velocity vanishes at the left bank. Inserting $\frac{\partial\psi^*}{\partial x^*} = 0$ and $x^* = -c$ into (3.22) yields

$$Ro_c = F_1\,(1 + c^2)/4 \tag{3.23}$$

If $Ro < Ro_c$, ψ^* is no longer given by (3.20) but by:

$$\psi^* \simeq \psi^{(o)} + \frac{F_1}{Ro}\Big[\underbrace{\psi_H^{(1)} - \psi^{(o)}/4 + (\psi^{(o)})^2/4}_{(B)} + \tilde{\Psi}_{SC} + \frac{(x^*-c)(x^*+\delta)}{16}\Big] \tag{3.24}$$

where $\tilde{\Psi}_{SC}$ is given by (2.42) with $D = 1/16$ and δ is to be determined.

To obtain the location of the separation line and δ, we equate

$\psi^*|_{y^*\to\infty}$ and $\frac{\partial\phi^*}{\partial y^*}|_{y^*\to\infty}$ evaluated from (3.24) to zero. As in previous cases these equations yield two solutions; the physically relevant solution is

$$d = c - 4c\left[\frac{Ro}{F_1(1 + c^2)}\right]^{1/2} \qquad (3.25)$$

and

$$\delta = c - \frac{2(1 + c^2)}{c}\left\{1 - 4\left[\frac{Ro}{F_1(1 + c^2)}\right]^{1/2}\right\} - 8Ro/F_1c \qquad (3.26)$$

which for $c^2 >> 1$ can be approximated by

$$d \simeq -4\sqrt{\frac{Ro}{F_1}} + c \qquad (3.27)$$

$$\delta \simeq -c + 8\sqrt{\frac{Ro}{F_1}} - 8Ro/F_1c \qquad (3.28)$$

The current width ($<2c$) is $4\sqrt{\frac{Ro}{F_1}} >> 1$ by (3.27).

Typical separating solutions ($Ro<Ro_c$) are shown in Figure 11(B) and (C). In most of the field the perturbation ($F_1\psi^{(1)}$) is smaller than the basic state ($\psi^{(o)}$), but at the separation line the two have the same value. For such cases the perturbation theory is not applicable a priori, and a further investigation is required.

It is clear that whether there is separation or not, the expanded solution (3.24) is valid in the vicinity of the outlet since the perturbation there is small. If $c^2>>1$ and $\sqrt{\frac{Ro}{F_1}} >>1$, the basin and the long-shore current are very wide in comparison to the channel; the final flow speed is very small ($\theta\left(\sqrt{\frac{F_1}{Ro}}\right)$) and so the non-linear terms in (3.10) can be neglected downstream. Under such conditions the equation controlling the flow downstream

$$\left.\begin{array}{ll}\text{is} & \nabla^2\psi^* \simeq F_1/8Ro \\ \text{with} & h^* \simeq 1 + \theta(F_1)\end{array}\right\} \quad (3.29)$$

This equation has a solution of ψ^*, which is identical to (3.24) with $B = 0$. It is easily verified that when the current width is small in comparison to the basin width, then $\lim_{y^*\to o} B = 0$; this shows that, for $c \gg 4\sqrt{\frac{Ro}{F_1}} \gg 1$, equation (3.24) yields the proper solution both near the outlet and far downstream.

In the exterior region the upper layer is assumed to have the same depth as the depth of the interior at the separation line. The solution to the exterior is equivalent to the one given in Section 2. Note that the solution presented in this section also describes motions in a layer with a flat bottom and a free surface in two types of cases:

a) a deep inert layer of density $(\rho - \Delta\rho)$ overlying this layer; and

b) a single layer system where the internal Froude number (F_1) is replaced by F.

B) Comparison with the quasi-geostrophic solution

The quasi-geostrophic solution may be obtained from equations (3.14) and (3.15) by considering $Ro \ll 1$, but constraining $F_1 \leq Ro^2$ (as required by the quasi-geostrophic theory) so that the asymptotic expansion in F_1 still holds. The result is

$$h^* = 1 + \theta(F_1/Ro) \tag{3.30}$$

and

$$\nabla^2\psi^* = 0 + \theta(F_1/Ro) \tag{3.31}$$

The latter equation subject to its boundary conditions (2.18) has the solution given by (2.23) and does not allow any deflection.

Outflow from a short "strait"

Consider Figure 10(B). The problem is to determine the behavior of the upper layer as it is compressed and accelerated upon entering the "strait," reaching a geostrophic balance and then spreading as it enters the basin. The adjustment in the basin is different from that considered in Figure 10(A), due to the non-uniform flow which is established upstream from the outlet. The "strait" is assumed to be relatively short so that friction can be neglected along it; at the same time, it is assumed to be long enough (θ(bRo)) so that the flow near the outlet is in geostrophic balance. It is also assumed that the depth of the layer from which the lighter fluid is advected into the strait is very large in comparison to the depth of the layer in which the adjustment is taking place.

Far upstream the velocities are assumed to be very small. Substitution of this boundary condition into (2.5) and (2.6) yields:

$$K(\psi) = f/H_i; \; G(\psi) = g\eta_i \tag{3.33}$$

where H_i is the depth of the layer upstream, η_i the positive upstream surface displacement and Ho the average depth of the upper layer in the "strait." The potential vorticity equation in the "strait " and basin becomes

$$\nabla_H \cdot \left(\frac{\nabla_H\psi}{h}\right) = - f\ (1 - h/H_i) \tag{3.34}$$

which for $h/H_i \ll 1$ reduces to

$$\nabla_H \cdot \left(\frac{\nabla_H\psi}{h}\right) = - f \tag{3.35}$$

The assumption $h \ll H_i$ requires that $K(\psi) \approx 0$ and so $G(\psi)$ is thus a constant everywhere. These values of $K(\psi)$ and $G(\psi)$ have been used for a different case by Whitehead et al (1974) who studied the dynamics of the lower layer in sea straits. Equation (3.35) states that the absolute vorticity is approximately zero, so the relative vorticity is large and negative, as in the case of the one layer model with a large step up. The upstream surface displacement η_i can be expressed in terms of the average velocity at the "strait" V_o; therefore

$$G(\psi) = V_o^2/2$$

In non-dimensional form, the potential vorticity and the Bernoulli equations are then

$$\nabla \cdot (\nabla\psi^*/h^*) = -1/(4Ro) \tag{3.36}$$

$$4F_1(\nabla\psi^*/h^*)^2 + 2(h^* - 1) = F_1 \tag{3.37}$$

These equations appear simpler than (3.8) and (3.9) found for the infinitely long "strait" (uniform flow) case. In the "strait", the velocity near the outlet is assumed to be independent of y; equation (3.35) yields the geostrophic solution with zero absolute vorticity:

$$v = V_o - fx \tag{3.38}$$

which enables one to evaluate ψ:

$$\psi = \int_{-b}^{x} (V_o - fx)\,[H_o + \frac{1}{g'}\int_{o}^{x} (fV_o - f^2x)dx]dx$$

where the second integral represents the inferface displacement $\xi(x)$. Expressed in non-dimensional variables, the latter equation takes the form:

$$\psi^* = \frac{1}{2}(x^* + 1) + (F_1 - 1)[(x^*)^2 - 1]/(8Ro) - \frac{F_1}{32Ro^2}[(x^*)^3 + 1] + \frac{F_1}{128Ro^3}[(x^*)^4 - 1] \tag{3.39}$$

where $Ro = V_o/2fb$ and is larger than 0.5 so that the flow at the "strait" touches both banks ($V^*(x^*) > 0$). Note that due to this limitation, the quasi-geostrophic theory probably cannot be applied to this case.

Equation (3.39) gives the boundary conditions for ψ^* at the outlet to the basin ($-1 \le x^* \le 1$; $y^* = 0$). Other basin boundary conditions are the same as those given by (2.18). It is further assumed that ψ^* and h^* possess asymptotic expansions in the form:

$$\left.\begin{aligned} \psi^* &= \psi^{(o)} + F_1\psi^{(1)} + \dots \\ h^* &= h^{(o)} + F_1 h^{(1)} + \dots \end{aligned}\right\} \tag{3.40}$$

where F_1 is smaller than unity and Ro is fixed and is not asymptotically small. By substitution of (3.40) into (3.36) and (3.37) and equating like powers of F_1 one obtains the zeroth order equations:

$$\left.\begin{aligned} \nabla^2\psi^{(o)} &= -1/4Ro \\ h^{(o)} &= 1 \end{aligned}\right\} \tag{3.41}$$

and the first order equations:

$$\left.\begin{aligned} h^{(1)} &= \frac{1}{2} - 2(\nabla\psi^{(o)})^2 \\ \nabla^2\psi^{(1)} &= -\frac{1}{8Ro} + \frac{1}{2Ro}(\nabla\psi^{(o)})^2 - 2\nabla \cdot \nabla[(\nabla\psi^{(o)})^2] \end{aligned}\right\} \qquad (3.42)$$

We will see shortly that $\psi^{(o)}$ is a more complicated function of x* and y* than previously, so that (3.42) cannot be solved easily. It will be shown, however, that separation can be understood from equation (3.41) alone.

The boundary conditions for the zeroth and first order equations are obtained by inserting (3.40) into (3.39) and collecting terms of the same order. One finds that the boundary conditions for $\psi^{(o)}$ are the same as (2.18) except at the outlet where

$$\psi^{(o)} = \frac{1 + x^*}{2} + [1 - (x^*)^2]\ Ro^{-1}/8 \qquad (3.43)$$

To simplify the homogeneous solution, $\psi_H^{(o)}$, it is divided into two parts: $\psi_H^{(o)} = \psi_{1H}^{(o)} + \psi_{2H}^{(o)}$; $\psi_{1H}^{(o)}$ satisfies the first term of (3.43) (therefore, its solution is given by (2.23)), and $\psi_{2H}^{(o)}$ satisfies the second. The Schwartz Christoffel transformation and the Fourier integral yield

$$\left.\begin{aligned} \psi_{2H}^{(o)} &= \frac{-\alpha\beta c^2}{2Ro\pi^3} \ln \frac{\beta^2 + (\alpha - \pi/2c)^2}{\beta^2 + (\alpha + \pi/2c)^2} \\ &+ \frac{1}{8Ro}\left[\tan^{-1}\left(\frac{\alpha + \frac{\pi}{2c}}{\beta}\right) - \tan^{-1}\left(\frac{\alpha - \frac{\pi}{2c}}{\beta}\right)\right]\left[\frac{1}{\pi} + \frac{4c^2(\beta^2 - \alpha^2)}{\pi^3}\right] \\ &+ c\beta/(2\pi^2 Ro) + \theta(\pi/(24c^2)) \end{aligned}\right\} \qquad (3.45)$$

The particular solution has the form:

$$\psi_p^{(o)} = -\frac{1}{8Ro}[(x^*)^2 - c^2] + \tilde{\psi}(x^*, y^*) \qquad (3.46)$$

where $\tilde{\psi}$ is given by (2.41) with $D = -Ro^{-1}/8$. At infinity the solution is equivalent to the solution of the step-up case; therefore a sufficiently small Rossby number causes separation. Under such conditions, relation (3.46) should be replaced by

$$\psi_{SC}^{(o)} = -\frac{1}{8Ro}(x^* + c)(x^* - \delta) + \tilde{\psi}_{SC}(x^*, y^*) \tag{3.47}$$

where $\tilde{\psi}_{SC}$ is given by (2.43) with $D = -Ro^{-1}/8$. To find the location of the separation line and δ, one uses the conditions and techniques described in previous sections. The results are:

$$\delta = 4\sqrt{2Ro} - c - 4Ro/c \tag{3.48}$$

and the location of the separation line is $d = \sqrt{4Ro} - c$ (3.49)

The critical condition is found when the separation line coincides with the right wall. Equation (3.49) yields:

$$Ro_c = c^2/2 \tag{3.50}$$

This value is typically much larger than that found for the infinitely long "strait" (uniform flow) case, and is somewhat larger than the one-layer case. Note that the zeroth order approximation is valid as long as

$$\frac{F_1}{Ro} \ll 1; \quad \frac{F_1}{32Ro^2} \ll 1; \quad \frac{F_1}{128Ro^3} \ll 1$$

Typical solutions with and without separation are shown in Figures 12(A) and (B).

4. LABORATORY EXPERIMENTS

Basic Design Considerations

The experimental apparatus (Figures 13 and 16) was designed to test qualitatively the three theories described previously. It was designed such that:

A) Frictional forces which arise due to vertical walls have a limited effect on the flow. To achieve this, apparatus characteristics were chosen such that the minumum channel Reynolds number is of the order of several hundred, and by designing the channel width and length so that the horizontal boundary layer thickness is small in comparison with the channel width (whenever possible). This boundary layer is not necessarily thin, however, compared to the separated current width. For example, Schlicting (1968) gives $5\sqrt{\frac{\nu\ell}{v}}$ for the former, which for $\ell \simeq 15$cm, $v \simeq 0.5$ cm/sec, and $\nu = 10^{-2}$ cm^2/sec is about 2.5cm, a thickness comparable to the separated current. Thus, the details of the final current will be influenced by side boundary friction.

It is expected that for one layer experiments frictional forces on the bottom will establish an Ekman layer of finite thickness $\pi\left(\frac{\nu}{\Omega}\right)^{1/2}$, which for $\Omega = 2$ rad/sec gives a thickness of about 2mm, much smaller than the working layer thickness of about 7cm. The associated "spin down" time scale $t \sim \theta\left[f^{-1}\ H\left(\frac{\Omega}{\nu}\right)^{1/2}\right]$, (Greenspan, 1968) for the influence of secondary motions upon the main layer is of θ (10sec.). The advection transport time scale for the basin is of θ (30sec), so we conclude that bottom friction and secondary circulations can also significantly influence the laboratory results of the one layer experiment.

B) The flow at the outlet is close to geostrophic balance and is as uniform as possible. This was accomplished by extending the channel length downstream from the filter so that the corresponding Rossby number based on the distance from the filter to the outlet was small.

One layer experiments

A) Apparatus and Method of Observation

A schematic diagram of the experimental apparatus is shown in Figure 13. The test section consists of a channel 7.65cm wide and a basin 30.48cm wide, 30.48cm long and 12.74cm high. The walls and bottom were constructed from 1.25 cm plexiglass plates (made thick to increase the rigidity of the system). The height of the bottom could be changed by removing or adding 2.54cm thick plexiglass plates in either the channel or the basin. This permitted the placement of steps up or down as desired.[1] Two filters were constructed (in the inlet and outlet) to produce a desired velocity distribution across the channel. Filters with a constant thickness (measured downstream along the y axis) produce a uniform velocity distribution due to the viscosity of the water and the porosity of the filter. A triangle-shaped filter

---

[1] The height of the step was chosen to be large in comparison to the surface variations caused by the rotation of the table (about 1cm in the basin).

(whose thickness varies linearly in x from almost zero cm at $x = a$ to 9 cm at $x = -a$) was used to produce a linear velocity distribution across the channel. An impeller 12v pump was used to maintain a flow of about 3 liters/minute through the channel. Typical flow speeds in the channel were 0.5 to 1.0cm/sec. To eliminate the influence of air flow on the fluid, the test container was covered with a clear flat plexiglass plate.

The system was mounted on a 80cm diameter turntable, driven by a variable speed AC motor with a single reduction gear drive. Before the experiments were performed, the basin was leveled to within 30 seconds of arc and centered to less than ± 0.1 cm of the rotation axis of the table. Short term stability of the rotation rate (in few revolutions) was checked by a strobe light and found to be within a fractional deviation of 0.1% with careful balance of the apparatus on the table.[1] The rotation rate was very stable over long periods of time and the deviation was not larger than 0.5% in the long runs (1 hour). The typical rotation rate was $\Omega = 2$ rad $\sec^{-1}$ and the Rossby number $\left(\frac{U}{4\Omega b}\right)$ varied between 0.01 and 0.05.

Water was used as the working fluid; for flow visualization, a DuPont Rodamine dye was injected into the fluid after a steady state had been reached. The amount of dye injected into the system was very small in comparison to the volume flux through the channel. The pure dye was slightly heavier than the water but not so heavy that its advection due to the centripetal or gravitational acceleration was noticeable. The latter was determined by comparing the spreading pattern of dye injected into a stationary container to spreading in a rotating container which had reached a "solid body" rotation with zero relative motion.

A 35mm camera was mounted on a stationary frame vertically above the rotating test container. To maximize clarity, camera shutter speed was set at 1/250 sec. A picture was taken every few seconds (on Kodak Tri-X film) as the dye was advected by the fluid.

B) Experimental procedure and results

Experiments were performed only for separating flows (super-critical Rossby numbers), since other flow patterns require a parabolic bottom with deviation of about 1cm over the basin. Construction of an

---

[1] Any weight mounted non-symmetrically on the table tends to introduce a periodic variability in the short-term rotation rate.

accurate parabolic bottom and associated apparatus would have been quite difficult. The depth of the resting fluid varied between 7.5 and 10cm.

Experiments with an abrupt step down ($\Delta H = +2.54$cm) showed a deflection to the right; a sudden step up ($\Delta H = -2.54$cm) produced a deflection to the left, as the theory predicts. These experimental results are shown in Figure 14; one may compare them with the theoretical prediction for approximately the same width ratio and step size shown earlier in Figure 6. Detailed comparison is impossible due to: a) the influence of friction and b) the difference between dye width and current width. Also, of course, depth is not constant. However, the photographs of Figure 14 do show high velocity near the basin wall as the theory predicts. About thirty experiments were performed with $\Omega = 1.9$ rad/see and $0.01 \leq Ro \leq 0.05$ (where $Ro \ll Ro_c \sim 2$); all showed the result mentioned above.

With a completely flat bottom (no step) the current deflected to the left (Figure 15) due to the parabolic shape of the surface which acts as a gradual step up on the inlet side of the basin.

When a linear velocity distribution with a cyclonic shear of $1/7.5\ \text{sec}^{-1}$ was introduced upstream, the deflection was neutralized (Figures 15, C, and D) as the theory predicts (Figure 9). The proper rotation rate for this experiment was determined by assuming that the gradual step up $\Delta H(r) \simeq \Omega^2 r^2/2g$ can be considered as an abrupt step located at the outlet. For such conditions (2.47) yields:

$$\Omega \sim (gH_o A/r^2)^{1/3}$$

For $A \sim \frac{1}{7.5}\ \text{sec}^{-1}$, $r \sim 15$ cm and $H_o \sim 5$ cm, the above relation gives $\Omega \sim 1.4$ rad/sec. A number of preliminary experiments and adjustments of the volume flux were needed to achieve the flow pattern shown in Figure 15.

Photographs (c) and (d) in Figure 14 and (a) and (b) in Figure 15 show a similar deflection, even though the step in the first two was about four times higher than the equivalent step in the last two. Theory predicts a stronger deflection in the first case; this disagreement may be due to bottom friction. The ratio between the thickness of the bottom boundary layer and the fluid depth was, in the first case, about twice as large as the ratio for the second case. Therefore, bottom friction was more important in the first case and perhaps retarded the deflection more effectively.

Two Layer Experiments

A) Apparatus

Two experimental systems were used to test the two-layer model theory (Figure 16). Apparatus shown in Fig. 16(A) was used to test an outflow from a channel with uniform velocity distribution, and Figure 16(B) apparatus to test an outflow from a short strait. All the mechanical, dynamical and observational details given in the previous section, except those which are discussed below, apply also to the two layer apparatus.

Before each experiment the upper layer was formed by pouring, very slowly, fresh water on top of a salt water layer. Salt concentration in the lower layer of Fig. 16(A) was 1.5% and 3.3% in Figure 16(B). The flow in the upper layer was laminar, so salt diffusion during each experiment (1.5 hours) was negligible. As judged from dye variation the interface remained relatively sharp and did not shift more than 1-2 mm.

Due to the relatively heavy load of the two layer apparatus, the short term stability of the turntable was worse than with the one layer apparatus, but the fluctuations did not exceed 0.3%. The long term stability was better than 1%. The experiments were performed at night in order to avoid power variations which, with a heavy load on the table, could cause rotational variations higher than those mentioned above. A typical rotation rate for the two layer experiment was Ω = 2.2 rad/sec. A potentially serious shortcoming of the Figure 16(B) apparatus was that the step effect upstream from the basin was produced by a double rigid sill (seen downstream from the filter in Figure 16) rather than by a lower layer as the theory assumed (see Figure 10(B)).

B) Experimental results

The results of the experiments with apparatus in Figures 16(A) and (B) are shown in Figure 17; the outflows deflect to the right and left respectively, as the theory predicts (Figs. 11(C),12(A)) . Photographs (c) and (d) in Figure 17 show a pattern somewhat less smooth than the others. This may be a result of the relatively high Reynolds number of the flow (about 1100) which could cause the current to be in a transition from laminar to turbulent flow.

Another possibility for flow instability might be baroclinic instability of the inclined interface which supports the velocity differences between the layers. Theory shows (Stern, 1974) that baroclinic instability can occur as long as the length scale is not much smaller than the internal Rossby deformation radius, λ', in both layers. In the experiment $L_u \sim$ 10cm; $\lambda'_u \sim$ 5cm and $L_\ell \sim$ 10cm; $\lambda'_\ell \sim$ 10cm where the subscript "u" denotes "upper layer" and the subscript "l" denotes lower layer. Therefore, baroclinic instability may have been present. Inertial instability was unlikely in the experiment, since the anticyclonic relative vorticity was distinctly less than 2Ω.

The apparatus of Fig. 16(B) was originally designed to test deflections resulting from a very large step up (which was a basic assumption in the short strait theory). Preliminary experiments with a step of about 95% of the upstream height were unsuccessful, however, due to large vertical velocities which arose near the filter and destroyed the interface between the layers. Thus, the fluid thickness was decreased by 50% in the actual experiments.

5. CONCLUSIONS

Summary of results

The results of the one layer theory (Section 2) can be summarized as follows:

i) An outflow from a channel with a uniform velocity distribution deflects to the right if the basin is deeper than the channel and to the left if it is shallower.

ii) There is a "critical" Rossby number, below which the current separates from one of the basin banks, forms a long-shore current with a linear velocity distribution, and produces (downstream) a stagnant domain beyond the separation line. The critical Rossby number is a function of the step size and of the ratio between the width of the basin to the width of the channel.

iii) Without a step the current spreads symmetrically, provided that $\frac{F}{Ro}$ is negligible. If $\frac{F}{Ro}$ is smaller than unity but is not entirely negligible, there will be a slight deflection to the right.

iv) When a non-uniform velocity distribution is introduced upstream in the channel, the direction of deflection may differ from that described above. The current deflects to the right if the sum of the initial relative vorticity and the vorticity created by the step is positive, and to the left if the sum is negative. If the sum of the two is zero, there will be a slight deformation in the vicinity of the outlet, but there will be no deflection downstream (provided that F/Ro is negligible.)

v) Rotation is important if the $\frac{\Delta H^*}{Ro}$ is not negligible.

The basic results described above also can be obtained by the quasi-geostrophic theory. However, this theory is more restrictive and requires that $Ro \ll 1$ and $\frac{\Delta H^*}{Ro^2} \lesssim 1$, in addition to the assumptions which have been made throughout the study. Hence, the full theory allows for flows which may be far from local states of geostrophic balance. Prediction (i) and the last part of prediction (iv) were tested in the laboratory, and the direction of deflection agrees with the theory in both cases.

The two layer theory predicts the following:

i) Outflow from a channel with a uniform velocity distribution (case (A)) deflects to the right if $\frac{F_1}{Ro} < 1$ and to the left (case (B)) if the initial vorticity in the channel is approximately equals to $-f$.

ii) Predictions (ii) and (v) of the one layer theory are also true for the two layer theory, but instead of the relative step size ΔH^*, one makes use of the Froude number for case (A), and a number of unity for case (B).

The quasi-geostrophic theory fails to describe the motions of the two layer model in all cases studied here. For case (A) it yields a symmetrical solution without a deflection, and it probably cannot be applied to case (B) since, for the latter, the Rossby number cannot assume values of less than 0.5.

Prediction (i) was tested in the laboratory and the direction of deflection agreed with that predicted by the theory.

5.2 Suggestions for further study

Some of the questions raised by this study are listed below:

i) What are the detailed processes of adjustment during separation and evolution toward geostrophic balance?

In principle, the solutions of Sections 2 and 3 could be diagnosed in terms of the governing equations by finite difference techniques. Presentation of the pressure field (η (x,y) or ξ (x,y) as well as the flow field (u(x,y); v(x,y); w(x,y)) would be useful.

ii) What are the details of the "exterior" flow near the basin inlet for the extreme cases, in which the width of the separated current is much smaller than the width of the basin?

The determination of this "exterior" flow is an important unsolved problem. It can be formulated relatively easily, but the solution to the non-linear equations in an irregular domain (and irregular boundary conditions) will be difficult to achieve.

iii) How is the adjustment affected if the angle between the channel and the basin is other than ninety degrees?

iv) How would the removed basin boundaries affect the adjustment if the initial channel flow has a separated stagnant region?

v) Can a buoyant outflow from a channel with a uniform flow deflect to the left? The two layer theory for an outflow from a channel with a uniform flow predicts a deflection to the right due to the velocity decrease as the flow enters the basin. The above theory is limited to cases in which F_1/Ro is small compared to unity; it might be that for other values of F_1/Ro the flow will deflect to the left, due to velocity increase.

vi) How is the adjustment affected by a pre-existing cross-flow current? How is it affected by external unsteady influences? It is expected that the question can probably be investigated by methods similar to those used in this study. However, for the second part of the question a different approach should be used, since the generalizations of the potential vorticity equation and the Bernoulli integral (equations (2.5) and (2.6)) are time independent.

ACKNOWLEDGEMENTS

The completion of this study is an important mile-stone in my life and enables me to thank the people who helped bring this about.

I should like to thank my major advisor Professor John A. Young for his suggestion of this research topic and his continuous guidance and inspiration throughout this study. Special gratitude is extended to the other members of my committee: Professor Theodore Green III who introduced me to physical oceanography and Professors John A. Hoopes, David D. Houghton, James F. Kitchell and Wolfgang R. Wasow. I had stimulating discussions on the work presented with Professor John R. Bennett from the Massachusetts Institute of Technology.

I wish to thank Prof. Peter Monkmeyer for providing the facilities of the Civil and Environmental Engineering Fluid Dynamics Laboratory in which the experiments were performed.

This research was supported by NOAA Grant 04-3-158-61. This study was submitted as a thesis in partial fulfillment of the requirements for the degree of Doctor of Philosophy (Ph.D.) in Oceanography and Limnology at the University of Wisconsin-Madison, 1976.

REFERENCES

Charney, J., 1955: The Gulf Stream as an Inertial Boundary Layer. Proc. Nat. Acad. Sci. 41, 10, 731-740.

Chow, V.T., 1959: Open Channel Hydraulics. McGraw-Hill Book Inc.

Clark, R.A. and N.P. Fofonoff, 1969: Oceanic flow over varying bottom topography. J. Mar. Res. 27, 2, 226-240.

Courant, B. and D. Hilbert , 1962: Methods of Mathematical Physics. Vol. II. Interscience Publishers.

Eckart, C., 1960: Hydrodynamics of Oceans and Atmospheres. Pergammon Press.

Ellison, T.H. and J.S. Turner, 1959: Turbulent entrainment in stratified flows. J. Fluid Mech. Vol. 6, pt. 3.

Forsythe, E.G. and W.R. Wasow, 1960: Finite Differences Methods for Partial Differential Equations. John Wiley and Sons, Inc., N.Y.

Gradshteyn, I.S. and I.N. Ryzhik, 1968: Table of Integrals, Series, and Products. Translated from Russian, Academic Press.

Greenspan, H.P., 1968: The Theory of Rotating Fluids. Cambridge University Press, London.

Gutman, L.N., 1972: Introduction to the Non-linear Theory of Mesoscale Meteorological Processes. Translated from Russian, NOAA, U.S. Dept. of Commerce.

Koh, R.C.Y., 1970: Mathematical models for the prediction of temperature distributions resulting from the discharge of heated water into large bodies of water. Water Quality Office, Environmental Protection Agency, U.S. Government Printing Office.

Krauss, W., 1973: Methods and Results of Theoretical Oceanography. Part I, Gebrüder Borntrager, Berlin.

Paul, J. and W. Lick, 1974: A numerical model for thermal plumes and rivers discharge. Proc. 17th Conf. on Great Lakes Research.

Pearson, C.E., 1974: Handbook of Applied Mathematics. Van Nostrand Reinhold Comp.

Proudman, J., 1952: Dynamical Oceanography, John Wiley and Sons.

Rossby, C.G., 1938: On the mutual adjustment of pressure and velocity distributions in certain simple current systems. J. Mar. Res. 1, 236-263.

Schlichting, H., 1968: Boundary Layer Theory. McGraw-Hill, Inc.

Stern, Melvin E., 1972: Hydraulically critical rotating flow. Phy. Fluids 15, 2062-2064.

_______________ , 1974: Ocean Circulation Physics. N.Y., San Francisco, London, Academic Press.

Stolzenbach, K.D. and D.R.F. Harleman, 1971: An analytical and experimental investigation of surface discharges of heated water. Water Quality Office, Environmental Protection Agency, U.S. Government Printing Office.

Stommel, H. and H.G. Farmer, 1952: Abrupt change in width in two-layer open channel flow. J. Mar. Res. 11, 205-214.

Takano, K., 1954: On the velocity distribution off the mouth of a river. J. Oceanog. Soc. Japan, Vol. 10, No. 2.

__________ , 1955: A complementary note on the diffusion of the seaward river flow off the mouth of a river. J. Oceanog. Soc. Japan, Vol. 4.

Van Dike, M., 1964: Perturbation Methods in Fluid Mechanics. Academic Press, New York.

Veronis, G. and C.C. Yang, 1972: Nonlinear source-sink flow in a rotating pie-shaped basin. J. Fluid Dynamics, Vol. 51, part 3, pp. 513-527.

Waldrop, W.R. and R.C. Farmer, 1974: Three-dimensional computation of buoyant plumes. J. Geophysical Res. 79, 9.

Whitehead, J.A., A. Leetmaa, and R.A. Knox, 1974: Rotating hydraulics of strait and sill flows, J. of Geophysical Fluid Dynamics, Vol. 6, pp. 101-125.

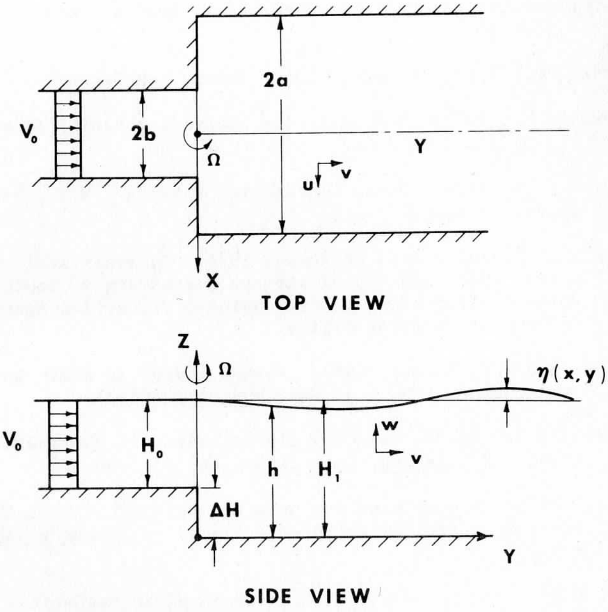

FIGURE 1: Geometry and definition of variables for the one-layer model. ΔH is measured upward from the basin bottom; η is measured upward from the undisturbed surface.

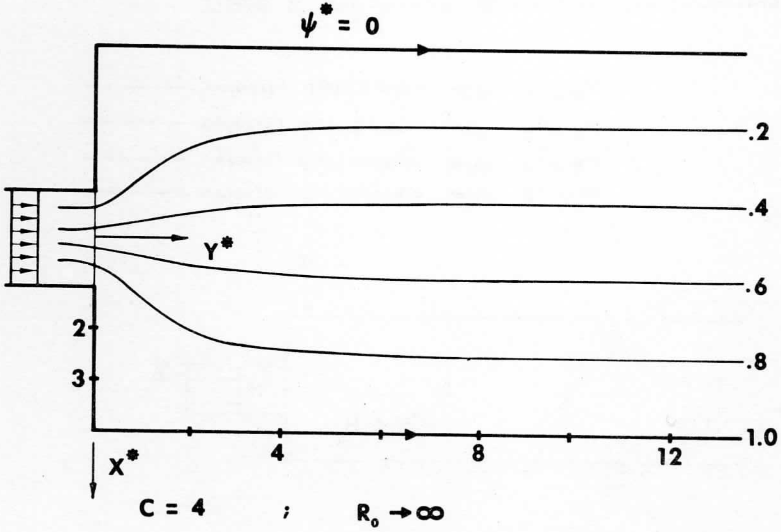

FIGURE 2: The homogeneous solution.

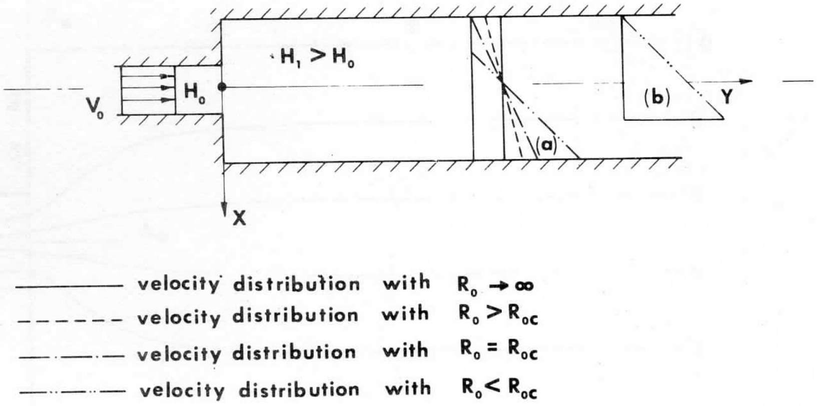

FIGURE 3: The velocity distribution far downstream.

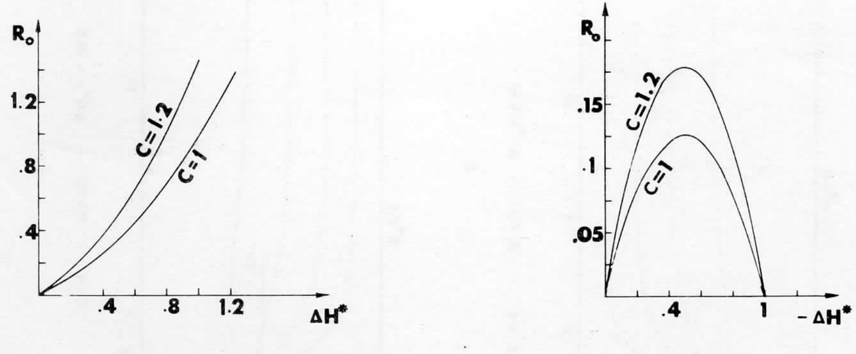

A

B

FIGURE 4: Separation regimes as a function of the Rossby number and the step size. "Critical" curves for each value of c are shown with separation regimes lying below each curve. A step up (B) and a step down (A).

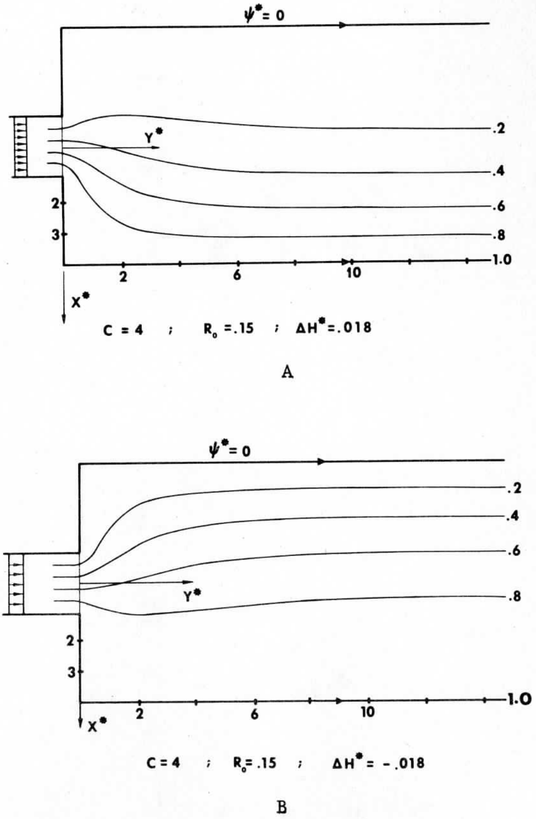

FIGURE 5: Streamlines for a step down (A) and a step up (B). "Subcritical" conditions ($Ro > Ro_c$).

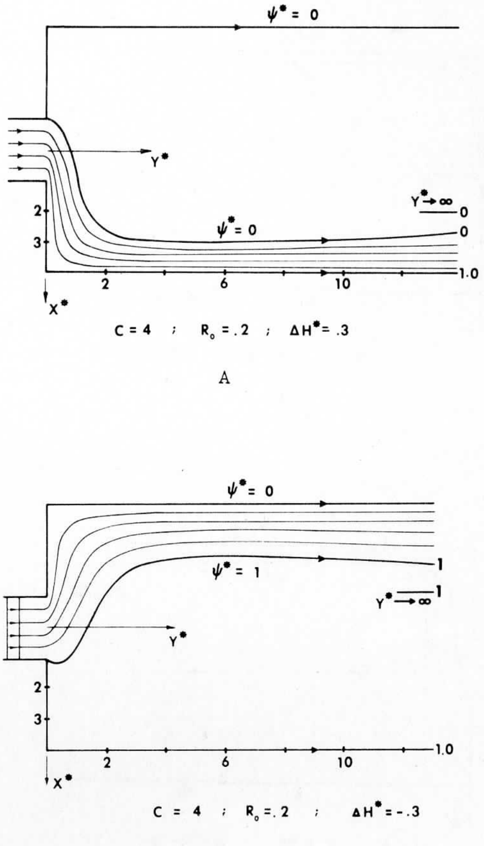

FIGURE 6: Same as Fig. 5, but with "supercritical" Rossby number ($Ro < Ro_c$). Step up (B) and step down (A).

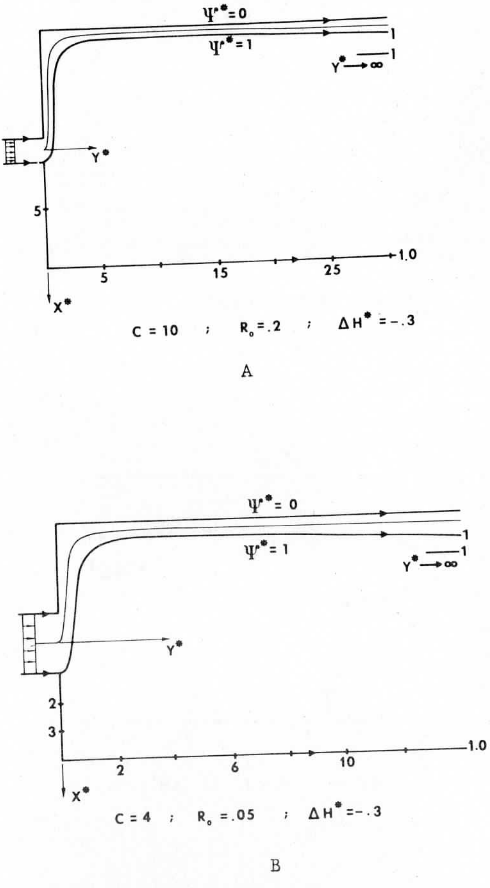

FIGURE 7: Same as Fig. 6, but with a wide basin (A), and a small Rossby number (B).

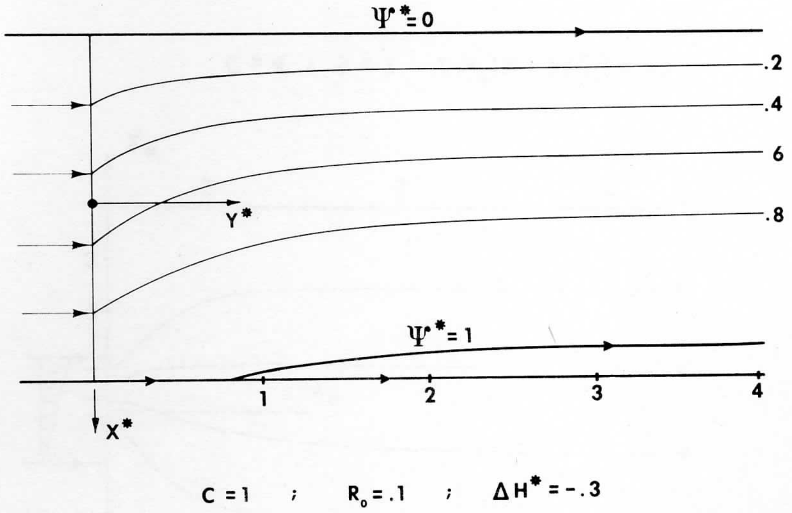

FIGURE 8: Streamlines for a channel and basin which have the same width. "Supercritical" ($Ro < Ro_c$) for a step up.

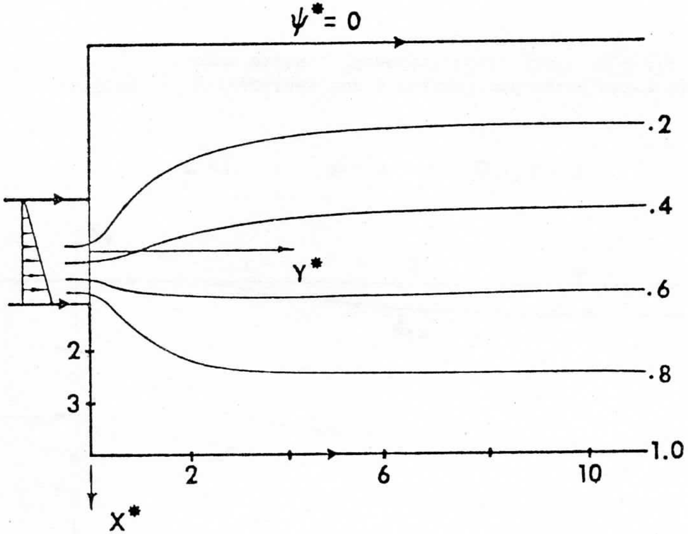

$C = 4 \; ; \; S = 2 \; ; \; \Delta H^*(4 + 2R_o^{-1}) = -1$

FIGURE 9: Streamlines for outflow from a channel with an upstream linear velocity distribution and a cancelling step up.

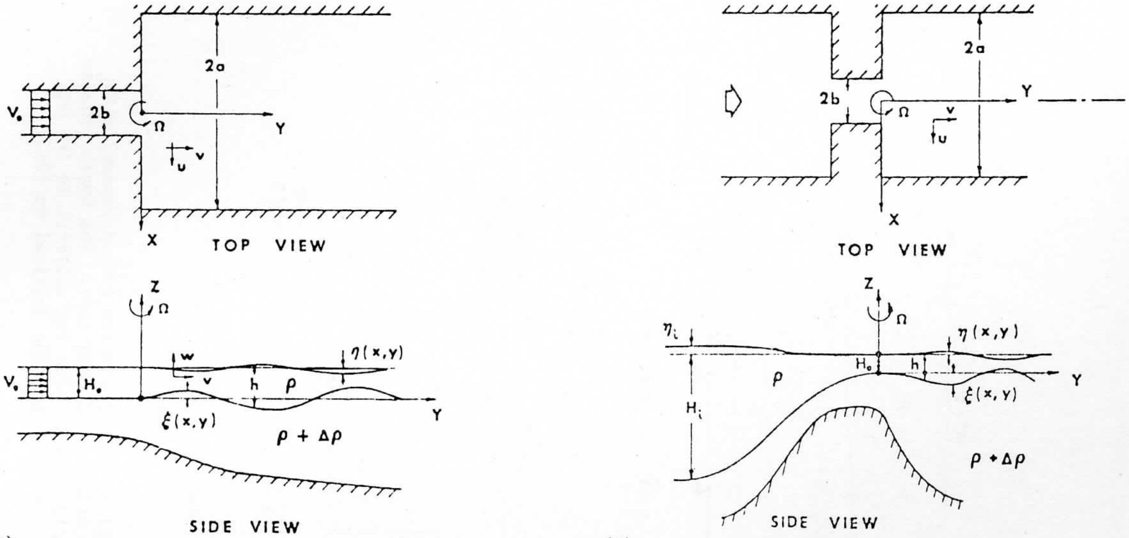

(A) (B)

FIGURE 10: Geometry adopted for the two-layer model.
Case A: Outflow from a channel with uniform velocity distribution.
Case B: Outflow from a short strait.
η and ζ are measured positively upward and downward, respectively.

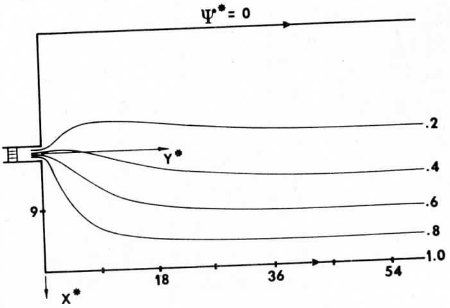

A

$C = 18 \quad ; \quad F_1/R_0 = .012$

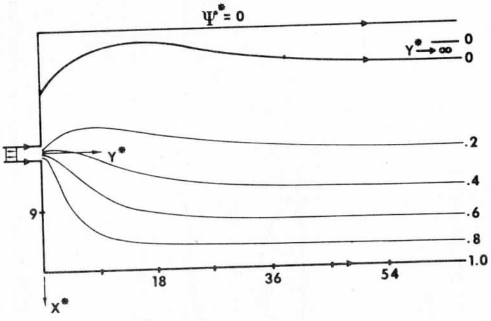

B

$C = 18 \quad ; \quad F_1/R_0 = .015$

FIGURE 11: Streamlines for an outflow from a channel with uniform velocity distribution. The Rossby number is slightly higher than the critical in (A) and slightly smaller than the critical in (B).

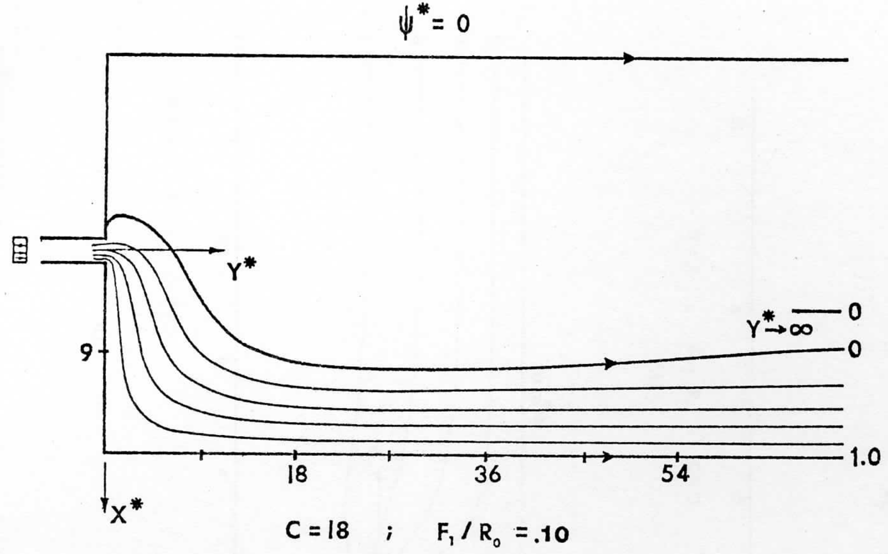

FIGURE 11.C: Streamlines for an outflowfrom a channel with uniform velocity distribution with a very small Rossby number. $Ro << Ro_c$.

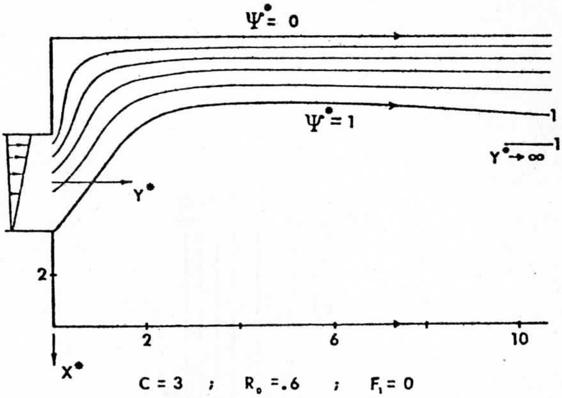

(A)

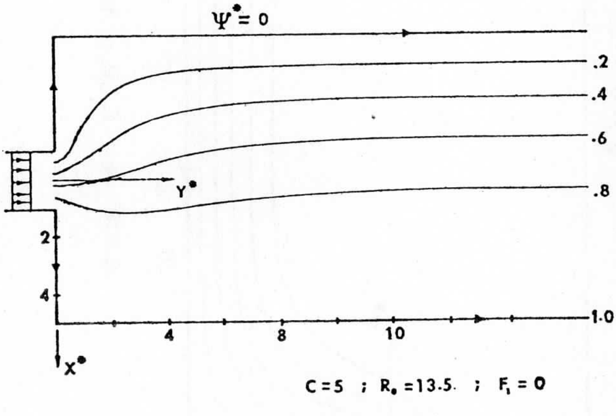

(B)

FIGURE 12.A: Streamlines for a separating outflow from a short strait. $Ro < Ro_c$.

FIGURE 12.B: Same conditions as Fig. 12.A, but for a non-separating flow with $Ro > Ro_c$. The flow at the outlet is almost uniform.

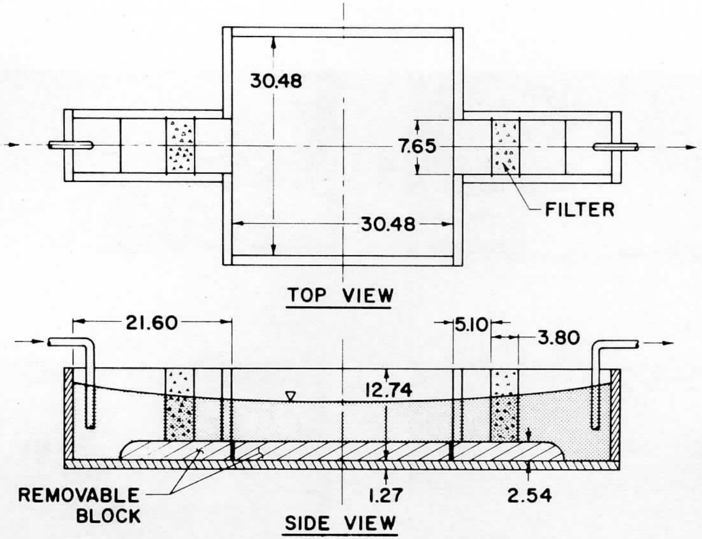

FIGURE 13: Schematic diagram of the one-layer experimental apparatus. All dimensions are given in centimeters.

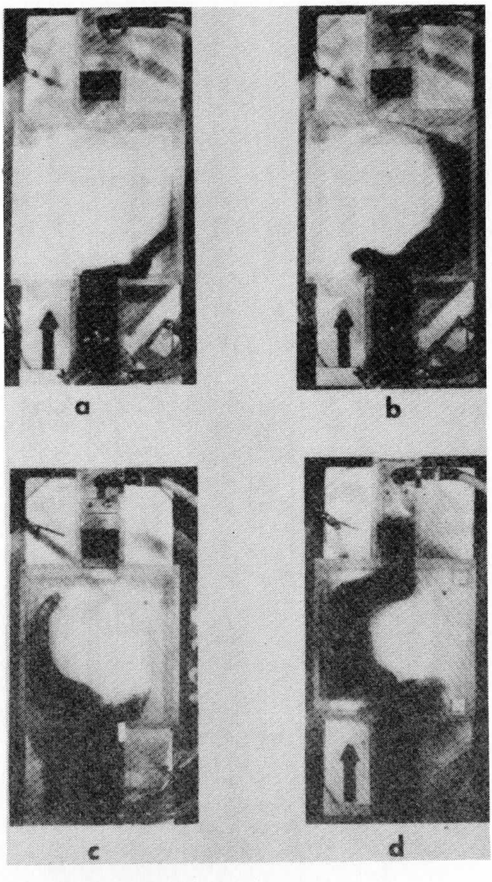

FIGURE 14: The flow pattern of the one layer experiment with the basin's bottom lower than the channel [(a) and (b)] and with the basin's bottom higher than the channel [(c) and (d)].

Physical constants: $C = 4$; $F \simeq 10^{-5}$; $\Omega = 1.9$ rad sec^{-1};

$Ro \simeq 0.018$; $\Delta H = 2.54$ cm.

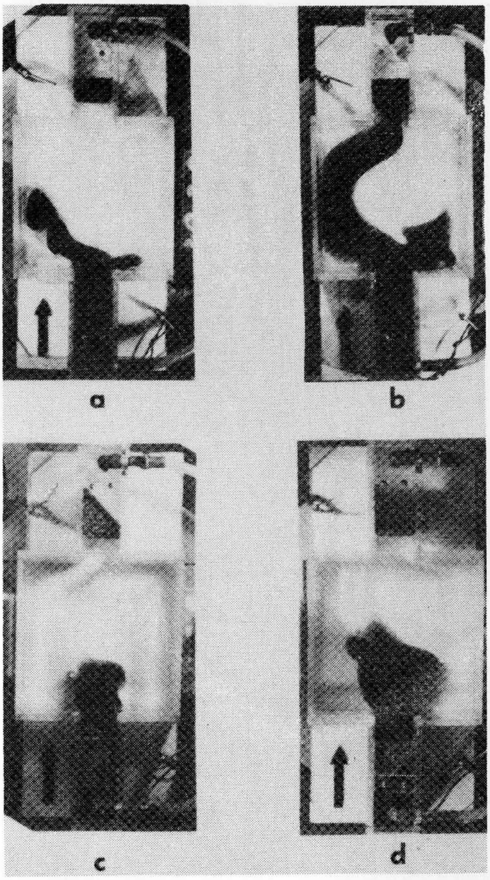

FIGURE 15: The flow pattern of the one layer experiment with a flat bottom and a uniform velocity distribution in the channel [(a) and (b)] and with a flat bottom and a linear velocity distribution in the channel [(c) and (d)].

Physical constants: $C = 4$; $F \simeq 10^{-5}$; $\Omega = 1.5$ rad sec^{-1};
$Ro \simeq 0.022$; $\Delta H(r) \sim 0.5$ cm; $A = 0.133$ sec^{-1}.

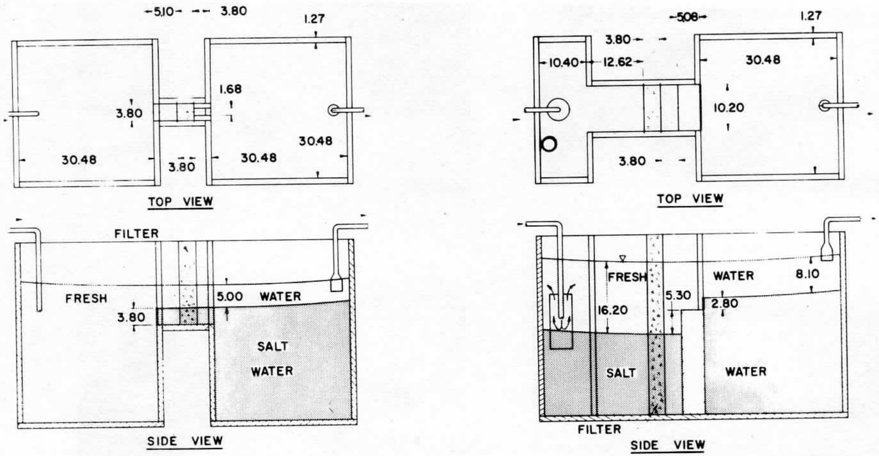

A

B

FIGURE 16: Schematic diagram of the two-layer experimental apparatus. (A) was used to test an outflow from a channel with uniform velocity distribution and (B) to test an outflow from a short "strait." All dimensions are in centimeters.

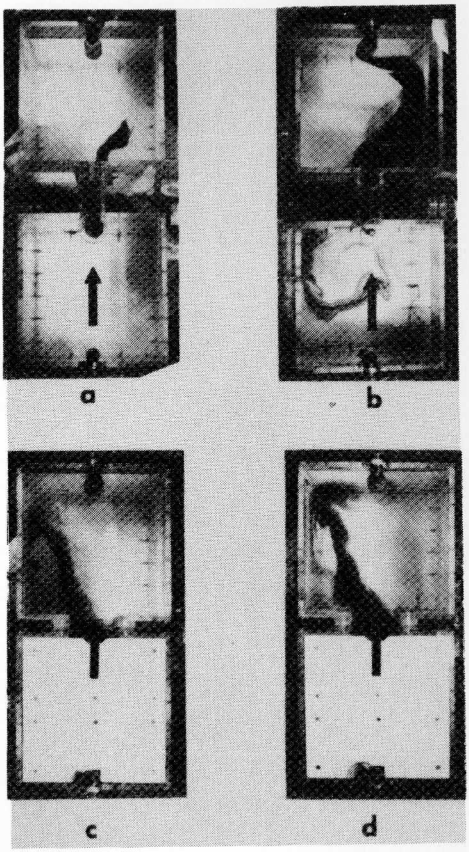

FIGURE 17: The flow pattern of the two layer experiment. Photos (a) and (b) show an outflow from a channel with uniform velocity distribution [apparatus A] while (c) and (d) show an outflow from a short strait [apparatus B].

Physical constants:

Apparatus (A): $C = 18$; $\Omega = 2.2$ rad sec^{-1}; $Ro \simeq 0.14$; $F_1 \simeq 0.013$

Apparatus (B): $C = 3$; $\Omega = 1.7$ rad sec^{-1}; $Ro \simeq 0.05$; $F_1 \simeq 0.010$

A NUMERICAL STUDY OF THE ROLE OF ADJUSTMENT IN A PROPAGATING JET STREAM

Nathaniel D. Reynolds

ABSTRACT

The role of gravity-inertia waves in the evolution of an upper tropospheric jet stream is studied. Solutions for the time changes in a simple jet stream maximum are found using a two-layer primitive equation model. Analyses are made of output from this model and from a companion two-layer quasi-geostrophic model to determine the nature of the quasi-geostrophic and gravity-inertia wave modes. Two 24-hour runs of the models were made: a "large domain" run with the wavelength of the jet equal to 4000 km; and a "small domain" run with a wavelength of 2000 km. The maximum velocity of the jet in each case was about 26 m/sec.

Analysis of vertical motions at various positions relative to the jet maximum reveals an apparent partial horizontal trapping of the gravity-inertia waves in the region of the jet. The pressure field in the small domain run appears to be altered by adjustment, while the small domain non-divergent velocity field and the large domain pressure and non-divergent velocity fields show no significant effect. The relationship of these results to the classical adjustment theory is explored.

1. INTRODUCTION

The synoptic and subsynoptic scale regions of high wind velocity in various portions of the atmosphere, commonly called jet streams, are known to have a pronounced influence on the weather. While there are some low-level jets, these regions of strong flow are usually found in upper parts of the troposphere. Palmen and Newton (1969) point out the close association of mid-latitude upper tropospheric jet streams with the significant cyclone and anticyclone activity at the surface. According to Miller (1972), severe weather occurrences are often dependent on strong winds in the middle levels, which are often present in the vicinity of upper tropospheric jet streams.

Vertical motion is a key atmospheric parameter, since upward vertical motion causes condensation, while clear weather is usually present wherever there is sinking motion. On the large scale, the secondary circulation pattern discussed by Reiter (1967) often gives a good first approximation to the vertical motions near the jet. The typical horizontal convergence and divergence pattern associated with the jet is shown in Fig. 1.1. This gives upward vertical motion (and hence cloudiness, in a moist environment) in quadrants 1 and 3, and downward vertical motion in 2 and 4.

However, satellite photos of synoptic situations with a strong jet present show that the distribution of cloudiness is not this simple; there are also asymmetries, small-scale features and features which are more transient present in the cloudiness pattern. Since these features are small in scale, their Rossby number is too large for them to be quasi-geostrophic in character. Therefore, these features are the effects of gravity-inertia waves, orographic processes, Ekman-layer instabilities or convection. In this study we focus our attention solely on gravity-inertia waves.

Eom (1975) and Uccellini (1975) have each completed case studies of synoptic situations with a strong jet in the upper troposphere where the effects of gravity-inertia waves were observed at surface synoptic and FAA weather stations. The phase velocities determined by Eom and Uccellini were close to those theoretically calculated for internal gravity-inertia waves using a simple two-layer tropospheric model.

The role of gravity-inertia waves in the general behavior of a rotating fluid in the presence of force imbalances has been studied in idealized form. The response of the fluid to these imbalances is often referred to as geostrophic adjustment. An important difference exists between adjustment in the real atmosphere and adjustment in laboratory studies. In the latter, it has customarily been assumed that the flow pattern approaches a final, steady state. This assumption has allowed investigators to get analytical solutions and draw some basic physical conclusions concerning the adjustment process.

Rossby (1937, 1938) laid the general framework for the study of geostrophic adjustment. He considered the behavior of a one-layer, inviscid, rotating ocean, initially flat, with a constant depth D, in a rotating coordinate system with an initial constant velocity u_i in the x-direction in a strip that extends from $x = -\infty$ to $+\infty$, $y = -a$ to $+a$, with zero velocity outside. He determined the steady, geostrophic, final state after adjustment is achieved, under the assumption that mass and momentum are conserved. A partitioning of the total initial energy into that which remains in the initial flow region and that which propagates away reveals the importance of the Rossby deformation radius, λ, to the problem, where $\lambda = \sqrt{gD/f}$, g is the acceleration of gravity, f is the Coriolis parameter, and $\sqrt{gD}$ is the shallow water gravity wave speed in a non-rotating framework. He finds the ratio of the final steady state velocity u_f to the initial velocity u_i in the initial flow region to be as follows:

$$\frac{u_f}{u_i} = \frac{\frac{\lambda}{a}}{1 + \frac{\lambda}{a} + \frac{a}{3\lambda}} . \qquad (1.1)$$

Now for a/λ large (i.e., for a large scale disturbance), the final velocity near the jet is nearly zero. Hence the kinetic energy of the initial flow has propagated away to infinity with the gravity-inertia waves. Since the final state is geostrophic, the final pressure distribution is uniform for a/λ large. Hence for large scale, the initial pressure distribution determines the final pressure and velocity distribution near the jet.

For the small scale (i.e., a/λ small), the velocity persists in the initial velocity region, and a pressure gradient develops during the adjustment process. Hence for small scales, the initial velocity distribution is the main determinant of the final state near the jet. We shall refer to these conclusions again later.

Cahn (1945) solved the time-dependent linearized Rossby problem, yielding time series of the solution, with special emphasis on the nature of the waves that propagated away from the jet maximum.

Obukhov's approach, as described by Blumen (1972) was to look at potential vorticity for a linear model. He suggested that the adjustment process could be treated as separate from, but occurring simultaneously with, the geostrophic flow evolution.

Blumen (1972), in his review article, constructed a linear analytical model capable of separating the gravity-inertia contribution from the quasi-geostrophic evolutions. He also references many other papers where analytical models, some of which are nonlinear, are developed. But the complete nonlinear solutions are complicated, may not necessarily fit into conventional perturbation analyses that have often been used, and do not necessarily approach a steady final state.

The purpose of this study is to determine the nature and effect of the gravity-inertia waves near an idealized jet, using numerical methods so that the assumptions of linearity, zonal flow and separability of solutions, used in analytical studies, are no longer necessary. The hydrostatic primitive equation system allows both the quasi-geostrophic evolution and the superimposed gravity-inertia contribution, and is therefore used here.

A two-layer primitive equation model and a two-level quasi-geostrophic model are used in this study. These models--used by Dobosy (1972) in studies where there was no mean jet present--were modified by the author in preparation for this present study. Difference maps between the primitive equation and the quasi-geostrophic model outputs show the contribution of gravity-inertia waves to the evolution of the pattern since they are present only in the former.

The two models, intended to be as simple as possible, differ in the treatment of the internal gravity-inertia wave mode. In all other respects, the models were constructed to be similar to each other, as possible; they have the following things in common:

1. Channel flow, with no flow through the north and south boundaries, and cyclic boundary conditions on the east and west boundaries.

2. Inviscid and adiabatic.

3. Constant Coriolis parameter $f = 2\Omega \sin\phi$ where ϕ is the latitude and Ω is the angular rotation rate of the earth.

4. No vertical motion ($\omega = dp/dt$) through the top.

5. Pressure as the vertical coordinate.

6. Two-layer model with horizontal velocity defined at 800 and 400 millibars.

7. Leap-frog (centered in both time and space) finite differencing.

The variables and the vertical grid layout for the two models are shown in Fig. 1.2. On the left-hand side are the quasi-geostrophic variables: the streamfunction ψ_1 and ψ_2; the static stability σ; and the vertical motion ω, which is nonzero only at the midlevel for this model. The primitive equation variables on the right-hand side of Fig. 1.2, include: the height, z, of the pressure surfaces at 1000, 600, and 200 millibars; the winds and static stability at 800 and 400 millibars; and the vertical motion at 1000 and 600 millibars.

Two experiments, each involving both models, were run: one had an east-west periodicty of 4000 km, the other a periodicity of 2000 km. Table 1.1 gives other information about the horizontal layout for the two experiments.

2. QUASI-GEOSTROPHIC MODEL

The quasi-geostrophic model used in this study is of the type called the "2 1/2-dimensional model" by Charney and Phillips (1953). The two basic equations that make up this model are the quasi-geostrophic thickness and vorticity equations.

The general form of the adiabatic thickness equation [Holton (1972), equation (7.10)] can be expressed as:

$$\frac{\partial}{\partial t}\left(-\frac{\partial\phi}{\partial p}\right) + u\frac{\partial}{\partial x}\left(-\frac{\partial\phi}{\partial p}\right) + v\frac{\partial}{\partial y}\left(-\frac{\partial\phi}{\partial p}\right) - \sigma\omega = 0 \qquad (2.1)$$

where ϕ is the geopotential, σ is the static stability defined by Holton to be $-(1/p\theta)\partial\theta/\partial p$, $\omega = dp/dt$ and u and v are the x- and y-components of velocity, respectively.

Now we proceed to write (2.1) in terms of model variables. Since we have the height, z, of a given pressure level given by $z = \phi/g$, where g is the acceleration of gravity, and if we redefine σ,

$$\sigma = -\frac{1}{pg\theta}\frac{\partial\theta}{\partial p} \quad , \qquad (2.2)$$

then we can write (2.1) in terms of the height of a pressure level.

$$\frac{\partial}{\partial t}\left(-\frac{\partial z}{\partial p}\right) + u\frac{\partial}{\partial x}\left(-\frac{\partial z}{\partial p}\right) + v\frac{\partial}{\partial y}\left(-\frac{\partial z}{\partial p}\right) - \sigma\omega = 0 \qquad (2.3)$$

Writing this for the two-layer model, using the vertical grid given in Fig. 1.3, we have:

$$\frac{\partial}{\partial t}\left(z_{800mb} - z_{400mb}\right) + u_{600mb}\frac{\partial}{\partial x}\left(z_{800mb} - z_{400mb}\right) + v_{600mb}\frac{\partial}{\partial y}\left(z_{800mb} - z_{400mb}\right) + \omega\sigma\Delta p = 0 \qquad (2.4)$$

In deriving equation (2.4), we have not used any of the quasi-geostrophic assumptions; hence, this equation is still valid for the primitive equation system. The only assumptions made so far are those of the equation of state, adiabatic motion, inviscid fluid motion, Poisson's equation, and the hydrostatic equation.

The quasi-geostrophic assumptions applicable to the thickness equation are:

1. Horizontal advection is by the geostrophic wind only.
2. The streamfunction, ψ, is geostrophic (i.e. $\psi = gz/f$).
3. Static stability is assumed to be a function of pressure only.

Assumption 2 implies that a thickness $\psi_2 - \psi_1$ is given by:

$$\psi_2 - \psi_1 = \frac{g}{f}(z_2 - z_1) \tag{2.5}$$

We can now represent u and v at 600 millibars in terms of the streamfunction ψ :

$$u = -\frac{\partial}{\partial y}(\psi_m), \qquad v = \frac{\partial}{\partial x}(\psi_m) \tag{2.6}$$

where $\psi_m = (\psi_1 + \psi_2)/2$.

Then the thickness equation, (2.4), becomes the following, with the help of (2.5) and the second assumption:

$$\frac{\partial}{\partial t}(\psi_2 - \psi_1) + \left[-\frac{\partial\psi_m}{\partial y}\frac{\partial}{\partial x}(\psi_2 - \psi_1) + \frac{\partial\psi_m}{\partial x}\frac{\partial}{\partial y}(\psi_2 - \psi_1)\right] - \frac{\omega\sigma g\Delta p}{f} = 0 \tag{2.7}$$

where $\Delta p = p_1 - p_2 = 400$ millibars. We can write equation (2.7) more concisely in the following form:

$$\frac{\partial}{\partial t}(\psi_2 - \psi_1) + J\left(\frac{\psi_1 + \psi_2}{2}, \psi_2 - \psi_1\right) - \frac{\omega\sigma g\Delta p}{f} = 0 \tag{2.8}$$

Here ψ_1 and ψ_2 refer to the stream function at the 800 and 400 millibar levels, respectively. The second term is the Jacobian operator, defined as:

$$J(F_1,F_2) = \frac{\partial F_1}{\partial x}\frac{\partial F_2}{\partial y} - \frac{\partial F_2}{\partial x}\frac{\partial F_1}{\partial y} \tag{2.9}$$

Taking the vorticity equation in the form with $-\partial\omega/\partial p$ substituted for the horizontal divergence (using the continuity equation),

$$\frac{\partial\zeta}{\partial t} + u\frac{\partial\zeta}{\partial x} + v\frac{\partial\zeta}{\partial y} + \omega\frac{\partial\zeta}{\partial p} - (f+\zeta)\frac{\partial\omega}{\partial p} - \left(\frac{\partial u}{\partial p}\frac{\partial\omega}{\partial y} - \frac{\partial v}{\partial p}\frac{\partial\omega}{\partial x}\right) = 0 \qquad (2.10)$$

where v is the y-component of velocity, and we let the vorticity ζ be represented as the Laplacian of a streamfunction:

$$\zeta = \nabla^2\psi \qquad (2.11)$$

The quasi-geostrophic assumptions applicable to the vorticity equation are:

1. The horizontal advection is due to the geostrophic wind only.
2. The streamfunction, ψ, is geostrophic, implying that the vorticity is equal to the geostrophic vorticity.
3. The tilting term and the vertical advection of vorticity are negligible.
4. Relative vorticity is ignored in the divergence term.

The above assumptions, applied to (2.10), yield the quasi-geostrophic vorticity equation:

$$\frac{\partial\zeta}{\partial t} + u\frac{\partial\zeta}{\partial x} + v\frac{\partial\zeta}{\partial y} - f\frac{\partial\omega}{\partial p} = 0. \qquad (2.12)$$

For the two layers, the $-f\frac{\partial\omega}{\partial p}$ term can be approximated by equations (2.13) and (2.14), using the assumption $\omega = 0$ at top and bottom:

$$-f\left.\frac{\partial\omega}{\partial p}\right|_{400\text{mb}} = f\,\frac{\omega_{600\text{mb}} - \omega_{200\text{mb}}}{\Delta p} = f\,\frac{\omega_{600\text{mb}}}{\Delta p} \qquad (2.13)$$

$$-f\left.\frac{\partial\omega}{\partial p}\right|_{800\text{mb}} = f\,\frac{\omega_{1000\text{mb}} - \omega_{600\text{mb}}}{\Delta p} = -f\,\frac{\omega_{600\text{mb}}}{\Delta p} \qquad (2.14)$$

Henceforth, we shall let ω represent ω at 600 millibars.

Finally, we represent the horizontal advection of vorticity in the vorticity equation in the Jacobian form:

$$u\frac{\partial\zeta}{\partial x} + v\frac{\partial\zeta}{\partial y} = J(\psi,\zeta)\ . \qquad (2.15)$$

A substitution of equations (2.11), (2.13), (2.14) and (2.15) into (2.12) yields the vorticity equation for each of the two layers:

$$\frac{\partial}{\partial t}(\nabla^2\psi_1) + J(\psi_1, \nabla^2\psi_1) + \frac{f\omega}{\Delta p} = 0 \tag{2.16}$$

$$\frac{\partial}{\partial t}(\nabla^2\psi_2) + J(\psi_2, \nabla^2\psi_2) - \frac{f\omega}{\Delta p} = 0 . \tag{2.17}$$

The three equations (2.16), (2.17), and (2.8) have only three unknowns; ψ_1, ψ_2, and ω ; hence, they form a closed system. To obtain only two equations and two unknowns we add equations (2.16) and (2.17) to obtain equation (2.19), and we subtract (2.17) from (2.16) to obtain (2.20), using (2.8) rewritten as:

$$\omega = \frac{f}{\sigma g \Delta p}\left[\frac{\partial}{\partial t}(\psi_2 - \psi_1) + J\left(\frac{\psi_1 + \psi_2}{2}, \psi_2 - \psi_1\right)\right] \tag{2.18}$$

to eliminate ω.

$$\nabla^2\left[\frac{\partial}{\partial t}(\psi_1 + \psi_2)\right] + J(\psi_1, \nabla^2\psi_1) + J(\psi_2, \nabla^2\psi_2) = 0 \tag{2.19}$$

$$\left[\nabla^2 - \frac{2f^2}{\sigma g(\Delta p)^2}\right]\frac{\partial}{\partial t}(\psi_1 - \psi_2) + J(\psi_1, \nabla^2\psi_1) - J(\psi_2, \nabla^2\psi_2) \tag{2.20}$$

$$- \frac{2f^2}{\sigma g(\Delta p)^2} J\left(\frac{\psi_1 + \psi_2}{2}, \psi_1 - \psi_2\right) = 0$$

In the model, we solve the equations (2.19) and (2.20) for $\frac{\partial}{\partial t}(\psi_1 + \psi_2)$ and $\frac{\partial}{\partial t}(\psi_1 - \psi_2)$ using the sequential over-relaxation method, directly giving us values for $\frac{\partial \psi}{\partial t}$ at both levels of the model. Then we use centered time differences to extrapolate the variables ψ_1 and ψ_2 forward in time, using a time step, Δt, of 15 minutes. The vertical motion is computed diagnostically by equation (2.18) only when needed for output purposes.

3. PRIMITIVE EQUATION MODEL

The primitive model equations include the adiabatic thickness equation (2.4), the equations of motion (3.1), and the continuity equation (3.2).

$$\frac{\partial u}{\partial t} + u\frac{\partial u}{\partial x} + v\frac{\partial u}{\partial y} + \omega\frac{\partial u}{\partial p} - fv + g\frac{\partial z}{\partial x} = 0$$
$$\frac{\partial v}{\partial t} + u\frac{\partial v}{\partial x} + v\frac{\partial v}{\partial y} + \omega\frac{\partial v}{\partial p} + fu + g\frac{\partial z}{\partial y} = 0 \tag{3.1}$$

$$\frac{\partial u}{\partial x} + \frac{\partial v}{\partial y} + \frac{\partial \omega}{\partial p} = 0 \tag{3.2}$$

The vertical grid of the primitive equation model, pictured in Fig. 1.2, is constructed with the velocities on the same pressure surfaces as the streamfunctions in the quasi-geostrophic model. The horizontal grid is unstaggered, as it is for the quasi-geostrophic model. The heights z_1, z_2, and z_3 are defined on the 1000, 600, and 200 millibar pressure surfaces, respectively. The vertical motion ω is zero at the top of the model, but is a computed variable at the bottom. This two-layer model construction admits both external and internal gravity waves, as well as the slow quasi-geostrophic flow evolution.

Equations (2.4), (3.1), and (3.2) can be written for a two-layer model. The equations of motion are given by (3.3), (3.4), (3.5) and (3.6), while the continuity equation is (3.7) and the thickness equations are given by (3.8) and (3.9).

$$\frac{\partial u_2}{\partial t} + u_2\frac{\partial u_2}{\partial x} + v_2\frac{\partial u_2}{\partial y} - \frac{\omega_2}{2\Delta p}(u_2 - u_1) - fv_2 + g\frac{\partial}{\partial x}\left(\frac{z_2 + z_3}{2}\right) = 0 \tag{3.3}$$

$$\frac{\partial u_1}{\partial t} + u_1\frac{\partial u_1}{\partial x} + v_1\frac{\partial u_1}{\partial y} - \left(\frac{\omega_1 + \omega_2}{2\Delta p}\right)\left(u_2 - u_1\right) - fv_1 + g\frac{\partial}{\partial x}\left(\frac{z_1 + z_2}{2}\right) = 0 \tag{3.4}$$

$$\frac{\partial v_2}{\partial t} + u_2\frac{\partial v_2}{\partial x} + v_2\frac{\partial v_2}{\partial y} - \frac{\omega_2}{2\Delta p}(v_2 - v_1) + fu_2 + g\frac{\partial}{\partial y}\left(\frac{z_2 + z_3}{2}\right) = 0 \tag{3.5}$$

$$\frac{\partial v_1}{\partial t} + u_1\frac{\partial v_1}{\partial x} + v_1\frac{\partial v_1}{\partial y} - \frac{\omega_1 + \omega_2}{2\Delta p}(v_2 - v_1) + fu_1 + g\frac{\partial}{\partial y}\left(\frac{z_1 + z_2}{2}\right) = 0 \tag{3.6}$$

$$\omega_2 = -\left(\frac{\partial u_2}{\partial x} + \frac{\partial v_2}{\partial y}\right)\Delta p \quad , \quad \omega_1 = \omega_2 - \left(\frac{\partial u_1}{\partial x} + \frac{\partial v_1}{\partial y}\right)\Delta p \tag{3.7}$$

$$\frac{\partial}{\partial t}(z_2 - z_1) + u_1\frac{\partial}{\partial x}(z_2 - z_1) + v_1\frac{\partial}{\partial y}(z_2 - z_1) + \frac{\omega_1 + \omega_2}{2}\sigma_1\Delta p = 0 \tag{3.8}$$

$$\frac{\partial}{\partial t}(z_3 - z_2) + u_2 \frac{\partial}{\partial x}(z_3 - z_2) + v_2 \frac{\partial}{\partial y}(z_3 - z_2) + \frac{\omega_2 + \omega_3}{2} \sigma_2 \Delta p = 0 \qquad (3.9)$$

Note that this model has two thickness equations, while the quasi-geostrophic model has only one.

The bottom boundary condition is given by equation (3.10), derived by Dobosy (1972), using the definition of ω, the hydrostatic equation, and the assumption of constant density at the flat bottom boundary. In this equation, $\vec{V}_0$ is the 1000 millibar wind and $\bar{\rho}$ is the mean air density at 1000 millibars.

$$\frac{\partial z_1}{\partial t} = \frac{\omega_1}{\bar{\rho} g} - z_1 \nabla \cdot \vec{V}_0 - \vec{V}_0 \cdot \nabla z_1 \qquad (3.10)$$

The numerical procedure at each time step is as follows:

1. Integrate downward using the continuity equation to calculate omega at 600 and then at 1000 millibars.
2. Solve for $\frac{\partial u}{\partial t}$ and $\frac{\partial v}{\partial t}$ for both levels, using equations (3.3) - (3.6).
3. Solve for $\partial z_1/\partial t$ using equation (3.10).
4. Solve for time derivatives of z_2 and z_3 using the thickness equations (3.8) and (3.9).
5. Determine values of velocities and heights using a centered time difference with Δt equal to three minutes.

In this model, the advection terms are in flux form, and the finite difference form is Scheme F given by Grammeltvedt (1969). This finite difference scheme is quadratic conservative, and so has no problem with nonlinear computational instability.

In the primitive equation model, static stability σ is a function of x, y, p and t. This allows the model to account for changes in stability, a factor which may potentially affect the vertical motions present and the wave speeds in the model. Since the primitive equation model has two thickness equations, we must calculate the static stability at 800 and 400 millibars in terms of other model variables. Holton (1972) gives σ as a function of geopotential, ϕ, in a manner equivalent to (3.11):

$$\sigma = \frac{1}{p\gamma}\frac{\partial z}{\partial p} + \frac{\partial^2 z}{\partial p^2} \qquad (3.11)$$

where γ is the ratio of specific heats, Cp/Cv. Since z is carried at 1000, 600 and 200 millibars, $\partial z/\partial p$ is determined at 800 and at 400 millibars. However, the second derivative can be specified at only one level independently (600 millibars) if we use a centered difference formula.

This is not the level at which we need to evaluate the static stability, so, to offset truncation error due to noncentering when evaluating σ at 800 and 400 millibars, we introduce two parameters A and B to multiply the second difference formula:

$$\sigma_2 = -\frac{1}{\gamma\Delta p}\left(\frac{z_3 - z_2}{\Delta p}\right) + \frac{A(z_3 - 2z_2 + z_1)}{(\Delta p)^2} , \quad \sigma_1 = -\frac{1}{2\gamma\Delta p}\left(\frac{z_2 - z_1}{\Delta p}\right) + \frac{B(z_3 - 2z_2 + z_1)}{(\Delta p)^2}$$

To calculate the values of A and B, we take standard atmospheric values of z_1, z_2, z_3 from the Smithsonian Meteorological Tables, and standard atmospheric values of σ as presented by Rak To Song (1969). These standard atmospheric heights are used as mean heights in the initialization of the model. This yields the following numerical values:

Pressure	z (meters)	$\sigma(m^3 sec^4 kg^{-2})$	Value of A or B
1000 mb	110		
800 mb		$1.2 \cdot 10^{-7}$	B = 0.472
600 mb	4205.5		
400 mb		$4.3 \cdot 10^{-7}$	A = 1.745
200 mb	11787		

Recall that the quasi-geostrophic model had static stability specified as a constant at 600 millibars. The determination of a consistent relationship between the static stability parameters of the two models is discussed later.

The gravity wave speeds of the model were tested against the theoretical gravity wave speeds appropriate for the two-layer model with no coordinate rotation. The easiest way to get approximate gravity wave speeds for this model is to linearize the primitive equations and solve the eigenvalue problem resulting from the assumption that each variable has a simple wave form. Eom (1975) solves this for the case where a non-zero mean velocity is present only in the upper layer of the model, and the thickness of the two layers is not the same. If we assume the mean velocity of each layer is zero and that each layer has the same thickness, Δp, the resulting gravity wave speeds are given in equation (3.12), with the + sign yielding the external wave and the - sign yielding the internal wave:

$$c_2^2 = \bar{\alpha}\Delta p + \frac{5}{4}A_1 + \frac{1}{4}A_2 \pm \sqrt{(\bar{\alpha}\Delta p)^2 + \frac{25}{16}A_1^2 + \frac{1}{16}A_2^2 + 2\bar{\alpha}\Delta p A_1 + \frac{3}{8}A_1A_2} \qquad (3.12)$$

Here, $A_1 = \frac{1}{2}\sigma_1 g(\Delta p)^2$, $A_2 = \frac{1}{2}\sigma_2 g(\Delta p)^2$, and $\bar{\alpha}$ is the mean specific volume at 1000 millibars.

The eigenfunctional relationships are given as:

$$\frac{\hat{u}_2}{\hat{u}_1} = \frac{-\frac{1}{2}A_1^2 + c^2 - \bar{\alpha}\Delta p}{\bar{\alpha}\Delta p + A_1}$$

$$\frac{\hat{z}_1}{\hat{u}_1} = \frac{\bar{\alpha}\Delta p(A_1 + 2c^2)}{2c(\bar{\alpha}\Delta p + A_1)}$$

$$\frac{\hat{z}_2}{\hat{u}_1} = \frac{c\left(2A_1 + \bar{\alpha}\Delta p - \frac{A_1\bar{\alpha}\Delta p}{2c^2}\right)}{\bar{\alpha}\Delta p + A_1} \qquad (3.13)$$

$$\frac{\hat{z}_3}{\hat{u}_1} = \frac{(2c^2 + A_2)(-\frac{1}{2}A_1 + c^2 - \bar{\alpha}\Delta p)}{c(\bar{\alpha}\Delta p + A_1)}$$

where $u_1 = \mathrm{Re}\{u_1 e^{ik(x-ct)}\}$, etc.

With $A_1 = 941\ \mathrm{m^2/sec^2}$, $A_2 = 3370\ \mathrm{m^2/sec^2}$ and $\bar{\alpha}\Delta p = 3.2 \cdot 10^4\ \mathrm{m^2/sec^2}$, we have an internal gravity wave speed of 259 m/sec. The model was tested for the values of c and other parameters, with the initial conditions being that which has u_1 specified by:

$$u_1 = (5\ \mathrm{m/sec})\ \sin\left\{\frac{2\pi}{L}(x - x_0)\right\} \qquad (3.14)$$

L is the length of the model, and x_0 is a reference point; the other variables were specified from u_1 according to the eigenfunctions (3.13). The internal gravity wave speed resulting from the model was 33 m/sec, and the external wave speed was 267 m/sec, which were considered to be in good agreement with the theoretical values.

4. INITIALIZATION OF THE MODELS

For both models, the streamfunction is specified in the form described in Section 5. In the quasi-geostrophic model, this is sufficient information to calculate the time derivative of ψ in the manner described in Section 2. Then ψ is extrapolated forward in time.

In the primitive equation model, the initialization is somewhat more involved. From the streamfunction, the non-divergent winds, $\vec{V}_\psi$, are directly calculated, where $V_\psi = -\vec{k} \times \nabla\psi$. Now the balance equation (4.1) is imposed so that the total time derivative of the horizontal divergence is zero; according to Thompson (1958), this would eliminate gravity waves from the initial conditions of a linear system. It also gives us departures, z', from the mean heights, $\overline{z}$, at 800 and 400 millibars, which are extrapolated linearly to 1000, 600, and 200 millibars, using equations (4.1). The height z is the sum of $\overline{z}$ and z', where $\overline{z}$ is set equal to the standard atmospheric height:

$$z'_{1000mb} = \frac{3}{2} z'_{800mb} - \frac{1}{2} z'_{400mb} \; ; \; z'_{600mb} = \frac{1}{2}\left(z'_{800mb} + z'_{400mb}\right) \; ;$$

$$z'_{200mb} = -\frac{1}{2} z'_{800mb} + \frac{3}{2} z'_{400mb} \qquad (4.1)$$

The form of the balance equation is somewhat different from the usual form. Before we consider this difference, a few remarks about the balance equation in general need to be made. The balance equation, as explained by Haltiner (1971) is derived from the divergence equation using a scale analysis. In the case where $\beta = 0$, the balance equation takes the form:

$$g\nabla^2 z = f\nabla^2\psi - 2J(u_\psi, v_\psi) \qquad (4.2)$$

The divergence equation itself is derived by taking the horizontal divergence of the local time derivative of the velocity. The divergence of the horizontal advection terms yields the Jacobian term in (4.2), plus some other terms which are neglected because they are small, according to scale analysis.

A test of the effect of the initial form of the balance equation was conducted. In one case, the finite difference form of the usual balance equation (4.2) was used. In the other case, the horizontal momentum advection involving only the non-divergent wind (in Grammeltvedt Scheme F form) was computed, and then the divergence of this horizontal advection was taken.

The equation that would have resulted if the above procedure had been carried out in analytical form is given as equation (4.3). Note that the analytical form of (4.3) is equivalent to the analytical form of (4.2), since the divergence of the non-divergent wind is zero.

$$g\nabla^2 z = f\nabla^2\psi - V\cdot\nabla(\nabla\cdot V_\psi) - (\nabla\cdot V_\psi)^2 - 2J(u_\psi, v_\psi) \tag{4.3}$$

There was little difference in the evolution of the large-scale jet, but details of the vertical motion field showed a quite different gravity wave pattern. Because of this difference, the latter finite difference form of the balance equation with the Grammeltvedt Scheme F form of the advection terms was used in this study. This was done so that the finite difference form of the advection terms in the model initialization would be more nearly consistent with the finite difference form of the advection terms in the predictive part of the model.

Vertical motion, ω_2, is calculated using the quasi-geostrophic omega equation (4.4). Since the balance equation model ω equation is rather unwieldy [see Haltiner (1972)], it was not used. The divergent component of velocity, $\vec{V}_\chi$, is calculated as the negative gradient of a wind velocity potential, χ, as in equation (4.5), the velocity potential having been calculated numerically by using equation (4.6), by the sequential over-relaxation method. The static stability, σ_i, is a constant here, and is specified at 600 millibars.

$$\left(\nabla^2 + \frac{f^2}{g\sigma_i}\frac{\partial^2}{\partial p^2}\right)\omega = \frac{f}{g\sigma_i}\left[\frac{\partial}{\partial p}\left(\vec{V}_\psi\cdot\nabla(\zeta + f)\right) - \nabla^2\left(V_\psi\cdot\nabla(\frac{\partial\psi}{\partial p})\right)\right] \tag{4.4}$$

$$\vec{V}_\chi = -\nabla\chi \tag{4.5}$$

$$\nabla^2\chi = \omega \tag{4.6}$$

To minimize interactions of the north and south boundaries with the rest of the model, the initial conditions had only light winds near these boundaries. Initially, vertical motion was specified to be zero for all grid points within $3\Delta y$ of each of these boundaries, in order to help suppress initial gravity waves in these regions. (The east and west boundaries present no problem due to the cyclic condition.) The velocity potential, unlike the other variables computed by relaxation, uses Neumann boundary conditions $\partial\chi/\partial y = 0$ on the north and south boundaries, in order to yield no flow across them.

5. INITIAL SPECIFICATIONS

The initial specification given the numerical models is a simple jet maximum, constructed from the streamfunction, ψ, prescribed at 800 and 400 millibars. This ψ is identical for both numerical models. For these experiments, the flow is initially equivalent barotropic (i.e., isopleths of the stream function at the two levels are parallel to each other). The upper level velocity field with a jet maximum of 26 meters per second is shown in Figures 5.1.a and 5.1.b. Also shown is the vertical motion at 600 millibars as calculated from the quasi-geostrophic omega equation.

The mathematical form of the streamfunction is:

$$\psi = c_1 \left\{ \frac{\tan^{-1}\left[\dfrac{c_2(y - y_0)}{L(x,y)}\right]}{\tan^{-1}\left[\dfrac{c_2 y_3}{L(x,y)}\right]} \right\} \tag{5.1}$$

where y_0 is the node of the arctangent function (here placed at the center of the model grid), and y_3 is the distance from the boundary to the center of the grid. The constant, c_2, determines the relative slopes in the y- direction near the center of the model and near the boundary. Equation (5.1) gives small gradients near the lateral boundaries of the model in comparison to their values near the center.

The function $L(x,y)$ counters c_2 and provides the crowding of the streamfunction isopleths in the region of the jet maximum and the spreading of these isopleths in regions along the jet axis where the flow is weaker. Its form is given as:

$$L(x,y) = a - b \cos \frac{2\pi}{\ell} (x - x_0) \tag{5.2}$$

where a and b are constant, x_0 is the region of the velocity maximum and ℓ is the wavelength associated with the jet core. Finally, the constant, c_1 is chosen to give the desired velocity maximum.

A non-trivial part of the initial specification is the determination of consistent relationships between the static stability parameters for the primitive equation model, the parameter used in the initialization for that model, and the parameter used in the quasi-geostrophic model. The static stability specification is critical, since the internal deformation radius and the magnitude of the vertical motion are dependent on it.

We shall first consider the constraint imposed by matching internal deformation radii. Recalling that the deformation radius, λ, is given by the gravity wave speed, c_{gw}, divided by the Coriolis parameter, as given in

(5.3), we compare the internal gravity wave speed for the linearized primitive equation system that would be appropriate for the quasi-geostrophic model grid with the internal gravity wave speed for the linearized primitive equation system for the primitive equation model. We consider a gravity wave with no v-component of velocity, no y-derivatives anywhere, and no coordinate rotation. In order to admit only the internal mode, the equation systems used here also include the assumption that $\omega = 0$ at 1000 millibars.

The primitive equations appropriate for the quasi-geostrophic grid are given in (5.4):

$$\lambda = \frac{c_{gw}}{f} \tag{5.3}$$

$$\frac{\partial u_1}{\partial t} + g \frac{\partial z_1}{\partial x} = 0 \tag{5.4}$$

$$\frac{\partial u_2}{\partial t} + g \frac{\partial z_2}{\partial x} = 0$$

$$\frac{\partial}{\partial t} (z_2 - z_1) = \omega_2 \sigma g \Delta p$$

$$\omega_2 = - \Delta p \frac{\partial u_2}{\partial x}$$

We assume that u_1, u_2, z_1, z_2 and z_3 have a simple wave form:

$$u_1 = \mathrm{Re}\ \{\hat{u}_1 e^{ik(x - ct)}\}, \text{ etc.,} \tag{5.5}$$

the solution to which yields the eigenvalue c:

$$c = \pm\ (\Delta p) \sqrt{g\sigma/2} \tag{5.6}$$

which is the internal gravity wave speed.

The linearized primitive equations used for the primitive equation grid are given by the equations labeled (5.7):

$$\begin{aligned}
&\frac{\partial u_1}{\partial t} + g\frac{\partial}{\partial x}\left(\frac{z_1 + z_2}{2}\right) = 0 \\
&\frac{\partial u_2}{\partial t} + g\frac{\partial}{\partial x}\left(\frac{z_2 + z_3}{2}\right) = 0 \\
&\frac{\partial}{\partial t}(z_2 - z_1) - \frac{\omega_2}{2}\sigma_1 g\Delta p = 0 \\
&\frac{\partial}{\partial t}(z_3 - z_2) - \frac{\omega_2}{2}\sigma_2 g\Delta p = 0 \\
&\omega_2 + \Delta p\frac{\partial u_2}{\partial x} = 0 \\
&\omega_2 - \Delta p\frac{\partial u_1}{\partial x} = 0
\end{aligned} \tag{5.7}$$

To obtain a wave solution, we let u_1, u_2', z_1, z_2, z_3, and ω_2 have a simple wave form as before. The determination of c is an eigenvalue problem, the solution of which is given as:

$$c^2 = g(\Delta p)^2(\sigma_1 + \sigma_2)/8 \tag{5.8}$$

therefore $c = \pm\, \Delta p\sqrt{g(\sigma_1 + \sigma_2)/8}$. Now for this to be equal to the gravity-wave speed for the quasi-geostrophic grid, we must have $\sigma/2 = (\sigma_1 + \sigma_2)/8$, or

$$\sigma = \frac{\sigma_1 + \sigma_2}{4} \tag{5.9}$$

The constraint imposed by matching initial vertical motions is different. The ω-equation (4.4), used in the primitive equation model initialization, is equivalent to the ω-equation (2.8) used in the quasi-geostrophic model. In equation (4.4), we note that $\left(\sigma_i\nabla^2 + \frac{\partial^2}{\partial p^2}\right)\omega$ is equal to something independent of σ_i. Here σ for the quasi-geostrophic mode, σ_i for the primitive equation initialization, and ω are all specified at 600 millibars. The value of σ

necessary for matching ω should then be simply the average of σ_1 and σ_2, giving us a σ twice as large as we had in the quasi-geostrophic model. This was tried, and surprisingly, the vertical motion that resulted in the primitive equation initialization using (4.4) and $\sigma_i = (\sigma_1 + \sigma_2)/2$ was nearly the same as that given by the quasi-geostrophic model using (2.8) and $\sigma = \frac{\sigma_1 + \sigma_2}{4}$. The reason for this must lie in the finite difference formulations of (4.4) and (2.8) but his was never completely resolved.

The vertical motion constraint was used, since the rate of propagation of the jet maximum, the only dynamical property that is dependent on the Rossby deformation radius in the quasi-geostrophic model, was not very sensitive to how σ was specified. With $\sigma_1 = 1.2 \cdot 10^{-7}$ m^3 sec^4/kg^2 and $\sigma_2 = 4.3 \cdot 10^{-7}$ m^3 sec^4/kg^2, the value of σ_i is the primitive equation initialization is $2.8 \cdot 10^{-7}$ m^3 sec^4/kg^2 and σ for the quasi-geostrophic model is equal to $1.4 \cdot 10^{-7}$ m^3 sec^4/kg^2.

For the primitive equation model prediction, the amplitude of ω averaged approximately one and one-half times as large as the amplitude of ω for the quasi-geostrophic model, although their amplitude initially had been nearly the same. In order to make the difference maps for ω most meaningful, it was necessary to normalize the vertical motions by the following procedure. First, we define the amplitude of omega to be the deviation of the maximum and minimum vertical motion from their average. Then the amplitude of the quasi-geostrophic ω was normalized to become the same as that of the primitive equation ω, by simple multiplication by the quotient

$$\frac{\text{primitive equation } \omega - \text{amplitude}}{\text{quasi-geostrophic } \omega - \text{amplitude}}$$

before any of the difference maps were made.

Several physical parameters that aid in understanding the dynamics of the models were considered. The Rossby number, R, tells us to what degree the flow present departs from geostrophic balance. The Froude number, F, tells us the relative importance of advection processes as compared with hydrostatic pressure restoration. The internal Rossby deformation radius, λ_i, gives us a natural unit of length for the adjustment process which occurs in the model. The aspect ratio, r, of the jet is the ratio of the half-width to the quarter wavelength. These parameters are defined as:

$$R = \frac{u}{fL_x}, \quad F = \frac{U}{c_i}, \quad \lambda_i = \frac{c_i}{f}, \quad r = \frac{L_x}{L_y} \tag{5.10}$$

where U is the typical x-component velocity present along the jet axis, L_x is the quarter wavelength, L_y is the half-width, f is the Coriolis parameter, and c_i is the internal gravity wave speed for f = 0.

Many of the parameters were fixed in this study. The static stability, although allowed to vary as discussed in Section 3, varied so little in the experiments that were run that we can consider it to be of a fixed scale. Hence the internal gravity-wave speed and the internal deformation radius are fixed. The Froude number was also fixed, requiring the U to be fixed. In order that the initial shape of the jet be the same throughout this study, the aspect ratio was fixed. As a result of fixing the above parameters, the Rossby number could be varied only by allowing L_x to vary.

Two numerical experiments of differing Rossby number were carried out. In one experiment, the models had a 20 x 20 grid with a grid spacing of 200 km. This experiment we shall call the large domain run. The other experiment, in which the models had a 20 x 40 grid, spaced 100 km apart, we shall call the small domain run. Further studies might involve changing some parameters that are fixed in this study.

The length, width, velocity, deformation radii, gravity wave speeds, Rossby numbers, and the Froude number for the two experiments are given in Table 5.1. Except for the jet-maximum velocity, the velocities given are averages along the upper layer jet axis, where the velocities for the two middle rows of grid points are averaged. The variable names associated with gravity wave speeds are subscripted in Table 5.1, denoting whether the wave is external (e) or internal (i). The Rossby numbers are calculated for each of the jet maximum velocities. Since we are primarily interested in internal waves, only the internal Froude number was calculated. And lastly, the ratio of the half-width to the internal deformation radius was determined.

6. ANALYSIS AND RESULTS

The models were run for twenty-four hours, with the results shown in Figures 6.1 to 6.11. In many of these figures, the position of the jet maximum at the given time is denoted as an X, and the initial position of the jet maximum is denoted as an O.

Results from the quasi-geostrophic model were smooth enough in time that they needed no time filtering. It was felt to be useful to filter the output from the primitive equation model to remove the small $2\Delta t$ and $4\Delta t$ oscillations and external gravity wave effects. A three point filter was used with relative weights of .6, 1, .6, with data taken from each one-half hour. (Time splitting was small enough to consider it safe to use an even number of time steps per data interval for filtering.) If a wave of the form $a_0e^{i\omega t}$ is passed through this filter, resulting in a wave of the form $b_0e^{i\omega t}$, then $b_0 = a_0[1 + 1.2\cos \omega\Delta t]/2.2$. The response b_0/a_0 from this filter for waves at period $T = n\Delta t$, equal to n times one-half hour, is given in Table 6.1. This effectively removes any oscillations of periods of less than about three hours.

Filtered results for the primitive equation model were printed out each hour. The center position of the jet was determined as being near the geometric center of the highest (or in some cases, second highest) isotach, and not necessarily at a grid point of the model. Isopleths of the model variables were placed with the aid of a contouring program which used linear interpolation in two directions to convert a 24 x 20 array into a 116 x 58 array. This enabled the line printer to print out each array in such a way that it would nearly fill one sheet of computer paper.

The jet core propagated somewhat less than one-half wavelength for the large domain run and somewhat more for the small domain during the model runs of 24 hours. The distance the jet maximum has propagated, in km, is given in Table 6.2. The propagation rate is 20% faster for the primitive equation model than it is for the quasi-geostrophic model in the large domain run, while the propagation rate is 20% slower for the primitive equation model in the small domain run. This may be due to the adjustment process, or it may result from uncertainties in analysis.

The quasi-geostrophic vertical motion at 24 hours, shown in Figure 6.1 for the large domain and in Figure 6.2 for the small domain, exhibits the very regular four quadrant pattern. There is a little shearing of this pattern after twenty-four hours, for both the large and small domain runs.

This pattern is also present in the vertical motion for the primitive equation model, but superimposed on it are other vertical motions, of more or less the same horizontal scale, with a time scale much less than the time scale for the quasi-geostrophic motions.

Keeping in mind the work of Obukhov, as discussed in Section 1, we can regard the primitive equation results as the sum of a slowly evolving quasi-geostrophic mode and a more rapidly varying gravity-inertial mode. To the extent that there are no phase shifts for the synoptic scale features between the primitive equation and the quasi-geostrophic model outputs,[1] we can consider the difference maps of ω, with the quasi-geostrophic ω subtracted from the primitive equation ω, as representing the vertical motion due to gravity-inertia waves. The difference maps for ω at 600 millibars, shown

---

[1] The positions of the jet maximum were never separated by more than two grid points for the two models.

in Figures 6.3 a-f and 6.4 a-f, reveal that, especially for the large domain, the primitive equation ω oscillates about the quasi-geostrophic ω for a few hours, after which the original difference pattern is gradually lost.

The difference pattern in these first few hours has a pattern similar to that of minus twice the Jacobian of the initial non-divergent winds, $J(u_\psi, v_\psi)$. Compare the Jacobian pattern for the large domain in Figure 6.5 with the three-hour vertical motion shown in Figure 6.3.a. Then at six hours there is comparatively little difference between the quasi-geostrophic ω and the primitive equation vertical motion, but at nine hours the pattern is, more or less, the reverse of what it is at three hours. Therefore, six hours is approximately a half-period for the gravity-inertia mode during the early part of the large domain run. In the small domain run, the Jacobian pattern also appears at three hours, but this pattern breaks down much sooner than in the large domain run.

The Jacobian pattern in the vertical motion is probably due to the fact that the balance equation was imposed on the initial pressure field for the primitive equation model, but not for the quasi-geostrophic model. However, the frequency of oscillation of this Jacobian pattern identifies it as a gravity-inertia mode.

The vertical motions were determined at various positions relative to the jet core. These positions are shown in Figure 6.6. Position 5 is placed at the center of the jet. The distance between positions 2 and 5 is three grid spacings, while the distance between positions 4 and 5 is only two grid spacings. Time series of the primitive equation ω at each of the nine positions are given in Figure 6.7 for the large domain run and in Figure 6.8 for the small domain run. The vertical motions are filtered; therefore there is no aliasing of high-frequency oscillations. The time series for the quasi-geostrophic ω are not shown here; they reveal a constant value or slight trend at each of the nine positions. The time series for the large domain primitive equation model show a 10-13 hour period, while the small domain primitive equation time series have a dominant period of 3-6 hours.

The dominant periodicities present in the time series appear to be due to a partial horizontal trapping of the gravity-inertia waves. Table 6.3 shows the "round trip" distances associated with various possible wave-trapping mechanisms and the time scales for these and other mechanisms, assuming the center of the jet to be the source region for gravity-inertia waves.

We shall consider four possible mechanisms that could lead to periodic motions in time. The first mechanism, reflection of wave energy by the lateral boundaries of the model, one which yields little physical relevance, is an undesirable boundary effect which often presents itself to those who build numerical models for describing fluid systems. Wave reflections from the boundary appear to be small in these numerical outputs.

Second, we can have a reflection of wave energy by a region of strong horizontal shear. Third, the waves can propagate along the jet axis and be reintroduced into the left-hand side of the model through the cyclic condition. Fourth, we consider the time scale of adjustment, which, according to Obukhov [cf. Blumen (1972)] is characteristically equal to 1/f. The period of oscillation associated with this is equal to the inertial period.

The periods presented in Table 6.3 were calculated by dividing the appropriate distances that a wave would need to travel by the gravity wave speed. In this calculation the internal wave speed for a non-rotating coordinate system was taken to be 33 m/sec. and the external wave speed was taken to be 260 m/sec. The group velocities for the rotating framework were calculated from the relation

$$c_{group} = \frac{c^2}{\sqrt{c^2 + f^2/k^2}}$$

where c is the gravity-wave speed for a non-rotating framework, c_{group} is the group velocity for a rotating coordinate system, f is the Coriolis parameter, and k is 2π divided by the appropriate length. The length used is twice the jet width for those processes which involve lateral gravity-inertia wave propagation, and equals the channel length for the mechanism of passing the wave through the boundary using the cyclic condition.

Although a rather simple approach is used here for calculating expected wave propagation rates, it must be pointed out that the gravity-inertia waves, as shown in the difference maps, are not of a simple type. The base state of vertical wind shear, for example, complicates the gravity-wave structure of this study. It is not known whether the vertical motion in a wave with two-dimensional structure would go to zero everywhere at some time.

Visual inspection of the time series yields a dominant 10-13 hour period for the large domain experiment and a dominant 3-6 hour period for the small domain run. The mechanism of partial horizontal trapping due to shear is the only one presented here that yields these dominant periods. Therefore, this may explain the oscillations seen in the time series.

In many of the later vertical motion maps, especially those from the small domain run, relatively strong downward motion to the right of the jet and upward motion to the left is noteworthy. This result is also reported by Mudrick (1974), in his work using models of much greater vertical resolution than those used here. Convergence at jet level to the right of the jet and divergence to the left would result in the observed vertical motions due to the continuity equation. It is not clear, however, what mechanism might be responsible for this effect.

The vertical motion field shows us that gravity-inertia waves are present in the primitive equation model, but the vorticity and geostrophic vorticity fields for the primitive equation model show us whether the non-divergent velocity or pressure field is affected more by adjustment. Classical adjustment theory does not answer this question, since the width scale of the jet is nearly equal to the deformation radius in this study. However, the pressure field should be affected more by adjustment in the small domain run than in the large, while the velocity field is affected more in the large domain run than in the small.

Oscillations in the vorticity field would show us to what extent the non-divergent velocity is affected by adjustment, while oscillations in the geostrophic vorticity would show us to what extent the pressure is affected by adjustment. (The geostrophic vorticity at 800 millibars and 400 millibars are calculated using equations (6.1) and (6.2), respectively.)

$$\zeta_g = g\nabla^2(z_1 + z_2)/f \qquad (6.1)$$

$$\zeta_g = g\nabla^2(z_2 + z_3)/f \qquad (6.2)$$

The 400-millibar vorticity patterns and geostrophic vorticity from the primitive equation model (Figures 6.9.a-6.9.b and 6.10.a-6.10.b) and the vorticity pattern from the quasi-geostrophic model (Figures 6.9.c and 6.10.c) exhibit an asymmetry largely due to shear; i.e., the region of the largest magnitude of relative vorticity near the jet is advected eastward relative to the region further from the jet in the y-direction. The 800-millibar vorticity and geostrophic vorticity maps are shown in Figure 6.11.a-6.11.d. We shall discuss the vorticity maps in more detail for the large domain run first.

At the 400-millibar level, the isopleths are very similar in shape for the primitive equation model vorticity, ζ, the primitive equation model geostrophic vorticity, ζ_g, and the quasi-geostrophic model vorticity, ζ_{QG}. However, ζ_g is asymmetrical; it has larger positive values near its maximum and the negative values near its minimum are less negative, owing to the Jacobian term in the balance equation used in the initialization. The very small oscillations in these fields may be due to truncation error.

At the 800 millibar level, the isopleths are still nearly the same for ζ, ζ_g and ζ_{QG}. In contrast to the 400 millibar level, both ζ and ζ_g show an asymmetry similar to that described above. The values of ζ are more nearly equal to ζ_g at 800 millibars than at 400 millibars. At neither level is $\zeta - \zeta_{QG}$ or $\zeta_g - \zeta_{QG}$ greater than 20% of ζ_{QG}, and it is not clear whether ζ or ζ_g is more nearly equal to ζ_{QG}. Hence, it is not clear whether the pressure field or the velocity field is affected more by adjustment in the large domain run.

In the small domain run, the quasi-geostrophic vorticity increased by 50% between t=0 and t=24 hours, and the vertical motions increased by 20% in that time period. Note that the vorticity pattern appears to be sheared quite a bit and is not well resolved. The Rossby number is .263 for the small domain run, which is higher than is usually assumed in the quasi-geostrophic equations.

Leaving the quasi-geostrophic results aside, the 400 millibar ζ_g and, to a lesser extent, the 800 millibar ζ_g and ζ have the type of asymmetry due to the Jacobian term that was discussed in the large domain vorticity results. Oscillations in ζ and ζ_g at 400 millibars are small, as well as oscillations in the 800 millibar ζ field. However, ζ_g showed pronounced small-scale oscillations at 800 millibars, as can be seen in Figures 6.11.a-6.11.d, indicating that the pressure field is affected more by adjustment than is the velocity field in the small domain run.

7. SUMMARY

(a) The vertical motion field in the quasi-geostrophic model is like that discussed by Reiter (cf. Fig. 1.1), while the primitive equation model has in addition smaller scale and higher frequency features due to gravity-inertia waves.

(b) The difference maps of vertical motion show a pattern similar to the Jacobian pattern shown in Figure 6.5 early in the integration. The primitive equation ω oscillates about the quasi-geostrophic state once, and then the pattern becomes more complicated.

(c) The time series show a 10-13 hour periodicity in the vertical motion in the large domain run and a 3-6 hour periodicity in the small domain run. These periodicities may result from partial horizontal trapping of the gravity-inertia wave due to shear.

(d) The pressure field at 800 millibars appears to be affected by adjustment more than the non-divergent velocity field in the small domain run. In the large domain run, there are no notable oscillations in either the pressure or non-divergent velocity fields. Hence the pressure field is affected more by adjustment in the small domain run than in the large domain.

(e) During the latter part of the twenty-four hour period, there is strong convergence to the right of the jet and strong divergence to the left, at jet level, especially in the small domain run.

(f) The geostrophic vorticity in both levels of the primitive equation model shows an asymmetry which can be traced to the Jacobian term in the balance equation. The vorticity in the lower level of this model also shows this effect.

(g) Finite difference errors in the initialization can influence the behavior of the gravity-inertia waves.

8. CONCLUSIONS

(a) The apparent partial horizontal trapping of the gravity-inertia wave by the primitive equation model indicates favorable conditions for a feedback of wave energy from the gravity-inertia mode to the low-frequency mode. This feedback cannot be adequately handled where the separation of scales approach, as discussed by Blumen (1972), is used.

(b) The vertical motion is a better variable than the pressure, vorticity, or non-divergent velocity for showing the presence of gravity-inertia waves, especially in situations where the length scale of the jet is of the same scale as the deformation radius.

The role of gravity-inertia waves in the evolution of a jet maximum is worth further study and additional numerical experimentation. Many of the parameters that are fixed in this study could be allowed to vary in future experiments. Varying these may aid in understanding the adjustment process. We would also suggest that some other physical constraints we have placed here, such as initial equivalent barotropy and relatively small Rossby number should be discarded in later studies, in order that the dynamical framework of the model jet may become more realistic.

Careful attention should be given to determining the physical origin of the gravity-inertia oscillations, particularly distinguishing between the effects of the initialization procedure and wave generation by internal jet dynamics.

Modifications to the modeling and analysis should be seriously considered for future applications. For example, the vertical staggering of variables should be made more nearly consistent for the two models. Quasi-geostrophic diagnosis of the primitive equation model output would yield a "quasi-geostrophic state", which can be compared with the primitive equation model state without the problems associated with the intercomparison of output from two different model predictions. (The quasi-geostrophic model is useful, however, for showing what quasi-geostrophic theory gives for the large-scale propagation characteristics of the jet.)

Finally, a detailed analysis of the ageostrophic wind vector should be considered, to determine whether its variations are according to quasi-geostrophic theory or gravity-inertia processes.

ACKNOWLEDGEMENTS

I would like to express my sincere appreciation to Professor David D. Houghton for his continued advice and encouragement throughout this study, and for his careful reading of the manuscript of this thesis. I would also like to thank Professor John A. Young for his helpful suggestions. Lastly, my thanks to Dr. Ronald Dobosy for helping me to get started in this project and for his briefing on the construction and operation of the numerical models.

This project was supported by National Science Foundation Grant #ATM75-0317 (formerly DES75-03617) and by National Oceanic and Atmospheric Administration Grant #04-6-158-44087.

This study was submitted as a thesis in partial fulfillment of the requirements for the degree of Master of Science (Meteorology) at the University of Wisconsin-Madison, 1976.

REFERENCES

Blumen, W., 1972: "Geostrophic Adjustment", Reviews of Geophysics and Space Physics, 10, 485-528.

Cahn, A., 1945: "An Investigation of the Free Oscillations of a Simple Current System", Journal of Meteorology, 2, 113-119.

Charney, J.G. and N.A. Phillips, 1953: "Numerical Integration of the Quasi-Geostrophic Equations for Barotropic and Simple Baroclinic Flows", Journal of Meteorology, 10, 71-99.

Dobosy, R., 1972: "Non-quasi-geostrophic Motions in a Travelling Rossby Wave", M.S. thesis, University of Wisconsin, 56 pp.

Eom, J.K., 1975: "Analysis of the Internal Gravity Wave Occurrence of 19 April 1970 in the Midwest", Monthly Weather Review, 103, 217-226.

Grammeltvedt, A., 1969: "A Survey of Finite Difference Schemes for the Primitive Equations for a Barotropic Fluid", Monthly Weather Review, 97, 384-404.

Haltiner, G.J., 1972: Numerical Weather Prediction, John Wiley and Sons, New York, London, Sydney, Toronto.

Holton, J.R., 1972: An Introduction to Dynamic Meteorology, Academic Press, New York and London.

Miller, R.C., 1972: Notes on Analysis and Severe-Storm Forecasting Procedures of the Air Force Global Weather Central, Air Weather Service Technical Report 200 (Rev.)

Mudrick, S.E., 1974: "A Numerical Study of Frontogenesis", Journal of the Atmospheric Sciences, 31, 869-891.

Palmen, E. and C. Newton, 1969: Atmospheric Circulation Systems, Academic Press, New York and London.

Reiter, E.R., 1967: Jet Streams: How Do They Affect Our Weather?, Anchor Books, Doubleday and Company, Garden City, New York.

Rossby, C.G., 1937-1938: "On the Mutual Adjustment of Pressure and Velocity Distributions in Simple Current Systems", I and II, Journal of Marine Research, 1, 15-28 and 239-263.

Song, Rak to, 1969: "A Numerical Study of the Three-Dimensional Structure and Energetics of Unstable Disturbances in Zonal Currents", Ph.D. dissertation, University of Wisconsin.

Thompson, P.D., 1958: "A Theory of Large Scale Disturbances in Non-Geostrophic Flow", Journal of Meteorology, 13, 251-261.

Uccellini, L.W., 1975: "A Case Study of Apparent Gravity-Wave Initiation of Severe Convective Storms", Monthly Weather Review, 103, 497-513.

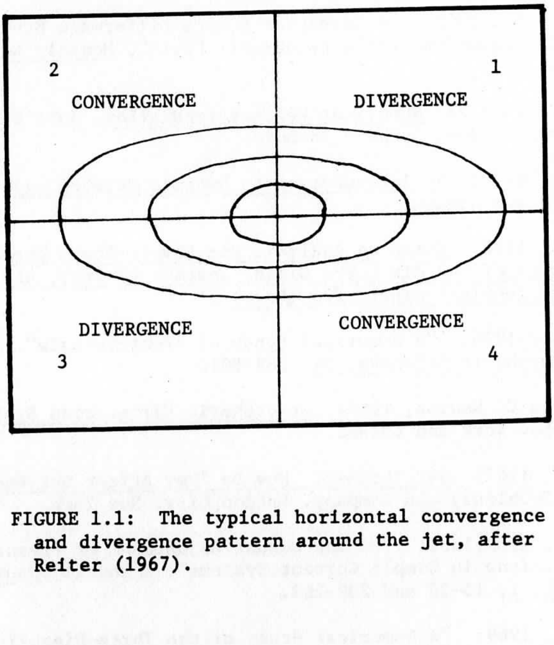

FIGURE 1.1: The typical horizontal convergence and divergence pattern around the jet, after Reiter (1967).

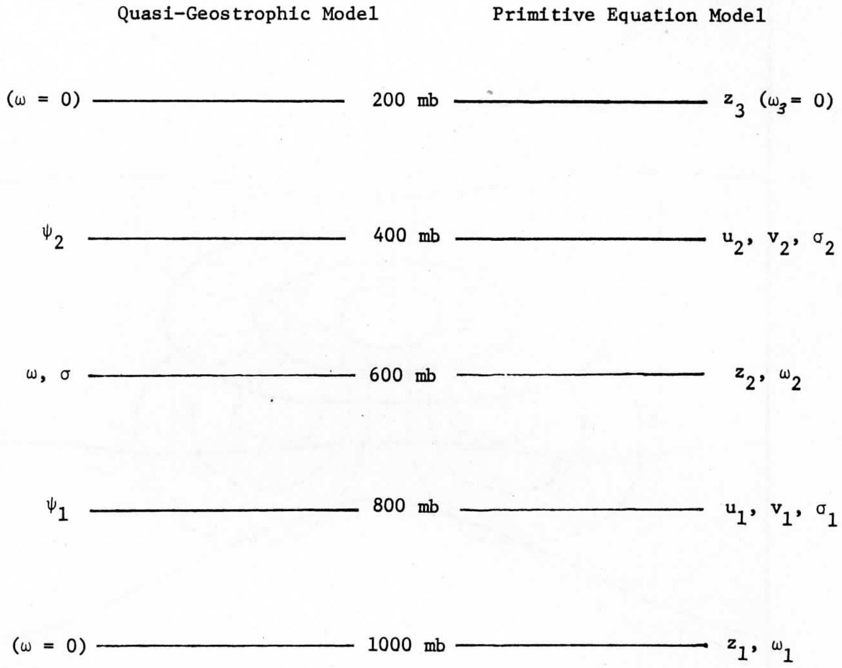

FIGURE 1.2: The vertical grid for the two models.

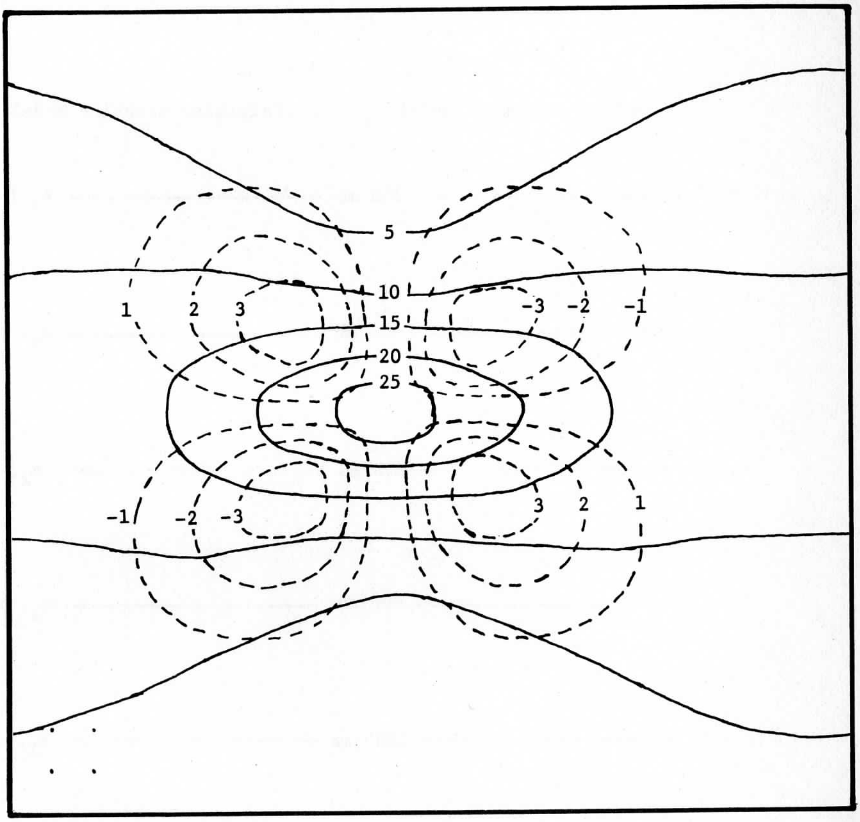

FIGURE 5.1.a: The initial 400-mb u-component of the wind for the large domain experiment in units of m/sec, and the initial 600-mb ω, shown in dashed lines, in units of 10^{-2} Newtons/(m^2-sec).

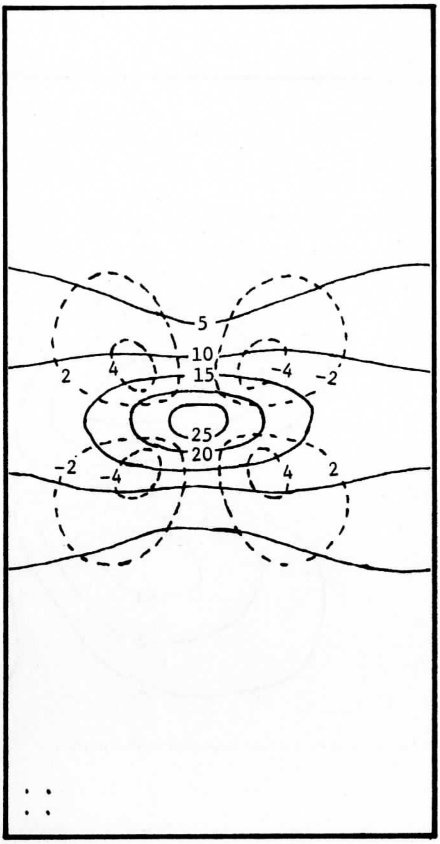

FIGURE 5.1.b: The initial 400-mb u-component of the wind for the small domain experiment in units of m/sec, and the initial 600-mb ω, shown in dashed lines, in units of 10^{-2} Newtons/(m^2-sec).

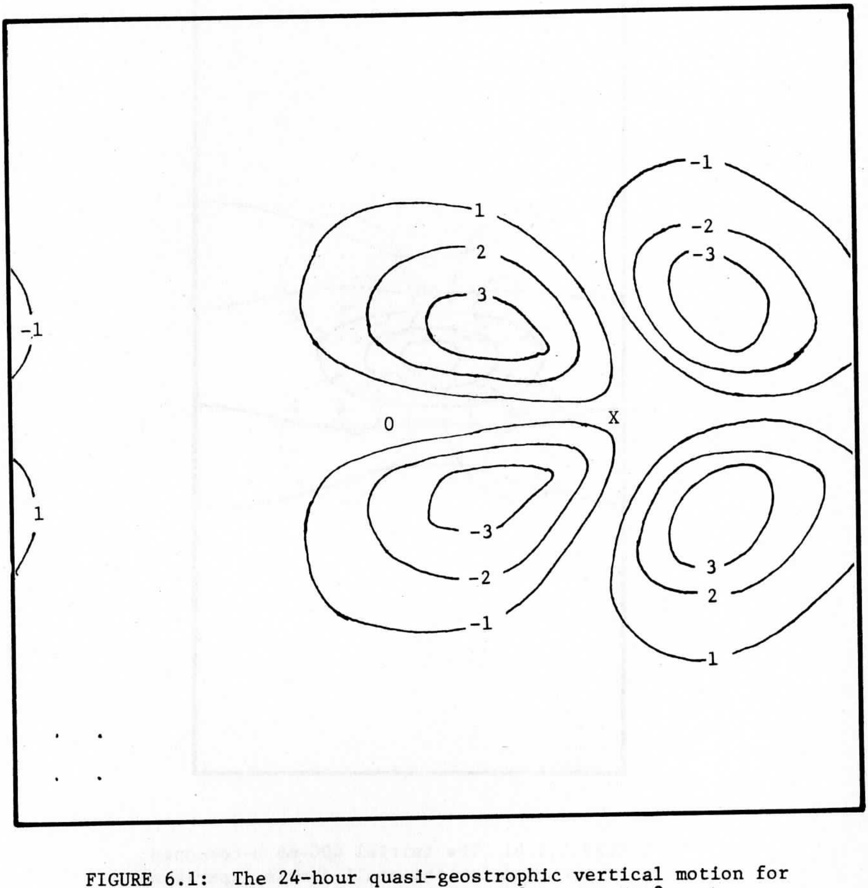

FIGURE 6.1: The 24-hour quasi-geostrophic vertical motion for the large domain run in units of 10^{-2} Newtons/(m^2-sec).

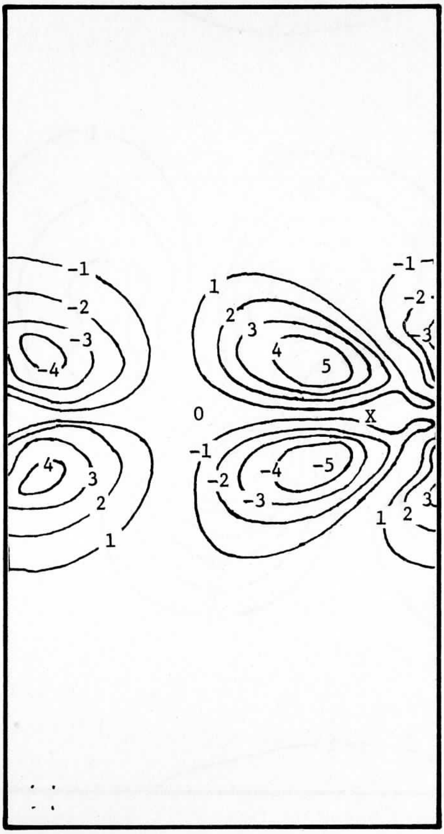

FIGURE 6.2: The 24-hour quasi-geostrophic vertical motion for the small domain run, in units of 10^{-2} Newtons/(m^2-sec).

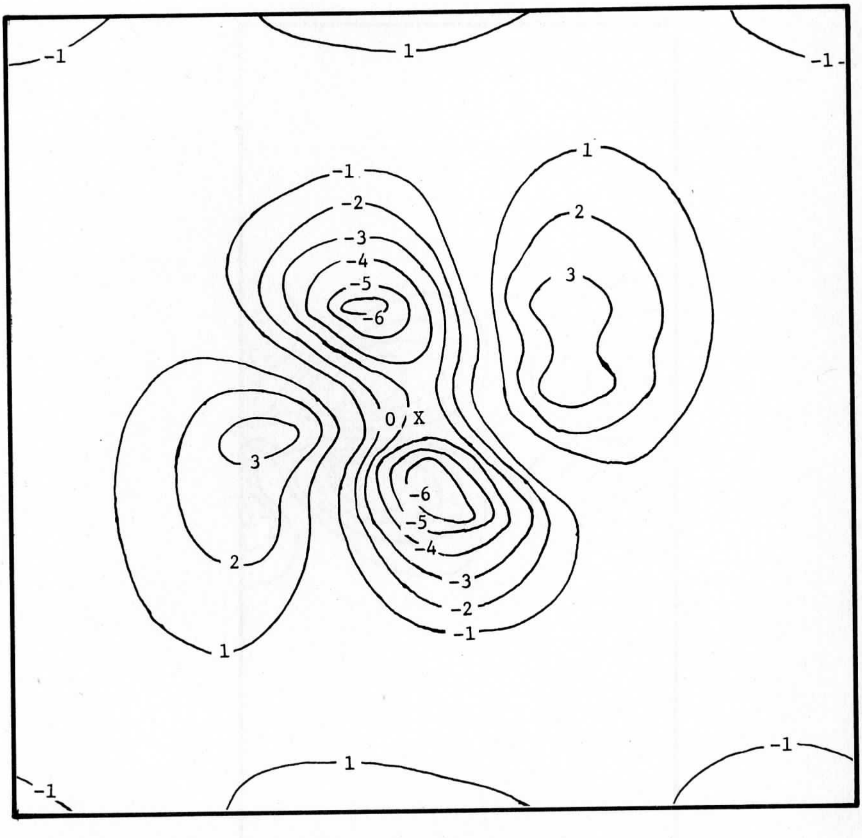

FIGURES 6.3.a - 6.3.f: Difference maps of the large domain 600-mb ω, the primitive equation ω minus the quasi-geostrophic ω, in units of 10^{-2} Newtons/(m^2-sec).

FIGURE 6.3.a: The difference map of ω at t = 3 hours.

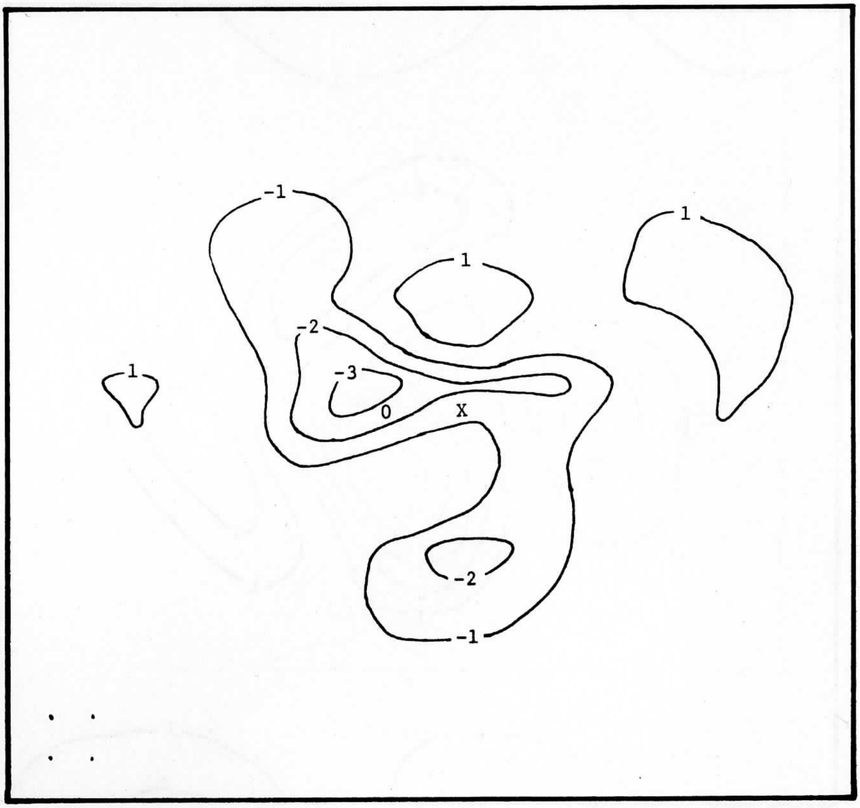

FIGURE 6.3.b: The difference map of ω at t = 6 hours.

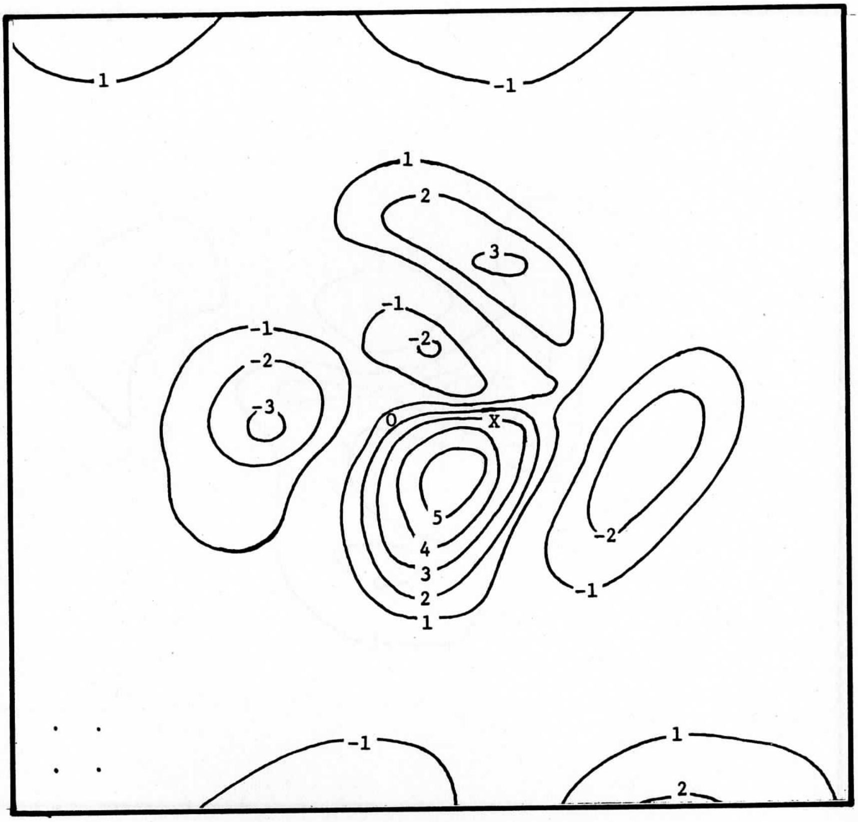

FIGURE 6.3.c: The difference map of ω at t = 9 hours.

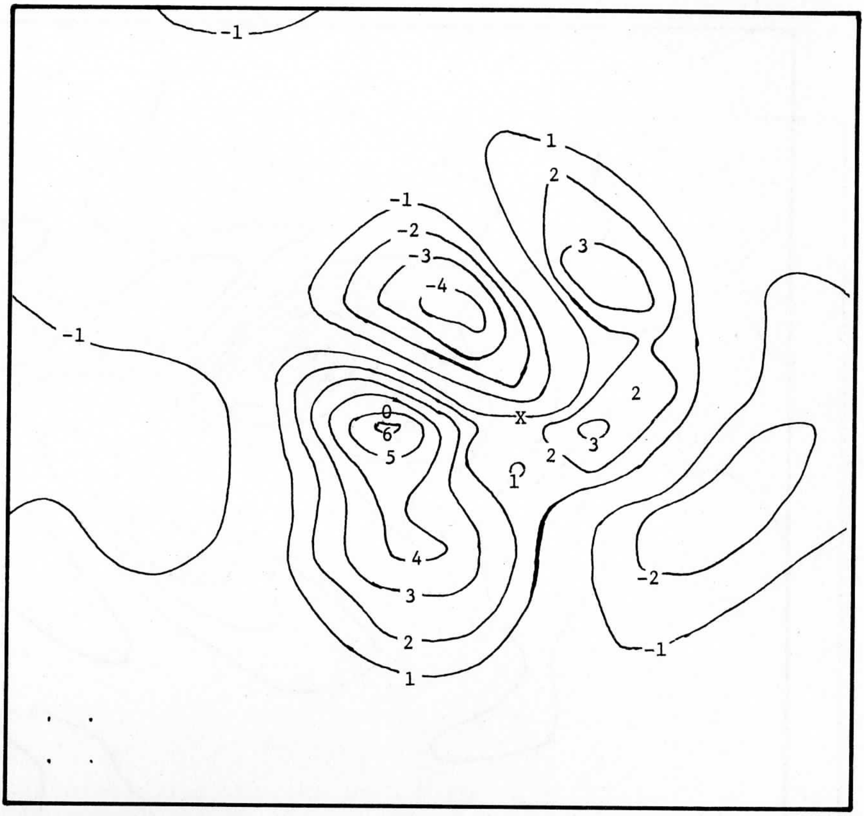

FIGURE 6.3.d: The difference map of ω at t = 12 hours.

FIGURE 6.3.e: The difference map of ω at t = 18 hours.

FIGURE 6.3.f: The difference map of ω at t = 24 hours.

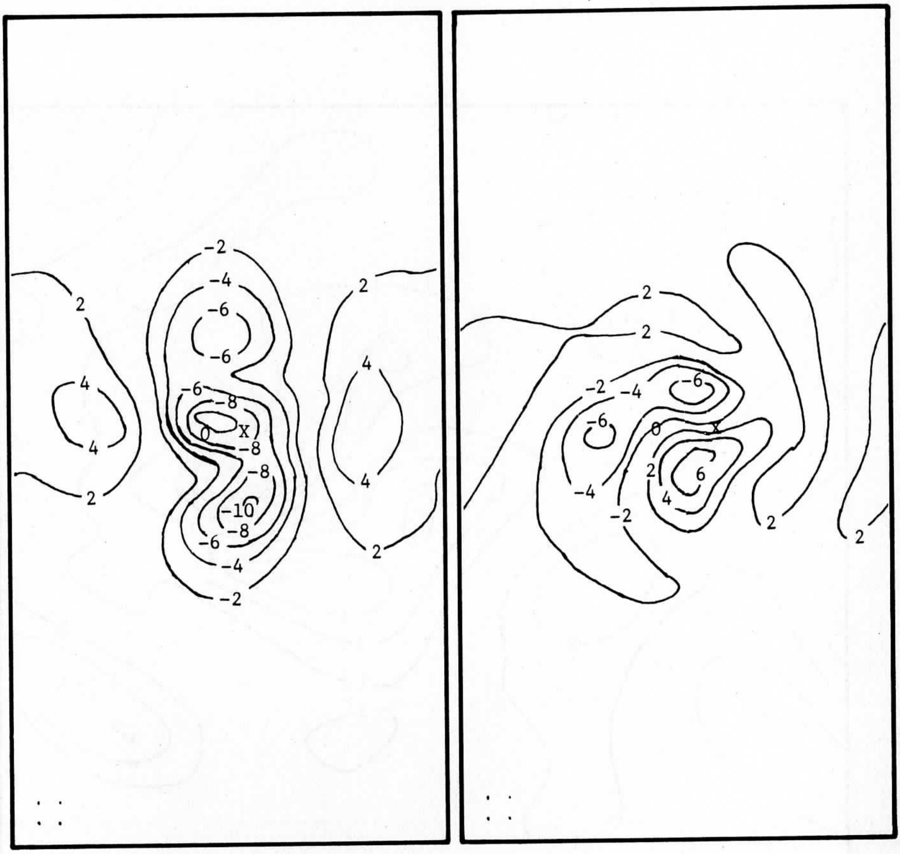

FIGURES 6.4.a - 6.4.f: Difference maps of the small domain 600-mb ω, the primitive equation ω minus the quasi-geostrophic ω, in units of 10^{-2} Newtons/(m^2-sec).

FIGURE 6.4.a: The difference map of ω at t = 3 hours.

FIGURE 6.4.b: The difference map of ω at t = 6 hours.

FIGURE 6.4.c: The difference map of ω at t = 9 hours.

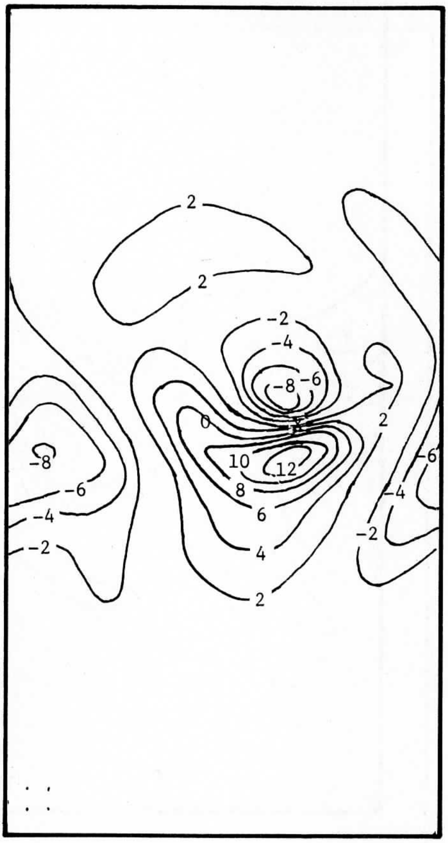

FIGURE 6.4.d: The difference map of ω at t = 12 hours.

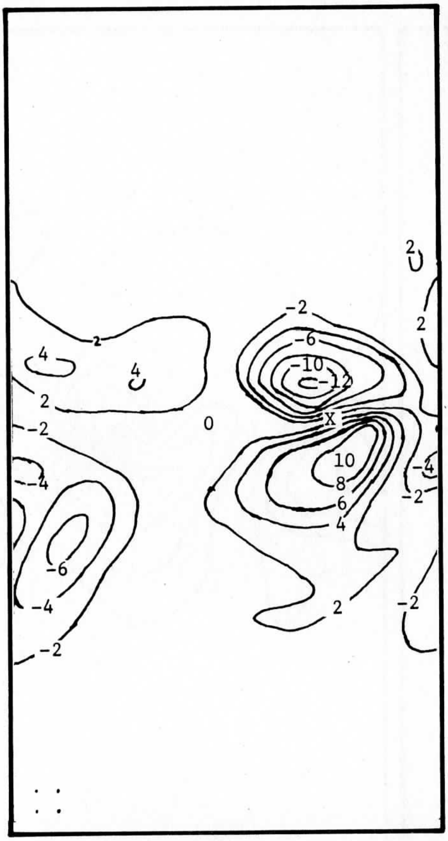

FIGURE 6.4.e: The difference map of ω at t = 18 hours.

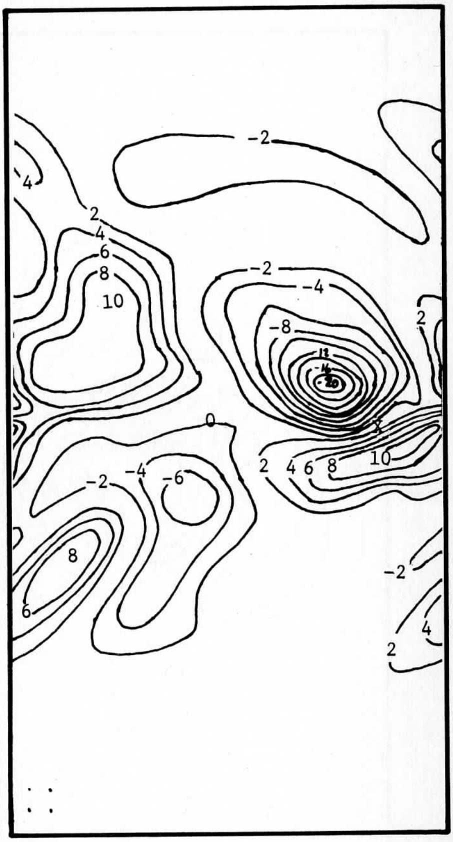

FIGURE 6.4.f: The difference map of ω at t = 24 hours.

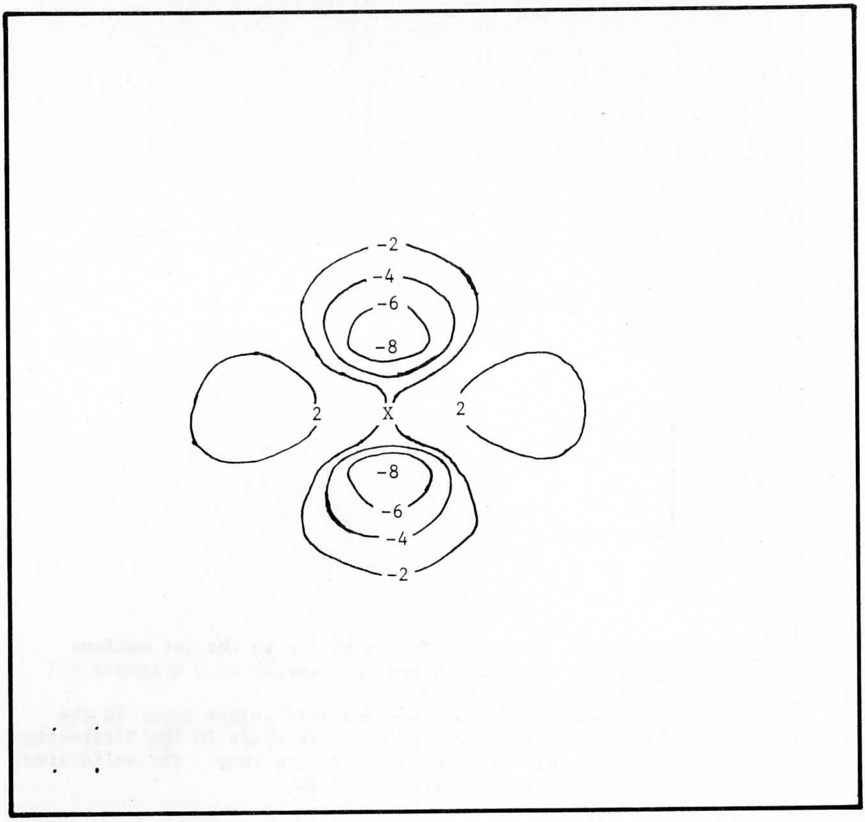

FIGURE 6.5: Minus twice the Jacobian of the initial non-divergent winds at 400 mb.

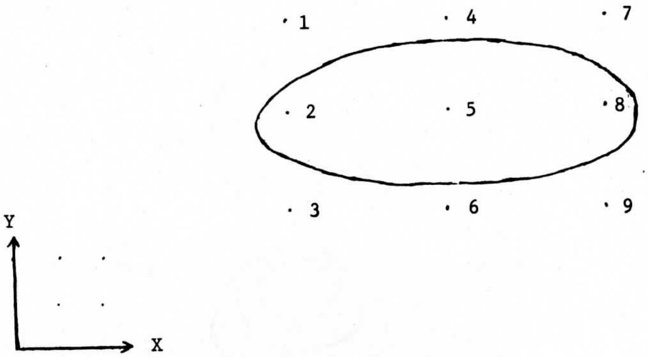

FIGURE 6.6: The positions relative to the jet maximum (position 5) at which the time series of ω (Figures 6.7 and 6.8) were obtained.

Adjacent positions are two grid points apart in the Y-direction and three grid points apart in the X-direction for both the large and small domain runs. The solid line is the 20 m/sec isotach at 400 mb.

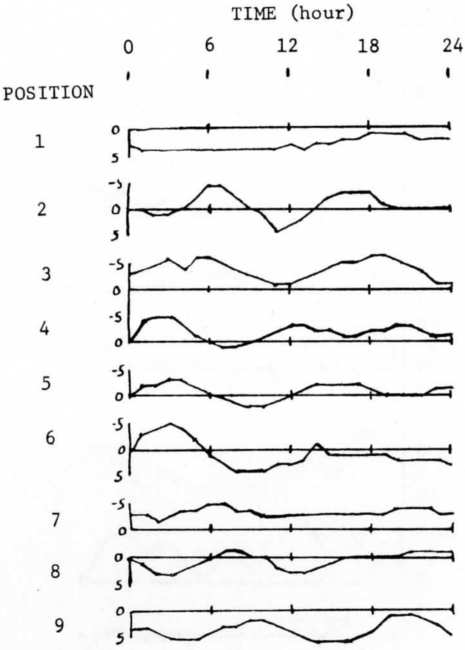

FIGURE 6.7: The time series of the large domain primitive equation 600-mb ω in units of 10^{-2} Newtons/(m^2-sec) at each of the nine positions relative to the jet shown in Figure 6.6.

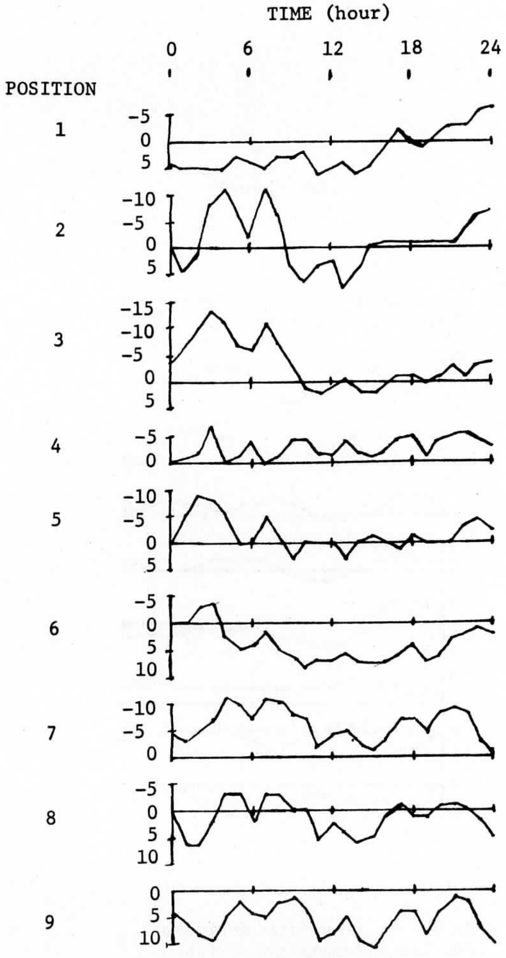

FIGURE 6.8: The time series of the small domain primitive equation 600-mb ω in units of 10^{-2} Newtons/(m^2-sec) at each of the nine positions relative to the jet shown in Figure 6.6.

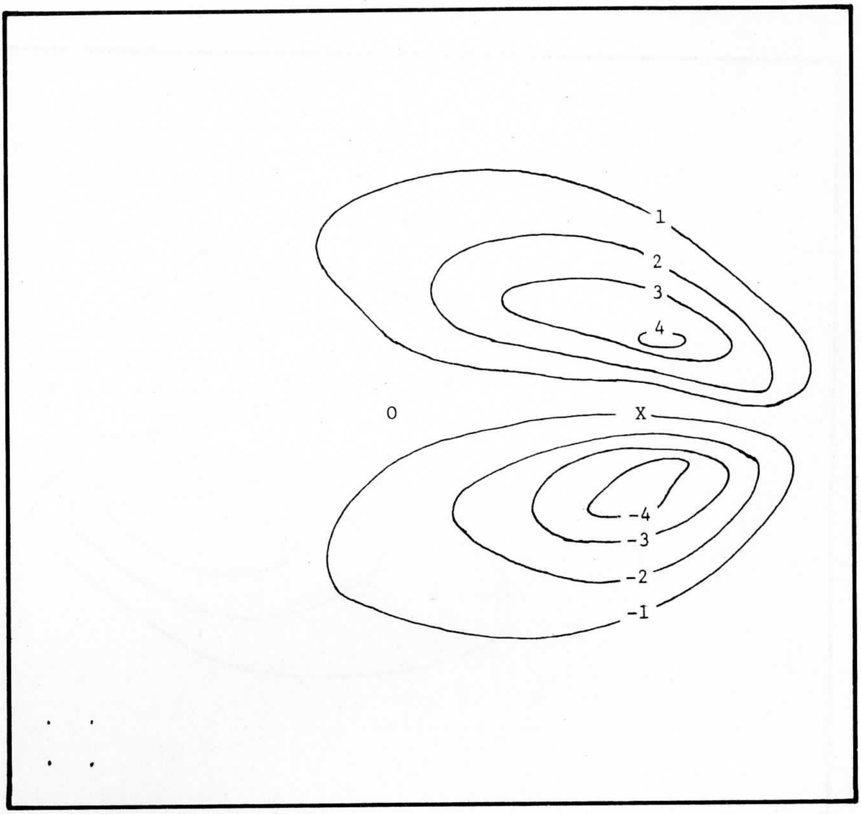

FIGURE 6.9.a: The 24-hour primitive equation model relative vorticity, ζ, at 400 mb for the large domain run, in units of 10^{-5} $\sec^{-1}$.

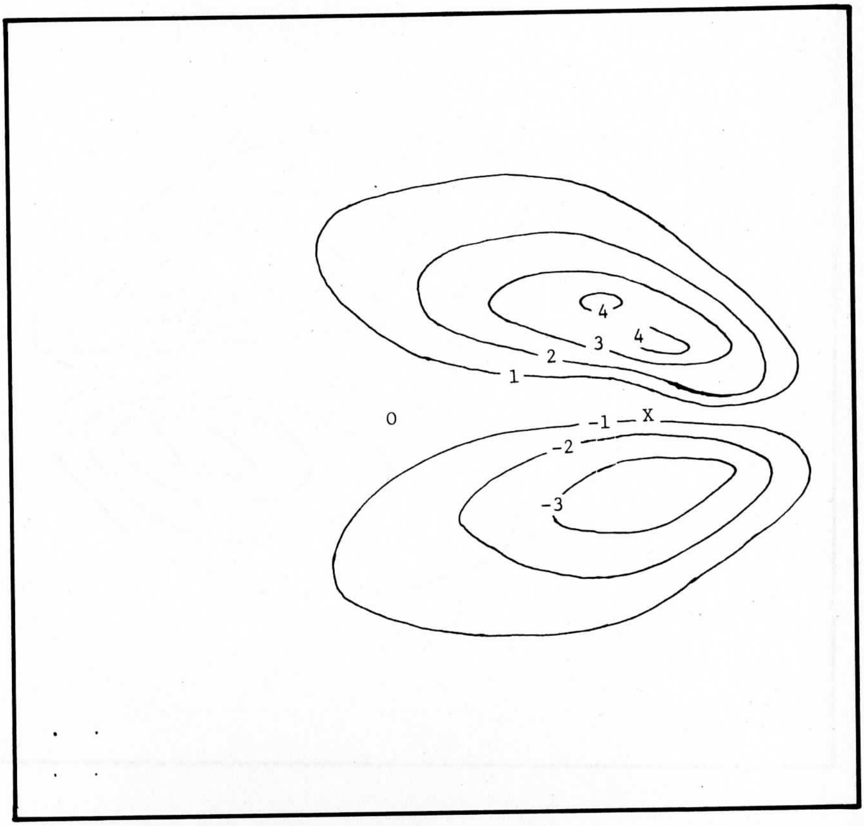

FIGURE 6.9.b: The 24-hour primitive equation model geostrophic vorticity, ζ_g, at 400 mb for the large domain run, in units of 10^{-5} sec^{-1}.

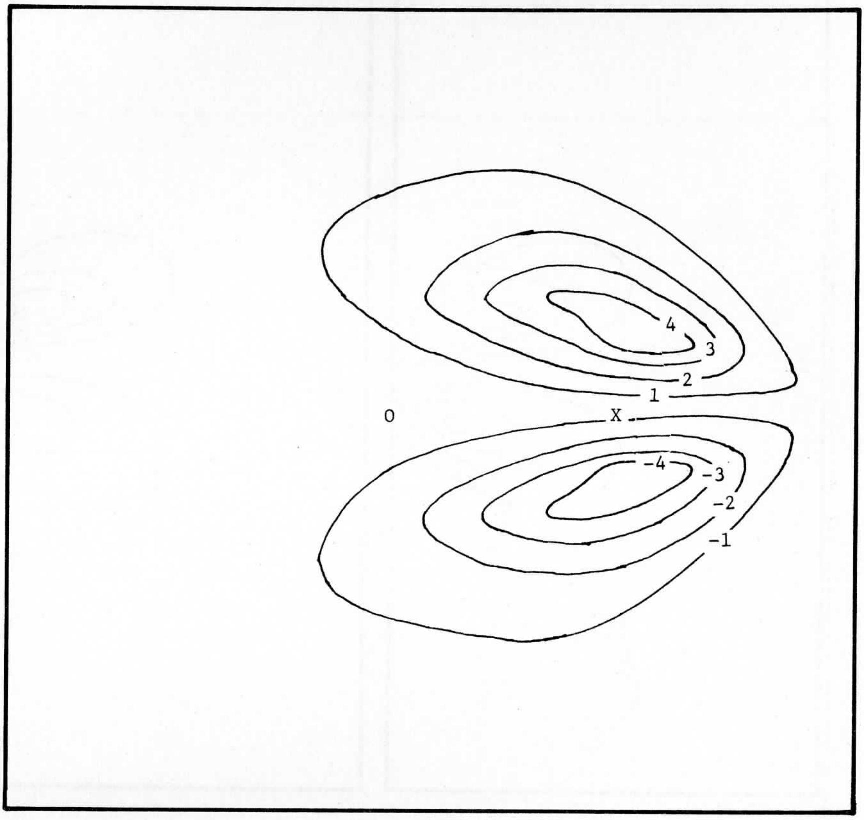

FIGURE 6.9.c: The 24-hour quasi-geostrophic model vorticity, ζ_{qg}, at 400 mb, for the large domain run, in units of 10^{-5} sec^{-1}.

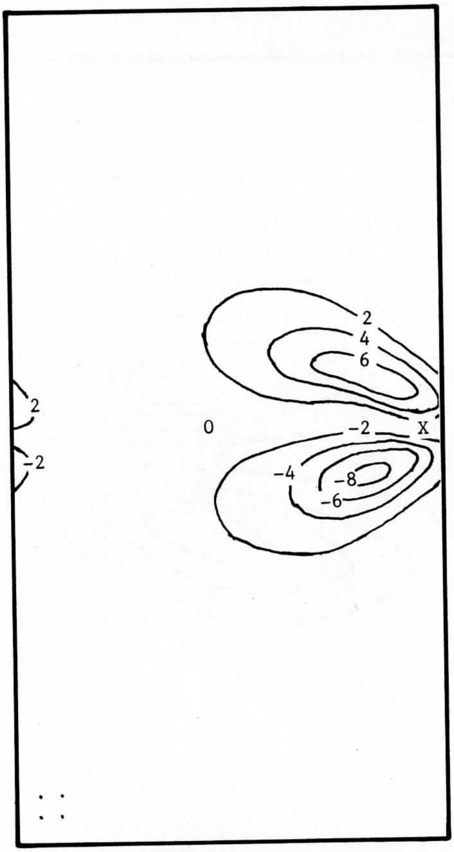

FIGURE 6.10.a: The 24-hour primitive equation model vorticity, ζ, at 400 mb, in units of 10^{-5} sec^{-1}, for the small domain run.

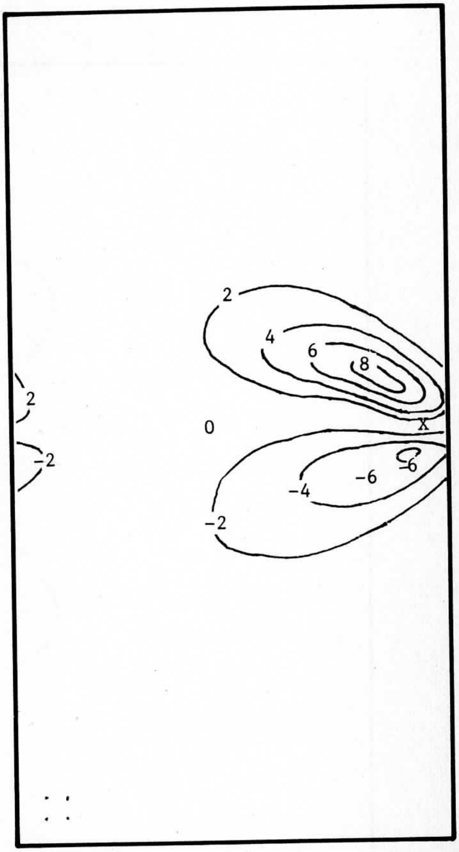

FIGURE 6.10.b: The 24-hour primitive equation model geostrophic vorticity, ζ_g, at 400 mb, in units of 10^{-5} sec^{-1}, for the small domain run.

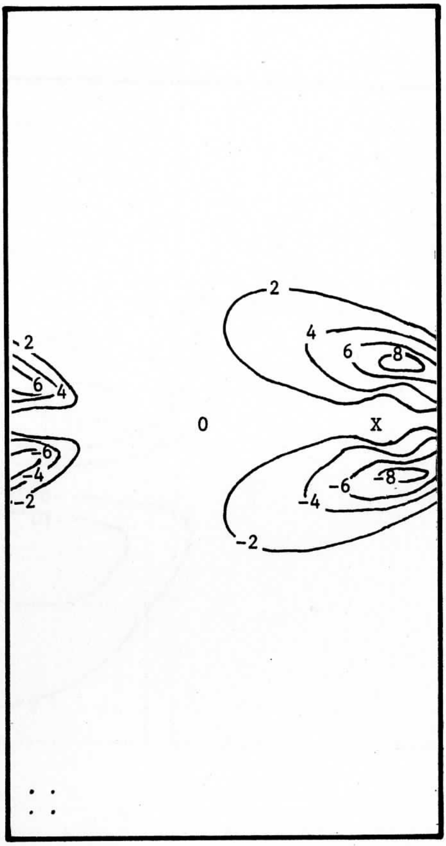

FIGURE 6.10.c: The 24-hour quasi-geostrophic model vorticity, ζ_{qg}, at 400 mb, in units of 10^{-5} sec^{-1}, for the small domain run.

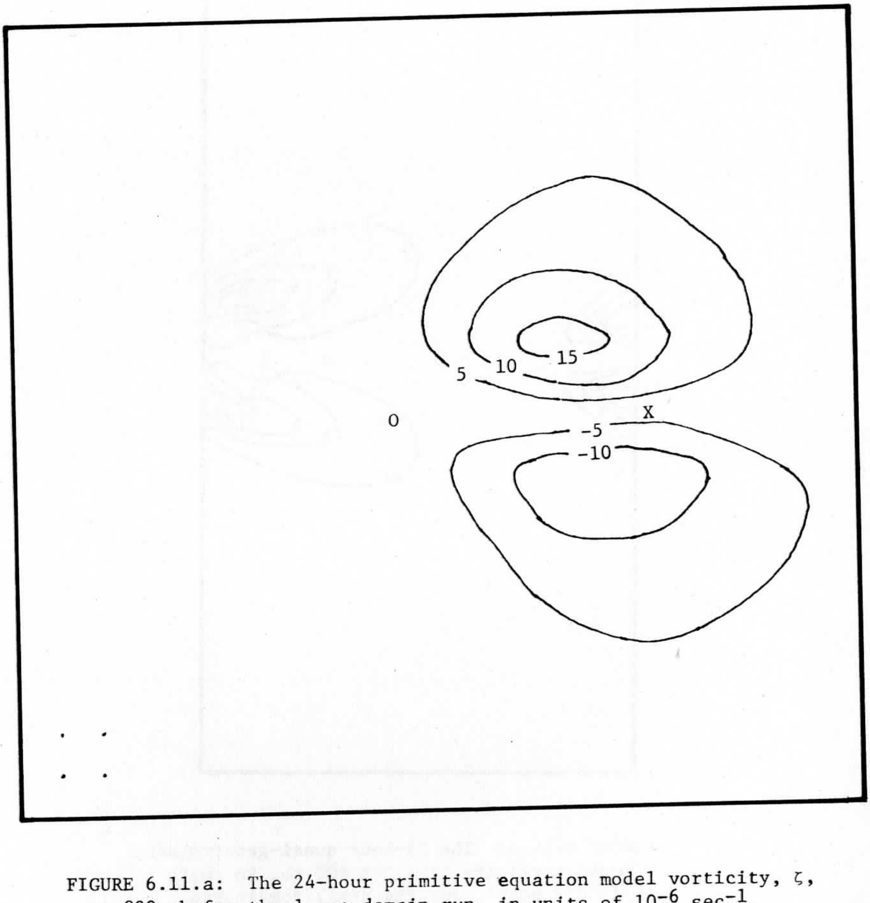

FIGURE 6.11.a: The 24-hour primitive equation model vorticity, ζ, at 800 mb for the large domain run, in units of 10^{-6} sec^{-1}.

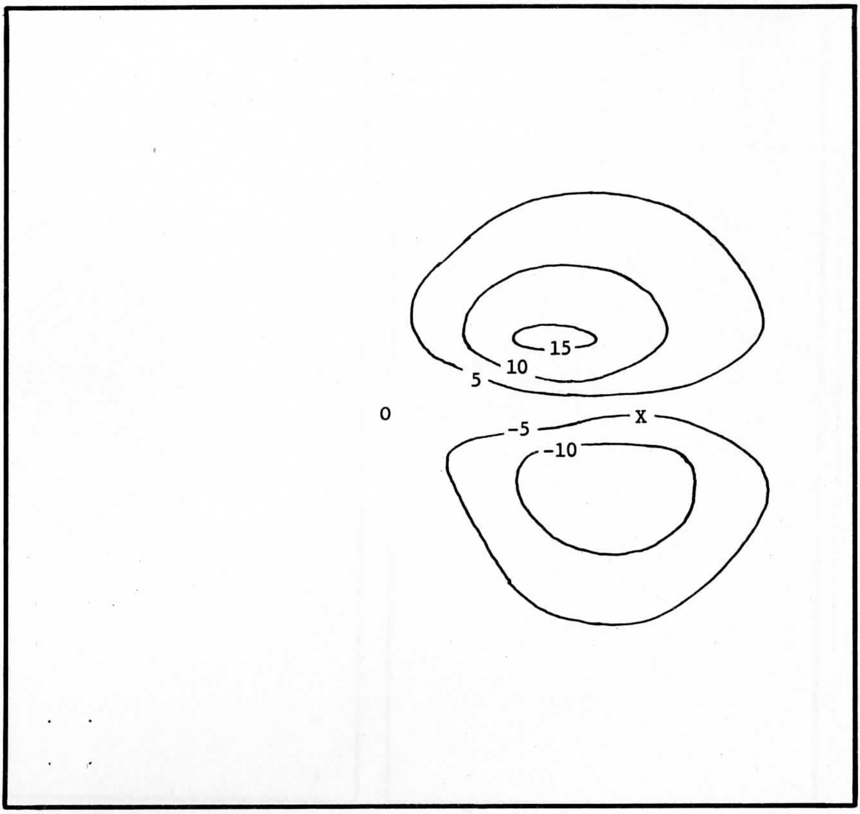

FIGURE 6.11.b: The 24-hour primitive equation model geostrophic vorticity, ζ_g, at 800 mb for the large domain run in units of 10^{-6} sec^{-1}.

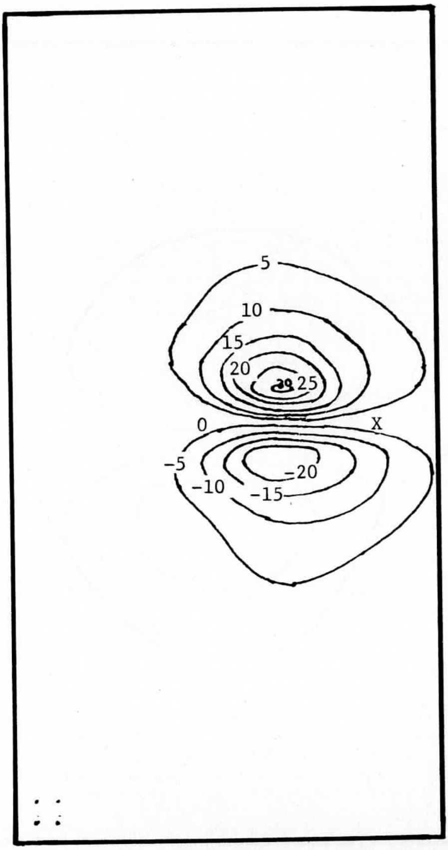

FIGURE 6.11.c: The 24-hour primitive equation model vorticity, ζ, at 800 mb for the small domain run, in units of 10^{-6} sec^{-1}.

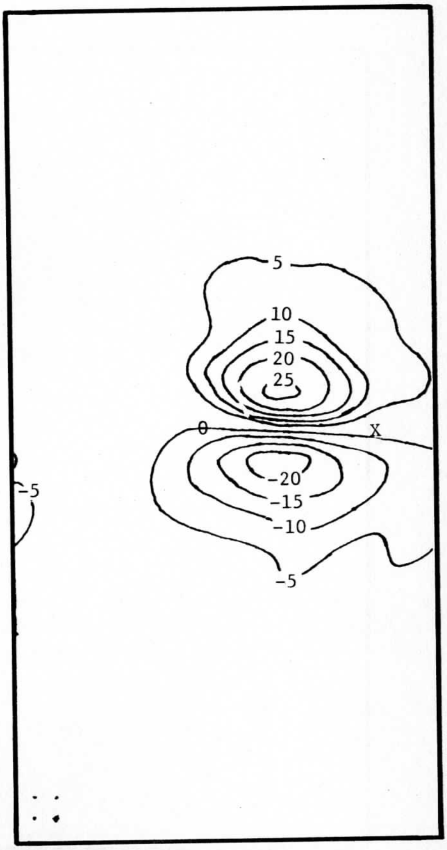

FIGURE 6.11.d: The 24-hour primitive equation model geostrophic vorticity, ζ_g, at 800 mb, for the small domain run, in units of 10^{-6} sec^{-1}.

TABLE 1.1

Horizontal Layout of the Two Experiments

Length of channel	4000 km.	2000 km.
Distance from center of model to lateral boundaries	1900 km.	1950 km.
Grid spacing: Number of kilometers per grid	200	100
Number of grids in x-direction	20	20
Number of grids in y-direction	20	40

TABLE 5.1

Parameters for Large Domain and Small Domain Experiments

Parameters	Large Domain Run	Small Domain Run
Channel length (km)	4000	2000
Channel width (km)	4000	4000
Quarter wavelength (km)	1000	500
Half width (km)	500	250
Velocities: (m/sec)		
jet maximum, upper level	26.3	26.5
jet axis average, upper level	17.2	17.0
jet axis average, the mean for the two levels	11.5	11.4
Rossby numbers:		
jet maximum, upper level	0.263	0.53
jet axis average, upper level	0.172	0.34
jet axis average, the mean for the two levels	0.115	0.23
Primitive Equation Model Only:		
Deformation radii: (km)		
external	2600	2600
internal	350	350
Gravity wave speeds: (m/sec)		
external	260	260
internal	35	35
Internal Froude number:	0.33	0.33
Width scale with respect to the internal deformation radius	1.43	0.71

TABLE 6.1

Filtered Output Response, $b_o(n)/a_o$, from the Primitive Equation Model

n	T(hr)	$2\pi/n$	$b_o(n)/a_o$
2	1	π	-0.091
3	1.5	$2\pi/3$	0.172
4	2	$\pi/2$	0.364
6	3	$\pi/3$	0.727
8	4	$\pi/4$	0.841
16	8	$\pi/8$	0.924

TABLE 6.2

Distance of Jet Core Maximum Propagation (km)

Number of Hours	6	12	18	24
Large Domain				
Quasi-Geostrophic	320	600	800	1080
Primitive Equation	360	640	960	1200
Small Domain				
Quasi-Geostrophic	280	540	780	1000
Primitive Equation	280	440	600	800

TABLE 6.3

Examination of Periodicities
Observed in Model Experiments

Mechanism:		Lateral Boundary Trapping	Time Scale of Adjustment
Large domain internal wave	Round trip distance (km)	4000 km	-----
	τ_{nr}	34 hrs	-----
	τ_r	47 hrs	17.5 hrs
Large domain external wave	Distance	4000 km	-----
	τ_{nr}	4.3 hrs	-----
	τ_r	4.3 hrs	17.5 hrs
Small domain internal wave	Distance	4000 km	-----
	τ_{nr}	34 hrs	-----
	τ_r	37 hrs	17.5 hrs
Small domain external wave	Distance	4000 km	-----
	τ_{nr}	4.3 hrs	-----
	τ_r	4.3 hrs	17.5 hrs

NOTE: τ_{nr} is the period for a non-rotating coordinate system, and τ_r is the period for a rotating coordinate system. τ_r is larger than τ_{nr} because rotation reduces the group velocity of gravity waves.

TABLE 6.3 (continued)

Mechanism:		Shear Trapping	Passing of wave along X-axis through cyclic condition
Large domain internal wave	Round trip distance (km)	1000 km	4000 km
	τ_{nr}	8.4 hrs	34 hrs
	τ_r	11.8 hrs	74 hrs
Large domain external wave	Distance	1000 km	4000 km
	τ_{nr}	1.1 hrs	4.3 hrs
	τ_r	1.1 hrs	4.3 hrs
Small domain internal wave	Distance	500 km	2000 km
	τ_{nr}	4.2 hrs	17 hrs
	τ_r	4.6 hrs	23.6 hrs
Small domain external wave	Distance	500 km	2000 km
	τ_{nr}	0.55 hrs	2.1 hrs
	τ_r	0.55 hrs	2.1 hrs

COMPARISON OF LAKE BREEZE DATA
WITH THE
NEUMANN-MAHRER NON-HYDROSTATIC NUMERICAL MODEL

Alfred J. Stamm

ABSTRACT

The Neumann-Mahrer (1971) computer model of the sea breeze was tested with data for lake breezes taken in Milwaukee on three days in 1973. Initial and boundary conditions of the model were adjusted to approximate the conditions on these days, and the model was adapted to accept an initial synoptic wind. The resultant winds, inflow boundaries, and surface pressures produced by the model were compared with the measurements made in Milwaukee.

The comparisons showed that the model responded correctly over a time scale of hours; however, wind and temperature gradients were somewhat low. When the grid spacing of the model was reduced from 5 to 1 km, the performance of the model was improved considerably. Since this model is non-hydrostatic, the pressure it predicts includes vertical accelerations, but considerable detail was still lacking in the surface pressure. The fact that the model agrees with reality indicates that the model could be useful in boundary layer studies.

Analysis of real lake breezes in Milwaukee requires an initial synoptic wind and a finer grid spacing. These were added to the model as part of this study.

NOMENCLATURE

Symbol	Meaning
f	Coriolis Parameter
g	Acceleration of Gravity
h	Height of the Constant Flux Layer (50 m)
H	Height of the Model (1950 m)
k_o	von Karman's Constant
K	Eddy Viscosity or Eddy Conductivity
L	Term in Flux Equation
m	Iteration Number
p	Pressure
p_h	Change in Hydrostatic Pressure from Initial Pressure

Symbol	Meaning
p^*	Non-Hydrostatic Pressure
p'	Change in Total Pressure from Initial Pressure
p''	Change in Pressure due to Divergence
r	Term in Flux Equation
R	Ideal Gas Constant
Ri	Richardson Number
t	Time
T	Temperature
U	Horizontal Wind Speed
u	Horizontal Velocity Component Perpendicular to Shore
u'	Change in u from Initial Velocity
u^*	Approximate u
v	Horizontal Velocity Component Parallel to Shore
v'	Change in v from Initial Velocity
V_f	Velocity of Front
w	Vertical Velocity
w'	Change in w from Initial Velocity
w^*	Approximate w
x	Horizontal Coordinate Perpendicular to Shore
z	Vertical Coordinate
z_o	Roughness Parameter
α	Nondimensional Constant (-0.03)
β	Term in Flux Equation
γ	Nondimensional Constant (1.0)
θ	Potential Temperature
$\overline{\theta}$	Average Potential Temperature for Layer
λ	Over Relaxation Coefficient
ρ	Air Density
ϕ	Latitude (43 deg)
ψ	Angle Between the Shoreline and Due North (-8 deg)
Ω	Earth's Rotational Speed

Symbol	Meaning
Subscripts	
A	Ahead of Front
B	Behind Front
i	Lateral Grid Number
j	Vertical Grid Number
$_o$	Initial (Except for k_o and z_o Defined Above)
s	Surface

1. INTRODUCTION

Purpose

The prediction of lake breezes has become important in recent years in controlling air pollution. The major parameter needed in determining air pollution trajectories is the detailed circulation of air currents, and a good numerical model can be of great value in estimating this circulation for candidate synoptic situations.

An ideal numerical model describing the lake breeze should be three dimensional (in space) to account for shoreline curvature and synoptic pressure gradients, the latter being constructed so that this pressure can change with time. The grid spacing should be fine enough to detect and describe the lake breeze front and the high gradients of pressure, temperature, and wind near the front.

A useful way to reduce the number of grid points and the complexity of the above model is to make it two dimensional instead of three dimensional. This, however, makes both a synoptic pressure gradient and shoreline curvature more difficult to handle. The coriolis terms must be modified so that the model appears to have an initial synoptic pressure gradient. The shoreline curvature remains a problem. In any case, a model should first be tested with a straight shoreline before the complexity of curvature is added.

A useful lake breeze numerical model is one with constantly changing boundary conditions. These boundary conditions depend not only on an external forcing function; they also depend on parameters determined within the model, especially the wind and temperature fields. Such a model would be extremely complex and would probably require enormous computer power. Fortunately one can still benefit from simpler models. It is even possible to use a model with an instability, provided the time to "blow-up" is longer than the time scale of the lake breeze.

The vertical fluxes of momentum, heat, and moisture in the first 50 m above the surface are needed to describe the surface interaction with the overlying atmosphere. In other words, the top of the surface layer can be thought of as the bottom boundary of the rest of the model. These fluxes depend on incoming and outgoing radiation, surface emissivity, conductivity, and moisture content, and atmospheric mixing. These quantities could be parameterized to give the above mentioned fluxes; alternatively, the fluxes could be part of a look-up-table determined by previous measurements for candidate synoptic situations. Work on the latter technique could be fruitful for the future.

In determining the vertical fluxes of momentum, heat, and moisture, a parameterization scheme is the least data intensive, and can be used if it can give realistic results. Whether or not the results are realistic can be determined by comparing the model output with nature.

Numerous models have been developed which give the general large-scale features of a lake breeze, but the crucial test is the smaller scale features near the lake breeze front. For example, the model should pick up the non-hydrostatic pressure changes which should occur near the front, and the large gradients of wind and temperature near the front should be reproduced by the model.

One of the better sea-breeze models is that of Neumann and Mahrer (1971, 1972, 1973). The model is non-hydrostatic and thus can be tested for these important features. The model is two dimensional (in space) and contains no moisture. The temperature and wind at the top of the surface layer are determined from the near surface vertical fluxes of heat and momentum, assumed to be constant in the surface layer. The eddy viscosity and conductivity for these fluxes are dependent on the Richardson number, and are determined by the method of Estoque (1963), which uses the surface temperature plus the temperature and wind for the level immediately above the surface layer determined by the model in the previous time step, as applicable to the surface layer for the present time step. This parameterization scheme was left intact as a first cut to see how realistic it was. The same was done for the lack of moisture in the model.

An important aspect of the model is the true soil surface temperature which must be specified as a changing boundary condition. The surface temperature unfortunately was not available for the test days in Milwaukee, so it was estimated from the shelter height temperatures which were available. The method used is described in Section 3. In principle, it may be possible to use a satellite to determine surface temperature, but these observations were not available for this study.

The model was modified in two ways. The model had no provision for a synoptic wind, but in mid-latitudes, a synoptic wind is usually present; therefore, a synoptic wind was added to the model. This is described in Section 2. The other major modification was a reduction of the grid spacing, to better examine the gradients of wind and temperature near the lake breeze front (see Section 2).

The main parameters used in comparing the model with the experimental data taken in Milwaukee were the surface pressure, wind and temperature gradients near the lake breeze front, and the inflow boundaries (in space and time). The results (see Sections 5 and 6) showed that the parameterization scheme worked surprisingly well and that moisture is a second order effect. On the other hand, both the synoptic wind and the smaller grid spacing were found to be very important parameters.

Background

A sea or lake breeze is a daytime mesoscale circulation occurring along a coastal region which has surface winds blowing from the sea onto the land. The time scale of this mesoscale phenomenon is 6-12 hrs, since it is caused by solar heating. The horizontal space scale can range from a few kilometers (in the case of a sea breeze opposing the synoptic scale wind) to over 100 km (in the tropics). Typical vertical scales range from 150 to 1500 m (Defant, 1951). Figure 1 summarizes a typical Lake Michigan lake breeze. An excellent description of a lake breeze is given by McPherson (1968), but the circulation becomes more complicated when there is an offshore synoptic scale wind as described by Koschmieder (1936).

Interest in sea breezes has existed since early Greek times, when Themistocles used the sea breeze to help destroy the Persian fleet in the Bay of Salamis (Neumann, 1973a). In more modern times, the present day vacationer often heads for the beach because the weather report indicates "cooler near the lake". For years, fishermen have used the night-time land breeze to sail their boats out to their favorite fishing spots, returning the following day with the sea breeze. Convective clouds produced by sea breezes over islands can be seen from great distances, and have been used over the ages by sailors looking for land.

The importance of sea breezes today is growing because the sea breeze is able to concentrate and recirculate air pollutants (Kauper, 1960; Lyons and Olsson, 1972). A better knowledge of the details of sea breezes is needed in order to determine the best locations of future urban expansion and unavoidable pollution sources as well as to control existing sources (IES, 1973).

Many authors have described the sea breeze, but one of the best descriptions is that by Dampier (1705), part of which is quoted here:

> "It comes in a fine, small, black Curle upon the Water, when as all the Sea between it and the Shore not yet reach'd by it, is as smooth and even as Glass in comparison; in half an Hour's time after it has reached the Shore it fans pretty briskly, and so increaseth gradually till Twelve a-Clock, then it is commonly

> strongest, and lasts so till Two or Three a very brisk Gale; about Twelve at Noon it also veers off to Sea two or three Points, or more in very fair Weather. After Three a-Clock it begins to die away again, and gradually withdraws its force till all is spent, and about Five a-Clock, sooner or later, according as the Weather is, it is lull'd asleep, and comes no more till the next Morning."

Many experimental studies have been made of sea breezes, from simple surface observations of wind and temperature by Davis et al. (1890) and pilot balloon studies of van Bemmelen (1922), to the glider studies of Wallington (1959, 1965) and Simpson (1964), to the multi-instrument assaults on the sea breeze in the intensive studies of Hsu (1969) and Lyons (1974). Jehn (1973) has created a sea breeze bibliography with over 500 experimental and theoretical entries.

Theoretical Developments and Numerical Models

Jeffreys (1922) described the sea breeze as an example of a wind in which friction effects exceed rotation and acceleration effects in the equation of motion. Haurwitz (1947) further developed the friction terms, giving frictional retardation of the sea breeze, and showed a diurnal rotation of the wind to be the effect of coriolis force. In both these models, as well as in the one by Defant (1951), the horizontal advection of temperature was omitted and other simplifications were made so that the equations could be solved analytically.

A nonlinear numerical model was developed by Pearce (1955), and Fisher (1961) improved on it by allowing a nonadiabatic lapse rate and a heat sink as well as a heat source. Estoque (1961) created a relatively realistic two dimensional (in space) hydrostatic numerical model of the sea breeze which is the basis of most models today; however, he had some problems with violation of continuity (Peterson, 1971). Moroz (1967) modified Estoque's model to apply it to Lake Michigan, but did not alleviate any of the inherent problems (Peterson, 1971). McPherson (1968) added another spatial dimension to Estoque's model in order to examine irregular Texas coastlines and found that convergence indeed depended on coastline shape. The importance of using three spatial dimensions with a curved coastline was further emphasized by Pielke (1974b). Pielke's (1973, 1974a) three dimensional hydrostatic model was generated to relate the sea breeze to observed convection in Florida; inclusion of surface roughness and better continuity conditions improved McPherson's model.

Neumann and Mahrer (1971) created a non-hydrostatic two dimensional model which is examined in this study. Pressure changes due to accelerations are taken into account as well as hydrostatic pressure changes. The model shows that surface pressure decreases with time on the land side of the sea breeze circulation. The authors state that the low deepens as it moves in with the front. Neumann (1973b) further states that the maximum heating of the air aloft takes place close to the front since the rising air in the front lifts the warm surface air up. This makes the front more pronounced. This model will be examined in greater detail in the next chapter.

Outline of Present Study

The purpose of this study was to compare experimental observations with the output of Neumann and Mahrer's sea breeze model. Observations were made on eight days in the summer of 1973 (Table 1). Of these, only three had a recognizable lake breeze front. The day with the most complete data set, 17 July, had the weakest front. The day with the strongest front, 30 June, had a fairly good data set, but synoptic scale conditions were changing. In spite of these limitations, interesting results were obtained.

A description of the experimental observations is given in Section 5. Comparisons of the model with the following observations were made:

- Change in near surface temperature with time during the frontal passage.
- Arrival time and speed of the lake breeze front.
- Height and penetration of the lake breeze inflow.
- Change in wind speed with time at a given location.
- Change in wind direction with time during frontal passage.
- Vertical velocity of winds in the front as estimated with the continuity equation.
- Change in surface pressure with time.

No temperature profiles were available, so comparisons with predicted temperature fields was impossible.

After conclusions have been drawn from the three case studies, the model will be critiqued and suggestions will be given for a future study.

2. CONSTRUCTION AND USE OF THE MODEL

Neumann and Mahrer were kind enough to provide a computer program listing for their sea breeze model. After altering the program to run on a Univac 1110, the model was tested to make sure that their results could be duplicated.

The model was designed for the Mediterranean Sea, so to make it applicable to Milwaukee, some changes had to be made. The only alteration involving a change in the equations of the model was the addition of a synoptic wind. A description of how this change affects the model is shown below. Alterations involving constants, initial conditions, and the time-changing surface temperature boundary condition are discussed in Section 3.

Model Characteristics

The model varies only in the z and x directions, where z is vertical and x is taken normal to the shoreline. This implies that the shoreline must be straight. Although most shorelines are curved, a straight shoreline was tested first. As will be seen in Figure 7, the variation of the shoreline from straight at Milwaukee is slight compared to the scale of the model.

The state of the atmosphere is taken to be "dry". Neumann and Mahrer (1974) suggest that a "moist" circulation is desirable; however, such a change would be major and is therefore outside the scope of this study. The significance of the lack of moisture in the model is discussed in Section 7.

The model is divided vertically into 20 layers, the bottom layer being half the thickness of the rest. The bottom layer is separated to make it possible to parameterize the surface effects. Thus the top of the surface layer is treated as the bottom boundary of the rest of the model.

Surface Layer

Two parameters--U (the horizontal wind speed) and θ (the potential temperature)--must be specified at the top of the surface layer (at h, or $z = 50$ m). Following Estoque (1961), the problem is solved by assuming that the vertical fluxes of momentum and heat are constant with height in the surface layer:

$$\frac{\partial}{\partial z}\left(K\frac{\partial U}{\partial z}\right) = 0\ ,\quad \frac{\partial}{\partial z}\left(K\frac{\partial \theta}{\partial z}\right) = 0 \qquad (2.01,\ 2.02)$$

U and θ are known at the surface. (At $z = 0$: $U = 0$, and θ is prespecified as a time-changing boundary condition.) U and θ at the level immediately above the surface layer (at $h + \Delta z$, or $z = 150$ m) are taken as the values determined by the model for the previous time step. The gradients of wind speed and temperature $\left(\frac{\partial U}{\partial z} \text{ and } \frac{\partial \theta}{\partial z}\right)$ therefore can be determined between $z = 0$ and $z = h + \Delta z$.

K in equations 2.01 and 2.02, which is the eddy viscosity and eddy conductivity (assumed equal), strongly depends on the Richardson number:

$$Ri = \frac{g}{\theta}\,\frac{\frac{\partial \theta}{\partial z}}{\left(\frac{\partial U}{\partial z}\right)^2} \qquad (2.03)$$

which gives the stability of the surface layer. The term g is the acceleration due to gravity, and $\bar{\theta}$ is the average potential temperature in the surface layer (taken as the average between the initial values of θ at $z = 0$ and $z = h$). The value of Ri divides the model into two regimes: forced convection where the wind shear $(\frac{\partial U}{\partial z})$ dominates and the atmosphere is stable ($Ri > -0.03$); and free convection where the lapse rate $(-\frac{\partial \theta}{\partial z})$ is positive and dominates, making the atmosphere unstable ($Ri \leq -0.03$). For a forced convection:

$$K = [k_o(z + z_o)(1 + \alpha Ri)]^2 \frac{\partial U}{\partial z} \tag{2.04}$$

where k_o is the von Karman constant (equal to 0.4), z_o is the roughness parameter (preset and discussed in Section 3), and α is a nondimensional constant (equal to -0.03). For free convection:

$$K = \gamma(z + z_o)^2 \left(\frac{g}{\bar{\theta}} \left|\frac{\partial \theta}{\partial z}\right|\right)^{1/2} \tag{2.05}$$

where γ is a nondimensional constant (equal to 1.0).

The solution of the above equations to give K, U, and θ at $z = h$ follows Estoque (1963) and is summarized in Appendix A.1.

Assuming that the wind direction is constant between levels h and $h + \Delta z$, u and v can be found for the level h from level $h + \Delta z$:

$$u_h = \frac{U_h}{U_{h+\Delta z}} u_{h+\Delta z} , \quad v_h = \frac{U_h}{U_{h+\Delta z}} v_{h+\Delta z} . \tag{2.06, 2.07}$$

The value of w at level h is found from the continuity equation (2.13) applied to the average u in the surface layer:

$$\frac{\partial u}{\partial x} + \frac{\partial w}{\partial z} = 0 \quad \text{thus:} \quad w_h = \frac{-\Delta z}{8\Delta x} [u_h(i+1) - u_h(i+1)] \tag{2.08}$$

where i is the lateral grid index and Δx is the lateral grid spacing.

No changes were made in Neumann and Mahrer's model for the surface layer.

The Equations of the Model

The equations of motion for the main body of the model are:

$$\frac{\partial u}{\partial t} + u \frac{\partial u}{\partial x} + w \frac{\partial u}{\partial z} = -\frac{1}{\rho}\frac{\partial p}{\partial x} + fv + \frac{\partial}{\partial z}\left(K \frac{\partial u}{\partial z}\right) - 2w\Omega \cos\phi \cos\psi \qquad (2.09)$$

$$\frac{\partial v}{\partial t} + u \frac{\partial v}{\partial x} + w \frac{\partial v}{\partial z} = -\ fu + \frac{\partial}{\partial z}\left(K \frac{\partial v}{\partial z}\right) - 2w\Omega \cos\phi \sin\psi \qquad (2.10)$$

$$\frac{\partial w}{\partial t} + u \frac{\partial w}{\partial x} + w \frac{\partial w}{\partial z} = -\frac{1}{\rho}\frac{\partial p}{\partial z} - g + 2\Omega \cos\phi\ (u \cos\psi + v \sin\psi) \qquad (2.11)$$

where Ω is the earth's rotational speed, ϕ is the latitude, and ψ is the angle between the shoreline (assumed straight) and due north. Thus, y is parallel to the shoreline and x is perpendicular to the shoreline. Above the surface layer, it is assumed that K decreases linearly to zero:

$$K(z) = K(h) \frac{H-z}{H-h} \qquad (2.12)$$

where H is the top of the model (z = 1950 m), and K(h) was determined in equations A.07 and A.08. In their first paper, Neumann and Mahrer (1971) neglected the last term in each equation. They added the last term in the third equation for the work of their second paper (1973). Neumann (1973b) stated that all of these terms should be retained when dealing with a sea breeze front if the grid is sufficiently fine (less than 1 km). Since a finer scale was tested in this study (see below), all of the terms were retained. The method by which pressure is determined from these equations is given in Appendix A.3.

The other equations remained as given in the original paper (1971):

The continuity equation is:

$$\frac{\partial u}{\partial x} + \frac{\partial w}{\partial z} = 0 \qquad (2.13)$$

The heat conduction equation is:

$$\frac{\partial \theta}{\partial t} + u \frac{\partial \theta}{\partial x} + w \frac{\partial \theta}{\partial z} = \frac{\partial}{\partial z}\left(K \frac{\partial \theta}{\partial z}\right) \qquad (2.14)$$

Initial Conditions -- Synoptic Winds

Neumann and Mahrer assumed that the initial winds were zero, but to make the model more applicable to mid-latitudes, a non-zero initial wind was imposed, simulating a synoptic wind.

Since the model is two dimensional, it is impossible to impose a synoptic pressure gradient parallel to the shoreline. Therefore it was assumed that the initial wind was in geostrophic balance; i.e. the initial coriolis force due to the initial wind exactly canceled the initial pressure gradient force.

To accomplish this initial balance, u and v in equations 2.09, 2.10 and 2.11 were divided into the initial wind field and the perturbation: $u = u_0 + u'$ and $v = v_0 + v'$. u_0 and v_0 are the initial winds at the start of the computation, and u' and v' are the change of the winds from the initial conditions (i.e. u' and v' initially are zero). Since the initial vertical velocity is zero, $w = w'$. The expansion of equations 2.09 and 2.11 into the equations used in the model is given in Appendix A.2.

Other initial conditions, including the initial lapse rate are discussed in Section 3.

Boundary Conditions

The following boundary conditions were used: The temperature and pressure at the top of the model were constant in time, as were all velocity components. The velocity components were all zero at the bottom of the model. At the lateral boundaries, non-hydrostatic pressure terms and vertical velocity were zero and horizontal velocity and temperature fields were continuous. The only change in boundary conditions from those given by Neumann and Mahrer (1971) was the rate at which the land surface temperature varied with time. This will be discussed in greater detail at the end of the next section. The roughness parameter will also be discussed in the next section.

Scale

The computer program received from Neumann and Mahrer (1972) had a horizontal grid spacing of 5 km, a vertical grid spacing of 100 m, and a time step of 2 min. Simulations with these values are called the coarse mesh model. The meteorological parameters were observed in considerable detail (Figure 2), so the horizontal grid spacing was reduced to 1 km and the time step to 1 min. At the same time, the over-relaxation coefficient, λ, for the iteration equation A.24, was raised from 0.70 to 0.78 according to the procedure given by Miyakoda (1960). This fine mesh model was used only with the 30 June case study simulation.

Size

Neumann and Mahrer's (1971, 1973) model extended 2 km vertically and 140 km laterally centered on the shoreline, producing 21 by 29 grid points. When the grid spacing was reduced in the present study, the same size was retained, giving 21 by 141 grid points. Finally, the lateral dimension was doubled (in the coarse mesh model only) since the lake breeze was reaching the boundary. Unless otherwise noted, all case study comparisons were made with this expanded coarse mesh model.

Other Considerations

Neumann and Mahrer smoothed their model in order to remove the possibility of a nonlinear instability. All three velocity components were smoothed in the following manner:

$$\overline{u_i} = 1/2\ u_i + 1/4\ (u_{i-1} + u_{i+1}) \qquad (2.15)$$

where i varied in the lateral directions only. Further detail of the smoothing technique is given in their paper on circular islands (1974). The smoothing was left unchanged.

Neumann and Mahrer ran their model for three days to allow the land and sea breezes to come to equilibrium. In trying to duplicate their results, it was found that the wind velocity differed between the start of the first day and the start of the second day. Since the wind velocity was being set to simulate actual conditions in the present study, the model was run only one day. When the model was run with a synoptic wind for two days, the winds for each day started differently but ended about the same. This will be discussed further in a later section.

In the solution of eddy viscosity for the case of forced conversion, one term of equation A.07 involves division by wind speed; thus 10^{-5} m/s was added to the wind speed in order to avoid division by zero. However, this term still dominates and causes the model to "blow up" when the model is started with zero wind velocity. Since this was the case of interest to Neumann and Mahrer, they set the term in question equal to zero for the first six hours of the model. The outcome was not significantly changed, because only the results of the second day of the model were used.

In the present study, the initial wind velocity is non-zero and the first day's results are desired; therefore, the term in question was set equal to zero for only one hour. No problems arose from this change.

Magnitude of Terms

Table 2 compares the magnitude of the terms in the x-, and z-equations of motion in an extreme case. The time is 1350 CDT in the fine scale model using the synoptic conditions for 30 June 1973 (see Section 5). The location is 1/2 km ahead of the front (4 km inland) and at a height of 250 m. The parameters are defined in the list of symbols and in Appendix A. Like the model, the advection and prognostic terms use forward differencing and the pressure and eddy terms use centered differencing. Note that the hydrostatic pressure gradient term in the z-equation of motion exactly cancels the buoyancy term (see Appendix A.2).

Two items are of special interest. First, the terms advected by the initial synoptic wind are dominant, indicating the importance of the initial wind. Second, the non-hydrostatic pressure terms are definitely significant.

The terms do not add up to zero for two reasons. First, there is a large round-off error, because insufficient digits were printed in the pressure output. The error is indicated in Table 2. The round-off errors of the other terms are at least an order of magnitude smaller. Second, the time difference used in Table 2 was 30 min, whereas the model time difference was 1 min. This amounts to a smoothing over time which probably underestimates the prognostic terms.

In this example, $u_\circ \frac{\partial u'}{\partial x}$ almost cancels $u' \frac{\partial u'}{\partial x}$ because the total velocity $u = u_\circ + u'$ is small near the front (where it changes direction). Farther from the front, these individual terms will probably be smaller, while their sum is larger. Note that the sum of the $\frac{\partial u}{\partial t}$ terms (the first five terms in the x-equation) is +6.6. This is smaller than the sum of the pressure gradient terms (+9.4) or the friction term (-9.7). Far from the front, the hydrostatic pressure gradient term should just about cancel the coriolis and friction terms since the rest of the terms are less significant.

In the vertical equation of motion, the dominant terms (not counting the hydrostatic pressure gradient change term and the buoyancy change term which cancel) are the vertical advection and non-hydrostatic pressure gradient terms. These and the rest of the terms become very small far from the front.

3. SPECIFICATIONS USED IN THE MODEL

Parameters Involved

In addition to the size and scale parameters discussed in the previous section, the following details must be specified at the start of Neumann and Mahrer's sea breeze model. They are divided into two groups: those parameters which change and those which do not change from the values used by Neumann and Mahrer (1972).

Specifications Left Unchanged

a) Average air density (ρ) = 1 kg/m^3

b) Initial surface pressure = 1000 mb

c) Richardson's Number cutoff = -0.03

d) Constant used in eddy flux calculations (α) = -0.03

e) Roughness parameter ($z_\circ$) = 0.02 m

f) Initial lapse rate = 6.5 deg/km

The last three items require further explanation:

Constant Used in Eddy Flux Calculations

The constant α (which multiplies the Richardson number in equation 2.04) is the eddy flux; for the case of forced convection, α was taken to be -3 by Estoque (1961). Neumann (1973b) changed this constant to -.03 after examining the flux of sensible heat under conditions of forced convection. Since heat flux was not measured in the present study, the constant was left as Neumann set it. A future study should examine heat flux in greater detail.

Roughness Parameter

Neumann and Mahrer used a roughness parameter equal to 0.02 m in their model. For an urban area, one would expect a higher value--perhaps as high as 1 m in the downtown area--while for water, a lower value, perhaps as low as 0.0001 m might be expected. However, the temperature ratio described later in this section indicates that an average of 0.02 m may be realistic. Using a roughness parameter of 1 m, the 50 m temperature derived by the model was only about 2°C lower than the surface temperature. Measurements taken in Madison (also described later in this section) indicate this temperature difference actually ranged from 5 to 20°C depending on the type of surface. The use of the 0.02 m roughness parameter approximated this temperature difference more realistically, so this value was retained. A knowledge of actual temperature profiles and how they change during the day is needed to determine a better roughness parameter.

The effect on the results of the model of changing the roughness parameter to 1 m is given in Section 6 (Table 13). It should be mentioned that Neumann and Mahrer (1974) later changed their model to include different roughness parameters over land and water. This was not done in the present study.

Initial Lapse Rate

A temperature profile at the site of the experiment is needed to determine the initial lapse rate. This information was unavailable. The next best information is the sounding taken at Green Bay. This was also unavailable on 30 June 1973, so the St. Cloud sounding was used because it was upwind of Milwaukee. This sounding showed a lapse rate of 6.2 deg/km between 250 m and 1400 m. This value is close enough to the 6.5 deg/km used by Neumann and Mahrer (1972) that a change is not warranted. On 17 July, Green Bay showed 7.1 deg/km between 275 m and 1350 m, and on 7 September, 7.2 deg/km between 340 m and 1580 m. These are also close to 6.5 deg/km, so Neumann and Mahrer's value was left unchanged for all three case studies. The effect of raising the lapse rate to 7.5 deg/km is given in Section 6 (Table 13).

Specifications Changed

a) Latitude (ϕ) = 43 deg

b) Angle between due north and shoreline (ψ) = -8 deg

c) Initial winds [$u_o(z)$, $v_o(z)$] -- see Appendix B

d) Water surface temperature (T_o) = 18°C (30 June)
= 19.5°C (17 July)
= 20°C (7 September)

e) Change of land surface temperature with time

Again, the last three items require further explanation.

Initial Synoptic Winds

As mentioned in the previous section, the model was modified to accept an initial synoptic wind that varied with height. On two of the simulation days, pilot balloon data was available. On 30 June, two stations had 800 CDT readings; however, there was a significant decrease in wind between 800 and 900 CDT for both stations. By 900 CDT, three of the four stations were operating, so the winds of these three stations were averaged at each level, then smoothed vertically. The result was used as the input to the model. The case studies given later will show a comparison between the model winds and the pilot balloon winds later in the day. It should be noted that by 1500 CDT the pilot balloons indicated an increase in synoptic wind. This was not taken into account in the model, but will be discussed with the results.

On 17 July, all four stations got an earlier start, but two of them were misreading their instruments at first. By 900 CDT three of the stations were useable so their data was averaged as for 30 June. On 7 September, no pilot balloon data was available; therefore, an average was taken of the 12 Z winds at Green Bay and Flint, Michigan. Interpolations were made between the seven values contained within the height of the model. The initial winds used in the model are given in Appendix B.

Initial Surface Temperature

In the model, the constant water surface temperature is taken as the initial surface temperature for both land and water. Due to limitations on equipment and personnel, water surface temperatures were not measured as part of this study. Water temperatures were later obtained from six different sources. A brief examination of this data showed that temperatures varied greatly with location (all near Milwaukee), depth and method of measurement, and day (i.e. synoptic situation--primarily wind direction). This variation is due to changes in upwelling that occur near the shore.

An upwelling area is generally only 1-2 km wide, which is negligible in a model with a grid spacing of 5 km. What is needed is the temperature away from the shore, and none of the measurements were taken there.

Richards and Rogers (1964) suggest a solution. A plot is made of daily water intake temperatures for a city's water supply. Since in the absence of upwelling, water is warmest at the surface, the peaks in the plot should represent downwelling of surface water to the level of the water intake several meters below the surface. A smoothed line connecting the peaks should therefore represent the water surface temperature.

Lyons (1972) has prepared such a plot for the 1967 Chicago water intake temperatures and this is shown in Figure 3. Chicago's intake is at 8 m below the surface compared with Milwaukee's 17 m; therefore, the surface water should reach the intake more often in Chicago. In addition, Mortimer (1971) shows that the water surface temperature near Chicago is as likely to represent lake center temperatures as is water temperature near Milwaukee. For these reasons, the Chicago data prepared by Lyons was used rather than generating a new data set for Milwaukee. The temperature of the envelope corresponding to the date of the simulation was used for the initial surface temperature. A similar curve prepared by Keen (1975) for Muskegon, Michigan for 1967 agreed to within 0.5°C for each of the 3 days used in the present study. The effect of lowering the water surface temperature by 1°C is given in Section 6 (Table 13).

Change of Overland Surface Air Temperature with Time

Air temperatures were read at various locations throughout the Milwaukee area at numerous times during the test days. All of these measurements were taken at or near the standard meteorological shelter height. The model, however, requires the actual ground temperatures as a boundary condition changing with time. Neumann and Mahrer (1971) used Kuo's (1968) theoretical predictions of land surface temperature which were based on Lettau and Davidson's (1957) compilations of data taken at O'Neill, Nebraska in 1953. It must be noted that temperature profiles taken on the Great Plains may not be applicable to an urban area where the roughness parameter should be much larger.

The solution to this problem is to use the model itself to give the surface temperatures by iteration. A surface temperature is tried and the 50 m temperature is generated and compared with the measurements. The problem now is that the observed temperatures were taken at 2 m not 50 m. This problem is less severe, however, since the 2 m temperature is between the surface and 50 m temperature and close to the 50 m temperature.

Since no literature could be found for ground versus 2 m and 50 m temperatures for urban environments, data was taken on a sunny day with scattered clouds in August in Madison, Wisconsin. Readings were taken of surface temperature as well as 1 and 2 m over grass, asphalt and concrete and also in a meteorological shelter on top of a 60 m building. The 2 m temperatures over all of the surfaces were about the same and 0 to 2°C higher than the shelter at the airport (MSN) depending primarily on the wind speed at 2 m. (Higher wind speeds gave lower temperatures.) Table 3 gives the percentage of the total temperature drop between the surface and 60 m which occurs between 2 m and 60 m. This is compared to the 25 August O'Neill data. (25 August was a sunny day with a few clouds, similar to the lake breeze days.) As can be seen, the O'Neill data corresponds closely with an average between the grass and asphalt weighted somewhat toward the asphalt. Therefore, it was decided to aim for the O'Neill ratio.

By trial and error a diurnal surface temperature equation containing the first three harmonics was developed for x between the shore and 20 km inland. x was set equal to 20 km in the following equation for points inland of 20 km:

$$T = T_\circ + a + \left(\frac{2x}{20\ \mathrm{km}} + b\right) \sin(15t + c) + d \sin(30t + e) + f \sin(45t + g)$$

where t is the time measured in hours and a-g are constants. This became the input to the model and the 50 m temperature was the output. Figure 4 shows the final temperature selected for the 30 June simulation. The input surface temperature, and 50 m and 150 m output temperatures are plotted, as well as the 2 m temperatures determined using the O'Neill ratios given in Table 3. Actual shelter temperatures from Mitchell Field and Timmerman Field are shown for comparison. Virtual temperatures were used to compensate for the "dry" model. Figures 5 and 6 show similar information for 17 July and 7 September. Table 3 gives the temperature ratios using the model temperatures for the surface and 50 m plus the average of Mitchell Field and Timmerman Field for the shelter temperatures. (17 July and 7 September use only the Timmerman Field temperatures later in the day since the Mitchell Field temperatures were affected by the cooling lake breeze after 1100 and 1400 CDT respectively.)

4. EXPERIMENTAL OBSERVATIONS

Milwaukee was chosen as the site for the experimental observations of the lake breeze in order to coordinate data collected with that taken by Lyons of the University of Wisconsin-Milwaukee. Milwaukee is centered on a bay 3.2 km long and about 10 km wide at the mouth (Figure 7). It faces 8 degrees to the north of east. The Menomonee River forms a lake-level valley running east-west through the center of the city. This valley extends 6.7 km inland with a width of 0.7 to 1 km before turning north and narrowing. Mitchell Park and Veterans Cemetery are on the ridge forming the southern boundary of this valley. Farther inland the hills are higher and more random.

Barographs

Barographs were located at the following sites:

(Figures in parentheses are the distance in km from the lake)

a) University of Wisconsin-Milwaukee, Science Complex (1.5)

b) Mitchell Field Airport (4.6)

c) County Institutions-Air Pollution Control Administration, Wauwatosa (11.5)

d) Carroll College, Geography Department, Waukesha (27.1)

e) W.E. Brown Residence, Pewaukee (29.6)

The barograph traces were digitized every half hour and converted to millibars. Using the Mitchell Field trace as a reference (since it had the best time resolution), the times of the other traces were adjusted by aligning sudden pressure changes which occurred at the times when no lake breeze was present. No attempt was made to determine an absolute pressure calibration or to relate the barographs by sea level pressure, since only pressure changes were of interest. A 1 hr normally weighted running mean was then applied to the data, and the traces were averaged or subtracted, one from another.

Pilot Balloons

Lyons had pilot balloons operating from four sites:

(The first figure is the distance in km from the lake, the second is the height in m above the lake)

a) City Marina (0, 1)

b) Miller's Building, roof-70 m (5.5, 81)

c) County Institutions (11.5, 62)

d) Waukesha County Airport (27.2, 97)

Usually, hourly ascents were made. The readings were computerized and converted to u, and v components at 90 m height intervals. Surface dry bulb and wet bulb temperatures were taken (except at 3) and wind speed and direction were estimated. Comments on cloud cover were also noted.

Teletype

Hourly Service A teletype data (pressure, temperature, dew point, wind, cloud cover) were recorded from two locations:

- Mitchell Field (4.6, 30)
- Timmerman Field (11.7, 45) no pressure available

Boundary Layer Instrument System

A Boundary Layer Instrument System (BLIS) was used to record details in surface pressure, temperature, and wind speed. This system was designed to be suspended on a balloon bourne tether line, but since this was impossible in Milwaukee due to lack of funds, lack of personnel and FAA regulations, the system was mounted on the roof of a car, 2.7 m above the ground. This system is described in greater detail in Appendix C and in the article by Burns (1975). Calibration of this system and data reduction are also described in Appendix C. The data which was received every 4 sec was averaged over 2 min intervals to simulate the model time step and then smoothed further with a running mean weighted by a Gaussian distribution.

The car with the BLIS mounted on it was stationed near the shore until the front passed over, then was driven inland to wait for frontal passage at the next site.

An urban environment presents difficulty in selecting sites that offer minimum interference by surrounding structures with meteorological instruments, especially with anemometers. The following sites were selected because they are relatively high, relatively open, yet accessible by car:

* Municipal Pier (0, 2) - prior to 28 August

  Lake Site (0, 1) - after 28 August

* Mitchell Park (3.9, 15)

* Veterans Cemetery (7.0, 40)

* County Institutions (11.5, 55)

* Sunny Slope Road at I-94 (15.7, 105)

* State Patrol District II Headquarters (22.7, 100)

* Michigan Wisconsin Pipe Line Company tower (25.2, 110)

The Lake Site was preferable over Municipal Pier, but it was being used by festivals early in the summer. All of the sites were at least 100 m from obstructions 2 m or more in height except the following:

Municipal Pier - 1 story buildings 20 m to the south and 50 m to the northeast

Mitchell Park - trees 50 m to the south

State Patrol - 1 story building 20 m to the south

Tower - radio tower 20 m to the southeast

On the occasions when 2 instruments were available (Table 4), the second was placed on a tether running between the roof and the top of a 10 m tower on top of the 7 story C&H Building (1.7 km inland). The signal from this instrument was received by the car-mounted receiver in the street below.

Other sites, not located on Figure 6, were occasionally used on a one-time basis, exclusively to determine the time of frontal passage in order to measure the velocity of the lake breeze front.

Other Data

- The anemometer trace taken at the Oak Creek Power Plant on the coast just south of Milwaukee was used on the day that the BLIS anemometer did not work.
- Synoptic maps, upper air data, and satellite photographs were occasionally used and will be mentioned in the text.

5. CASE STUDIES

30 June 1973

The surface and 500 mb synoptic maps for 30 June 1973 at 0700 CDT are shown in Figure 8. A ridge to the west was headed toward Milwaukee. Winds at 500 mb over Wisconsin were 10-12 m/s from the NW. By 1600 CDT the surface high had moved to central Illinois, giving the winds in Wisconsin a more southerly component. The surface winds at Mitchell Field averaged about 5 m/s from the west until 1500 CDT when they increased to 7 m/s and shifted toward southwesterly. The winds at Timmerman Field were similar.

The day started out clear, but by 1100 CDT Mitchell Field was reporting broken clouds at 1000 m with towering cumulus in all quadrants. The cloud cover was eight tenths by then, and remained from seven to nine tenths for the rest of the day.

The lake breeze front suddenly crossed the shoreline at the Municipal Pier at 1237 CDT. An hour later it had reached Mitchell Park. The frontal speed thus averaged 1.1 m/s. This compares to 0.90 m/s in the original coarse grid model, 0.69 m/s in the expanded coarse grid model, and 0.77 m/s in the fine grid model. The front did not reach as far inland as Mitchell Field, Millers Building, or Veterans Cemetery. Note that in this report, unless otherwise indicated, the frontal passage is determined by the time at which the wind near the surface changes direction.

Table 4 gives the temperature and humidity at four locations throughout Milwaukee. The drop in temperature and increase in humidity at the Marina were dramatic between 1200 and 1300 CDT. The lake breeze did not reach any of the other locations.

In one hour, the temperature at the Marina dropped 4°C. This compares to a temperature drop (at 50 m) of 3.8°C in the fine mesh model and 0.3°C in the coarse mesh model. The latter continued to drop giving a 2.6°C drop in 3 hr. Thus it can be seen that the fine mesh model advects temperature faster than the coarse mesh model. A comparison can also be made of the temperature gradient across the front.

Table 5 gives the temperature increase when moving from the shore across the front to 5 km inland as a function of time relative to the front crossing the shore. As can be seen, the temperature gradient across the front for the model is similar to the actual case, but only the fine mesh model generates this gradient rapidly enough.

Figure 9 shows a portion of the Oak Creek Power Plant anemometer trace. The lake breeze front started coming through at 1257 CDT. The wind which had been from the northwest at 5 m/s suddenly switched to easterly for a short burst of 2-4 m/s lasting less than 2 min. This was followed by a 6 min calm, interspaced with short weak bursts of wind from the west and southwest. The lake breeze then started in earnest at 1305 CDT with a 4 m/s burst from the east southeast. This detail is impossible to detect in the model; however, it gives an idea of the frontal dimensions which can be used along with the change in horizontal wind to make a rough estimate of the vertical wind.

The continuity equation can be used to find the vertical velocity:

$$\frac{\partial u}{\partial x} + \frac{\partial w}{\partial z} = 0 \tag{5.1}$$

$$\text{or} \quad \Delta w = \frac{-\Delta u}{\Delta x} \Delta z = - \frac{\Delta u \; \Delta z}{V_f \; \Delta t} \tag{5.2}$$

where Δw represents a change in vertical velocity from zero to a maximum, Δu is the change in the average x-component of velocity (-7.2 m/s), Δz is the height of the inflow (215 m taken from Figure 9a), V_f is the frontal velocity (1.1 m/s), and Δt is the time during which the horizontal velocity changed (8 min). Thus, the vertical velocity at the top of the inflow is about 2.9 m/s. This result is greater than the 1.5 m/s observed by Lyons (Keen, 1975) with a tetroon (constant level balloon) on another occasion in Milwaukee, but less than the 8 m/s observed by Wallington (1959) in England with a glider.

The vertical wind is a function of the frontal width. Lyons (1974) states that a synoptic wind opposing the lake breeze causes the frontal convergence zone to become more narrow. The frontal zone observed by Wallington (1959) was about 100 m wide. A frontal zone of 500 m ($V_f \; \Delta t$) estimated above is thus not unreasonably narrow.

The maximum vertical velocity given by the coarse mesh model was 0.16 m/s. For the fine mesh model it was 0.56 m/s. Since the front as defined above was only 500 m wide, the 1 km grid spacing of the fine mesh model is even too great.

Shortly after 1500 CDT the synoptic wind overpowered the lake breeze at the Oak Creek Power Plant for a period of 20 min before returning to a lake breeze flow. This is similar to Koschmieder's (1936) observations with a strong offshore synoptic wind. Since the synoptic wind was not increased in the model, this phenomenon was not simulated. The wind returned to synoptic flow at 1800 CDT. The model, on the other hand, still had a lake breeze flow at 1900 CDT when the model was stopped.

Lyons has four crews measuring pilot balloon winds on this day. The winds were generally westerly at the surface changing to north westerly at 2000 m altitude. These measurements also indicate an increasing southerly component to the wind as the day passed, as well as an increase in wind about 1400 or 1500 CDT. The lake breeze never reached the first inland station; therefore, only the data taken at the Marina is presented here. Figure 10a shows a time cross-section of the u-component (perpendicular to the shore) of the wind.

The low level winds increased for a short time between 1000 and 1100 CDT while the mid-level winds were decreasing. The upper level winds remained fairly constant until about 1400 CDT when they increased the same as the inland stations. The frontal crossing brought an increase of mid-level winds and a reversal of low level winds.

The output of the coarse mesh model (5 km grid spacing) is shown in Figure 10b. (Note that all model data shown includes a synoptic wind unless otherwise noted. The 17 July case study will show the effects of no synoptic wind.) As might be expected, the winds in the model change rather gradually. The lake breeze front crosses the shore about the same time in both the model and the pilot balloon data (see Table 13), but the front in the model moves somewhat slower. (It took about 82 min to reach 3.9 km inland rather than 60 min.) The maximum lake breeze wind and maximum inflow height at the shore are similar in the model and the pilot balloon measurements, but these maxima occur more than 2 hr later in the model. Continuity requires the synoptic wind to speed up in order to pass over the inflow wind. The pilot balloons indicate a greater increase in speed than does the model. Finally the increase of the synoptic wind about 1400 CDT (not put into the model) retarded the lake breeze. This difference probably helped cause the maximum front penetration of about 4.5 km to occur around 1430, whereas the model's front continued inland until after 1900 reaching 14 km.

Figure 11a shows the same cross-section for the fine mesh model (1 km grid spacing). The gradients are sharper and more like the measurements than the coarse mesh model shows.

Note the oscillation which sets in at 1430 CDT. It started about 15 km inland and moved toward the shore at 4.3 m/s until it reached 7 km inland where it speeded up to 7.3 m/s and continued out into the lake. The average period of the oscillations was 57 min. The oscillations could be caused by a computational instability related to the length of the model time step. When the grid spacing was reduced from 5 km to 1 km, the time step was only reduced from 2 min to 1 min.

The Courant Friedrichs Lewy Criterion for stability of finite difference schemes is one check of this problem. Three forms of this criterion are pertinent to the equations of motion used in the model; the first use was used by Neumann and Mahrer (1971) and the latter two are from Monin (1972).

1. $\Delta t \leq \frac{(\Delta z)^2}{2\ K}$ Maximum K in fine mesh model = 32.2 m /s

$\Delta t \leq 155$ s (60 s was used)

(Note: This term is more critical in the coarse mesh model. The maximum K was 34.9 m^2/s requiring $\Delta t \leq 143$ s. Δt equal to 120 s was used.)

2. $\Delta t \leq \frac{\Delta x}{u}$ Maximum u in fine mesh model = 7.6 m/s

$\Delta t \leq 132$ s (60 s was used)

3. $\Delta t \leq \frac{\Delta z}{w}$ Maximum w in fine mesh model = 1.9 m/s

$\Delta t \leq 53$ s (60 s was used)

Only the third condition fails, but the maximum w used in the calculation occurred only once. The parameter w is generally much smaller. The fact that the model did not 'blow up' as it did when a 180 s time step was tried in the coarse mesh model further indicates that the oscillation is not a computational instability.

Gravity waves are not unusual in atmospheric models, and these oscillations could well be gravity waves. As will be seen later in Figure 15, the pressure amplitude of these oscillations is about 0.3 mb. Satellite phots (ATS and DMSP) did not indicate cloud bands of the type produced by gravity waves and the barographs showed no waves greater than 0.2 mb amplitude, but smaller ones might have gone undetected. Others have observed gravity waves associated with sea breezes. Gossard and Munk (1954) observed waves with amplitdues about 0.4 mb, periods about 12 min, and phase velocities about 12 m/s. The amplitudes are similar to those observed in the fine model, but the periods are shorter and the phase velocities are larger than the model. Donn, Milic, and Brilliant (1956) observed longer periods (25 to 40 min), but did not calculate the other parameters.

Since the oscillations did not correspond to conditions observed on 30 June 1973, only the output of the fine model up to 1400 LDT will be considered in the rest of this paper. The oscillations could probably be eliminated by horizontal smoothing (Neumann and Mahrer, 1974).

To show the differences between running the coarse mesh model 12 hr and 36 hr, the second day time cross section is given in Figure 11b. As was mentioned in Section 1, the winds for each day started differently but ended about the same. This matter will be discussed further in Section 6.

The v-component (parallel to the shore) of the wind is less important but is included for completeness. The pilot balloon data is given in Figure 12a and the coarse mesh model data (day 1) in Figure 12b. The real-world v-component decreased much more rapidly than the model showed. In fact, in the model, the v-component never became positive. Table 6 compares the wind direction change in one hour with the frontal passage at the shore. The v-component in the fine mesh model was almost the same as in the coarse mesh model, but with slightly sharper gradients, so it will not be shown here.

The surface pressure taken by 5 barographs is shown in Figure 13. The arrow shows the approximate time the front passed the University of Wisconsin-Milwaukee (UWM). (The exact time is unknown.) The front did not pass the other stations. Figure 14 puts the same data into a form which can be compared with other data, subtracting out the synoptic pressure trend which varies over 3 mb during the course of the day. By assuming that the far inland stations were not affected by the lake breeze (since the frontal penetration was shallow), these inland stations were subtracted from the stations of interest. Figure 14a shows the surface pressure difference between UWM 1.5 km inland and Carroll College 27.1 km inland. The latter was chosen because the barograph there had the best resolution of the three inland barographs. Figure 14b shows the difference between UWM and the average of the three inland stations. As a control, Figure 14c shows the difference between Mitchell Field (MKE) 4.6 km inland and the average of the three inland stations.

As the front passed UWM at about 1300 CDT, several pressure changes were observed. Prior to frontal passage, both UWM and MKE showed a slight increase in pressure. This may be due to low level convergence ahead of the front (Figure 1). Byers (1949) states that under a thunderstorm, surface friction may cause convergence at the surface to be less than divergence aloft, giving a decrease in pressure. To the side, the pressure would be correspondingly increased. The situation should be similar for a lake breeze front. As the front passes, Figures 14a and b show a slight decrease in pressure followed by a definite rise in pressure. These are not seen in the control (Figure 14c). The decrease could be a combination of vertical accelerations, divergence aloft (which should occur slightly toward the lake from the low level convergence due to the slope of the front), warm air being forced up, and an increase in water vapor from over the lake. The final pressure rise is probably hydrostatic; that is, the cool air moving in from over the lake.

The surface pressures resulting from the fine mesh model are given for five grid locations in Figure 15. Looking at 1700 CDT from the top, the traces are 30 km offshore, 10 km offshore, shore, 10 km inland, and 30 km inland. The pressures of the inland points decrease at the same rate with increasing surface temperature. The offshore points decrease at the same rate with increasing surface temperature. The offshore points decrease only after the warm air is advected over the lake. As mentioned previously, the 10 km inland curve shows the first signs of oscillation.

Figure 16 shows the same parameters, except this time for the shore through 5 km inland at 1 km intervals (respectively from the top looking at 1400 CDT). The arrows indicate the time of frontal passage at each of the grid points. About one half hour before frontal passage, the pressure starts decreasing relative to those from grid points farther inland. About ten minutes after frontal passage, the pressure starts to increase. This increase continues for about 40 min before leveling off or decreasing slightly. The last curve behaves differently because the oscillation starts about the same time as the frontal passage. The pressure dip is about 0.1 mb and the rise about 0.4 mb.

In order to compare the model with the barograph data, the pressure at one grid point was subtracted from the pressure at another grid point. UWM, 1.5 km inland, was approximated by the grid point 5 km inland in the coarse mesh model, and 2 km inland in the fine mesh model. In both cases, Carroll College, 27.1 km inland, was approximated by the grid point 30 km inland. Figure 17A shows the results of the coarse mesh model, 17B the results of the fine mesh model, 17C the results of the Boundary Layer Instrument System (BLIS) located at Mitchell Park. The arrow indicates the time of the model frontal passage at the UWM grid point for 17A and 17B, and at Mitchell Park for 17C.

There is no pressure rise prior to the frontal passage in the model. This may be because the model requires that the total horizontal divergence of a vertical column be zero (Mahrer, 1973). Sometime before frontal passage, the relative pressure starts to fall and after the frontal passage it rises again. These effects occur very slowly for the coarse model compared to the barographs. The fine model on the other hand responds more quickly than the barographs. This may be related to the lack of resolution in the barographs. Figure 13 shows wiggles on the barograph traces that could be dynamic effects, but these are wiped out in the averaging process which was done to increase the pressure resolution of the less accurate barographs. (See also Figure 29a.)

An instrument with better resolution than the barograph is needed to check the model, and BLIS provides this resolution (see Appendix C). In fact, BLIS even picks up pressure changes due to turbulence, so the data it collects must be smoothed (see Appendix C for an example of a BLIS raw pressure trace). The average of the three inland barographs indicated a pressure rise of just under 0.1 mb during the time of the BLIS record, so no compensation was made for synoptic pressure changes.

The smoothed BLIS pressure trace is shown in Figure 17c. The pressure starts rising 15 min prior to frontal passage and starts falling just before frontal passage. The pressure drop might be hydrostatic, but it is probably due to accelerations. A slight upturn in pressure is indicated just before the instrument was turned off, but this upturn is inconclusive. Therefore, a 5 min reading taken several hours later was averaged, corrected for synoptic pressure change using the three inland barographs, and plotted as an x on the figure. By that time the pressure had indeed risen. The short term pressure changes are greater for BLIS than for either model or the barographs, indicating that the latter are not resolving all of the acceleration effects.

The pressure dip is more gradual, smaller in magnitude, and ends sooner in the fine model than indicated by BLIS. The model divergence limitation mentioned earlier, the lack of moisture in the model, and the large grid size compared to the frontal dimensions probably all contribute to this difference.

Two questions concerning the final pressure rise will be considered here. Is the pressure rise of the correct magnitude? And does the absence of moisture in the model increase the pressure rise significantly? (The less dense moist air advected from over the lake should reduce the pressure; see Section 7.)

The barographs indicate a pressure rise of 0.2 mb, only half that given by the fine mesh model; however, an independent check would be useful, since it is difficult to read the barographs to within 0.1 mb.

The temperature and relative humidity taken before and after the frontal passage (Table 4) can be used to determine the hydrostatic pressure change. First, a questionable assumption is made that the temperature and humidity change is the same throughout the inflow layer (in this case, 300 m high) as it is near the surface. This is really a worse case (maximum pressure change) estimate, since the change near the surface should be maximum. A second assumption is that the pressure is the same ahead (A) and behind (B) the front at the top of the inflow layer. A check of the model output showed that this is a fairly good assumption.

The hydrostatic equation is used:

$$\frac{\partial p}{\partial z} = -\rho g = -\frac{pg}{RT} \quad \text{or} \quad p = p_s e^{-\frac{gz}{RT}} \qquad (5.3)$$

where p_s is the surface pressure. Therefore:

$$p_A = p_{sA} e^{-\frac{gz}{RT_A}} = p_B = p_{sB} e^{-\frac{gz}{RT_B}} \qquad (5.4)$$

$$p_{sB} e^{-\frac{gz}{RT_B}} = (p_{sB} - \Delta p)\, e^{-\frac{gz}{RT_A}} \qquad (5.5)$$

$$\Delta p \equiv p_{sB} - p_{sA} = p_{sB}\,[1 - e^{-\frac{gz}{R}\left(\frac{1}{T_B} - \frac{1}{T_A}\right)}] \qquad (5.6)$$

Using this equation, the pressure change at the surface Δp is 0.47 mb using the temperatures in Table 4, and 0.43 mb using virtual temperatures. These are the same order of magnitude as the pressure rise in the fine model (0.4 mb). The humidity in this case is negligible. It depresses the pressure change only 10%.

17 July 1973

The surface and 500 mb synoptic maps for 17 July 1973 at 0700 CDT are shown in Figure 18. Milwaukee was still under the influence of the high which had been over Green Bay a day earlier. The shallow trough to the west was moving very slowly and the weak front did not reach Milwaukee for over two days. Winds at 500 mb over Wisconsin were 7-10 m/s from the west. The surface winds over Mitchell Field were 2-5 m/s from the south prior to frontal passage when they switched to southeasterly and increased to 6-7 m/s. The winds at Timmerman Field were similar.

17 July started with thin ground fog which dissipated by 0800 CDT. The day remained clear most of the time with a few cumulus occasionally visible. The maximum cloud cover reported by Mitchell Field was two tenths at 1300 CDT.

The progression of the lake breeze front is shown in Figure 19. The error bars indicate that the front passed through during that time interval, and an x indicates the time is known to within a few minutes. The distance from shore is measured directly to the shore, and is related to how far north or south the point is located (due to the curvature of the shore). In other words, Mitchell Park is actually farther west than Mitchell Field but it is closer to the lake (Figure 7). Therefore, to be completely accurate, all of the points in Figure 19 should be in a straight east-west line. The fact that they are not gives an error which is difficult to estimate.

Another error can be attributed to the topography of the land. For one thing, the lake breeze moves faster up the valley than along the ridge.

This can be seen in Figure 19 by observing the point marked "in valley" which is 0.7 km north of Mitchell Park, but which is in the valley rather than on the ridge.

Even with these problems, it is easy to see that the front moved slowly (0.6 m/s) until it reached about 8 km inland. It then speeded up considerably (2.4 m/s), because the temperature gradient is larger later in the day after the sun has been heating the land for several hours.

The frontal position given by the model is also plotted in Figure 19. Since 17 July had the weakest synoptic wind opposing the lake breeze of the three case studies, this day was chosen to compare the model with and without a synoptic wind. In this case study, the frontal arrival is defined by a lake breeze wind greater than 0.2 m/s. The frontal passage is indicated for each location by an arrow. Unlike 30 June, when there was a significant drop in temperature as the front passed, the temperature on 17 July merely stopped increasing. Thus, the farther inland the station, the higher the maximum temperature. The relative humidity of these inland stations is, therefore, correspondingly lower. Only the Marina had an increase in relative humidity with frontal passage, indicating that very little excess humidity moved inland with the lake breeze.

As a comparison, Table 8 gives temperatures at 50 m for the model with a synoptic wind. (The model without a synoptic wind is similar except that the temperatures peak earlier and are therefore lower.) The first arrow indicates frontal passage as defined by wind shift, and the second arrow indicates frontal passage as defined by maximum vertical wind. Note that at a given time, the temperature in the vicinity of the front is slightly higher than the temperatures farther inland. The maximum temperatures of the model are similar to the measured maximum virtual temperatures, but the model temperatures start to fall after the passage of the front defined by the maximum vertical wind. This may be because the temperatures are measured at a higher altitude in the model (50 m) than in the actual case (2 m). The lower measurement is more affected by surface heating, which continues after the cooling lake breeze starts.

Pilot balloon measurements were taken at four locations, but two of the stations had errors most of the day (wrong by 180 deg) and a third took no readings after 1100 CDT. Therefore, only the lakeshore data is presented. A time cross-section of the wind component perpendicular to the shore is given in Figure 20a. The inflow started shortly before 900 CDT and increased in two stages, reaching a maximum height of 830 m at 1500 CDT. The maximum inflow speed of 4.4 m/s occurred at a height of 270 m between 1330 and 1400 CDT, whereas the maximum return flow of about 5 m/s occurred 1 1/2 hr later at a height of 1350 m.

The time cross-section for the same parameter derived from the model with a synoptic wind is shown in Figure 20b. The wind speeds are similar to the actual case. Here the return flow reached a maximum slightly before and slightly less than the inflow maximum. The heights of the maxima were similar to the actual case, however. The inflow height at 1500 was only 30 m higher than actually measured, but in the model the height continued to increase after this time whereas the pilot balloons indicated a decrease.

The model without the synoptic wind is shown in Figure 21a. If the initial 1-2 m/s synoptic wind is added to the results of this case, the main difference between it and the case with the synoptic wind built into the model is that the inflow boundary rises faster and both the inflow and return flow peak later.

To see what happens farther inland, see Figure 21b, which shows a time cross-section of wind 10 km inland for the case of the model with the synoptic wind. It is similar to the lakeshore case except that the inflow rises faster and then levels off. The inflow maximum of 6.6 m/s is also greater. For comparison, the 1600 CDT pilot balloon at Millers recorded an inflow maximum of 6.3 m/s at about 300 m height. At County Institutions, the inflow was over 3 m/s and still increasing when the soundings were stopped for the day. The inflow heights were similar to the model (within 100 m) for both locations.

The component of the wind parallel to the shore at the shore is given in Figure 22. The pilot balloons (Figure 22a) indicated a decrease in wind speed below 800 m about the time the front crossed. This was followed several hours later by an increase to greater than the original speed. On the other hand, the model (Figure 22b) showed almost no change in wind speed. The model without a synoptic wind (not pictured) also showed little change in wind speed.

The change in wind direction in 1 hr at the time of the frontal passage is given in Table 9. The original synoptic wind was added to the winds of the non-synoptic wind model to obtain the figures in Table 9, since there was no wind and hence no wind direction before the front started. The measured wind change was much smaller and much slower on 17 July than on 30 June, therefore, the model was able to change as rapidly as the actual weather conditions.

The surface pressure taken by 5 barographs is shown in Figure 23. The arrow shows the approximate time of frontal passage, with the broad arrow indicating greater uncertainty. Note the slight increase in pressure relative to the downward trend at the time of frontal passage for the three inland stations. This is similar to the increase in pressure observed by Hornickel (1942).

Figure 24 presents the same data after one station has been subtracted from another to remove the synoptic pressure trend. On 17 July, the lake breeze front passed over all of the stations, so that all of the stations were affected by the lake breeze; however, some stations were affected before others. The "up-down-up" pattern of observed pressure on 30 June should be followed by another "down" as the front passes the inland station.

This in turn should be followed by a leveling off of the pressure--perhaps somewhat higher than the original pressure, since the cooling effect of the lake is less pronounced farther from the lake.

The difference between the pressure traces taken at UWM and Wauwatosa is shown in Figure 24a. Again, the times of the frontal passages are indicated by arrows. (Note that the early "down" may have been a spurious effect on the Wauwatosa barograph--see Figure 24c.) The final "down" started about 1 1/2 hr after the frontal passage at the surface. The total rise in pressure between frontal passages was just under 0.4 mb.

Figure 24b is similar to 24a, except that the second frontal passage occurred later in the day. Thus, the middle "up" is broken into two parts; the second amounts to a decrease in pressure ahead of the inland front. Unlike the previous case, there was a decrease in relative pressure (or an increase in inland pressure) simultaneously with the second frontal passage. This was followed later by a further drop in pressure. The total pressure rise between frontal passages was just over 0.4 mb in this case.

Figure 24c shows the difference in pressure between the two inland stations used in the two previous cases. As might be expected, the pressure rise between frontal passages was less (about 0.2 mb).

The surface pressure resulting from the model is given in Figure 25 (the model with a synoptic wind in Figure 25a and the model without a synoptic wind in Figure 25b). The curves from the top represent the surface pressures at 30 and 10 km offshore, the shoreline, and 5, 10, 15, and 30 km inland. The initial pressure fall is identical for both cases because the heating is the same. In the latter case, the pressures fall less far because the lake breeze reverses the pressure trend earlier.

In the case of the model with the synoptic wind, the pressure at one grid point was subtracted from that an another grid point for comparison with the barograph data. Figure 26a corresponds to Figure 24b with UWM, 1.5 km inland, being represented by the grid point 5 km inland and Waukesha, 27.1 km inland, by the grid point 30 km inland. Here the single arrows indicate the frontal passage as defined by the surface wind shift, and the double arrows indicate the frontal passage as defined by the maximum vertical wind. In the model, the double pressure rise is similar in shape to that indicated by the barographs but is much greater (almost 2 mb).

Figure 26b corresponds to Figure 24c. Again the shape is similar, but the rise is much greater for the model. The positions of the pressure peaks relative to the maximum vertical wind indicate that this vertical wind is carrying warm air aloft. (This is confirmed by observing the model's temperature fields.)

The BLIS data is shown in Figure 26c. The pressure started falling 20 min before the frontal passage which may have indicated warm air being pushed up ahead of the front as in the case of the model. The pressure started falling fast as the front passed, then shot up again 5 min later.

The speed of these changes indicate that acceleration effects were probably the predominant effects. As in the 30 June case study, the model acts more slowly than the BLIS data; the BLIS indicates what is actually happening.

A comparison of 30 June data with 17 July data indicates that the later date had greater hydrostatic effects due to the increased heating and greater frontal height (allowing the warm air--and later, cool air--to be forced higher).

7 September 1973

The surface and 500 mb synoptic maps for 7 September 1973 at 0700 CDT are shown in Figure 27. A weak ridge was centered over northeastern Iowa. Nine hours later (1600 CDT), the high was centered just north of Milwaukee. Winds at 500 mb over Wisconsin ranged from 15-25 m/s from the WNW. The surface winds over Mitchell Field were 3-4 m/s also from the WNW prior to frontal passage (about 1430 CDT), when they switched to ESE and increased to 4-5 m/s. The winds at Timmerman Field remained from the WNW all day except for a single reading from the north at 1300 CDT.

The day started clear, but by 900 CDT, a line of cirrostratus clouds moved in from the south to form an almost complete cloud cover. Cumulus clouds started forming about 1100 CDT and increased thereafter, especially in the west. The cumulus and cirrostratus clouds remained the rest of the day.

The lake breeze started late due to the moderate opposing synoptic wind, but unlike 30 June, the start of the lake breeze at the coast was very sporadic. Beginning about 930 CDT there were occasional gusts of wind off the lake, but they appeared to be very shallow and penetrated less than 1 km inland. Sometime after noon the lake breeze started in earnest. The front passed National Avenue at 11th Street (2.3 km inland) at 1402 and Mitchell Park at 1442 CDT, indicating a frontal speed of 0.67 m/s. The front passed Mitchell Field about 1435 CDT, indicating that the front must have hit the shore at the center of Milwaukee (in the bay) later than it hit the shore farther south (beyond the bay - see Figure 7). Recall that Mitchell Field is farther inland than Mitchell Park. The front never reached Veterans Cemetery.

The front in the model crossed the shore at 1400 CDT, and by 1700 CDT it had moved 8.6 km inland. A six point linear regression over this interval gave a frontal speed of 0.73 m/s; however, a detailed examination showed that the front started at 0.91 m/s and decreased to 0.53 m/s before increasing again. The maximum penetration was 13.2 km at 1830 CDT, when it turned and started retreating. This time compares favorably with the actual retreat of the lake breeze about 1900 CDT.

The humidity and temperatures taken at 3 locations in the Milwaukee area are given in Table 10. The arrow again indicates the frontal passage.

As in the 30 June case, the temperature dropped significantly, but this time humidity rose only slightly (probably because the measuring point was much farther inland).

The temperature gradient across the front changes with time and is compared to the model temperatures (5 and 10 km inland and 50 m high) in Table 11. As in the case of 30 June, the temperature gradient in the model is smaller and develops more slowly. The decrease in temperatures observed at Mitchell Field and in the model 5 km inland are both shown in Figure 6 of Section 2. The decrease in the model is slower, but the amount of decrease is similar.

Pilot balloon data was not available for 7 September, so wind comparison is somewhat difficult. An indication of wind shift can be seen in Table 12, however, by comparing winds before and after frontal passage at Mitchell Field (surface) and the model 5 km inland (50 m height). As in the 30 June case, the actual wind change is faster than occurs in the model. The total change in the model also is less, even over several hours.

The surface pressure taken by 4 barographs is shown in Figure 28. The single arrow shows the approximate time of frontal passage; the two broad arrows indicate the front passed sometime during that time interval.

Figure 29a shows an enlargement of the Mitchell Field barograph trace at the time of frontal passage. (The wind shift occurred between 1400 and 1500 CDT.) Remembering that the pressure is dropping rather smoothly outside of this interval, the perturbation from this uniform drop indicates a pressure rise of about 0.1 mb, followed by a pressure fall of over 0.2 mb and a final rise to the original pressure. Based on the BLIS data, the front probably passed as the pressure started to fall; this point is marked with an arrow.

The microbarograph was not operating at Carroll College and the other inland barographs are less reliable, so only the difference between UWM and Mitchell Field is presented (Figure 29b). The problem is the unknown time of frontal passage at UWM. It occurred sometime between 1030 and 1300 CDT. In any case, the pressure started falling before frontal passage and rose again during inland frontal passage.

The corresponding pressure difference from the model is shown in Figure 29c. (The stations are simulated by the grid points 5 and 10 km inland, so that the frontal passage--marked by arrows--occurs later.) There is a slight pressure fall followed by a pressure rise. The fall is smaller than the barographs indicate, and the rise is much greater.

In order to show the pressure fall more clearly, the grid points 5 and 30 km inland are used in Figure 30a. There is a slight rise before the pressure fall. The BLIS data is also shown in Figure 30 after correcting for the pressure fall shown in Figure 28. Figure 30b, taken at the shore, indicates an uncertain time of frontal passage, since the wind was changing direction often during the interval. The general decrease in pressure over and above the synoptic trend implies that more and more warm air is being forced aloft by the low level convergence.

Figure 30c showing the BLIS data taken at Mitchell Park, demonstrates the double front which was observed--one at 1429 and the other at 1442 CDT. The other piece of data later in the day indicates that the pressure rose again (just over 1 mb) after the frontal effects passed. This compared to 0.4 mb in the model, although the model was still rising when the model was turned off. The barographs indicated that the pressure was changing rapidly when the BLIS was operating, so the BLIS data was corrected for this change by using the average of the 4 barographs.

6. CONCLUSIONS

Neumann and Mahrer's (1971) sea breeze model was modified so that it could be applied to Milwaukee. Three minor changes were made: latitude; angle between the shoreline and due north; and surface temperature (as a function of time). This basic model was then compared to four variations:

a) Using the output of the first 12 hr of the run rather than 24 to 36 hr (i.e., using first day instead of second day).

b) Adding an initial synoptic wind.

c) Expanding the model to twice the lateral dimension.

d) Reducing the grid spacing from 5 to 1 km.

The effects of these model alterations, as well as changes in the initial water temperature, roughness parameter, and lapse rate, are summarized in Table 13. The columns indicate variations of the model. The only fine-mesh model variation is column B. The rows indicate various model output parameters. For example, 6E says that the maximum surface pressure difference from the shore to 5 km inland is 1.07 mb for the model in which the water temperature was reduced by 1°C. 7E says that this maximum occurred at 1500 CDT.

Several effects of the model changes can be noted. Reducing the water temperature while keeping the ground temperature the same (i.e. increasing the temperature difference between water and land) causes the inflow front to arrive earlier (though the front moves at the same speed after it arrives). The inflow velocity and height increase, as does the surface pressure gradient. In other words, there is a stronger lake breeze.

Increasing the lapse rate has the same effect.

Increasing the roughness parameter is more difficult to compare, because the surface temperature must be lowered to keep the 2 m air temperature the same. The results indicate a later and slower front and a slower inflow velocity, but a greater inflow height and a greater surface pressure gradient. In other words, heating extends higher, but friction is increased.

Reducing the grid spacing, slightly reduces the inflow wind, inflow extent, and surface pressure gradient while increasing the vertical velocity considerably. More details on the differences between the fine mesh model and the coarse mesh model are given later in this section.

A typical lake breeze, as measured by Lyons and Olsson (1972) is compared with the 30 June 1973 fine mesh model in Figures 31 and 32. Figure 31 shows streamlines and wind profiles. In spite of the fact that these are two different days, and that the 30 June lake breeze inflow is much smaller, the flow patterns are similar. Note that the highest point of the inflow boundary is just toward the shore of the front, and that the maximum wind velocity is just above this boundary in both cases. Figure 32 shows that the isentropes and lapse rates are also similar. The 30 June case did not have a synoptic subsidence inversion. The slight rise in temperature at the top of the model is due to the fixed temperature boundary condition. Note the increase in temperature just above the inflow boundary in both cases, due to the warm surface air being pushed up over the inflow air.

Even though the Lyons and Olsson lake breeze penetrated much farther inland and extended to a greater altitude than did the 30 June 1973 lake breeze, the flow and potential temperature patterns are similar for both days.

The conclusions of the comparison of the model (and its variations) with the measurements made in Milwaukee are given below by meteorological parameter.

Temperature

The experiment did not include temperature soundings, so only temperatures near the surface could be compared. The surface temperatures far inland were used as a boundary condition of the model. Therefore, only those temperatures affected by the lake breeze could be used for a meaningful comparison. Table 14 summarizes the decrease in the 50 m model temperature and the 2 m measured temperature with frontal passage.

The fine mesh model duplicated very well the temperature fall following the passage of the front. The coarse mesh model, on the other hand, responded very slowly. The light opposing synoptic wind on 17 July allowed the coarse mesh model to "keep up" with observed temperature variations, and in fact, produced a larger temperature drop than was measured.
7 September was similar to 30 June with respect to temperature drop during frontal passage.

Lake Breeze Inflow

The lake breeze crossed the shoreline within about 1/2 hr of the measured time for all variations of the model; the fine mesh model was a bit early, and the coarse mesh model a bit late. The frontal speed was also of the right order of magnitude, but it was somewhat slow when a strong opposing synoptic wind was present (Table 13). In the case of the light opposing synoptic wind, the front moved too fast, at least at first. This means that the model front traveled inland too far too soon.

In all cases, the model front traveled too far inland. This may be because the heating later in the day was set too large. The only way to properly check this would be to obtain temperature profiles and check them against the model.

The height of the inflow was determined very well by the model up to about 1500 CDT. In this case, the coarse model was slightly better than the fine model. After 1500 CDT, the same problem which caused the front to move too far inland--afternoon heating--probably caused the inflow height to be too great.

It should be mentioned that the first day of the model simulated all of the parameters noted above and all those mentioned in Table 13 better than the second day of the model. This is probably because the initial model wind speed for the first day was more correct. There seems to be no advantage in running the model a second day when a synoptic wind is specified. It should be noted, however, that no attempt was made to introduce the correct night-time surface temperatures. This correction might improve the second day results.

When no synoptic wind is put into the model, the front starts too soon and moves too fast, because the synoptic wind retards the front. (In all cases studied, the synoptic wind opposed the lake breeze.)

Wind Speed

The wind speed was set as an initial condition of the model; however, the wind change in time made a good point for comparison. The measured wind made large changes due to turbulence, convection, and synoptic changes, none of which were adequately represented in the model. The mean flow, which is what really is of interest, was well represented in the model.

The presence of a broad convergence zone, as in the case with the low opposing synoptic wind, allowed the model to follow the changes in wind speed fairly well. However, decreasing the convergence zone required a finer mesh model in order to build the necessary gradients rapidly. Both fine and coarse mesh models ultimately obtained the proper lake breeze speed and return flow speed. The height of these maximum speeds was also correct.

Wind Direction

The component of wind parallel to the shore did not change rapidly enough in either the fine or coarse mesh models. This is reflected in the rate at which the wind changed direction as the front passed (Table 15), and was especially true for the case with the large opposing synoptic wind, 30 June. The fine mesh model helped make the change more rapid, but the model was still much slower than the actual case. 7 September had a lesser problem. 17 July had a light enough wind that the coarse mesh model could keep up with the real case.

Vertical Wind

The vertical winds produced by the model were not as great as those calculated from measured horizontal winds. This may be because of inaccurate calculation, or because the model had too coarse a mesh even with 1 km grid spacing. Better measurements of vertical velocity are needed.

Pressure

The surface pressure changes can be a good parameter to measure the success of the model. In a sense, they summarize the changes in the temperature field. In the case of the Neumann and Mahrer model, they can also reflect wind accelerations. Table 13 shows that the maximum pressure gradients were practically the same for all of the model variations; however, the fine-scale model produced a more correct pressure change with time.

The barographs used in this study lacked the necessary sensitivity to properly test the model, but the BLIS data showed that the pressure changes of the model were of the correct magnitude for the 30 June and 7 September case studies. In the 17 July case study, the variations in pressure were in the correct direction, but were too large. This problem is probably related to the temperature profiles generated, and further study with soundings are needed to clarify the problem. The problem could be in the surface temperature, the initial lapse rate, the roughness parameter, or the constant used in the eddy flux calculations.

The details of the pressure change during frontal passage are related to the vertical wind. A space scale even finer than 1 km would be necessary to simulate these variations. Again, this lack is not a serious drawback, since most applications of the model do not require this detail.

Summary

The Neumann and Mahrer numerical sea breeze model performed surprisingly well under the tested conditions after the following changes were made:

1. An initial synoptic wind which varied with height was added.

2. The horizontal grid spacing was reduced from 5 km to 1 km.

Running the model a second day did not seem necessary.

7. CRITIQUE OF THE MODEL

The sea breeze model developed by Neumann and Mahrer (1971), performed well in the Milwaukee test after two changes were made:

a) The addition of a synoptic wind.

b) The reduction of horizontal grid spacing.

This section discusses these changes and other less important changes which might be made in the model.

The first and absolutely necessary change was the addition of a synoptic wind. The method used to produce this wind in the present study worked adequately, and an extra spatial dimension need not be added to the model just to produce the pressure gradient which generates this wind. It might be of interest to try to change the synoptic wind with time, either suddenly or gradually. This might have helped the 30 June simulation.

The next most important change which is recommended is the reduction of grid spacing. This allows the gradients to build faster, so that reality is simulated better. The method used (creating more grid points) was the easiest to implement, but two alternatives are available which use less computer time. (The fine grid scale is needed only in the vicinity of the lake breeze front, but the boundaries must extend a long distance from the shore line.)

The first alternative, used by both Fisher (1961) and Estoque (1962), is a geometrically increasing grid spacing as the grid points are farther from shore. Fisher also increased the vertical grid spacing with distance from the surface. The problem is: If the front moves far inland, the grid spacing that it sees is increased, making a comparison with shore front conditions difficult. This problem might be overcome by using a uniform fine grid spacing near the shore and an increased grid spacing near the model boundaries as done by Walsh (1974).

A second alternative, suggested by Neumann (1973b), is to use a region of reduced grid spacing which can move with the front. This might be difficult to implement, however.

As mentioned previously, Neumann and Mahrer (1974) changed their model to permit a different roughness parameter over the water and over the land. This could be taken one step further by using a large roughness parameter near the shore where the buildings are large and a smaller roughness parameter farther inland, away from the city.

It would be interesting to try to eliminate the model requirement that the total horizontal divergence of a vertical column be zero (Mahrer, 1973). Another way might be found to get rapid convergence. This elimination becomes increasingly important as the grid spacing becomes smaller.

One point that should be addressed is whether or not it is important to have a non-hydrostatic model. Again, as grid spacing is reduced, the non-hydrostatic terms become more important. In the 30 June simulation with the fine mesh model, the maximum observed deviation of pressure from its instantaneous hydrostatic value was 0.3 mb (7 km inland at 1430 CDT). The corresponding hydrostatic disturbance pressure at this point and time was 1.8 mb. At this point, the non-hydrostatic term was significant. The coarse model, on the other hand, showed very small non-hydrostatic effects. This confirms the statement by Walsh (1974): "It is inconsistent to use a horizontal grid increment of 4 km and a total depth of 2 km, as Neumann and Mahrer did, if non-hydrostatic effects are thought to be significant." Table 2 also showed the importance of the non-hydrostatic pressure near the front.

Adding moisture to the model is indeed desirable, as pointed out by Neumann and Mahrer (1974). The change which moisture makes in Milwaukee is small, however, unless there is sufficient moisture to create clouds. The pressure can be changed by the presence of moisture, as is shown by unpublished airplane data taken by Lyons in Chicago in 1967 and given in Appendix B. When the front was 20 km inland, the surface temperature drop was 0.4°C over a 5 km distance, moving from inland of the front to shoreward of the front. The virtual temperature drop was 0.1°C. On the other hand, at 900 m height there was a temperature rise of 0.4°C and a virtual temperature rise of 0.7°C. From the data it was possible to calculate the hydrostatic pressure drop across the front. Using the temperature without moisture gave 0.05 mb, and using virtual temperature gave 0.21 mb. This example is probably an extreme case for Lake Michigan, since it is more normal to have a pressure rise across a front (i.e. more cool air from over the lake) (Lyons, 1974).

To summarize this section, Neumann and Mahrer have created a sea breeze computer model which can be used for lake breezes of the type which occur in Milwaukee. Two adaptations are necessary:

a) Addition of an initial synoptic wind.

b) Reduction of grid spacing.

Other minor changes might make the model more useful.

8. RECOMMENDATIONS FOR FURTHER RESEARCH

The research presented in this thesis will now be examined to see how it could be expanded to further compare the sea breeze model with experimental data.

Examples will be presented to show how the model could be used.

The data needed to test and use the model can be divided into four groups:

a) Data needed to start the model (i.e., initial and boundary conditions).

b) Data needed to test the model (diagnostic data).

c) Data needed to use the model. (The main difference between this and the first group is that the surface temperature boundary condition must be predicted rather than measured.)

d) Data that might be required if a more accurate surface layer parameterization scheme is to be developed.

Data Needed to Start the Model

The main inital conditions needed to start the model are the temperature field and the wind field. If moisture were to be added to the model, the initial moisture field would also be needed. If the model initial conditions are kept constant in the x direction, a single radiosonde sounding could be used. The model is constant in the x direction only when the land temperature is the same as the water temperature; thus the sounding should be made at the time in the diurnal cycle when this is true. (For the test cases in the present study, this time was 700 CDT on 30 June, 730 CDT on 17 July, and 900 CDT on 7 September.) It is assumed that the vertical wind velocity is zero at this time, but this assumption must be tested.

It is desirable to have greater vertical resolution of the data than ordinarily available with radiosondes, so the radiosonde should be weighted for a slow ascent and should provide continuous data output rather than slow baroswitching. The WHAT (Winds, Heights, And Temperatures) system of radiosonde described by Frenzen and Prucha (1975) would work well.

The concept of no initial variation in the x direction must be tested. If the test data (see next section) shows a significant difference between the temperature structures above the land and the water even at the time that the land and water temperatures are equal, two or more radiosonde ascents may be required, over land and over the water.

The main boundary condition needed for the model is a representative surface temperature. One problem, especially in an urban environment, is the variation of surface albedo, emissivity, conductivity, and moisture content from one location to another. What is needed is a representative spatial average. A satellite borne radiometer automatically averages over the temperatures within the instantaneous field of view. A radiometer on a geostationary satellite is needed to give the diurnal change of surface temperature. This satellite data was not available for the time of the test cases in the present study but should be used in a future study. The lake surface temperature can also be determined with a satellite radiometer (Strong, 1974).

Two other initial conditions are the surface pressure and air density, obtainable from the surface observations taken at the time of the soundings. Neither value is very critical.

The three constants--roughness parameter, Richardson number cutoff, and the constant, α, which multiplies the Richardson number (equation 2.04)--should be more accurately determined by comparing the derived model temperature and wind fields with the measured fields and adjusting the model for the best solution.

Data Needed to Test the Model

The data in the previous section is sufficient to operate but not to test the model; test data must be much more extensive, and must be measured throughout the day. Close spacing of data is needed near the front to accurately determine the large gradients of wind, temperature, and pressure. The main parameters needed to test the model are the wind, temperature, and pressure fields. The latter are needed mainly in the vicinity of the front, because they can be derived elsewhere using the hydrostatic condition. Since the pressure field is significantly non-hydrostatic near the front, these observations are required separately.

The moisture fields should also be measured. While moisture is not used in the model, it is important to determine the significance of this lack of moisture in the model. If moisture is added later to the model, this data will also be needed to test the new model.

The following approximate instrument resolutions are required for this experiment: horizontal wind velocity ±0.5 m/s; vertical wind velocity ±0.1 m/s; temperature ±0.1°C; and pressure ±0.05 mb. Since pressure and temperature differences between two points (in time and space) will be taken, instrument sensitivity is more important than absolute accuracy. The pressure element must be exposed properly so as not to measure dynamic pressure changes due to wind fluctuations. The readings could be averaged over 1 min intervals to simulate the model time step and remove eddy fluctuations. The BLIS instruments, which are described in Appendix C, provide this resolution and allow for the averaging of 30 wind samples and 15 temperature, pressure, and moisture samples per minute.

Ideally, the wind (three dimensional), temperature, and pressure should be available for every grid point at every time step. In 12 hours the fine mesh model has 2961 grid points and 720 time steps. In addition, the parameters must be checked in the y direction (parallel to the coast) to make sure that the use of a two dimensional model is valid. Since the model cannot be tested at every point at every time step, efforts should be made to sample the flow (and therefore test the model) at representative points at which the flow is changing the most. A realistic approach is given below.

A suitable line could be suspended from a blimp, and 5 BLIS instruments suspended on this line--two instruments within the inflow, two within the return flow and one near the transition level between the inflow and return flow. A blimp has the advantage of longevity over an airplane and mobility over a tethered balloon.

The blimp could fly back and forth across the leading edge of the front--about 5 to 10 km on each side of the front--so that the averaging of the data would be both temporal and spatial. The model output then would similarly have to average both temporally and spatially. For example, assume that the inflow is 5 m/s away from the shore, the return flow is 5 m/s toward the shore, and the blimp is moving at 10 m/s (ground speed) away from the shore. A 1 min average would then mean a 300 m average in the inflow and a 900 m average in the return flow. The numbers would be reversed by reversing the blimp. Thus without changing the averaging time (so that succeeding averages remain one step apart in the model) one could average over a different number of eddies. An easier comparison with the model could be made if the blimp flew with a ground speed of 1 km/min (16.7 m/s). Each successive grid point for comparison would then come from successive time steps in the model.

The location (within 100 m) and altitude (within 2 m) of the blimp would have to be measured and recorded. The latter could be done with a radioaltimeter (e.g. Levanon, et al., 1974). A simple navigation system using the streets as a reference will determine ground speed to within 1 m/s. Before turning at each end of the pass, the blimp could provide a sounding by raising and lowering the line at a known rate by an amount equal to the distance between the lower instruments. The blimp could cross the front about every hour.

Several times during the day the blimp could make a traverse parallel to the shoreline to check the assumption that the parameters do not change in this direction. The blimp experiment should be conducted near the front, where the major atmospheric changes occur; radiosondes could fill in the gaps away from the front. (Intercomparisons should be made between the blimp in the sounding mode and the radiosondes.)

If possible, two blimps (one in the urban area and one in a rural area) could operate simultaneously, to determine the urban effects on the roughness parameter in particular and to study heat and momentum fluxes in general.

In addition to the blimp, a TV tower a short distance from the shoreline (e.g. WTMJ-TV in Milwaukee) could be equipped with a tether line and

3 to 5 BLIS instruments. These instruments could serve as a reference for the blimp instruments and also could determine a more accurate vertical wind velocity since the instruments would be fixed. These instruments could also be used to perform a spectral analysis of the wind, temperature, and pressure before and after the front passed.

A single BLIS should be placed at a fixed point far enough inland to use as a reference unaffected by the lake breeze. A BLIS on a boat or breakwater could provide a corresponding surface reference over the water. In conjunction with other BLIS instruments about 20 km north and south, these instruments would form a grid to measure gravity waves and estimate synoptic winds from surface pressure (Johnson, 1965).

The frontal movement at the surface can be tracked by a person in a car. Again, at least two transections (one urban and one rural) should be taken. These persons should also measure air temperature.

The height of the mixing layer is valuable in testing the eddy fluxes produced by the model. This parameter could be measured by the blimp in a slow sounding mode, but to save blimp time for other measurements, an acoustic sounder might be used instead. The acoustic sounder should be located a short distance inland (5-10 km) to record both before and after the frontal passage.

Data Needed to Use the Model

It is important to minimize the amount of data required to operate the model, in order to make real-time operation of the model practical. Once the proper values of the roughness parameter, Richardson number cutoff, and α have been determined, only the initial wind and temperature fields and surface temperature change with time are needed. If the starting time is chosen so that the variation of temperature and wind is minimal in the x direction, then only a single radiosonde sounding (of the type described under operation of the model) is required for the initial conditions.

The surface temperature change with time is a bigger problem for real-time use of the model. One possible empirical method might be to determine the change in surface temperature with a satellite for various environmental conditions (i.e., sun angle, wind, cloudiness, and soil moisture). The results of this experiment, which could be separate from the model test experiment, would form a look-up-table. The wind and cloudiness would then have to be predicted for the day in question.

Data Required for More Accurate Surface Layer Parameterization

If the above empirical scheme to determine surface temperature was found to be impractical, or if the surface layer parameterization scheme did not produce consistently good results in the above test, the surface layer fluxes of heat and momentum should be derived from a more accurate parameterization scheme. To develop this improved parameterization scheme, the following data should be available for the test days: short wave radiation, both incoming and reflected (including percentage of time within each hour interval that the sun is behind a cloud), net radiation, soil moisture, evaporation, ground temperature and air temperature at several heights above the ground, wind at several heights above the ground, and surface emissivity and albedo. Several of these parameters can be obtained from a satellite, and, in fact, the satellite will do the required spatial averaging; however, independent measurements of these parameters at several locations is still desirable.

Use of the Model

Most pollution models are based on diffusion of pollutants as they move downstream and vertically. A lake breeze, however, can concentrate and recirculate air pollutants (Kauper, 1960; Lyons and Olsson, 1972). One of the best uses of the sea breeze model discussed in this section would be to predict this pollution circulation.

One could create an air pollution prediction model by inserting a pollution source inventory (including source rates and source temperatures) into the model discussed earlier, then tracking how advection, convection, and diffusion distributes the pollution. This would create time-changing pollution fields. Since the pollution sources are not uniform parallel to the shoreline (cars may be distributed uniformly, but smokestacks are not), the model would probably have to be expanded to three spatial dimensions.

Another possibility would be to couple this model with a mesoscale air pollution transport model (e.g., Keen, 1976), which computes streamlines and time-integrated trajectories of pollutants once the four dimensional wind field has been determined. The model discussed in this section would give this wind field.

ACKNOWLEDGMENTS

I wish to extend sincere thanks to many individuals who aided in the research set forth in this report. The inspiration and expertise of Prof. Verner E. Suomi was especially valuable, as was the advice and consultation of Profs. Heinz Lettau, John A. Young, and Theodore Green.

Special thanks go to Prof. Jehuda Neumann and Dr. Ytzhaq Mahrer of the Hebrew University of Jerusalem, Israel, for providing the software for the computer model tested in this study. They also took time to explain the details of the model. Prof. Walter Lyons and Dr. Cecil Keen who provided considerable data from the University of Wisconsin, Milwaukee also deserve special thanks.

Of the many others who provided help or data for this study, I would especially like to mention Stanley Burns, James Maynard, and other Space Science and Engineering Center personnel who built and provided the BLIS equipment which became a major part of this study; Fred Rehm and Robert Redovitch of the Milwaukee County Air Pollution Control Administration who let me use their site and provided me with barograph data; William Braier and Frank Petranech who let me use the roof of the C&H Building; Michael Thaller of Carroll College, William E. Brown of Pewaukee, and the NOAA Environmental Data Service for barograph and other data; and Eric Smith and Ralph Dedecker who helped with programming.

Finally I thank my wife Ginny who not only offered understanding and encouragement, but also helped collect data.

This study was supported in part by a gift from the Wisconsin Alumni Research Foundation through the University of Wisconsin-Madison Graduate School (project 140083), the National Oceanographic and Atmospheric Administration grant 04-3-158-61 and contract BOA-3-35314, the National Aeronautic and Space Administration contract NAS5-21798, and the National Science Foundation grant ATM75-17200.

This report was submitted as a thesis, in partial fulfillment of the requirements for the degree of Doctor of Philosophy (Ph.D.) in Meteorology at the University of Wisconsin-Madison, 1976.

REFERENCES

Berman, Elizabeth A., 1974: Private Communication.

Burns, Stanley G., 1975: Boundary-Layer Instrumentation System, *Atmospheric Technology*, No. 6, 123-128, National Center for Atmospheric Research.

Byers, Horace R., 1949: *The Thunderstorm, Report of the Thunderstorm Project*, U.S. Dept. of Commerce, Weather Bureau.

Dampier, William, 1705: Discourse of Winds, Breezes, Storms, Tides, and Currents, *Voyages and Descriptions*, London.

Davis, W. M., L. G. Schultz, and R. DeC. Ward, 1890: An Investigation of the Sea-Breeze, *Ann. Astron. Obs. Harvard Col.*, Vol. 21, Part 2, 215-263.

Defant, Friedrich, 1951: Local Winds, *Compendium of Meteorology*, Am. Meteor. Soc., Boston, 655-672.

Donn, William L., Patricia L. Milic, and Renee Brilliant, 1956: Gravity Waves and the Tropical Sea Breeze, *J. Meteor.*, Vol. 13, 356-361.

Neumann, J. and Y. Mahrer, 1971: A Theoretical Study of the Land and Sea Breeze Circulation, J. Atmos. Sci., Vol. 28, 532-542.

Neumann, J. and Y. Mahrer, 1972: Private communication, computer listing.

Neumann, J. and Y. Mahrer, 1973: Evolution of a Sea Breeze Front: A Numerical Study, Climatological Research, The Hermann Flohn 60th Anniversary Volume, Meteor. Institute, Univ. Of Bonn, 481-492.

Neumann, J. and Y. Mahrer, 1974: A Theoretical Study of the Sea and Land Breezes of Circular Islands, J. Atmos. Sci., Vol. 31, 2027-2039.

Pearce, R.P., 1955: The Calculation of a Sea-Breeze Circulation in Terms of the Differential Heating Across the Coastline, Quart. J. Royal Meteor. Soc., Vol. 81, 351-381.

Peterson, Ernest W., 1971: Comments on "A Numerical Study of the Effect of a Coastal Irregularity of the Sea Breeze," J. Appl. Meteor., Vol. 10, 599-600.

Pielke, Roger A., 1973: A Three-Dimensional Numerical Model of the Sea Breezes Over South Florida, NOAA Technical Memorandum ERL WMPO-2.

Pielke, Roger A., 1974a: A Three-Dimensional Numerical Model of the Sea Breezes Over South Florida, Mon. Wea. Rev., Vol. 102, 115-139.

Pielke, Roger A., 1974b: A Comparison of Three-Dimensional and Two-Dimensional Numerical Predictions of Sea Breezes, J. Atmos. Sci., Vol. 31, 1577-1585.

Richards, T. L. and G. K. Rodgers, 1964: An Investigation of the Extremes of Annual and Monthly Evaporation from Lake Ontario, Proc. 8th Conf. Great Lakes Res., 283-293.

Simpson, J. E., 1964: Sea-Breeze Fronts in Hampshire, Weather, Vol. 19, 208-220.

Strong, Alan E., 1974: Great Lakes Temperature Maps by Satellite (IFYGL), Proc. 17th Conf. Great Lakes Res., 321-333.

Van Bemmelen, W., 1922: Land-und Seebrise in Batavia, Beiträge zur Physik der Freien Atmos., Band 10, 169-177.

Wallington, C. E., 1959: The Structure of the Sea Breeze Front as Revealed by Gliding Flights, Weather, Vol. 14, 263-270.

Wallington, C. E., 1965: Gliding Through a Sea Breeze Front, Weather, Vol. 20, 140-144.

Koschmieder, Harald, 1936: Danziger Seewindstudien I: Nachweis und Beschreibung, sowie Beiträge zur Kinematic und Dynamik des Seewindes, Heft 8, Forschungsarbeiten des Meteorologischen Institutes Danzig.

Kuo, H. L., 1968: The Thermal Interaction between the Atmosphere and the Earth and Propagation of Diurnal Temperature Waves, J. Atmos. Sci., Vol. 25, 682-706.

Lettau, Heinz H., and Ben Davidson, 1957: Exploring the Atmosphere's First Mile, Vol. 2, Permagon Press, New York, 377-577.

Levanon, Nadav, Ferrel G. Stremler and Verner E. Suomi, 1975: A New Approach to Lightweight Radar Altimeters, Proc. IEEE, Vol. 62, 784-792.

Lyons, Walter A., 1972: The Climatology and Prediction of the Chicago Lake Breeze, J. Appl. Meteor., Vol. 11, 1259-1270.

Lyons, Walter A., 1974: Private communication.

Lyons, Walter A. and Lars E. Olsson, 1972: Mesoscale Air Pollution Transport in the Chicago Lake Breeze, J. Air Pollution Control Assoc., Vol. 22, 876-881.

Lyons, Walter A., and Steven R. Pease, 1972: A Year-Round All-Sky Time-Lapse Camera System Designed for Mesoscale Cloud Mapping, Proc. 15th Conf. Great Lakes Res., 507-520.

Mahrer, Y., 1973: Private Communication.

McPherson, Ronald D., 1968: A Three-Dimension Numerical Study of the Texas Coast Sea Breeze, Report No. 15, Atmos. Sci. Group, Univ. of Texas at Austin.

Miyakoda, K., 1960: Test of Convergence Speed of Iterative Methods for Solving 2 and 3 Dimensional Elliptic-Type Differential Equations, J. Meteor. Soc. Japan, Vol. 38, 107-124.

Monin, Andrei S., 1972: Weather Forecasting as a Problem in Physics, Translated by Paul Superak, MIT Press, Cambridge Mass., 58-59.

Moroz, William J., 1967: A Lake Breeze on the Eastern Shore of Lake Michigan: Observations and Model, J. Atmos. Sci., Vol. 24, 337-355.

Mortimer, C. H., 1971: Large-Scale Oscillatory Motions and Seasonal Temperature Changes in Lake Michigan and Lake Ontario, Center for Great Lakes Studies Special Report No. 12, Univ. of Wisconsin-Milwaukee.

Neumann, J., 1973a: The Sea and Land Breezes in the Classical Greek Literature, Bull. Am. Meteor. Soc., Vol. 54, 5-8.

Neumann, J., 1973b: Private Communication.

Estoque, M. A., 1961: A Theoretical Investigation of the Sea Breeze, Quart. J. Roy. Meteor. Soc., Vol. 87, 136-146.

Estoque, M. A., 1962: The Sea Breeze as a Function of the Prevailing Synoptic Situation, J. Atmos. Sci., Vol. 19, 244-250.

Estoque, M. A., 1963: A Numerical Model of the Atmospheric Boundary Layer, J. Geophyscial Res., Vol. 68, 1103-1113.

Fisher, Edwin L., 1961: A Theoretical Study of the Sea Breeze, J. Meteor., Vol. 18, 216-233.

Frenzen, Paul, and Lad L. Prucha, 1975: The WHAT System: A Digitized Radiosonde and Double-Theodolite Balloon-Tracking System for Planetary Boundary-Layer Investigations, Atmospheric Technology, No. 6, 129-134, National Center for Atmospheric Research.

Gossard, Earl, and Walter Munk, 1954: On Gravity Waves in the Atmosphere, J. Meteor., Vol. 11, 259-269.

Haurwitz, B., 1947: Comments on the Sea-Breeze Circulation, J. Meteor., Vol. 4, 1-8.

Hornickel, K., 1942: Danziger Seewindstudien III: Zur Aerologie des Seewindes, Heft 11, Danziger Meteorologishce Forschungsarbeiten.

Hsu, Shih-Ang, 1969: Mesoscale Structure of the Texas Coast Sea Breeze, Report No. 16, A mos. Sci. Group, Univ. of Texas at Austin.

IES, 1973: Monitoring and Control of Regional Air Pollution: Southeastern Wisconsin, Environmental Monitoring Systems Studies Report 4, Institute for Environmental Studies, Univ. of Wisconsin-Madison.

Jeffreys, Harold, 1922: On the Dynamics of Wind, Quart. J. Roy. Meteor. Soc., Vol. 48, 29-47.

Jehn, K. H., 1973: A Sea Breeze Bibliography, 1664-1972, Report No. 37, Atmos. Sci. Group, Univ. of Texas at Austin.

Johnson, Warren Buford Jr., 1965: Atmospheric Boundary-Layer Dynamics over the Forests of Northeastern Wisconsin, PhD Thesis, Dept. of Meteor., Univ. of Wisconsin-Madison.

Kauper, E. K., 1960: The Zone of Discontinuity between the Land and Sea Breezes and its Importance to Southern California Air Pollution, Bull, Am. Meteor. Soc., Vol. 41, 410-422.

Keen, Cecil S., 1975: Private Communication.

Keen, Cecil S., 1976: Trajectory Analysis of Meso Air Pollution Transport in Lake Michigan Shoreline Environment, Center for Great Lakes Studies Special Report No. 29, Univ. of Wisconsin-Milwaukee.

LIST OF FIGURES

Figure

LIST OF TABLES

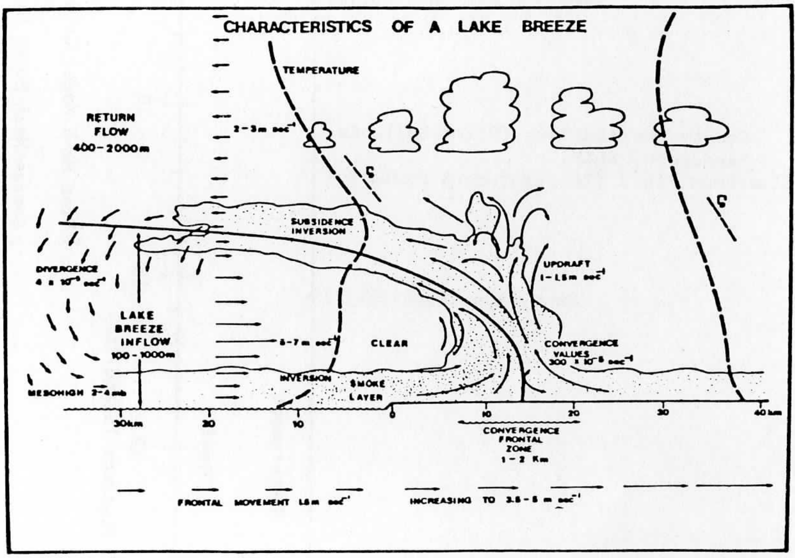

FIGURE 1: Summary of observed characteristics of well-developed Lake Michigan lake breezes (Keen, 1975).

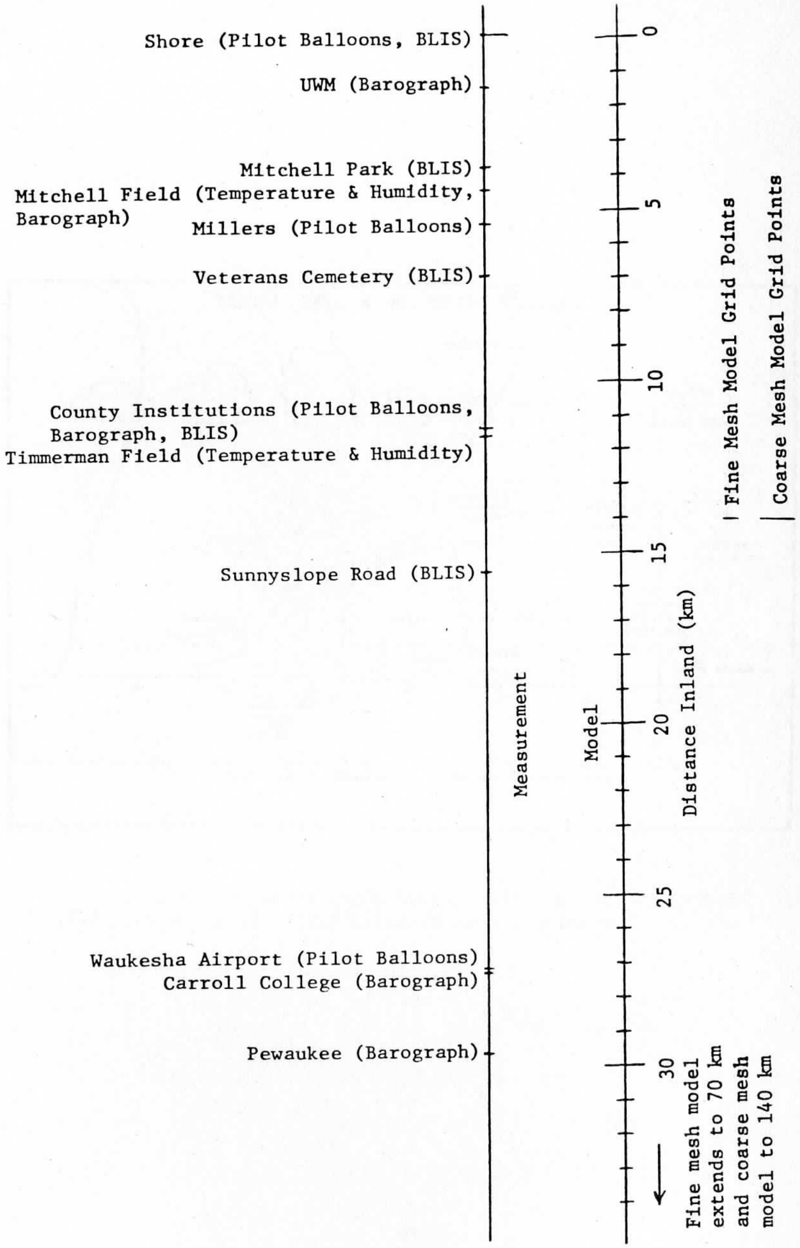

FIGURE 2: Comparison of Model Scale with Milwaukee Measuring Locations

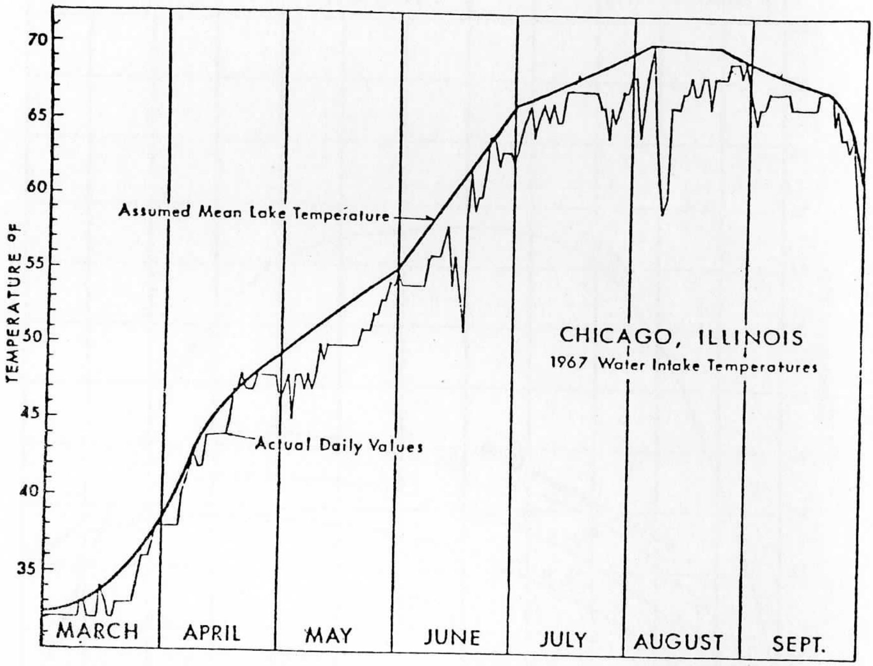

FIGURE 3: Lake water temperatures recorded at the Chicago water intake during 1967. Actual value of temperature depends on local upwelling and downwelling. The heavy curve is an envelope of the warmer temperatures, and is representative of the mean lake surface temperature in regions of no upwelling (Lyons, 1972).

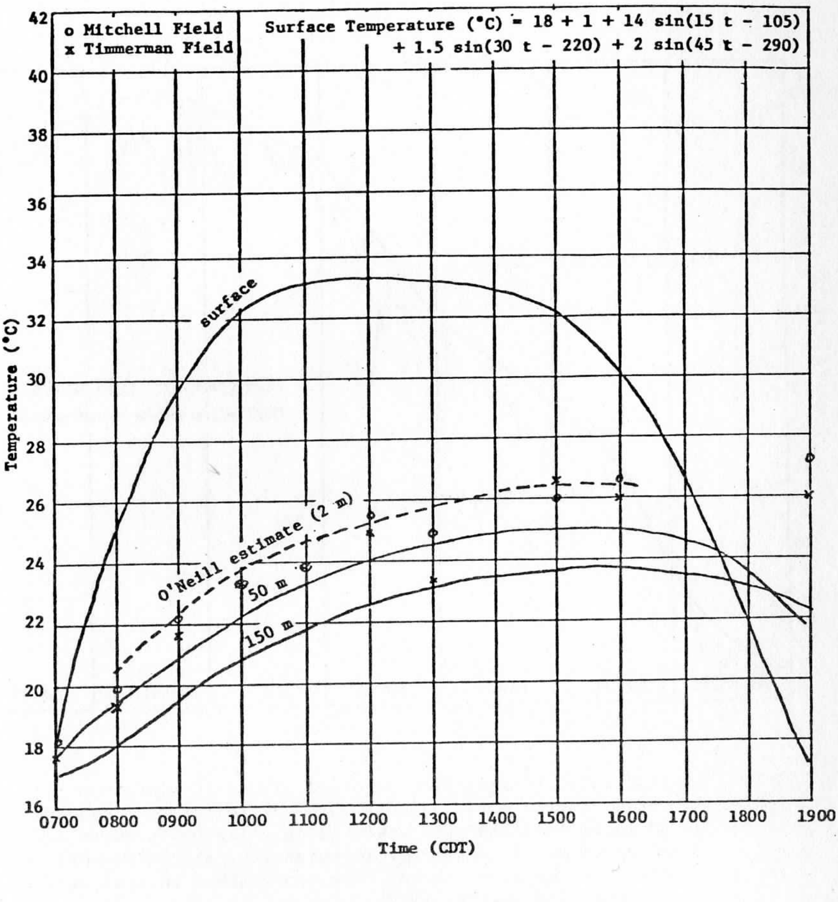

FIGURE 4: 30 June Model Temperatures

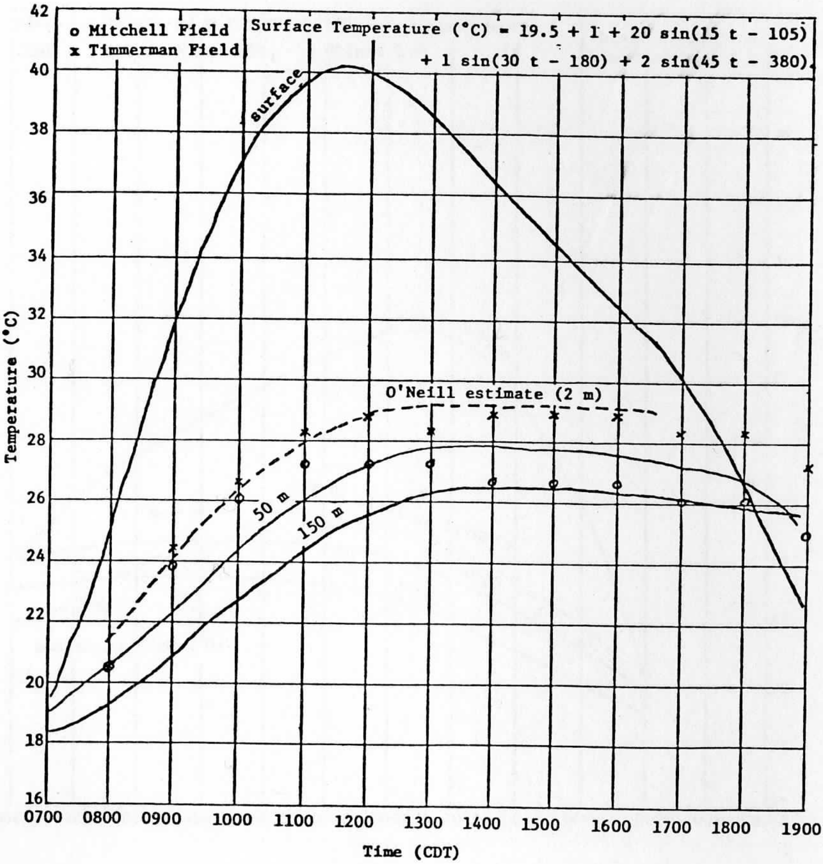

FIGURE 5: 17 July Model Temperatures

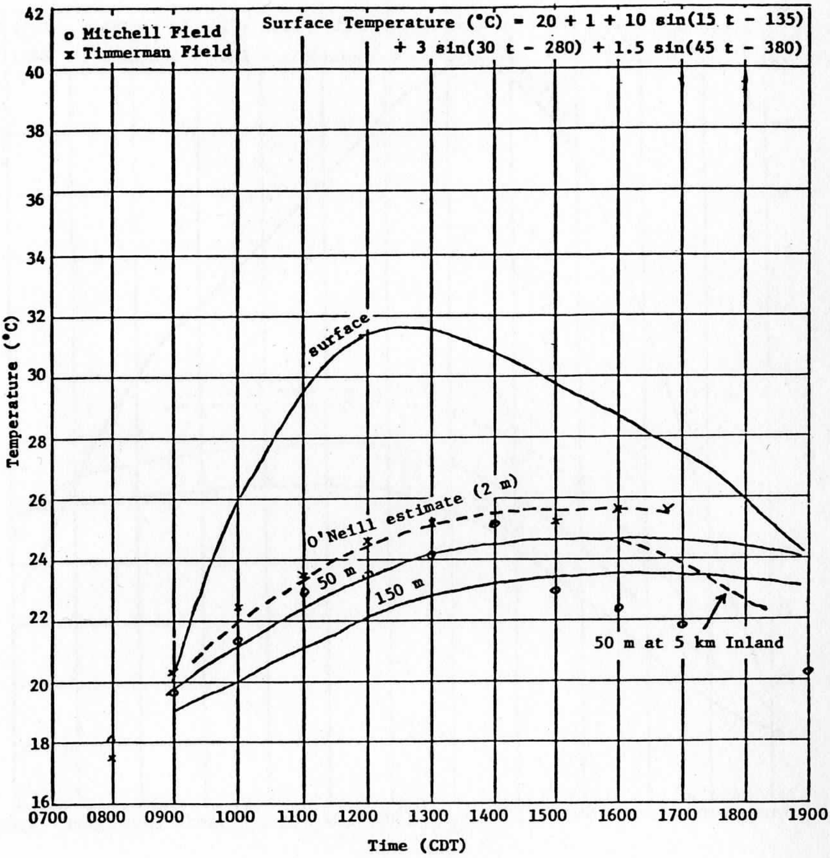

FIGURE 6: 7 September Model Temperatures

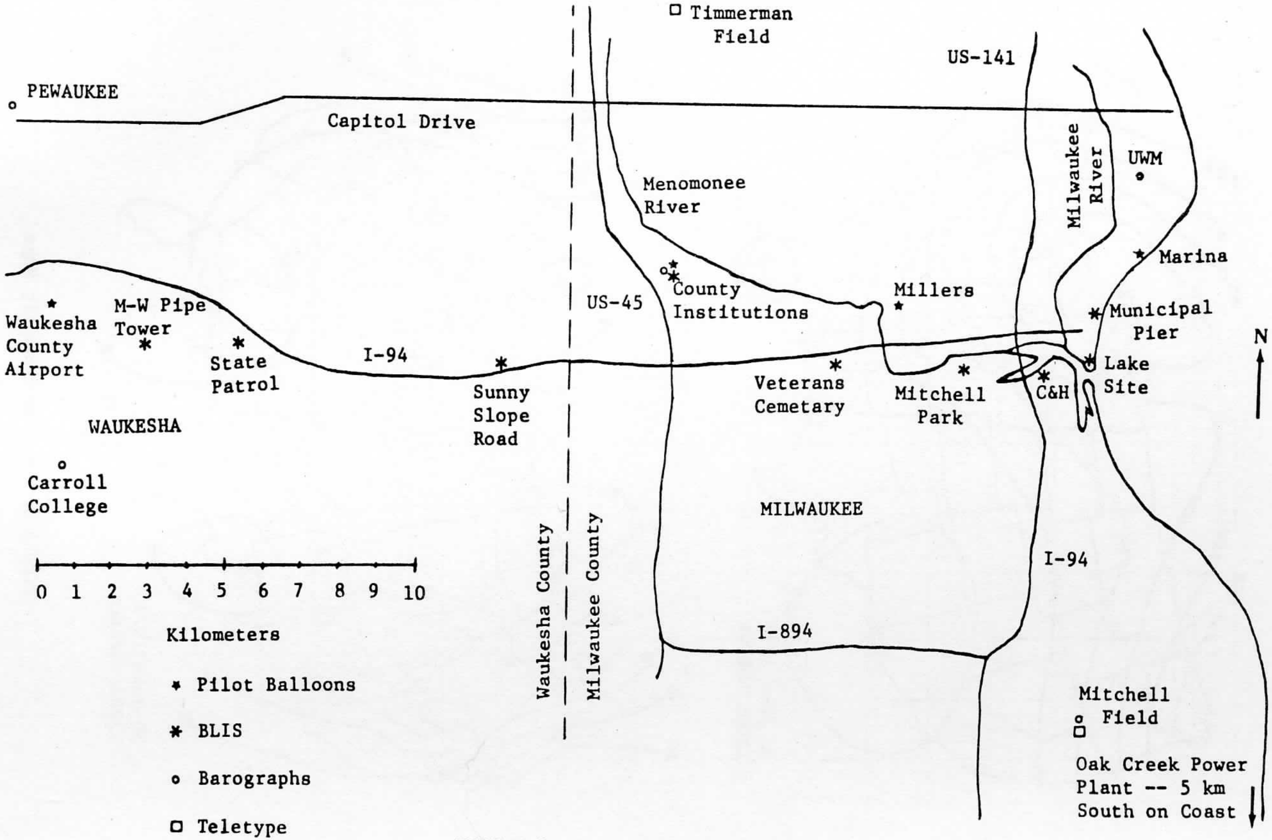

FIGURE 7: Map of the Experiment Area

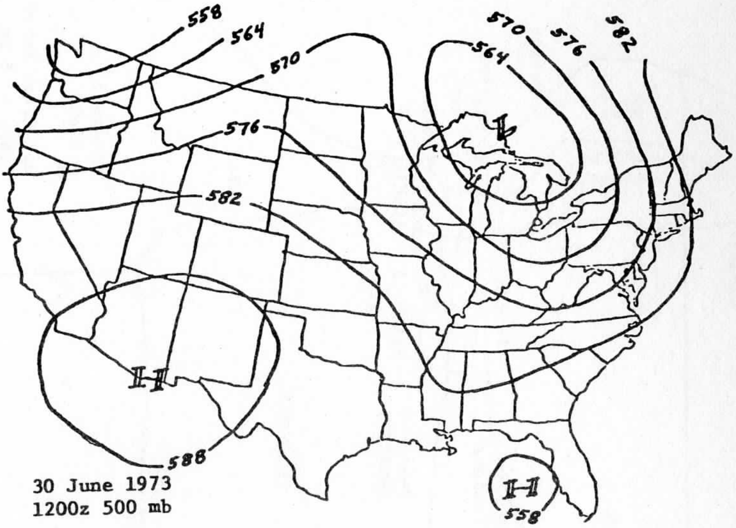

30 June 1973
1200z 500 mb

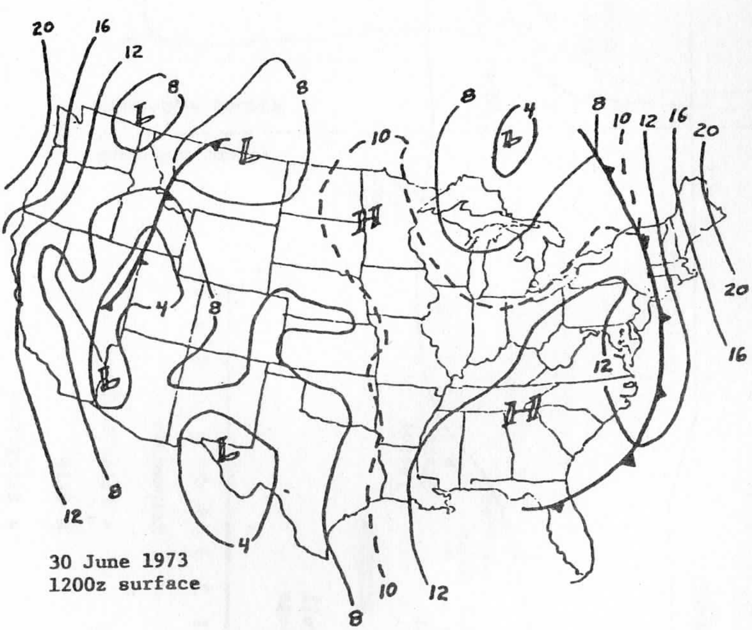

30 June 1973
1200z surface

FIGURE 8: 30 June Synoptic Maps

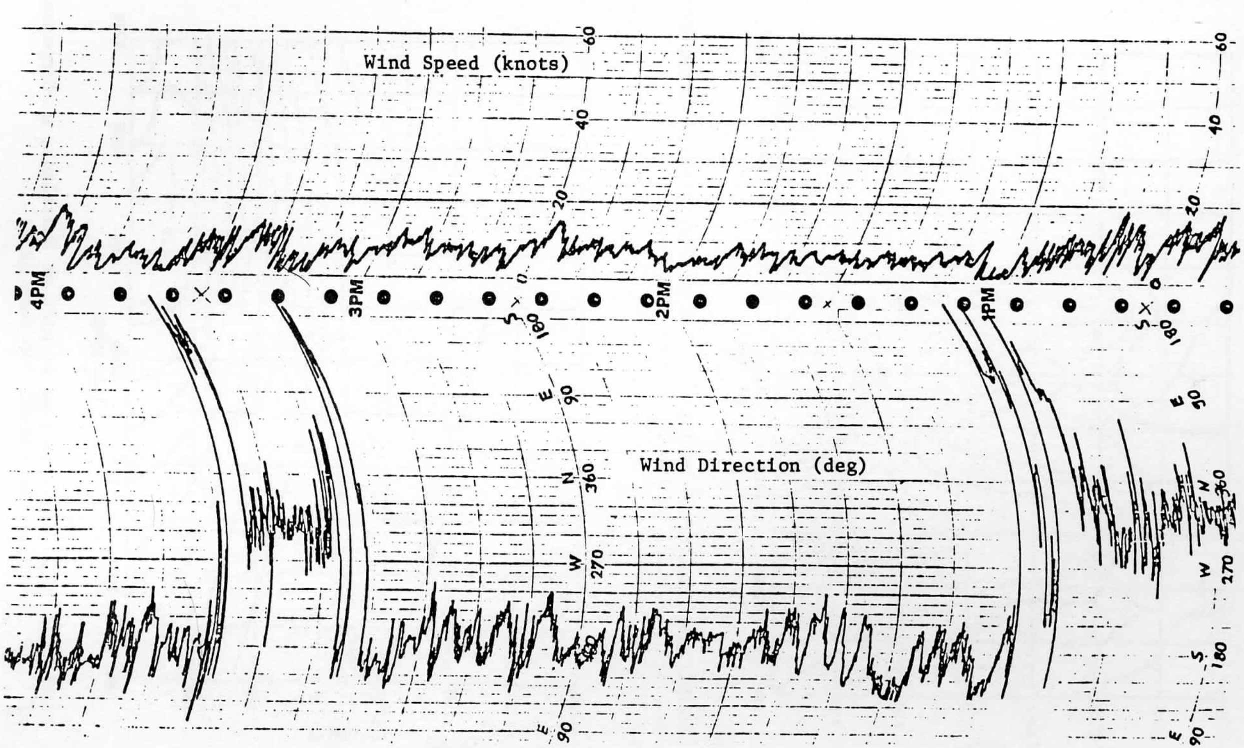

FIGURE 9: Oak Creek Power Plant Anemometer Trace
30 June 1973.

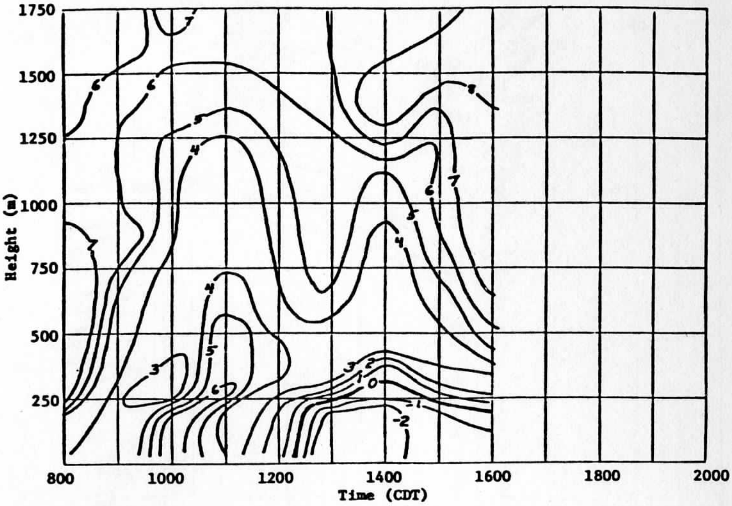

FIGURE 10A: Time Cross Section of Wind at Shoreline, u-Component (Pilot Balloons, 30 June 1973)

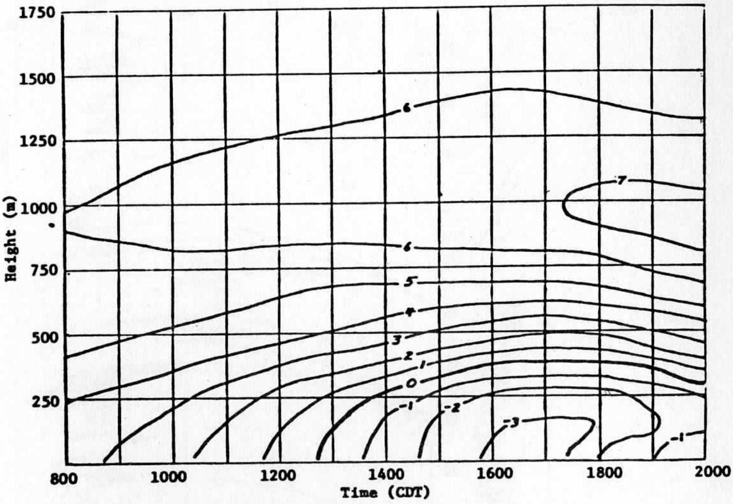

FIGURE 10B: Time Cross Section of Wind at Shoreline, u -Component (Coarse Mesh Model, 30 June 1973)

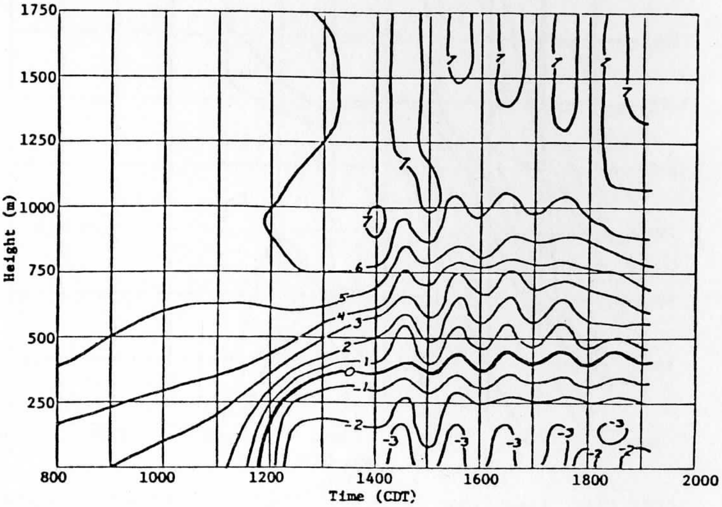

FIGURE 11A: Time Cross Section of Wind at Shoreline, u-Component (Fine Mesh Model, 30 June 1973)

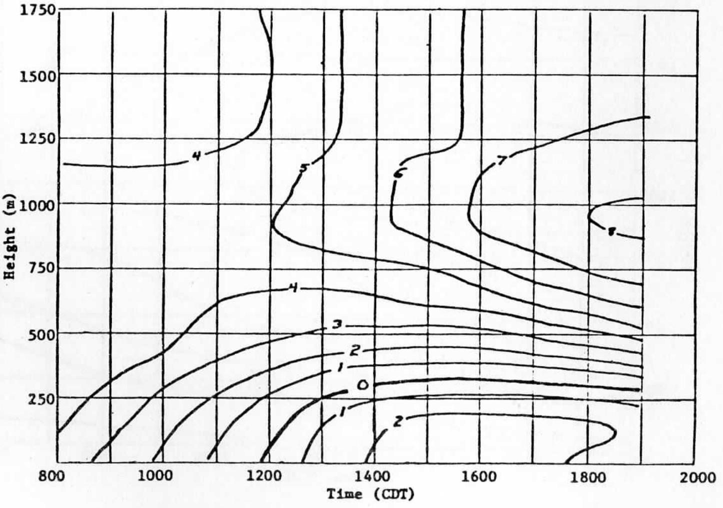

FIGURE 11B: Time Cross Section of Wind at Shoreline, u-Component (Coarse Mesh Model, Day 2, 1 July 1973)

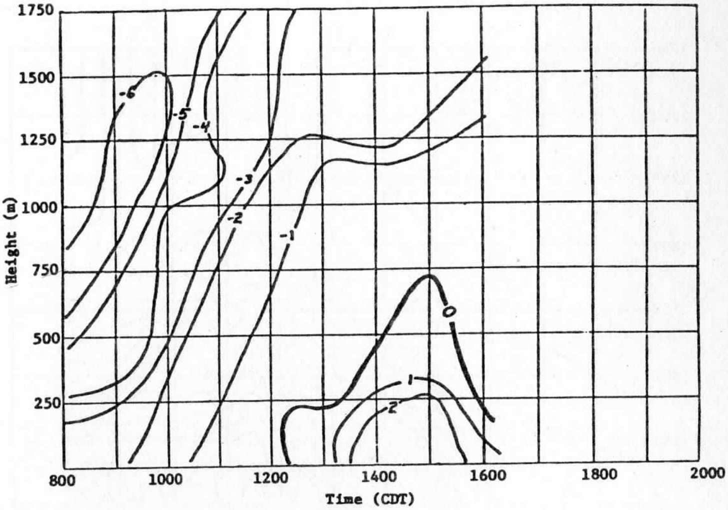

FIGURE 12A: Time Cross Section of Wind at Shoreline, v-Component (Pilot Balloons, 30 June 1973)

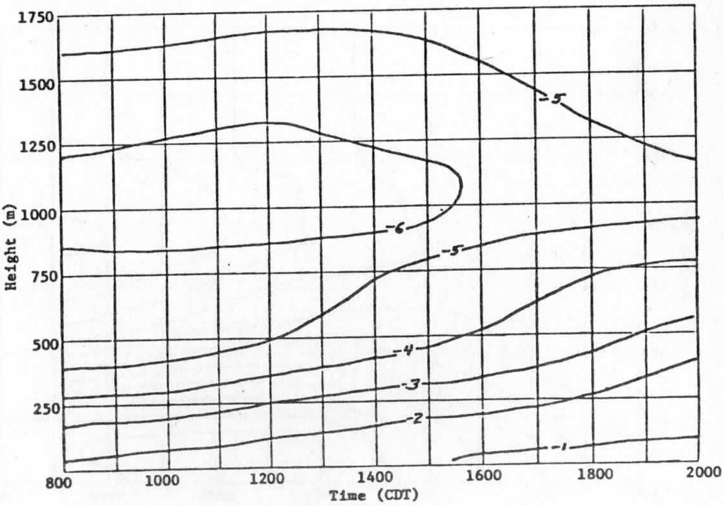

FIGURE 12B: Time Cross Section of Wind at Shoreline, v-Component (Coarse Mesh Model, 30 June 1973)

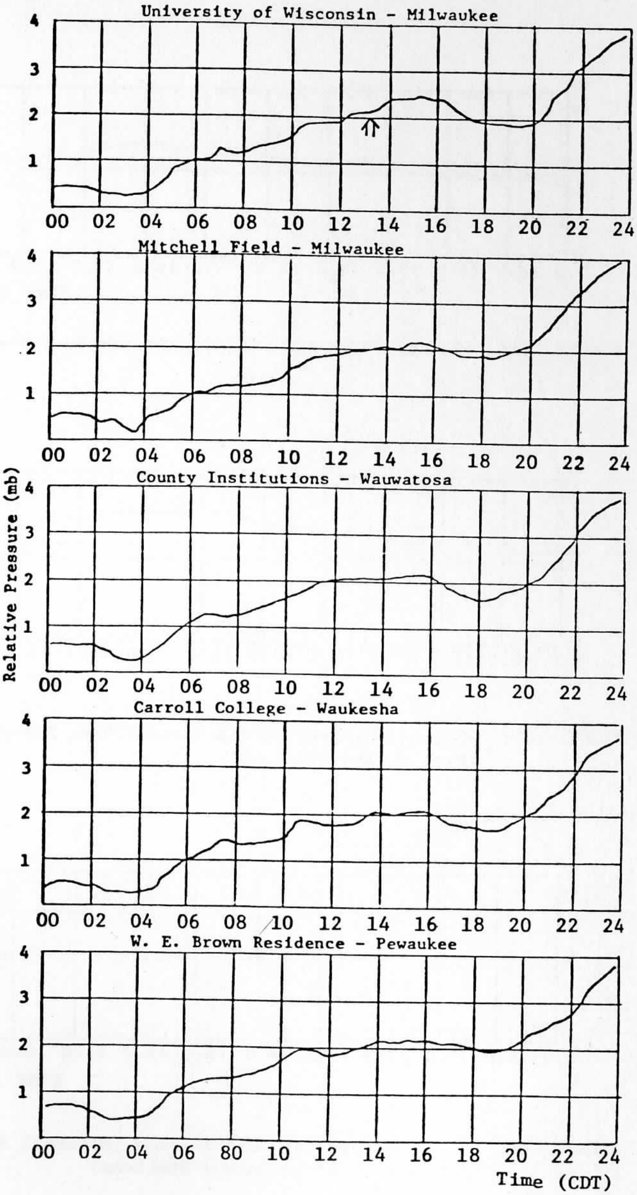

FIGURE 13: 30 June Barograph Traces

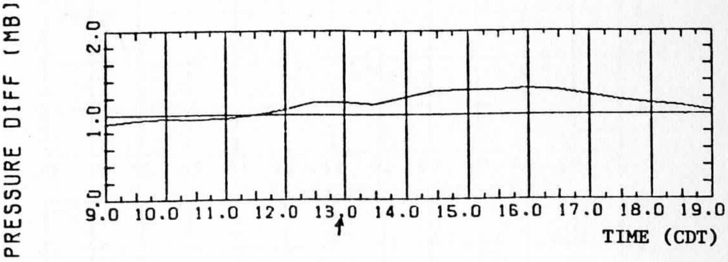

FIGURE 14A: 30 June Barograph Differences (UW-M, Waukesha)

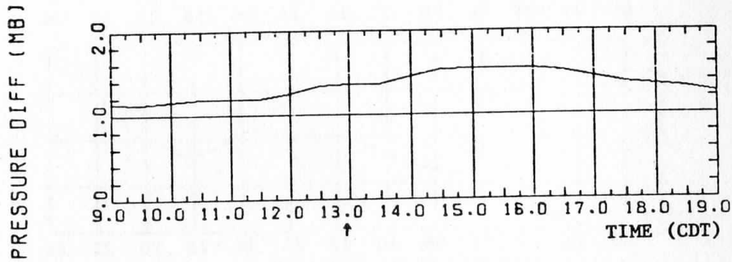

FIGURE 14B: 30 June Barograph Differences (UW-M, Average of Three Inland Stations)

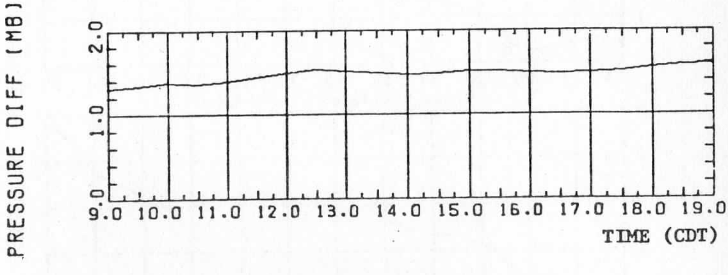

FIGURE 14C: 30 June Barograph Differences (Mitchell Field, Average of Three Inland Stations)

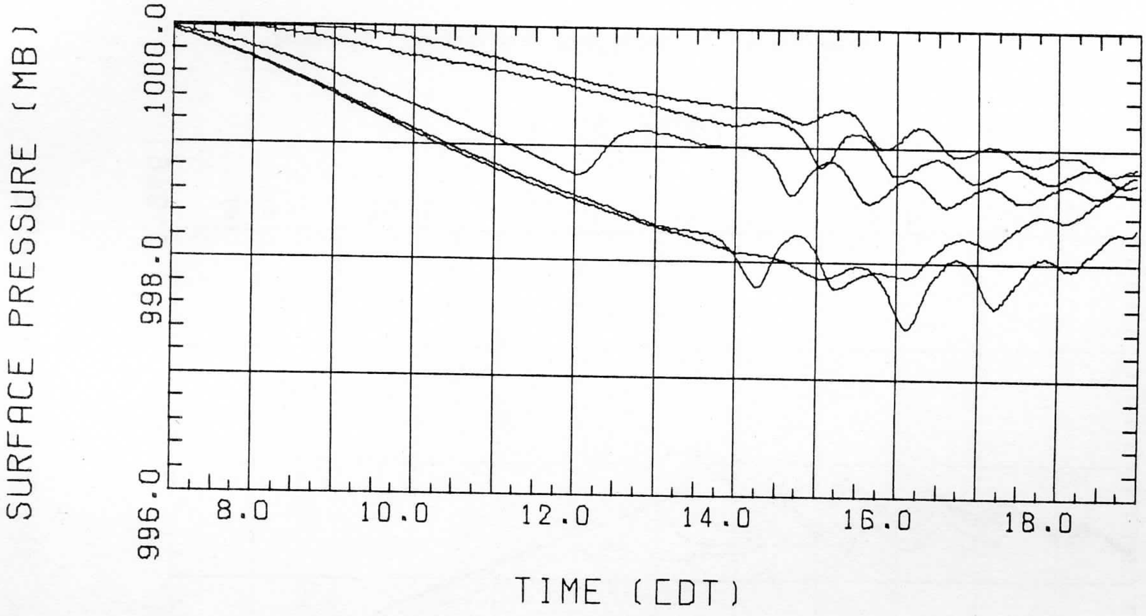

Curves from top represent grid points 30 and 10 km offshore, shore, and 10 and 30 km inland.

FIGURE 15: 30 June Fine Mesh Model Surface Pressures

Curves from top represent grid points at shore and 1, 2, 3, 4, and 5 km inland

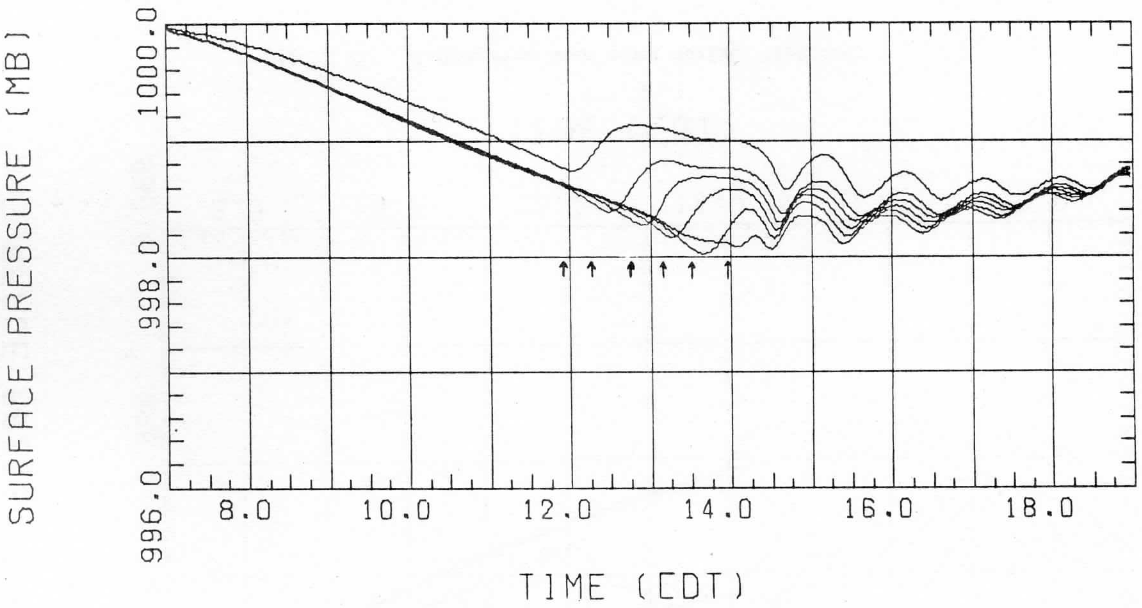

FIGURE 16: 30 June Fine Mesh Model Surface Pressures

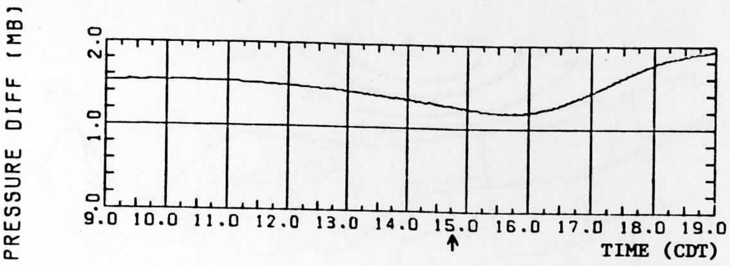

FIGURE 17A: 30 June Coarse Mesh Model Surface Pressure Difference (5 km Grid Point - 30 km Grid Point)

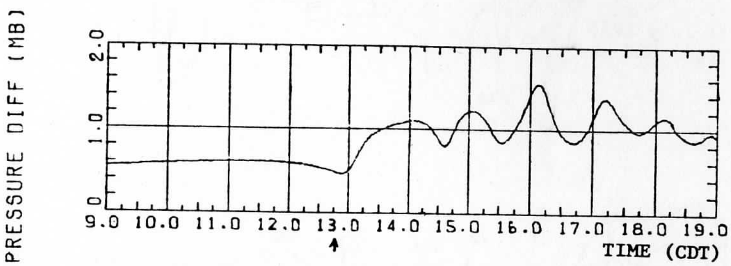

FIGURE 17B: 30 June Fine Mesh Model Surface Pressure Difference (2 km Grid Point - 30 km Grid Point)

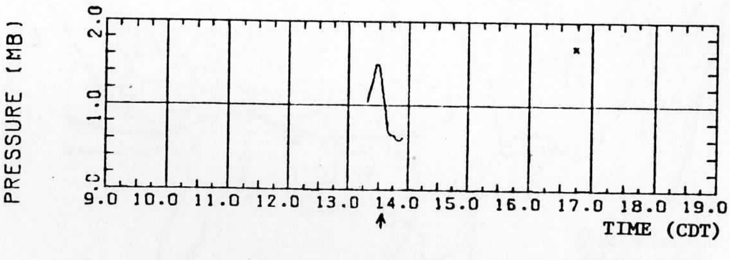

FIGURE 17C: 30 June Mitchell Park BLIS Surface Pressure (20-min Running Average of 2-min Average)

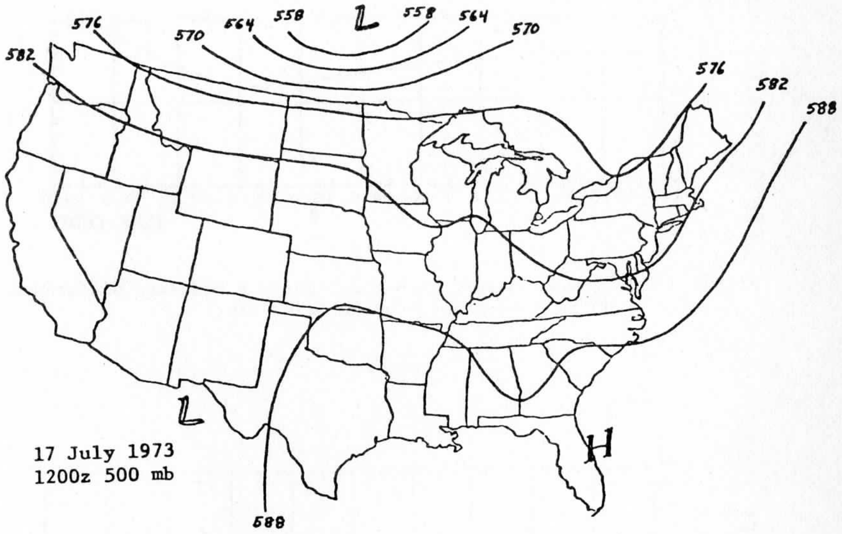

17 July 1973
1200z 500 mb

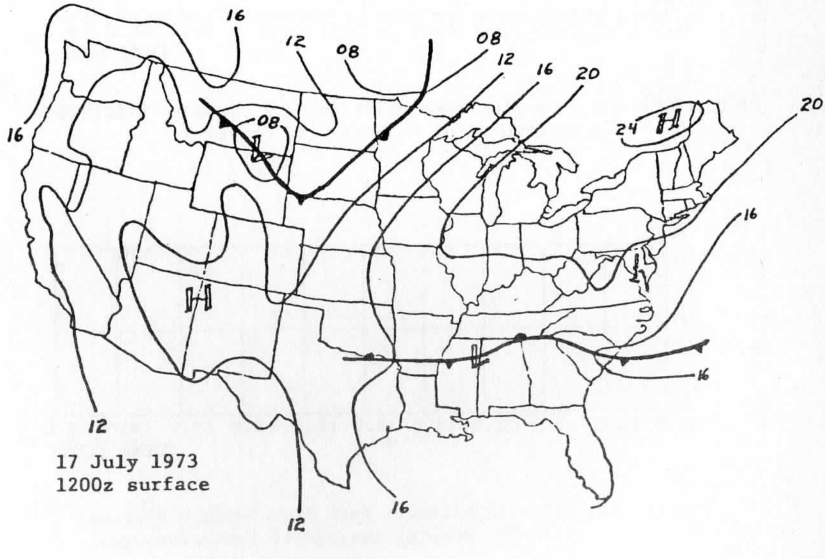

17 July 1973
1200z surface

FIGURE 18: 17 July Synoptic Maps

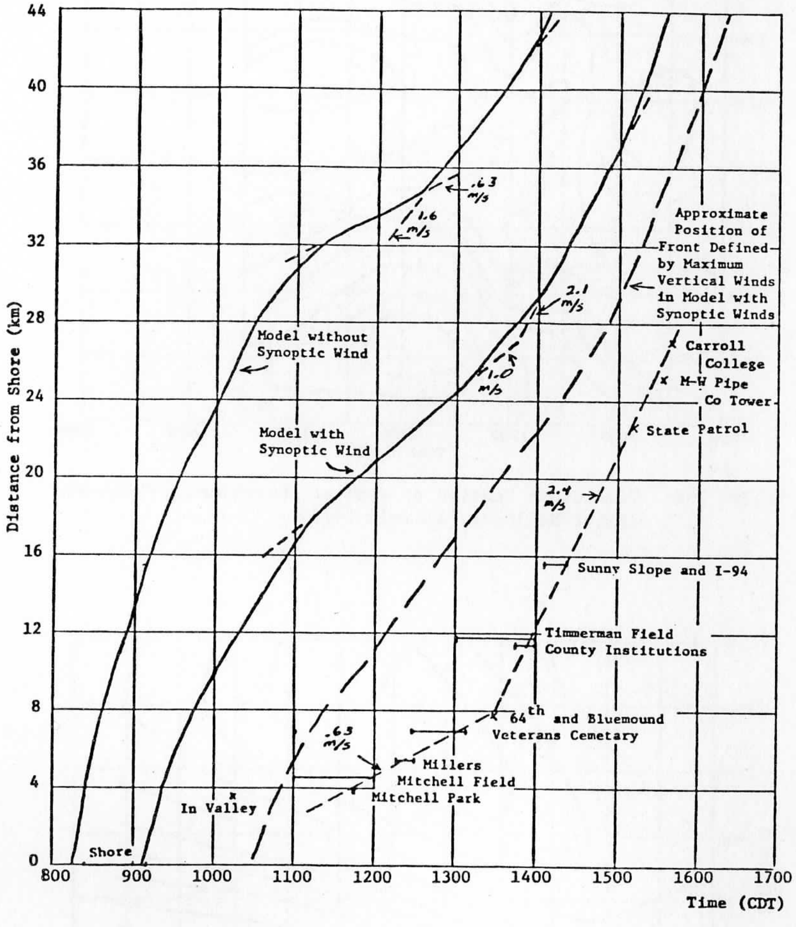

FIGURE 19: 17 July Frontal Position

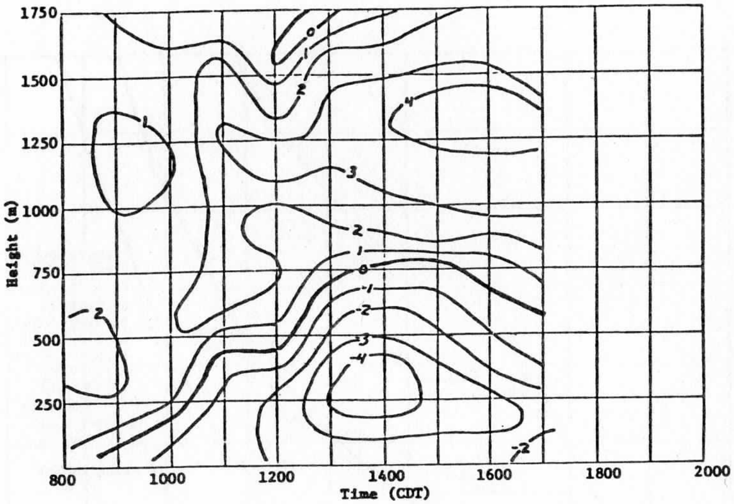

FIGURE 20A: Time Cross Section of Wind at Shoreline, u-Component (Pilot Balloons, 17 July 1973)

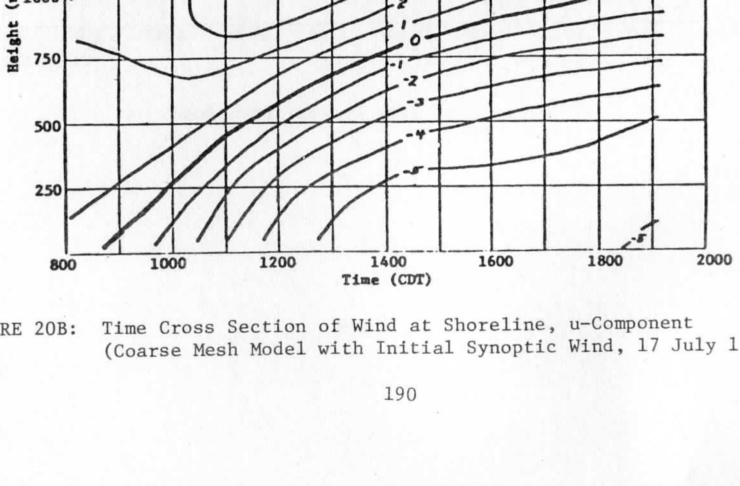

FIGURE 20B: Time Cross Section of Wind at Shoreline, u-Component (Coarse Mesh Model with Initial Synoptic Wind, 17 July 1973)

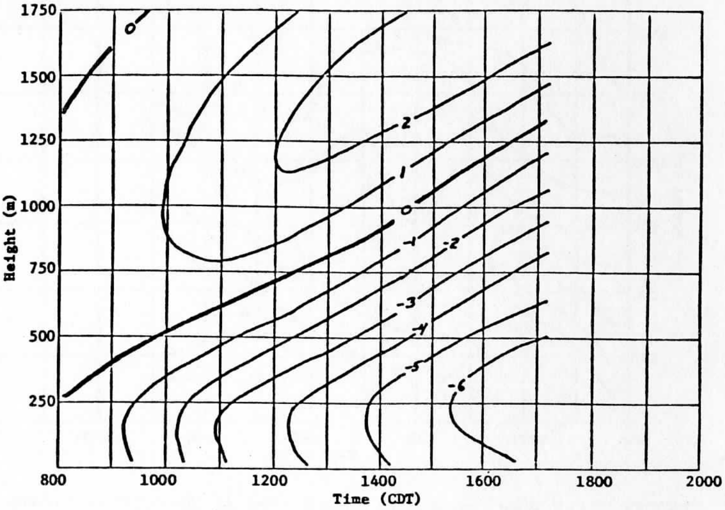

FIGURE 21A: Time Cross Section of Wind at Shoreline, u-Component (Coarse Mesh Model without Synoptic Wind, 17 July 1973)

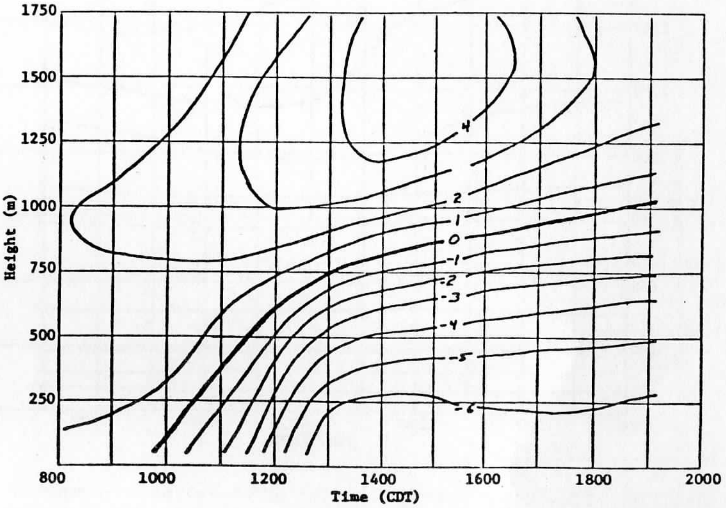

FIGURE 21B: Time Cross Section of Wind 10 km Inland, u-Component (Coarse Mesh Model with Initial Synoptic Wind, 17 July 1973)

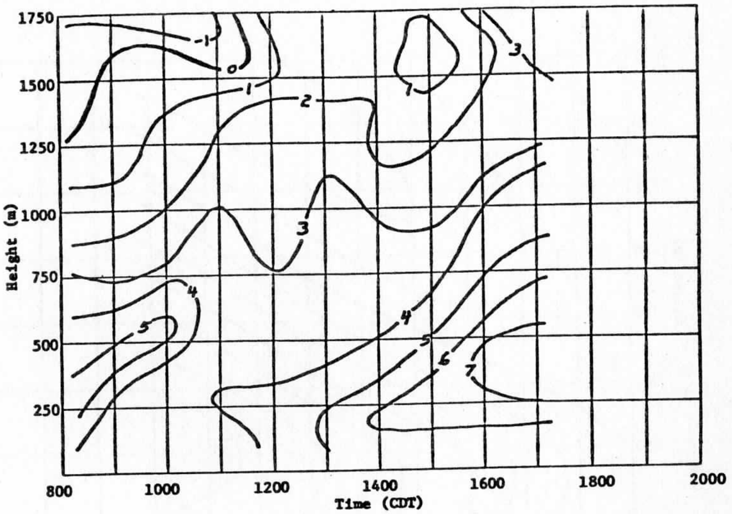

FIGURE 22A: Time Cross Section of Wind at Shoreline, v-Component (Pilot Balloons, 17 July 1973)

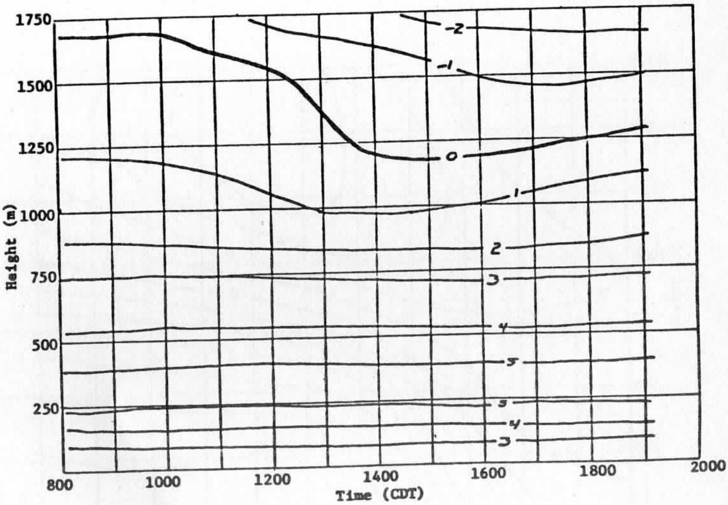

FIGURE 22B: Time Cross Section of Wind at Shoreline, v-Component Coarse Mesh Model with Initial Synoptic Wind, 17 July 1973)

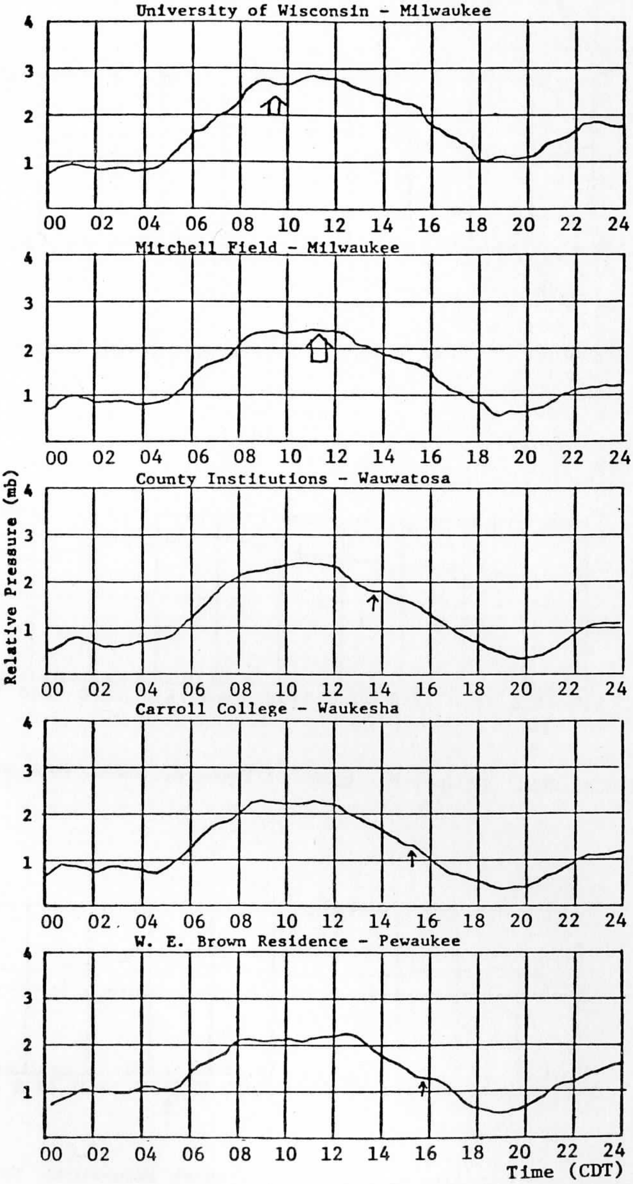

FIGURE 23: 17 July Barograph Traces

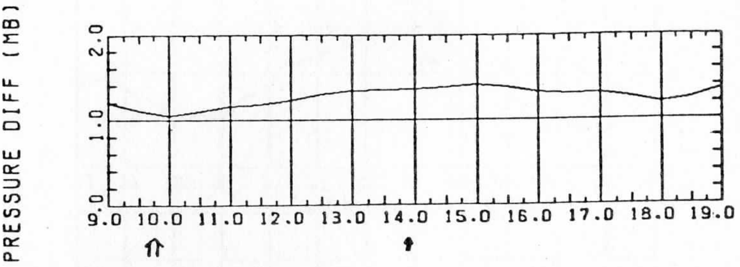

FIGURE 24A: 17 July Barograph Differences (UW-M, Wauwatosa)

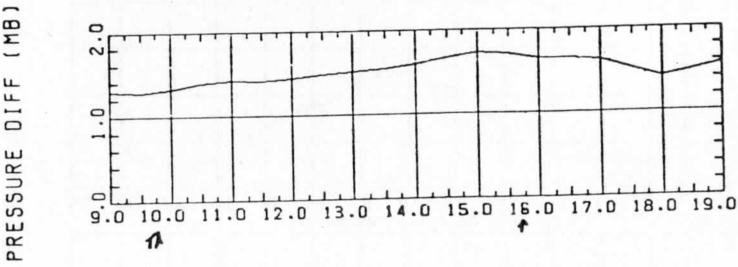

FIGURE 24B: 17 July Barograph Differences (UW-M, Waukesha)

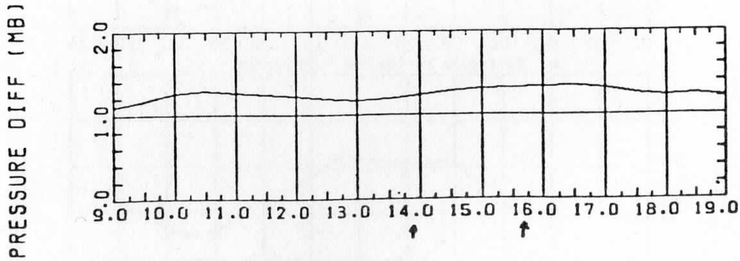

FIGURE 24C: 17 July Barograph Differences (Wauwatosa, Waukesha)

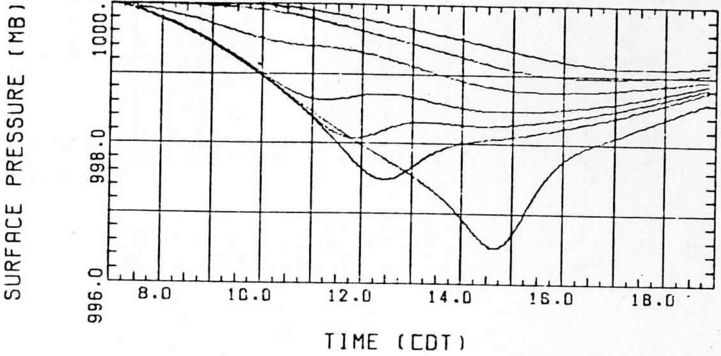
Curves from top represent grid points 30 and 10 km offshore, shore, and 5, 10, 15, and 30 km inland

FIGURE 25A: Surface Pressure (17 July Coarse Mesh Model with Synoptic Wind)

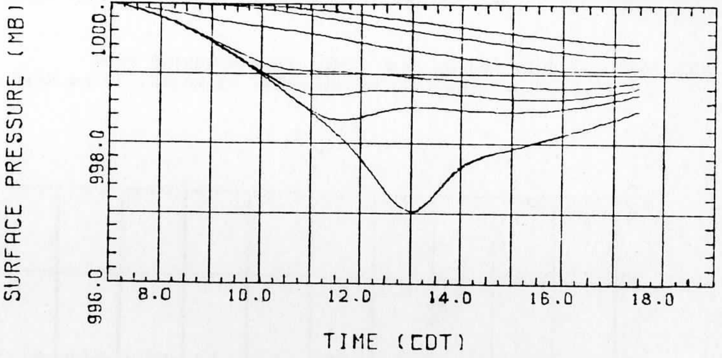
Curves from top represent grid points 30 and 10 km offshore, shore, and 5, 10, 15, and 30 km inland

FIGURE 25B: Surface Pressure (17 July Coarse Mesh Model without Synoptic Wind)

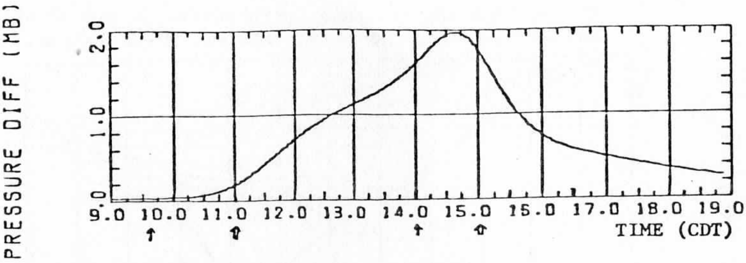

FIGURE 26A: 17 July Coarse Mesh Model with Synoptic Wind
(Surface Pressure Differences: 5 km vs. 30 km Grid Point)

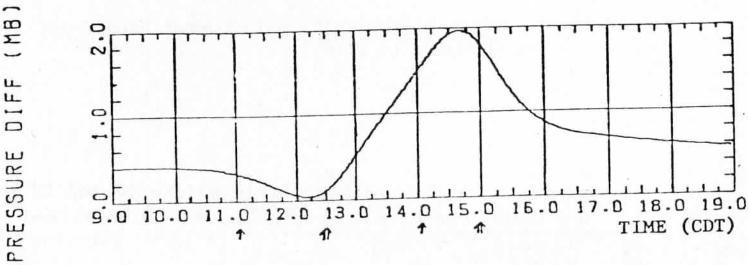

FIGURE 26B: 17 July Coarse Mesh Model with Synoptic Wind
(Surface Pressure Differences: 15 km vs. 30 km Grid Point

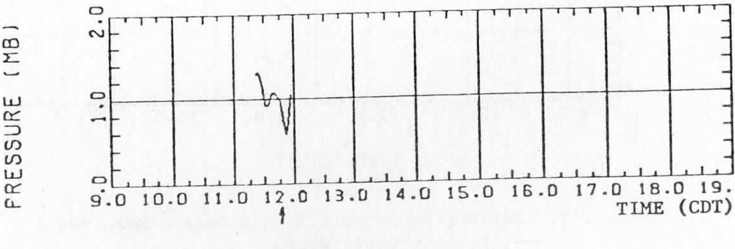

FIGURE 26C: 17 July Mitchell Park BLIS Surface Pressure

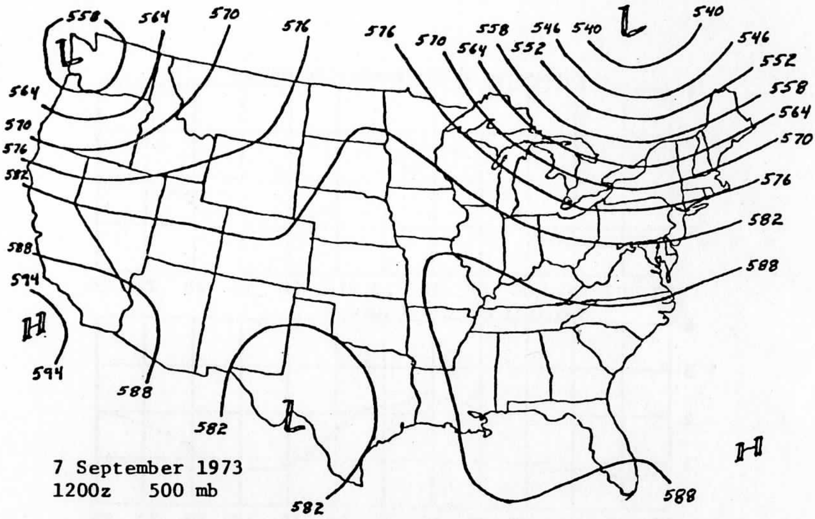
7 September 1973
1200z 500 mb

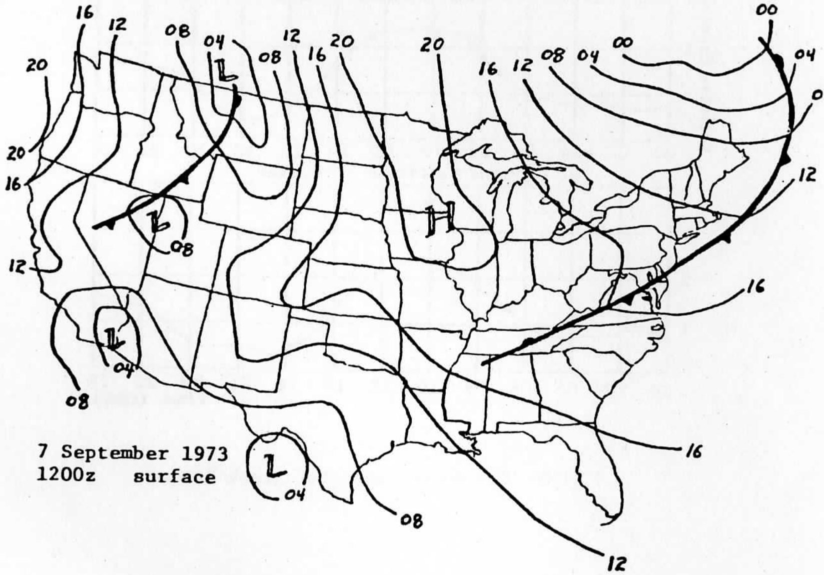
7 September 1973
1200z surface

FIGURE 27: 7 September Synoptic Maps

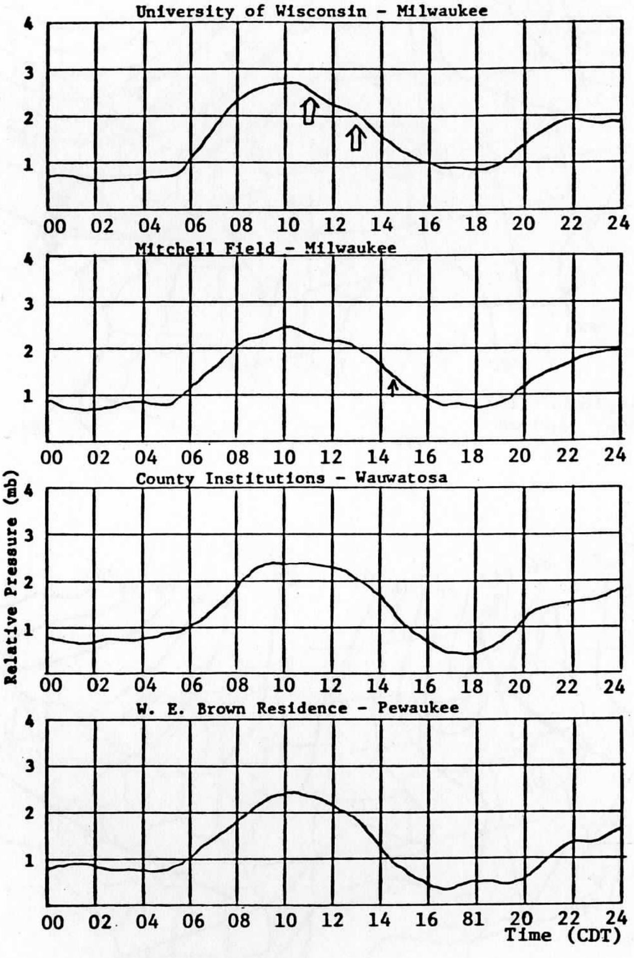

FIGURE 28: 7 September Barograph Traces

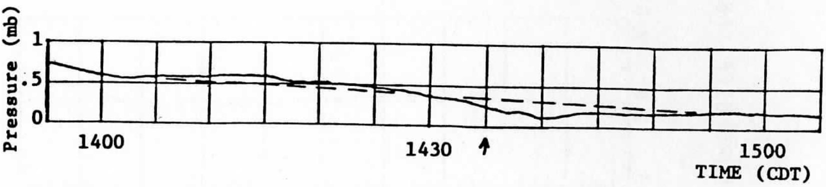

FIGURE 29A: Mitchell Field Barograph Detail

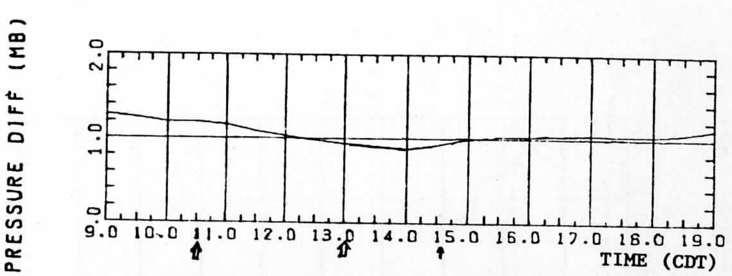

FIGURE 29B: 7 September Barograph Differences
(UW-M, Mitchell Field)

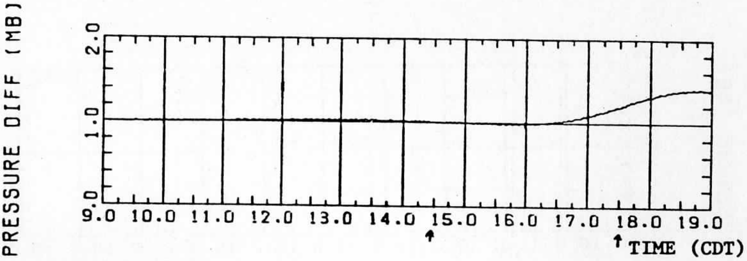

FIGURE 29C: 7 September Coarse Mesh Model
(5 km vs. 10 km Grid Point)

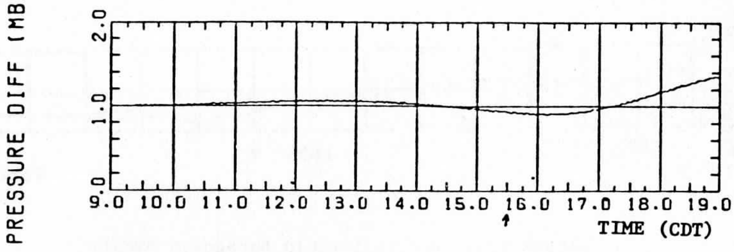

FIGURE 30A: 7 September Coarse Mesh Model
(5 km vs. 30 km Grid Point)

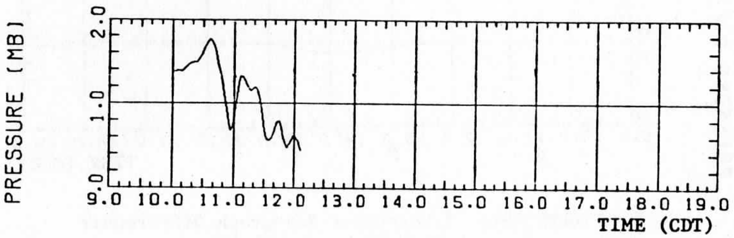

FIGURE 30B: 7 September Lake Site BLIS Surface Pressure

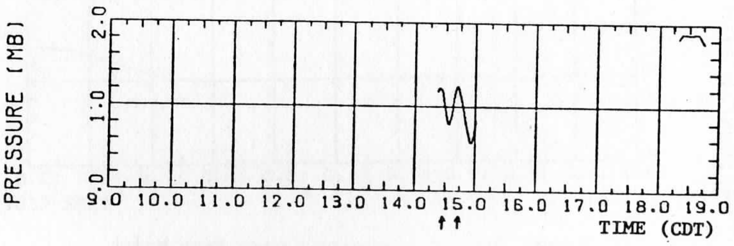

FIGURE 30C: 7 September Mitchell Park BLIS Surface Pressure

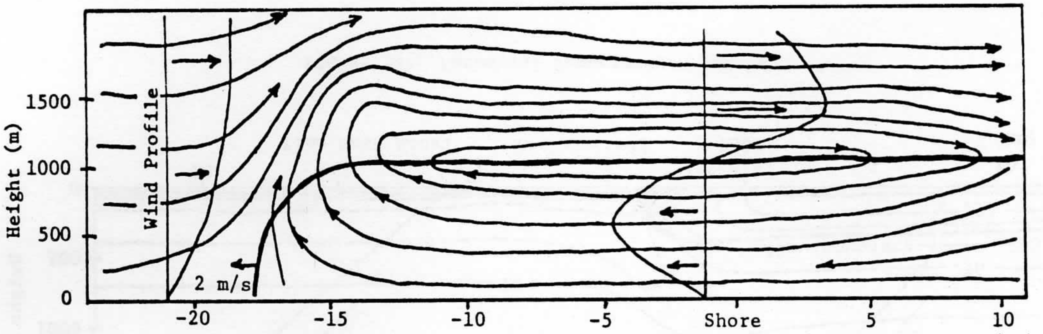

Measured Data (Lyons and Olsson, 1972)

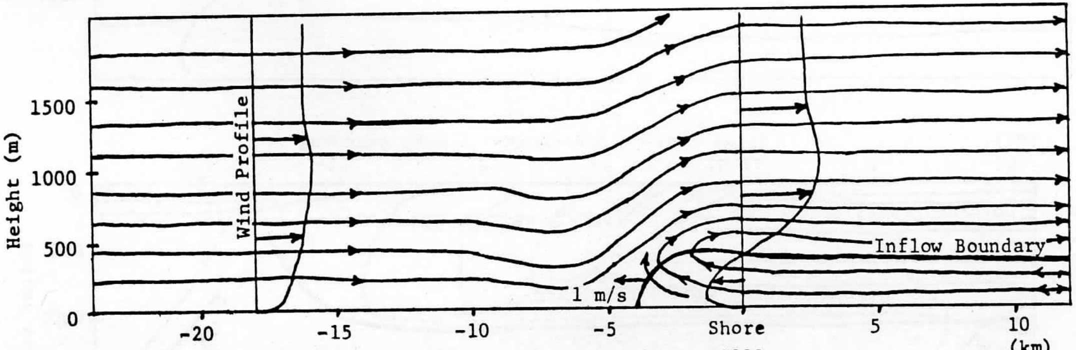

Fine Mesh Model 30 June 1973 1330

FIGURE 31: Streamlines and Wind Profiles

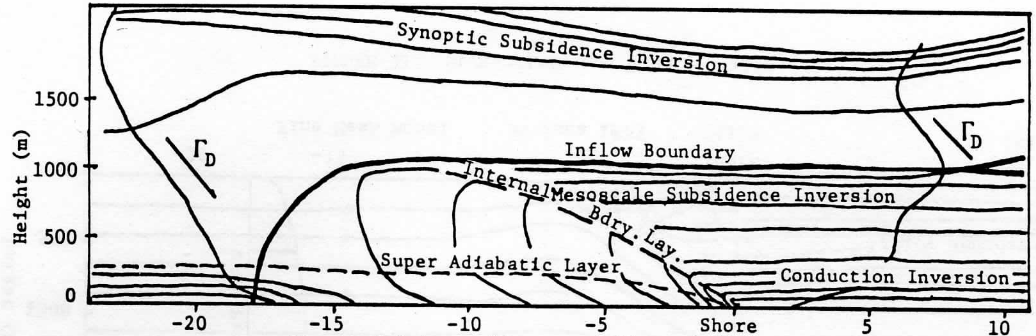

Measured Data (Lyons and Olsson, 1972)

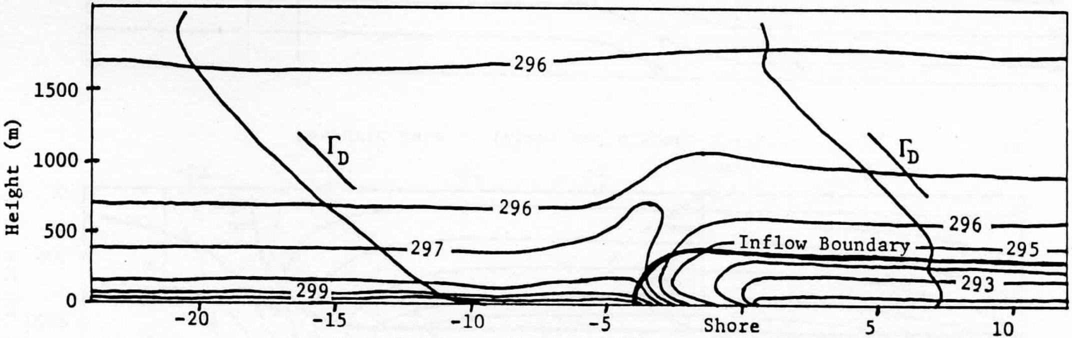

Fine Mesh Model 30 June 1973 Shore 1330

FIGURE 32: Potential Temperatures and Lapse Rates

TABLE 1

Data Days: Lake Michigan at Milwaukee, 1973

Day	Synoptic Wind	Lake Breeze Front	Lyons' Data Available	BLIS Comments
30 June	W	Strong, not far inland	yes	no winds
11 July	NE	none	yes	-
15 July	NE	none	no	-
16 July	E	none	yes	-
17 July	S-SW	Weak, far inland	yes	-
28 Aug.	SW	none; wind too strong	yes	2 instruments
7 Sept.	SW-W	Moderate, not far inland	no	2 instruments
23 Oct.	SE-SW	none	no	-

TABLE 2

Magnitude of Terms

(For explanations see text. All numbers are 10^{-4} m/s^2.)

x-equation of Motion		z-equation of Motion	
$\frac{\partial u'}{\partial t}$	= -15.6	$\frac{\partial w'}{\partial t}$	= $+2.4$
$u_o \frac{\partial u'}{\partial x}$	= -111.3	$u_o \frac{\partial w'}{\partial x}$	= $+8.4$
$u' \frac{\partial u'}{\partial x}$	= $+103.6$	$u' \frac{\partial w'}{\partial x}$	= -7.8
$w' \frac{\partial u_o}{\partial z}$	= $+12.2$	$w' \frac{\partial w'}{\partial z}$	= $+16.7$
$w' \frac{\partial u'}{\partial z}$	= $+17.7$	$-2\Omega \cos\phi(u'\cos\psi+v'\cos\psi)$	= $+3.8$
$\frac{1}{\rho} \frac{\partial p_h}{\partial x}$	= $+26.0 \pm 2.6$	$\frac{1}{\rho} \frac{\partial p^*}{\partial z}$	= -34.7 ± 8.9
$\frac{1}{\rho} \frac{\partial p^*}{\partial x}$	= -15.6 ± 2.6	$\frac{1}{\rho} \frac{\partial p_h}{\partial z}$	= $+2252.1$
$-fv'$	= -2.1	$\frac{\rho'}{\rho_o} g$	= -2252.1
$-\frac{\partial}{\partial z}[K(\frac{\partial u_o}{\partial z} + \frac{\partial u'}{\partial z})]$	= -9.7	total	= -11.2
$2w'\Omega \cos\phi \cos\psi$	= $+0.6$		
total	= $+5.8$		

TABLE 3

Temperature Ratios

Time (CDT)	1000	1200	1400
Over grass	20	27	26
Over asphalt	7	8	10
O'Neill	16	13	16
30 June model (z_o = 0.02)	11	14	16
30 June model (z_o = 1)	40	30	50
17 July model	17	13	11
7 September model	18	10	11

TABLE 4

30 June 1973

Measured Temperature (°C) / Relative Humidity (%)

Time (CDT)	Marina	Mitchell Field	Timmerman Field	Waukesha Airport
0800	18.5 / 73	18.5 / 76	18.0 / 76	-
0900	21.0 / 64	20.5 / 68	20.0 / 74	-
1000	22.0 / 55	21.5 / 64	21.5 / 61	20.5 / 81
1100	23.0 / 52	22.0 / 64	22.0 / 58	21.0 / 77
1200	23.0 / 57	24.0 / 58	23.5 / 58	24.0 / 75
1300	19.0 / 86	23.5 / 58	21.5 / 63	25.0 / 70
1400	19.0 / 86	-	-	25.0 / 67
1500	18.5 / 86	24.5 / 56	25.0 / 52	26.0 / 64
1600	18.5 / 90	25.0 / 53	24.5 / 56	26.5 / 61

TABLE 5

30 June 1973

Temperature Increase Across Front (°C) - Shore to 5 km Inland

Time (relative to frontal passage)	Measured (4.6 km)	Fine Model	Coarse Model Day 1	Coarse Model Day 2	Non-extended Coarse Model
-0.5 hr	1.0	0.6	1.3	1.4	1.3
0.5 hr	4.5	4.1	1.7	1.9	1.9
1.5 hr	-	5.3	3.1	3.0	3.8
2.5 hr	6.0	5.0*	4.5	4.1	4.5

* Shore to 10 km inland since front had passed 5 km inland

TABLE 6

30 June 1973 at Shore

Change in Wind Direction (deg) in 1 hr

	Before	After	Change
Pilot Balloon	274	103	189
Coarse Mesh Model	342	32	50
Fine Mesh Model	319	58	99

TABLE 7

17 July 1973

Measured Temperature (°C) / Relative Humidity (%)

Time (CDT)	Marina	Mitchell Field	Millers	Timmerman Field	Carroll College
0800	19.0 / 82	19.0 / 84	-	19.0 / 81	20.5 / -
0900	19.5 / 83	22.0 / 70	23.0 / 64	23.0 / 68	22.5 / -
1000	→ 19.5 / 87	24.5 / 55	23.0 / 62	25.0 / 52	24.5 / -
1100	20.0 / 87	25.5 / 53	25.5 / 45	26.5 / 46	26.0 / -
1200	20.0 / 87	→ 25.5 / 46	-	27.0 / 45	27.0 / -
1300	19.0 / 91	25.5 / 52	→ 24.5 / 48	26.5 / 44	27.5 / -
1400	19.5 / 91	25.0 / 53	25.0 / 46	→ 27.0 / 41	29.0 / -
1500	20.0 / 83	25.0 / 55	25.0 / 46	27.0 / 41	31.0 / -
1600	20.5 / 87	25.0 / 53	25.0 / 49	27.0 / 41	→ 30.0 / -
1700	20.0 / 87	24.5 / 55	25.0 / 49	26.5 / 47	30.0 / -
1800	-	24.5 / 55	-	26.5 / 48	28.0 / -

TABLE 8

17 July 1973 Simulation

Model Temperatures (°C) at 50 m height

Time (CDT)	Distance Inland Shore	5 km	10 km	15 km	20 km	25 km	30 km
0800	20.0	20.5	20.5	20.5	20.5	20.5	20.5
0900	21.0	22.2	22.2	22.3	22.3	22.3	22.3
1000	→21.8	→24.1	→24.3	24.3	24.3	24.3	24.3
1100	→21.6	→25.0	26.2	→26.3	26.2	26.1	26.1
1200	21.2	23.8	→26.0	→27.8	→27.9	27.5	27.3
1300	21.1	22.9	24.0	25.7	→28.4	→28.7	28.2
1400	20.9	22.4	23.2	23.9	25.2	→28.1	→28.8
1500	20.8	22.0	22.9	23.5	24.2	26.0	→27.0
1600	20.7	21.8	22.3	22.8	23.2	23.6	24.1
1700	20.6	21.5	21.9	22.3	22.7	23.0	23.3
1800	20.5	21.2	21.4	21.7	22.0	22.2	22.5

TABLE 9

17 July 1973 at Shore

Change in Wind Direction (deg) in 1 hr

	Before	After	Change
Pilot Balloon	185	157	28
Synoptic Wind Model	181	152	29
Non-synoptic Wind Model	182	155	27

TABLE 10

7 September 1973

Measured Temperature (°C) / Relative Humidity (%)

Time (CDT)	Mitchell Field	Timmerman Field	Carroll College
0800	16.5 / 68	16.0 / 70	17.0 / -
0900	18.5 / 62	19.0 / 65	19.5 / -
1000	20.0 / 57	21.0 / 55	21.0 / -
1100	21.5 / 47	22.0 / 49	22.0 / -
1200	22.0 / 49	23.5 / 46	22.0 / -
1300	23.0 / 47	24.0 / 46	23.5 / -
1400	24.0 / 45	24.0 / 46	24.5 / -
1500	→21.5 / 54	24.0 / 46	24.5 / -
1600	21.0 / 54	24.5 / 45	25.5 / -
1700	20.5 / 55	24.5 / 45	24.0 / -

TABLE 11

7 September 1973

Temperature Increase Across Front (°C) to 10 km Inland

Time (Relative to Frontal Passage)	Actual (7.1 km)	Model (5 km)
-0.5 hr	0	0.1
0.5 hr	2.5	0.3
1.5 hr	3.5	1.3
2.5 hr	4.0	1.9

TABLE 12

7 September 1973 5 km Inland

Change in Wind Direction (deg)

	Before	After	Change
MKE (1 hr)	320	110	150
Model (1 hr)	328	42	74
Model (2 hr)	328	77	109

TABLE 13

30 June Model Output

A Coarse mesh model base run from which others are compared
B Fine mesh model (5 km → 1 km)
C Expanded size Day 1 (140 km → 280 km)
D Expanded size Day 2
E Water temperature reduced (18°C → 17°C)
F Roughness parameter increased (.02 m → 1 m)
G Lapse rate changed (6.5 deg/km → 7.5 deg/km)

1 Time (±5 min) of wind reversal at shore and 50 m height (CDT)
2 Maximum lake breeze wind perpendicular to shore at 50 m height (m/s)
3 Time of wind velocity given in 2 (CDT)
4 Maximum vertical wind at 5 km inland and 550 m height (m/s)
5 Time of vertical wind given in 4 (CDT)
6 Maximum surface pressure difference from shore to 5 km inland (mb)
7 Time of pressure difference given in 6 (CDT)
8 Maximum inflow height (±10 m) at shore by 1500 CDT
9 Maximum inflow penetration (±.5 km) by 1500 CDT at 50 m height
10 Frontal speed (m/s)

NOTE: 50 m is lowest non-zero wind height; 1, 8 and 9 were interpolated; 10 used linear regression over data from shore crossing to 1500 CDT.

	A	B	C	D	E	F	G	Actual
1	1245	1140	1255	1150	1215	1310	1240	1235
2	4.21	3.16	3.13	2.61	4.65	1.31	4.47	3.00
3	1800	1530	1700	1600	1750	1600	1700	1300
4	.165	.559	.155	.152	.178	.123	.176	
5	1530	1400	1600	1600	1500	1330	1500	
6	.96	.90	.91	.90	1.07	1.02	.98	
7	1530	1330	1600	1530	1500	1500	1530	
8	380	350	320	350	430	410	410	310
9	7.5	6.3	5.5	7.0	9.0	7.5	8.0	4.5
10	.90	.77	.69	.58	.91	.79	.93	1.10

TABLE 14

Temperature Fall with Frontal Passage (^{o}C)

Date	Distance Inland	Time	Measured	Coarse Model	Fine Model
30 June	Shore	1 hr	4.0	0.3	3.8
30 June	Shore	3 hr	4.5	2.6	3.1
17 July	Shore	1 hr	0.0	0.2	-
17 July	30 km	1 hr	1.0	1.8	-
7 Sept.	5 km	1 hr	2.5	0.2	-
7 Sept.	5 km	3 hr	3.5	2.3	-

TABLE 15

Change in Wind Direction (deg)

Date	Distance Inland	Time	Measured	Coarse Model	No-Wind Model	Fine Model
30 June	Shore	1 hr	189	50	-	99
17 July	Shore	1 hr	28	29	27	-
7 Sept.	5 km	1 hr	150	74	-	-
7 Sept.	5 km	2 hr	160	109	-	

APPENDIX A

Mathematics of the Model

Section A.1: Solution of the Constant Flux Equations

Estoque (1963) showed how U and θ are determined at height h. Note that U at the surface is zero. The value of θ at the surface and the constants z_o, k_o, g, γ, α, L, h and Δz are preset and are discussed in Section 3 of this report. The values of K for forced and free convection (equations 2.04 and 2.05) are substituted into the constant flux equations (2.01 and 2.02) which are then integrated with respect to height (z). The fluxes (of momentum and heat, respectively) are then evaluated at height h and become (for forced convection):

$$[K \frac{\partial U}{\partial z}]_h = \beta^2 (\Delta U)^2 , \qquad [K \frac{\partial \theta}{\partial z}]_h = \beta^2 \Delta U \Delta \theta \qquad \text{(A.01, A.02)}$$

and for free convection:

$$[K \frac{\partial U}{\partial z}]_h = \gamma r(\frac{gr}{\theta} \Delta\theta)^{1/2} \Delta U, \qquad [K \frac{\partial \theta}{\partial z}]_h = \gamma r(\frac{gr}{\theta} \Delta\theta)^{1/2} \Delta\theta \qquad \text{(A.03, A.04)}$$

where $\Delta\theta$ and ΔU are the change from the surface to $h + \Delta z$,

$$\beta = \frac{k_o(h + z_o)}{\Delta z + (h + z_o) \ln(\frac{h + z_o}{z_o})} [1 + \frac{\alpha g(h + z_o)\Delta\theta}{\theta(\Delta U)^2}] \qquad \text{(A.05)}$$

and

$$r = \frac{1}{\Delta z(h + z_o)^{-4/3} - 3[(h + z_o)^{-1/3} - z_o^{-1/3}]} \qquad \text{(A.06)}$$

By assuming that the fluxes in the surface layer are equal tothe fluxes in the layer Δz above the surface layer, K can be determined at height h. For forced convection:

$$[K]_h = \frac{\beta \Delta U}{\frac{1}{k_o(h + z_o)} - \frac{\alpha g \Delta\theta}{\theta \beta (\Delta U)^2}} \qquad \text{(A.07)}$$

and for free convection:

$$[K]_h = \gamma(\frac{gr}{\theta} \Delta\theta)^{1/2}(h + z_o)^{4/3} \qquad \text{(A.08)}$$

U and θ can now be determined at height h, for forced convection:

$$U_h - U_{h+\Delta z} = -\frac{\partial U}{\partial z}\Delta z = -\frac{L\beta^2(\Delta U)^2\Delta z}{K} \qquad (A.09)$$

$$\theta_h - \theta_{h+\Delta z} = -\frac{\partial \theta}{\partial z}\Delta z = -\frac{L\beta^2\Delta U\Delta\theta\Delta z}{K} \qquad (A.10)$$

and for free convection:

$$U_h - U_{h+\Delta z} = -\frac{\partial U}{\partial z}\Delta z = -\frac{L\gamma r(\frac{gr}{\theta}\Delta\theta)^{1/2}\Delta U\Delta z}{K} = -\frac{Lr\Delta U\Delta z}{(h + z_\circ)^{4/3}} \qquad (A.11)$$

$$\theta_h - \theta_{h+\Delta z} = -\frac{\partial \theta}{\partial z}\Delta z = -\frac{L\gamma r(\frac{gr}{\theta}\Delta\theta)^{1/2}\Delta\theta\Delta z}{K} = -\frac{Lr\Delta\theta\Delta z}{(h + z_\circ)^{4/3}} \qquad (A.12)$$

where L is a constant which depends on the number of levels and represents the fact that K at h + Δz is less than K at h.

Equations A.09 to A.12 are used in the model to determine U and θ at height h, which is considered the bottom boundary of the rest of the model. Equations A.07 and A.08 determine K at height h. This value is used in equation 2.12 to determine the K needed for the equations of motion (A.205 and A.206) and the heat of conduction equation (2.14).

Section A.2: Expansion of the Equations of Motion into the Terms used in the Model

This section of the appendix derives the equations of motion used in the model from equations 2.09, 2.10 and 2.11. Equation 2.09 is repeated here for reference:

$$\frac{\partial u}{\partial t} + u\frac{\partial u}{\partial x} + w\frac{\partial u}{\partial z} = -\frac{1}{\rho}\frac{\partial p}{\partial x} + fv + \frac{\partial}{\partial z}\left(K\frac{\partial u}{\partial z}\right) - 2w\Omega\cos\phi\cos\psi \qquad (2.09)$$

As stated in Section 2 of this report, u, v and w are expanded into the initial velocities u_o and v_o (w is initially zero) plus the change in velocity from the initial conditions of u', v' and w':

$$u = u_o + u' , \qquad v = v_o + v' , \qquad w = w' \qquad (A.201)$$

Since u_o and v_o are the initial conditions, they do not change in time. It is also assumed that they do not change in the x direction, but they can vary in the z direction:

$$\frac{\partial u_o}{\partial t} = \frac{\partial u_o}{\partial x} = \frac{\partial v_o}{\partial t} = \frac{\partial v_o}{\partial x} = 0 \qquad (A.202)$$

Pressure is also divided into an initial pressure, p_o, and the change from the initial pressure, p': $p = p_o + p'$. It is then assumed that the initial wind is in geostrophic balance with the initial pressure:

$$\frac{1}{\rho}\frac{\partial p_o}{\partial x} = fv_o , \qquad \frac{1}{\rho}\frac{\partial p_o}{\partial y} = -fu_o \qquad (A.203)$$

Expanding equation 2.09 using equations A.201 gives:

$$\frac{\partial u_o}{\partial t} + \frac{\partial u'}{\partial t} + u_o\frac{\partial u_o}{\partial x} + u_o\frac{\partial u'}{\partial x} + u'\frac{\partial u_o}{\partial x} + u'\frac{\partial u'}{\partial x} + w'\frac{\partial u_o}{\partial z} + w'\frac{\partial u'}{\partial z}$$
$$= -\frac{1}{\rho}\frac{\partial p_o}{\partial x} - \frac{1}{\rho}\frac{\partial p'}{\partial x} + fv_o + fv' + \frac{\partial}{\partial z}\left[K\left(\frac{\partial u_o}{\partial z} + \frac{\partial u'}{\partial z}\right)\right] - 2w'\Omega\cos\phi\cos\psi \qquad (A.204)$$

Use of equations A.202 and A.203 reduces this to:

$$\frac{\partial u'}{\partial t} + u_o\frac{\partial u'}{\partial x} + u'\frac{\partial u'}{\partial x} + w'\frac{\partial u_o}{\partial z} + w'\frac{\partial u'}{\partial z}$$
$$= -\frac{1}{\rho}\frac{\partial p'}{\partial x} + fv' + \frac{\partial}{\partial z}\left[K\left(\frac{\partial u_o}{\partial z} + \frac{\partial u'}{\partial z}\right)\right] + 2w'\Omega\cos\phi\cos\psi \qquad (A.205)$$

Similarly, equation 2.10 yields:

$$\frac{\partial v'}{\partial t} + u_\circ \frac{\partial v'}{\partial x} + u' \frac{\partial v'}{\partial x} + w' \frac{\partial v_\circ}{\partial z} + w' \frac{\partial v'}{\partial z}$$

$$= - fu' + \frac{\partial}{\partial z}[K(\frac{\partial v_\circ}{\partial z} + \frac{\partial v'}{\partial z})] - 2w'\Omega \cos\phi \sin\psi \qquad (A.206)$$

The term p' in the above equations contains a hydrostatic change component p_h and a non-hydrostatic component, p*: $p' = p_h + p^*$. In other words:

$\frac{1}{\rho}\frac{\partial p_h}{\partial z} = - \frac{\rho'}{\rho}$ g. It is assumed that the vertical hydrostatic pressure gradient cancels the buoyancy and initial vertical coriolis terms:

$$g = - \frac{1}{\rho}\frac{\partial p_\circ}{\partial z} - \frac{1}{\rho}\frac{\partial p_h}{\partial z} + 2\Omega \cos\phi \; (u_\circ \cos\psi + v_\circ \sin\psi) \qquad (A.207)$$

Equation 2.11 can now be expanded using equations A.21; by using equation A.27 the expansion can be reduced to:

$$\frac{\partial w'}{\partial t} + u_\circ \frac{\partial w'}{\partial x} + u' \frac{\partial w'}{\partial x} + w' \frac{\partial w'}{\partial z} = - \frac{1}{\rho}\frac{\partial p^*}{\partial z} + 2\Omega \cos\phi \; (u' \cos\psi + v' \sin\psi)$$

$$(A.208)$$

The non-hydrostatic pressure terms are now separated from the rest of the prognostic equations, giving:

$$\frac{\partial u'}{\partial t} = \frac{\partial u^*}{\partial t} - \frac{1}{\rho}\frac{\partial p^*}{\partial x} , \qquad \frac{\partial w'}{\partial t} = \frac{\partial w^*}{\partial t} - \frac{1}{\rho}\frac{\partial p^*}{\partial z} \qquad (A.209,\ A.210)$$

where $\frac{\partial u^*}{\partial t}$ represents all of the terms in equation A.205 except the first with p' changed to p_h, and $\frac{\partial w^*}{\partial t}$ represents all of the terms in equation except the first term and the p* term:

$$\frac{\partial u^*}{\partial t} = - u_\circ \frac{\partial u'}{\partial x} - u' \frac{\partial u'}{\partial x} - w' \frac{\partial u_\circ}{\partial z} - w' \frac{\partial u'}{\partial z} - \frac{1}{\rho}\frac{\partial p_h}{\partial x} + fv'$$

$$+ \frac{\partial}{\partial z}[K(\frac{\partial u_\circ}{\partial z} + \frac{\partial u'}{\partial z})] - 2w'\Omega \cos\phi \cos\psi \qquad (A.211)$$

$$\frac{\partial w^*}{\partial t} = - u_\circ \frac{\partial w'}{\partial x} - u' \frac{\partial w'}{\partial x} - w' \frac{\partial w'}{\partial z} + 2\Omega \cos\phi \; (u' \cos\psi + v' \sin\psi) \quad (A.212)$$

The terms u* and w* are now determined from equations A.211 and A.212 for the next time step, where u* and w* at the old time are set equal to u' and w' at the old time. The solution of equations A.209 and A.210 to give u' and w' at the new time step is given in Appendix Section A.3.

Section A.3: Solution of the Equations of Motion

When dealing with a non-hydrostatic model, the pressure and velocity are interdependent. Neumann and Mahrer therefore solved the equations of motion as follows.

The approximate velocities u* and w* were found as shown in Appendix Section A.2. The difference between the true velocities u' and w' for the next time step and these approximate velocities are the non-hydrostatic pressure p* terms. Equations A.209 and A.210 are rewritten (at the new time) as:

$$u' = u^* - \frac{\Delta t}{\rho}\frac{\partial p^*}{\partial x} \quad , \qquad w' = w^* - \frac{\Delta t}{\rho}\frac{\partial p^*}{\partial z} \qquad \text{(A.31, A.32)}$$

where Δt is the time step interval. In other words, u* and w* represent all of the rest of the terms in the equations of motion (A.205 and A.208).

The above equations are differentiated and combined with the continuity equation (2.13) to give:

$$\frac{\partial u^*}{\partial x} + \frac{\partial w^*}{\partial z} = \frac{\Delta t}{\rho}\left[\frac{\partial^2 p^*}{\partial x^2} + \frac{\partial^2 p^*}{\partial z^2}\right] \qquad \text{(A.33)}$$

This diagnostic balance equation thus gives the non-hydrostatic pressure, p*, in terms of the approximate velocities while demanding that the new velocities, u' and w', satisfy the continuity equation. This equation is solved for p*, using the accelerated Liebmann method (see Miyakoda, 1960). The form used is:

$$p^*(m+1) = p^*(m) + \frac{2(1+\lambda)}{\frac{1}{\Delta x^2} + \frac{1}{\Delta z^2}}\left[\frac{\partial^2 p^*(m)}{\partial z^2} + \frac{\partial^2 p^*(m)}{\partial x^2}\right] - 4\rho\,\frac{\Delta z^2}{\Delta t}\left(\frac{\partial u^*}{\partial x} + \frac{\partial w^*}{\partial z}\right) \qquad \text{(A.34}$$

where m is the iteration number, λ is the over-relaxation coefficient, and Δx and Δz are the grid spacings. In finite difference form, this is:

$$\begin{aligned} p^{*m+1}(i,j) = {} & p^{*m}(i,j) + \frac{1+\lambda}{2(\Delta x^2 + \Delta z^2)}\{\Delta x^2[p^{*m}(i,j+2) + p^{*m+1}(i,j-2)] \\ & + \Delta z^2[p^{*m}(i+2,j) + p^{*m+1}(i-2,j)] - 2[\Delta x^2 + \Delta z^2]p^{*m}(i,j)\} \\ & - \frac{2\rho\Delta z}{\Delta t\Delta x}\{\Delta x[w^*(i,j+1) - w^*(i,j-1)] + \Delta z[u^*(i+1,j) \\ & - u^*(i-1,j)]\} \qquad \text{(A.35)} \end{aligned}$$

where i and j are indices in the x and z directions, respectively. The term $p^{*(m\,=\,0)}$ is the non-hydrostatic pressure from the previous time step. Air density, ρ, is determined by the equation of state:

$$\rho = \frac{p_o(i,j) + p_h(i,j) + p^*(i,j)}{RT(i,j)} \qquad (A.36)$$

where p_o is the initial pressure and p_h is the change in hydrostatic pressure from the initial pressure. The last term in parentheses is determined prior to iteration using the old p* to determine ρ. The equation is iterated until the first term in parentheses is sufficiently small. The number of iterations per time step is typically 30 for the coarse mesh model and 45 for the fine mesh model.

Once p* is determined for the new time step, u' and w' are found using equations A.31 and A.32. This process imposes the incompressibility condition (equation 2.13) on the pressure field.

To make convergence more rapid, the sum of horizontal divergence in a vertical column is first set equal to zero:

$$\sum_{z=0}^{z=h} \frac{\partial u}{\partial x} = 0 \qquad (A.37)$$

The term u is adjusted by changing the horizontal hydrostatic pressure gradient such that:

$$\frac{\partial \bar{u}}{\partial x}(\text{new}) = \frac{\partial \bar{u}}{\partial x}(\text{old}) - \frac{\Delta t}{\rho} \frac{\partial^2 \bar{p}''}{\partial x} = 0 \qquad (A.38)$$

where the bar indicates a vertical average over the model and p" is the change in hydrostatic pressure needed to accomplish the change in u.

APPENDIX B

Supplementary Data

Table B.1

Initial Winds Used in Model (m/sec)

Height (m)	30 June		17 July		7 September	
	u_o	v_o	u_o	v_o	u_o	v_o
0	0	0	0	0	0	0
50	3.5	-2.0	0.6	2.5	2.9	-1.2
150	4.0	-2.8	1.1	3.9	3.1	-1.6
250	4.2	-3.6	1.4	5.2	3.3	-2.1
350	4.6	-4.4	1.7	5.3	3.4	-2.7
450	5.1	-5.2	1.6	4.5	3.0	-3.4
550	5.1	-5.5	1.6	4.0	2.5	-5.2
650	5.3	-5.5	1.5	3.6	2.1	-6.8
750	5.5	-5.5	1.6	3.0	2.4	-7.3
850	5.8	-5.8	1.9	2.3	2.8	-7.7
950	6.0	-6.4	2.0	1.6	3.2	-8.0
1050	5.8	-6.4	1.9	1.5	4.4	-7.8
1150	5.7	-6.4	1.8	1.3	5.5	-7.6
1250	5.4	-6.0	1.7	0.9	6.7	-7.4
1350	5.2	-5.8	1.5	0.9	7.5	-7.7
1450	5.2	-5.6	1.3	0.7	8.3	-8.1
1550	5.2	-5.4	1.2	0.6	9.1	-8.5
1650	5.2	-5.0	1.0	0.1	9.8	-8.6
1750	5.2	-4.6	1.0	-0.8	10.5	-8.6
1850	5.2	-4.4	1.1	-1.1	11.1	-8.6
1950	5.2	-4.4	1.1	-1.1	11.1	-8.6

Table B.2

Lyons' Moisture Data

These data are derived from unpublished data taken with an airplane over Chicago on 13 August 1967. Supplementary data taken on this same day were published by Lyons and Olsson (1973). The pressure column is derived from the hydrostatic equation, assuming that the pressure at 1700 m is 825 mb throughout the area. The pressure is at the bottom of the interval indicated, and the temperatures are the average over the 100 m interval. The distances are from the coast: 22 km (inland) is 2 km ahead of the front; 17 km is 3 km gehind the front; and -10 km is offshore.

	Temperature			Virtual Temperature			Pressure from Temperature			Pressure from Virtual Temperature		
Height (m)	22 km	17 km	-10 km	22 km	17 km	-10 km	22 km	17 km	-10 km	22 km	17 km	-10 km
1700	283.0	283.0	283.0	283.3	283.3	283.3	835.01	835.01	835.01	835.00	835.00	835.00
1600	283.4	283.5	283.6	283.8	284.0	284.0	845.14	845.13	845.13	845.11	845.10	845.10
1500	284.1	284.1	284.2	284.6	284.7	284.7	855.36	855.35	855.34	855.31	855.30	855.30
1400	284.7	284.7	284.7	285.3	285.4	285.3	865.68	865.67	867.67	865.61	865.60	865.60
1300	285.3	285.4	285.5	286.0	286.2	286.2	876.10	876.09	876.08	876.01	875.98	875.99
1200	286.1	286.2	286.4	286.9	287.1	287.3	886.62	886.61	886.59	886.50	886.47	886.46
1100	286.9	287.1	287.3	287.8	288.1	288.2	897.23	897.22	897.19	897.08	897.03	897.03
1000	287.8	288.1	288.3	288.7	289.3	289.3	907.94	907.91	907.88	907.75	907.69	907.68
900	288.7	289.1	289.2	289.6	290.3	290.2	918.75	918.70	918.66	918.52	918.42	918.42
800	289.8	290.1	290.2	290.7	291.4	291.3	929.63	929.58	929.53	929.37	929.25	929.25
700	290.9	291.1	291.1	291.8	292.4	292.2	940.61	940.55	940.50	940.31	940.17	940.17
600	292.0	292.1	292.0	292.9	293.4	293.0	951.67	951.60	951.57	951.33	951.17	951.19
500	293.1	293.2	292.0	294.0	294.5	293.0	962.83	962.75	962.76	962.45	962.26	962.34
400	294.3	294.2	292.3	295.3	295.5	293.2	974.06	973.99	974.07	973.64	973.45	973.62
300	295.4	295.3	293.1	296.5	296.7	294.1	985.39	935.32	985.49	984.92	984.72	984.99
200	296.9	296.7	293.3	298.1	298.1	294.6	996.79	996.72	997.03	996.27	996.06	996.47
100	298.6	239.2	293.6	299.8	299.7	295.3	1008.25	1008.20	1008.69	1007.68	1007.47	1008.06

APPENDIX C

Boundary Layer Instrument System

The Boundary Layer Instrument System (BLIS) was developed at the University of Wisconsin-Madison Space Science and Engineering Center to measure the three wind vectors, plus pressure, temperature and humidity while suspended on a balloon-borne tether line. It transmits a full set of data every 4 seconds to a ground receiver, where the data are recorded. The three sensors used in this study are described below and summarized in Table C.1. The other sensors, the telemetry and the data logic are described by Burns (1975).

Wind speed is measured with a three-cup anemometer coupled to an optically revolving disc, producing a pulse output every two degrees of rotation. The anemometer was calibrated by mounting the BLIS package ahead of and above a car which was then driven at constant speed around a measured indoor track. The BLIS output was averaged over a timed interval of several track laps. This procedure was repeated several times at several speeds to develop a sound statistical base for calibration. The result was a linear calibration curve, for which 1 m/sec corresponded to 32.2 ± 0.6 output pulses (counts).

Temperature was measured by an oscillator-coupled thermistor, shielded from direct and reflected solar radiation. Eight calibration points (obtained in a large oven checked for temperature gradients) were fitted to a quadratic polynomial spline (Berman, 1974).

Pressure was measured by an aneroid capsule with an attached capacitive transducer coupled to an oscillator. Since the aneroid was temperature sensitive, it was thermally insulated and its temperature monitored by a thermistor. Figure C.1 shows a typical BLIS output, giving air temperature (left scale), relative pressure (right scale) and aneroid temperature (similar to left scale, but several degrees higher). The slow change in aneroid temperature indicates that the rapid pressure fluctuations are due to actual turbulence rather than to air temperature fluctuations affecting the aneroid. The reason for the large aneroid temperature change is that the instrument was transported in a warm car. Thermal lag caused the temperature to continue to rise after removal of the instrument from the car before falling to the outside ambient temperature.

The aneroid was calibrated in a vacuum chamber. The result is not linear over 100 mb, but is essentially linear over the 3 mb range encountered in the test cases. A separate slope was calculated for each of the three test cases, based on the atmospheric pressure of the days involved. Temperature dependence was determined in a well vented oven while the atmospheric pressure was monitored outside the oven. The result was linear, so a correction was easily made to the case study data.

We also examined whether the aneroid acted like a pressure tube and responded to changes in wind speed. Figure C.2 is a typical detail of wind speed and pressure, showing that the aneroid does not respond directly to changes in wind speed. (The relative pressure scale can be found by dividing the temperature scale by three.)

The BLIS instrument package (Figure C.3) was mounted 1.34 m over the roof of a car (a total of 2.74 m above the ground). The large antenna was used to maximize the signal received from the instrument package, since no pre-amplifier was available for use in this experiment. A receiver in the car picked up the digital signal and sent it to an interface where the voltages were changed to audible tones which were then recorded on a standard tape recorder. All equipment was powered by the car battery, through an inverter.

Back in the laboratory in Madison, the tape was played back through the interface toa ground station where the signal was converted into decimal data representing the various sensor outputs. This data was then punched on a paper tape and fed into a computer for analysis.

Table C.1

Sensor Performance

Parameters	Absolute Accuracy	Relative Accuracy	Range
Wind Speed	0.5 m/sec	0.027 m/sec	0.5 to 25 m/sec
Temperature	within 0.1°C	within 0.03°C	0 to 50°C
Pressure	0.5 mb	within 0.05 mb	850 to 1040 mb

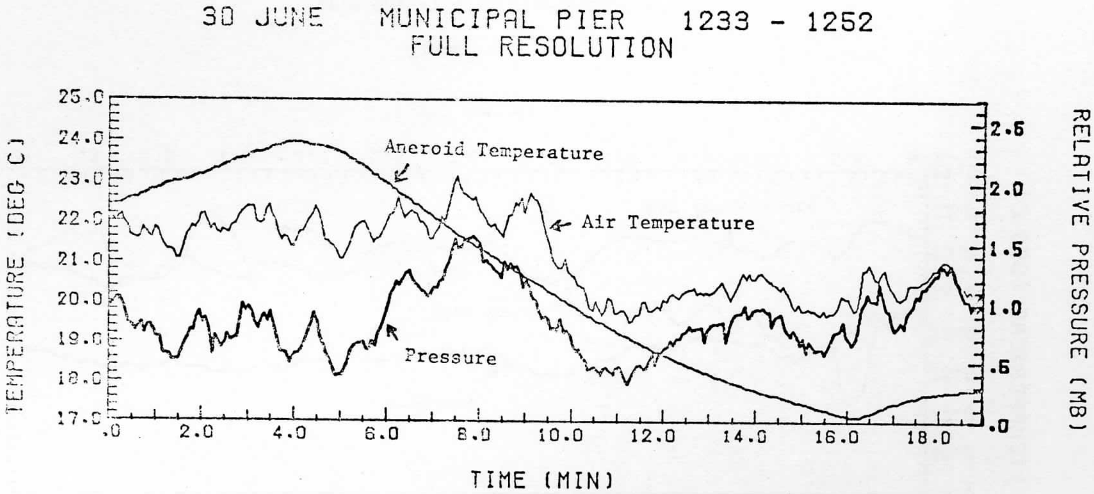

FIGURE C.1

BLIS Detail with Aneroid Temperature

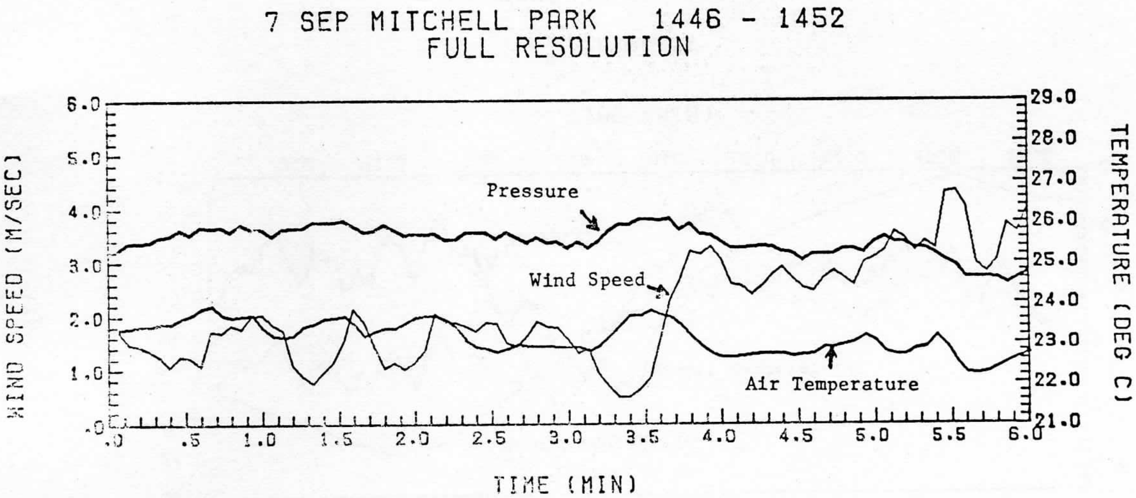

FIGURE C.2

BLIS Detail with Wind Speed

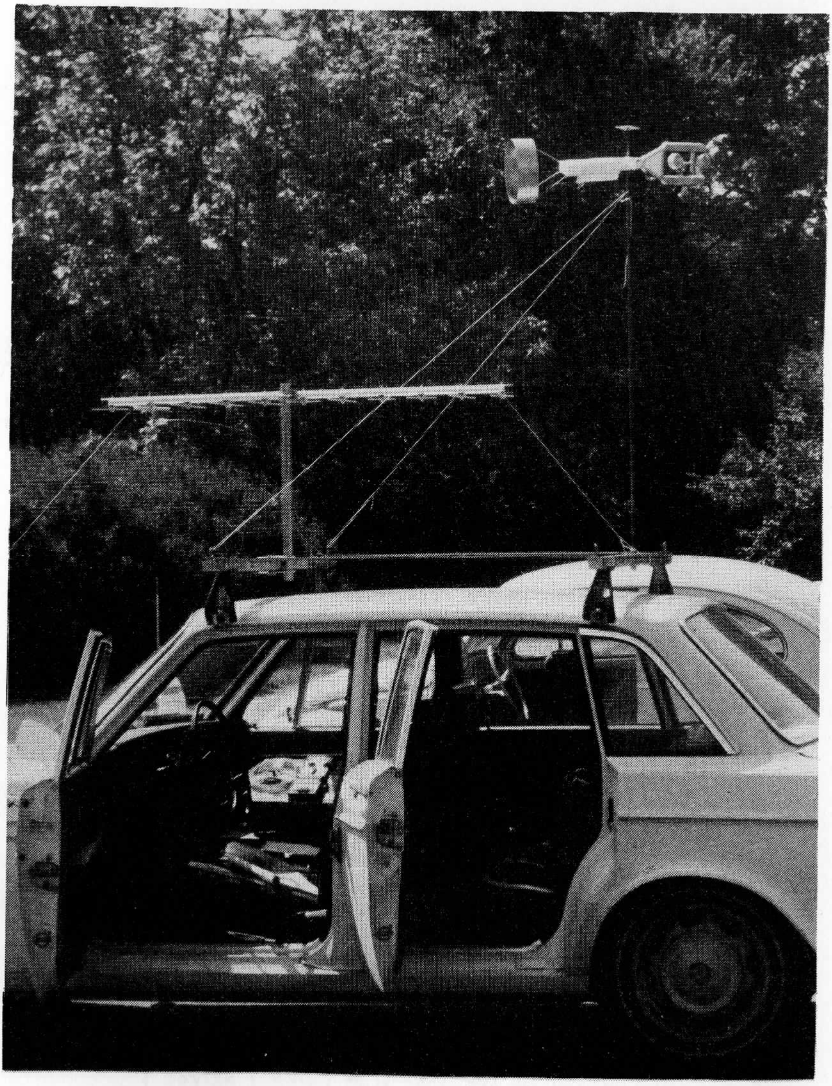

FIGURE C.3

BLIS Setup

APPENDIX D

Computer Program Listing

```
@FOR,SIZ SEABREEZE
C
C        NEUMANN AND MAHRER NON-HYDROSTATIC SEA BREEZE MODEL
C        MODIFIED BY ALFRED STAMM  1975
C
C        I1 = MAXIMUM LATERAL GRIDS
C        I2 = MAXIMUM VERTICAL GRIDS
C
      PARAMETER I1=141,I2=21
      DIMENSION B1(I1),B2(I1),C(I1),D(I1),Z(I1),ZK(26,I1),ZR(26,I1)
      DIMENSION PL(I2),TL(I2),TEL(I2),VO(I2),UO(I2),ITERP(0800),RJ(I1)
      DIMENSION TR(I1,3),U2(I1,3),IPR(26),IA(30)
      DIMENSION Q(I1,I2),P(I1,I2),P1(I1,I2),T(I1,I2),TF(I1,I2),TE1(I1,I2
     *),U(I1,I2),U1(I1,I2),V(I1,I2),V1(I1,I2),W(I1,I2),W1(I1,I2)
      REAL LAMDA,LRATE
C
C        REQUEST 66 LINES PER PAGE
C
      CALL URPRTM (0,0)
C
C        DIMENSIONS
C
C        L = LATERAL GRIDS IN MODEL
C        M = VERTICAL GRIDS IN MODEL
C        L1 = L - 1
C        M1 = M - 1
C        L2 = L - 2
C        M2 = M - 2
C
      L=I1
      M=I2
      L1=L-1
      M1=M-1
      L2=L-2
      M2=M-2
C
C        CONSTANTS
C
C        ALAMDA = OVER-RELAXATION COEFFICIENT ( DEPENDENT ON L AND M )
C        CP = SPECIFIC HEAT OF AIR AT CONSTANT PRESSURE
C        DT = INTEGRATION TIME STEP SIZE ( SECONDS )
C        DX = LATERAL DIMENSION STEP SIZE ( METERS )
C        DZ = VERTICAL DIMENSION STEP SIZE ( METERS )
C        EPS = CONVERGENCE VALUE
C        F = CORIOLIS PARAMETER ( SIN )
C        FC = CORIOLIS PARAMETER ( COS )
C        G = ACCELERATION OF GRAVITY ( METERS / SECONDS**2 )
C        H = HEIGHT OF CONSTANT FLUX LAYER ( METERS )
C        HTRAN = HEIGHT OF TRANSITION LAYER ( METERS )
```

```
C        HTOT = TOTAL HEIGHT ( METERS )
C        HOUR = HOUR ( HOURS )
C        IDAY = DAY NUMBER (DAYS )
C        ITER = ITFRATION STEP
C        ITMAX = ITERATION LIMIT
C        KOUNT = NUMBER OF TIME STEPS
C        LRATE = LAPSE RATE ( DEGREES KELVIN PER METER )
C        O = HOUR 7 IN LOCAL DAYLIGHT TIME ( HOURS )
C        PI = PI
C        PO = INITIAL SURFACE PRESSURE ( MILLIBARS )
C        R = GAS CONSTANT ( METERS**2 / SECONDS**2 / DEGREE )
C        ROEBAR = AVERAGE DENSITY ( GRAMS / CENTIMETER**3 )
C        RPD = RADIANS PER DEGREE
C        PSI = ANGLE BETWEEN DUE NORTH AND SHORELINE ( DEGREES )
C        TC = KELVIN - CENTIGRATE CONVERSION CONSTANT
C        TIME = SEVEN HOURS PAST VALUE OF HOUR ( HOURS )
C        TIMLIM = HOURS TO RUN INTEGRATION ( HOURS )
C        TO = INITIAL SURFACE TEMPERATURE ( CENTIGRADE )
C        VK = VON KARMANS CONSTANT
C        ZO = ROUGHNESS PARAMETER ( METERS )
C        NUM = OUTPUT COUNTER ( EVERY NUM TIME STEPS )
C        ISTOP = 1 IF ITMAX IS EXCEEDED
C        ITOV = ITERATION OVERFLOW COUNT
C        ITOVER = NUMBER OF ITERATION OVERFLOWS
C        IPT = PRINTOUT NUMBER
C
      ALAMDA=.78
      CP=1004.
      DT=60.
      DX=1000.
      DZ=100.
      EPS=1.E-7
      F=1.E-4
      FC=1.06E-4
      G=9.8
      H=50.
      HTRAN=FLOAT(M-2)*DZ
      HTOT=H+HTRAN
      HOUR=0.
      IDAY=1
      ITER=0
      ITMAX=200
      KOUNT=-1
      LRATE=.0065
      O=7.
      PI=3.141592
      PO=1000.
      R=287.
      ROEBAR=1.E-3
      RPD=PI/180.
      PSI=-8.*RPD
      TC=273.16
      TIME=0.
      TIMLIM=12.95
      TO=18.
      VK=.4
```

```
      ZO=2.E-2
      NUM=-1
      ISTOP=0
      ITOV=0
      ITOVER=0
      IPT=0
C
C        COMBINED TERMS
C
C        DT2 = 2. * DT
C        DX2 = 2. * DX
C        DZ2 = 2. * DZ
C        DTQ = DT ** 2
C        DXQ = DX ** 2
C        DZQ = DZ ** 2
C        DTDX = DT / DX
C        DTDZ = DT / DZ
C        DZQDXQ = DZQ / DXQ
C        HPDZ = H + DZ
C        HPZO = H + ZO
C        FDT = F * DT
C        FCDT = FC * DT
C        RDT = R * DT
C
      DT2=2.*DT
      DX2=2.*DX
      DZ2=2.*DZ
      DTQ=DT**2
      DXQ=DX**2
      DZQ=DZ**2
      DTDX=DT/DX
      DTDZ=DT/DZ
      DZQDXQ=DZQ/DXQ
      HPDZ=H+DZ
      HPZO=H+ZO
      FDT=F*DT
      FCDT=FC*DT
      RDT=R*DT
C
C        ARRAYS
C
C        B1 = TERM NEEDED TO COMPUTE HORIZONTAL DIVERGENCE
C        B2 = PRESSURE CORRECTION FOR HORIZONTAL DIVERGENCE
C        C = TERM NEEDED TO COMPUTE HORIZONTAL DIVERGENCE
C        D = TERM NEEDED TO COMPUTE HORIZONTAL DIVERGENCE
C        TL = INITIAL TEMPERATURE PROFILE IN DEGREES KELVIN
C        PL = INITIAL PRESSURE DISTRIBUTION IN MILLIBARS
C        TEL = INITIAL POTENTIAL TEMPERATURE PROFILE
C        TR = TOTAL POTENTIAL TEMPERATURE
C        U2 = ABSOLUTE VELOCITY AT TOP OF CONSTANT FLUX LAYER
C        Q = DIVERGENCE - PRESSURE INTERMEDIATE RESULT
C        P = HYDROSTATIC DISTURBANCE PRESSURE
C        P1 = NON-HYDROSTATIC DISTURBANCE PRESSURE ( INSTANTANEOUS DEVIATION )
C        T = TEMPERATURE
C        TE = DISTURBANCE POTENTIAL TEMPERATURE
C        TE1 = HOLD TE
```

```
C       U = ACROSS SHORE VELOCITY
C       U1 = HOLD U
C       V = ALONG SHORE VELOCITY
C       V1 = HOLD V
C       W = VERTICAL VELOCITY
C       W1 = HOLD W
C       UO = INITIAL ACROSS SHORE VELOCITY ( METERS PER SECOND )
C       VO = INITIAL ALONG SHORE VELOCITY ( METERS PER SECOND )
C       Z = EDDY DIFFUSIVITY
C       IPR = PUNCH OUTPUT
C       IA = PRINT OUTPUT
C       ITERP = NUMBER OF ITERATIONS PER TIME STEP
C       ZK = EDDY DIFFUSIVITY PRINTOUT
C       RJ = RICHARDSON NUMBER
C       ZR = RICHARDSON NUMBER PRINTOUT
C
      B1(1)=0.
      B2(1)=0.
      C(1)=0.
      D(1)=0.
      DO 1 I=2,L
      B1(I)=0.
      B2(I)=0.
      C(I)=1./(2.-C(I-1))
    1 D(I)=0.
      TL(1)=TO+TC
      PL(1)=PO
      TEL(1)=TL(1)*(1000./PL(1))**(R/CP)
      DO 2 J=2,M
      HT=DZ
      IF (J.EQ.2) HT=H
      TL(J)=TL(J-1)-LRATE*HT
      PL(J)=PL(1)*(TL(J)/TL(1))**(G/(R*LRATE))
    2 TEL(J)=TL(J)*(1000./PL(J))**(R/CP)
      DO 3 I=1,L
      DO 3 J=1,3
      TR(I,J)=0.
    3 U2(I,J)=0.
      DO 4 I=1,L
      DO 4 J=1,M
      Q(I,J)=0.
      P(I,J)=0.
      P1(I,J)=0.
      T(I,J)=TL(J)
      TE(I,J)=0.
      TE1(I,J)=0.
      U(I,J)=0.
      U1(I,J)=0.
      V(I,J)=0.
      V1(I,J)=0.
      W(I,J)=0.
    4 W1(I,J)=0.
C
C     READ IN INITIAL WINDS
C
      READ 122,(UO(I),I=1,20)
```

```
      READ 122,(VO(I),I=1,20)
      DO 70 J=20,I2
      UO(J)=UO(20)
   70 VO(J)=VO(20)
C
C         EDDY CALCULATION TERMS
C
C         ALPHA = NON-DIMENSIONAL CONSTANT USED IN COMPUTING EDDY TERMS
C         BCON = TERM USED FOR FORCED CONVECTION
C         BETA = TERM USED FOR FORCED CONVECTION
C         HTERM = HEIGHT TERM USED IN COMPUTING EDDY TERMS
C         LAMDA = NON-DIMENSIONAL CONSTANT USED IN COMPUTING EDDY TERMS
C         RCON = TERM USED FOR FREE CONVECTION
C         RTERM = TERM USED FOR FREE CONVECTION
C         RICUT = RICHARDSON NUMBER CUTOFF
C         TEBR = AVERAGE POTENTIAL TEMPERATURE OF CONSTANT FLUX LAYER
C
      ALPHA=-.03
      BCON=0.
      BETA=0.
      HTERM=(HTOT-HPDZ)/(HTOT-H)+1.
      LAMDA=1.
      RCON=1./(DZ*HPZO**(-4./3.)-3.*(HPZO**(-1./3.)-ZO**(-1./3.)))
      RTERM=HPZO**(4./3.)
      RICUT=-.03
      TEBR=(TEL(1)+TEL(2))/2.
C
C         HORIZONTAL DIVERGENCE TERMS
C
      S1=1.25
      S2=FLOAT(L-3)+.25
C
C         OUTPUT FORMATS
C
  101 FORMAT ('1INITIAL PRESSURE FIELD',/)
  102 FORMAT ('0')
  103 FORMAT (15F8.1)
  104 FORMAT (30I4)
  105 FORMAT ('0INITIAL POTENTIAL TEMPERATURE FIELD',/)
  106 FORMAT (' HYDROSTSTIC DISTURBANCE PRESSURE IN .01 MB',/)
  107 FORMAT (' NON-HYDROSTATIC DISTURBANCE PRESSURE IN .01 MB',/)
  108 FORMAT (' TEMPERATURE IN .1 DEG C',/)
  109 FORMAT (' VELOCITY ACROSS SHORE IN .01 M/SEC',/)
  110 FORMAT (' VELOCITY ALONG SHORE IN .01 M/SEC',/)
  111 FORMAT (' VERTICAL VELOCITY IN .001 M/SEC',/)
  112 FORMAT ('0INITIAL TEMPERATURE FIELD',/)
  113 FORMAT (' DISTURBANCE POTENTIAL TEMPERATURE IN .1 DEG K',/)
  114 FORMAT ('1DAY =',I4,6X,'TIME =',F6.2)
  115 FORMAT (26I3)
  116 FORMAT (29I4)
  117 FORMAT ('0TIME STEP =',I6,/)
  118 FORMAT (' -70 -65 -60 -55 -50 -45 -40 -35 -30 -25 -20 -15 -10  -5
     *  0   5  10  15  20  25  30  35  40  45  50  55  60  65  70')
  119 FORMAT (' -50*-49*-48*-47*-46*-45*-44*-43*-42*-41*-40*-39*-38*-37*
     *-36*-35*-34*-33*-32*-31*-30*-29*-28*-27*-26*-25*-24*-23*-22*-21')
  120 FORMAT (' -20*-19*-18*-17*-16*-15*-14*-13*-12*-11*-10**-9**-8*-7**
```

```
     **-6**-5**-4**-3**-2**-1***0***1***2***3***4***5***6***7***8***9')
  121 FORMAT (20I6)
  122 FORMAT (20F4.1)
  123 FORMAT (' DIVERGENCE IN .00001 /SEC',/)
  124 FORMAT (' FINAL ITERATION =',I6,/)
  125 FORMAT (' ITERATION OVERFLOW =',I5,/)
  126 FORMAT (13E9.4)
C
C        OUTPUT INITIAL PARAMETERS
C
      PRINT 101
      PRINT 103,PL
      PRINT 112
      PRINT 103,TL
      PRINT 105
      PRINT 103,TEL
      GO TO 38
C
C        OUTPUT PARAMETERS
C
   50 NUM=0
      PRINT 114,IDAY,TIME
      PRINT 106
      DO 83 N=1,8
      PRINT 118
      DO 82 K=1,3
      DO 81 J=20,1
      IN=30
      IF (K.EQ.1) IN=29
      DO 80 II=1,IN
      IF (K.EQ.1) I=5*II-4
      IF (K.EQ.2) I=II+20
      IF (K.EQ.3) I=II+50
      IF (N.EQ.1) IA(II)=P(I,J)*100
      IF (N.EQ.2) IA(II)=P1(I,J)*100
      IF (N.EQ.3) IA(II)=(T(I,J)-TC)*10
      IF (N.EQ.4) IA(II)=TE(I,J)*10
      IF (N.EQ.5) IA(II)=(U(I,J)+UO(J))*100
      IF (N.EQ.6) IA(II)=(V(I,J)+VO(J))*100
      IF (N.EQ.7) IA(II)=W(I,J)*1000
      IF (N.EQ.8) Q(I,J)=Q(I,J)*RDT/4./DZQ*T(I,J)/(PL(J)+P(I,J)+P1(I,J))
   80 IF (N.EQ.8) IA(II)=Q(I,J)*100000
      IF (K.GE.2) PRINT 104,IA
   81 IF (K.EQ.1) PRINT 116,(IA(JJ),JJ=1,29)
      IF (K.EQ.1) PRINT 119
   82 IF (K.EQ.2) PRINT 120
      IF (N.LE.7) PRINT 114,IDAY,TIME
      IF (N.EQ.1) PRINT 107
      IF (N.EQ.2) PRINT 108
      IF (N.EQ.3) PRINT 113
      IF (N.EQ.4) PRINT 109
      IF (N.EQ.5) PRINT 110
      IF (N.EQ.6) PRINT 111
   83 IF (N.EQ.7) PRINT 123
      IPT=IPT+1
C
```

```
C        STORE EDDY DIFFUSIVITY AND RICHARDSON NUMBER FOR LATER PRINTOUT
C
      DO 72 I=1,L
      ZR(IPT,I)=RJ(I)
   72 ZK(IPT,I)=Z(I)
      IF (ISTOP.EQ.1) STOP 2
      GO TO 41
C
C        BEGIN TIME INTEGRATION LOOP
C
   38 KOUNT=KOUNT+1
      NUM=NUM+1
      HOUR=FLOAT(KOUNT)*DT/3600.
      IF(HOUR.GT.TIMLIM) GO TO 61
      TIME=HOUR+0
      IDAY=1
   39 IF(TIME.LT.24.) GO TO 40
      TIME=TIME-24.
      IDAY=IDAY+1
      GO TO 39
C
C        CHECK TO SEE IF OUTPUT IS REQUIRED
C
   40 IF (NUM.GE.30) GO TO 50
C
C        COMPUTE ABSOLUTE VELOCITY AND TOTAL POTENTIAL TEMPERATURE
C        IN BOUNDARY LAYER
C
   41 DO 5 I=1,L
      DO 5 J=1,3
      U2(I,J)=SQRT((U(I,J)+UO(J))**2+(V(I,J)+VO(J))**2)+1.E-5
    5 TR(I,J)=TE(I,J)+TEL(J)
C
C        COMPUTE EDDY TERMS AND ADJUST ABSOLUTE VELOCITY AND TOTAL
C        POTENTIAL TEMPERATURE AT TOP OF CONSTANT FLUX LAYER
C
C        SET BCON IF HOUR GT 1
C
      IF (HOUR.GT.1.)BCON=-ALPHA*G
      DO 8 I=1,L
C
C        COMPUTE RICHARDSON NUMBER
C
      RI=G*HPDZ*(TR(I,3)-TR(I,1))/(TEBR*U2(I,3)**2)
      RJ(I)=RI
C
C        CHECK RICHARDSON NUMBER SIZE FOR BRANCHING
C
      IF (RI.GT.RICUT) GO TO 6
C
C        FREE CONVECTION
C
      Z(I)=LAMDA*SQRT(G*RCON*(TR(I,1)-TR(I,3))/TEBR)*HPZO**(4./3.)
      U2(I,2)=U2(I,3)-DZ2*RCON*U2(I,3)/(HTERM*RTERM)
      TR(I,2)=TR(I,3)-DZ2*RCON*(TR(1,3)-TR(I,1))/(HTERM*RTERM)
      GO TO 7
```

```
C
C        FORCED CONVECTION
C
    6 BETA=VK*HPZO/(DZ+HPZO*ALOG(HPZO/ZO))*(1.-(BCON*HPDZ*(TR(I,3)-TR(I,
     11)))/(TEBR*U2(I,3)**2))
      Z(I)=BETA*U2(I,3)/(1./(VK*HPZO)+BCON*(TR(I,3)-TR(I,1))/(TEBR*BETA*
     1U2(I,3)**2))
      U2(I,2)=U2(I,3)-DZ2*BETA**2*U2(I,3)**2/(HTERM*Z(I))
      TR(I,2)=TR(I,3)-DZ2*BETA**2*U2(I,3)*(TR(I,3)-TR(I,1))/(HTERM*Z(I))
C
C        ADJUST U,V AND TE AT TOP OF CONSTANT FLUX LAYER
C
    7 U(I,2)=U2(I,2)/U2(I,3)*U(I,3)
      V(I,2)=U2(I,2)/U2(I,3)*V(I,3)
      TE(I,2)=TR(I,2)-TEL(2)
C
C        HOLD TE
C
    8 TE1(I,2)=TE(I,2)
C
C        SMOOTH VELOCITY COMPONENTS U,V AND W AND HOLD
C
      DO 9 I=2,L1
      DO 9 J=2,M1
      U1(I,J)=.5*U(I,J)+.25*(U(I+1,J)+U(I-1,J))
      V1(I,J)=.5*V(I,J)+.25*(V(I+1,J)+V(I-1,J))
    9 W1(I,J)=.5*W(I,J)+.25*(W(I+1,J)+W(I-1,J))
C
C        SET BOUNDARIES OF U, V, AND TE AND HOLD
C
      DO 10 J=2,M1
      U1(1,J)=U1(2,J)
      U1(L,J)=U1(L1,J)
      V1(1,J)=V1(2,J)
      V1(L,J)=V1(L1,J)
      TE1(1,J)=TE1(2,J)
   10 TE1(L,J)=TE1(L1,J)
C
C        COMPUTE TEMPERATURE AND HYDROSTATIC DISTURBENCE PRESSURE FROM TOP D
C
      THICK=DZ
      DO 11 J=1,M1
      N=M-J
      IF (N.EQ.1) THICK=H
      DO 11 I=1,L
      T(I,N)=(TE(I,N)+TEL(N))*((PL(N)+P(I,N)+P1(I,N))/1000.)**(R/CP)
   11 P(I,N)=(G*THICK/R*(PL(N)/TL(N)-PL(N)/T(I,N))-P(I,N+1))/(G*THICK/(R
     1*T(I,N))-1.)
C
C        APPLY CONTINUITY EQUATION AT TOP OF CONSTANT FLUX LAYER TO SOLVE FO
C
      DO 12 I=2,L1
      W(I,2)=-DZ*(U(I+1,2)-U(I-1,2))/(8.*DX)
C
C        HOLD W
C
```

```
   12 W1(I,2)=W(I,2)
C
C        FIND NEW VALUES FOR U, V, W, AND TE USING THE THREE EQUATIONS OF
C        MOTION AND THE HEAT CONDUCTION EQUATION
C
      DO 16 I=2,L1
      DO 16 J=3,M1
      U(I,J)=U1(I,J)
     1-RDT*T(I,J)*(P(I+1,J)-P(I-1,J))/(DX2*(PL(J)+P(I,J)+P1(I,J)))
     2+DT/DZQ*(U1(I,J+1)+UO(J+1)+U1(I,J-1)+UO(J-1)-2.*U1(I,J)-2.*UO(J))
     3*FLOAT(M-J)*Z(I)*DZ/HTRAN-Z(I)*DT*(U1(I,J+1)+UO(J+1)-U1(I,J-1)
     4-UO(J-1))/(DZ2*HTRAN)
      V(I,J)=V1(I,J)
     1+DT/DZQ*(V1(I,J+1)+VO(J+1)+V1(I,J-1)+VO(J-1)-2.*V1(I,J)-2.*VO(J))
     2*FLOAT(M-J)*Z(I)*DZ/HTRAN-Z(I)*DT*(V1(I,J+1)+VO(J+1)-V1(I,J-1)
     3-VO(J-1))/(DZ2*HTRAN)
      W(I,J)=W1(I,J)
      TE(I,J)=TE1(I,J)
     1+DT/DZQ*(TE1(I,J+1)+TEL(J+1)+TE1(I,J-1)+TEL(J-1)-2.*(TE1(I,J)+TEL(
     2J)))*FLOAT(M-J)*Z(I)*DZ/HTRAN
     3-Z(I)*DT*(TE1(I,J+1)+TEL(J+1)-TE1(I,J-1)-TEL(J-1))/(DZ2*HTRAN)
C
C        VERTICAL ADVECTION TERMS
C
      IF(W(I,J).GT.0.) GO TO 13
      U(I,J)=U(I,J)-DTDZ*W1(I,J)*(U1(I,J+1)+UO(J+1)-U1(I,J)-UO(J))
      V(I,J)=V(I,J)-DTDZ*W1(I,J)*(V1(I,J+1)+VO(J+1)-V1(I,J)-VO(J))
      W(I,J)=W(I,J)-DTDZ*W1(I,J)*(W1(I,J+1)-W1(I,J))
      TE(I,J)=TE(I,J)-DTDZ*W1(I,J)*(TE1(I,J+1)+TEL(J+1)-TE1(I,J)-TEL(J))
      GO TO 14
   13 U(I,J)=U(I,J)-DTDZ*W1(I,J)*(U1(I,J)+UO(J)-U1(I,J-1)-UO(J-1))
      V(I,J)=V(I,J)-DTDZ*W1(I,J)*(V1(I,J)+VO(J)-V1(I,J-1)-VO(J-1))
      W(I,J)=W(I,J)-DTDZ*W1(I,J)*(W1(I,J)-W1(I,J-1))
      TE(I,J)=TE(I,J)-DTDZ*W1(I,J)*(TE1(I,J)+TEL(J)-TE1(I,J-1)-TEL(J-1))
C
C        HORIZONTAL ADVECTION TERMS
C
   14 IF ((U1(I,J)+UO(J)).GT.0.) GO TO 15
      U(I,J)=U(I,J)-DTDX*(U1(I,J)+UO(J))*(U1(I+1,J)-U1(I,J))
      V(I,J)=V(I,J)-DTDX*(U1(I,J)+UO(J))*(V1(I+1,J)-V1(I,J))
      W(I,J)=W(I,J)-DTDX*(U1(I,J)+UO(J))*(W1(I+1,J)-W1(I,J))
      TE(I,J)=TE(I,J)-DTDX*(U1(I,J)+UO(J))*(TE1(I+1,J)-TE1(I,J))
      GO TO 16
   15 U(I,J)=U(I,J)-DTDX*(U1(I,J)+UO(J))*(U1(I,J)-U1(I-1,J))
      V(I,J)=V(I,J)-DTDX*(U1(I,J)+UO(J))*(V1(I,J)-V1(I-1,J))
      W(I,J)=W(I,J)-DTDX*(U1(I,J)+UO(J))*(W1(I,J)-W1(I-1,J))
      TE(I,J)=TE(I,J)-DTDX*(U1(I,J)+UO(J))*(TE1(I,J)-TE1(I-1,J))
C
C        CORIOLIS TERMS
C
      V(I,J)=V(I,J)-FDT*(U1(I,J)     )-FCDT*W1(I,J)*COS(PSI)
      W(I,J)=W(I,J)+FCDT*((U1(I,J)     )*COS(PSI)+(V1(I,J)     )*SIN(PSI))
   16 U(I,J)=U(I,J)+FDT*(V1(I,J)     )-FCDT*W1(I,J)*SIN(PSI)
C
C        COMPUTE SURFACE POTENTIAL TEMPERATURE ON SHORE
C
```

```
      LL=L/2
      J=0
      DO 17 I=LL,1,-1
      J=J+1
      IF (J.GT.20) J=20
      VAR=FLOAT(J)*.5/5.
   17 TE(I,1)=1.+(14.+VAR)*SIN(RPD*(15.*TIME-105.))+1.5*SIN(RPD*(30.*
     *TIME-220.))+2.0*SIN(RPD*(45.*TIME-290.))
C
C       SMOOTH POTENTIAL TEMPERATURE ACROSS SHORELINE
C
      TE(LL+1,1)=TE(LL,1)/2.
C
C         SET BOUNDARIES OF U, V, AND TE
C
      DO 18 J=2,M1
      U(1,J)=U(2,J)
      U(L,J)=U(L1,J)
      V(1,J)=V(2,J)
      V(L,J)=V(L1,J)
      TE(1,J)=TE(2,J)
   18 TE(L,J)=TE(L1,J)
C
C       HOLD TE
C
      DO 19 I=1,L
      DO 19 J=1,M1
   19 TE1(I,J)=TE(I,J)
C
C         DEMAND THAT THE VERTICAL SUM OF HORIZONTAL DIVERGENCE BE ZERO
C
      DO 20 I=1,L
      B1(I)=S1*(U(I,M1)+UO(M1))/S2
      DO 20 J=2,M2
   20 B1(I)=B1(I)+(U(I,J)+UO(J))/S2
      DO 21 I=2,L1
   21 D(I)=(ROEBAR/DTDX*(B1(I-1)-B1(I))+D(I-1))*C(I)
      DO 22 I=2,L1
      N=L-I+1
   22 B2(N)=B2(N+1)*C(N)+D(N)
C
C         ADJUST U AND P TO SATISFY DIVERGENCE CONDITION
C
      DO 23 I=2,L1
      DO 23 J=3,M1
   23 U(I,J)=U(I,J)-DTDX/ROEBAR*(B2(I+1)-B2(I))
      DO 24 I=2,L1
      DO 24 J=2,M1
   24 P(I,J)=P(I,J)+B2(I)
C
C         CALCULATE DIVERGENCE OF APPROXIMATE VELOCIOIES
C
      DO 25 I=2,L1
C
C         ON TRANSITION LAYER TOP AND BOTTOM BOUNDARIES
C
```

```
      Q(I,2)=(4.*(W(I,3)-W(I,2))-(W(I,4)-W(I,2)))/DZ2+(U(I+1,2)-U(I-1,2)
     1)/DX2
      Q(I,M)=(W(I,M2)-4.*W(I,M1))/DZ2
      DO 25 J=3,M1
C
C        IN LAYER
C
   25 Q(I,J)=(U(I+1,J)-U(I-1,J))/DX2+(W(I,J+1)-W(I,J-1))/DZ2
C
C        PRESSURE DUE TO DIVERGENCE OF APPROXIMATE VELOCITIES
C
      DO 26 I=2,L1
      DO 26 J=2,M
   26 Q(I,J)=4.*DZQ/RDT*Q(I,J)/T(I,J)*(PL(J)+P(I,J)+P1(I,J))
C
C        BALANCE PRESSURE FIELD WITH CONVERGENCE TECHNIQUE
C
      ITER=0
   27 K=0
C
C        MAIN BODY OF LAYER
C
      DO 28 I=3,L2
      DO 28 J=4,M2
      RES=P1(I,J+2)+P1(I,J-2)-(2.+2.*DZQDXQ)*P1(I,J)+DZQDXQ*(P1(I+2,J)+P
     11(I-2,J))-Q(I,J)
      IF (ABS(RES).LE.EPS) GO TO 28
      K=K+1
      P1(I,J)=P1(I,J)+(1.+ALAMDA)*RES/(2.+2.*DZQDXQ)
   28 CONTINUE
C
C        BOUNDARIES
C
      DO 30 I=3,L2
C
C        BOTTOM BOUNDARY
C
      RES=P1(I,5)-(1.+2.*DZQDXQ)*P1(I,3)+DZQDXQ*(P1(I+2,3)+P1(I-2,3))-Q(
     1I,3)
      IF (ABS(RES).LE.EPS) GO TO 29
      K=K+1
      P1(I,3)=P1(I,3)+(1.+ALAMDA)*RES/(1.+2.*DZQDXQ)
C
C        TOP BOUNDARY
C
   29 RES=P1(I,M1-2)-(1.+2.*DZQDXQ)*P1(I,M1)+DZQDXQ*(P1(I+2,M1)+P1(I-2,M
     11))-Q(I,M1)
      IF (ABS(RES).LE.EPS) GO TO 30
      K=K+1
      P1(I,M1)=P1(I,M1)+(1.+ALAMDA)*RES/(1.+2.*DZQDXQ)
   30 CONTINUE
      DO 32 J=4,M2
C
C        LEFT BOUNDARY
C
      RES=P1(2,J+2)+P1(2,J-2)-(2.+DZQDXQ)*P1(2,J)+DZQDXQ*P1(4,J)-Q(2,J)
```

```
      IF (ABS(RES).LE.EPS) GO TO 31
      K=K+1
      P1(2,J)=P1(2,J)+(1.+ALAMDA)*RES/(2.+DZQDXQ)
C
C        RIGHT BOUNDARY
C
   31 RES=P1(L1,J+2)+P1(L1,J-2)-(2.+DZQDXQ)*P1(L1,J)+DZQDXQ*P1(L-3,J)-Q(
     1L1,J)
      IF (ABS(RES).LE.EPS) GO TO 32
      K=K+1
      P1(L1,J)=P1(L1,J)+(1.+ALAMDA)*RES/(2.+DZQDXQ)
   32 CONTINUE
C
C        CORNERS
C
      RES=P1(2,5)-(1.+DZQDXQ)*P1(2,3)+DZQDXQ*P1(4,3)-Q(2,3)
      IF (ABS(RES).LE.EPS) GO TO 33
      K=K+1
      P1(2,3)=P1(2,3)+(1.+ALAMDA)*RES/(1.+DZQDXQ)
   33 RES=P1(2,M-3)-(1.+DZQDXQ)*P1(2,M1)+DZQDXQ*P1(4,M1)-Q(2,M1)
      IF (ABS(RES).LE.EPS) GO TO 34
      K=K+1
      P1(2,M1)=P1(2,M1)+(1.+ALAMDA)*RES/(1.+DZQDXQ)
   34 RES=P1(L1,M-3)-(1.+DZQDXQ)*P1(L1,M1)+DZQDXQ*P1(L-3,M1)-Q(L1,M1)
      IF (ABS(RES).LE.EPS) GO TO 35
      K=K+1
      P1(L1,M1)=P1(L1,M1)+(1.+ALAMDA)*RES/(1.+DZQDXQ)
   35 RES=P1(L1,5)-(1.+DZQDXQ)*P1(L1,3)+DZQDXQ*P1(L-3,3)-Q(L1,3)
      IF (ABS(RES).LE.EPS) GO TO 36
      K=K+1
      P1(L1,3)=P1(L1,3)+(1.+ALAMDA)*RES/(1.+DZQDXQ)
C
C        STEP ITERATION COUNT
C
   36 ITER=ITER+1
C
C        ITERATION LIMIT CHECK
C
      IF (ITER.LE.ITMAX) GO TO 64
      ITER=0
      ITOVER=ITOVER+1
      ITOV=200
      IF (ITOVER.GT.10) GO TO 61
C
C        CONVERGENCE CHECK
C
   64 IF (K.GT.0) GO TO 27
C
C        ADJUST U AND W AFTER BALANCING PRESSURE FIELD
C
      KOU=KOUNT+1
      ITERP(KOU)=ITER+ITOV
      ITOV=0
      DO 37 I=2,L1
      DO 37 J=3,M1
      U(I,J)=U(I,J)-RDT*(P1(I+1,J)-P1(I-1,J))*T(I,J)/(DX2*(PL(J)+P(I,J)+
```

```
     1P1(I,J)))
  37 W(I,J)=W(I,J)-RDT*(P1(I,J+1)-P1(I,J-1))*T(I,J)/(DZ2*(PL(J)+P(I,J)+
     1P1(I,J)))
C
C       PUNCH SURFACE PRESSURE
C       -60,-50,-40,-30,-20,5,10,30 KM PLUS EVERY KM FROM -15 TO +2
C
  62 DO 60 I=1,26
     IF (I.LE.5) J=10*I+1
     IF (I.GE.6) J=50+I
     IF (I.EQ.24) J=76
     IF (I.EQ.25) J=81
     IF (I.EQ.26) J=101
     PR=P(J,1)+P1(J,1)+PL(1)
     IP=PR*100
     IF (IP.LT.100000) IP=IP+1000
  60 IPR(I)=IP-100000
     PUNCH 115,IPR
C
C       BRANCH FOR NEXT TIME STEP
C
     GO TO 38
C
C       AT END PRINT OUT
C       1.  NUMBER OF TIME STEPS
C       2.  FINAL ITERATION NUMBER
C       3.  NUMBER OF ITERATION OVERFLOWS
C       4.  NUMBER OF ITERATIONS FOR EACH TIME STEP
C       5.  EDDY DIFFUSIVITY FOR EACH OUTPUT TIME
C       6.  RICHARDSON NUMBER FOR EACH OUTPUT TIME
C
  61 PRINT 117,KOUNT
     PRINT 124,ITER
     PRINT 125,ITOVER
     PRINT 121,ITERP
     PRINT 102
     DO 73 J=1,L
  73 PRINT 126,(ZK(I,J),I=1,13)
     PRINT 102
     DO 74 J=1,L
  74 PRINT 126,(ZK(I,J),I=14,26)
     PRINT 102
     DO 75 J=1,L
  75 PRINT 126,(ZR(I,J),I=1,13)
     PRINT 102
     DO 76 J=1,L
  76 PRINT 126,(ZR(I,J),I=14,26)
     ISTOP=1
     GO TO 50
     END
•XQT
 0.0 3.5 4.0 4.2 4.6 5.1 5.1 5.3 5.5 5.8 6.0 5.8 5.7 5.4 5.2 5.2 5.2 5.2 5.2 5.2
 0.0-2.0-2.8-3.6-4.4-5.2-5.5-5.5-5.5-5.8-6.4-6.4-6.4-6.0-5.8-5.6-5.4-5.0-4.6-4.4
•FIN
```

REPORTS AVAILABLE FROM

THE UNIVERSITY OF WISCONSIN PRESS, BOX 1379, MADISON, WISCONSIN 53701

97024. Studies in Atmospheric Energetics Based on Aerospace Probings: Annual Report, 1966. 129 pages. 1967. $5.00

97026. Studies in Atmospheric Energetics Based on Aerospace Probings: Annual Report, 1968. 162 pages. 1969. $5.00

97027. Radiation Experiment in the Vicinity of Barbados: Final Report, NSF Grant Ga. 12603. 100 pages. 1970. $5.00

97028. The Study of Radiation in a Tropical Atmosphere: Final Report. 100 pages. 1970. $5.00

97029. The Educational and Social Uses of Communications Satellites: A Bibliography. 42 pages. 1970. $3.50

97030. Measurements from Satellite Platforms: Annual Scientific Report on NAS5-11542, 1968-69. 388 pages. 1970. $10.00

97031. A Pilot Study on the Application of Geosynchronous Meteorological Satellite Data to Very Short Range Terminal Forecasting. 113 pages. 1970. $5.00

97032. Studies of the Atmosphere Using Aerospace Probings: Annual Report 1969. 243 pages. 1970. $7.50

97033. Teleconferencing: A Bibliography. 42 pages. 1971. $3.50

97034. Legal and Political Aspects of Satellite Telecommunication: An Annotated Bibliography. 126 pages. 1971. $7.50

97035. Multidisciplinary Studies of the Social, Economic and Political Impact Resulting from Recent Advances in Satellite Meteorology: An Interim Report, Vol. 1. 459 pages. 1971. $15.00

97036. Multidisciplinary Studies of the Social, Economic and Political Impact Resulting from Recent Advances in Satellite Meteorology: An Interim Report, Vol. 2. 431 pages. 1971. $15.00

97037. Measurements from Satellite Platforms: Annual Scientific Report on NAS5-11542, 1969-70. 180 pages. 1971. $7.50

97038. Studies of the Atmosphere Using Aerospace Probings: Annual Report, 1970. 69 pages. 1971. $5.00

97039. Legal Aspects of Satellite Teleconferencing. 213 pages. 1971. $7.50

97040. Teleconferencing in Wisconsin. 240 pages. 1971. $10.00

97041. Measurements from Satellite Platforms: Annual Scientific Report on NAS5-11542, 1970-71. 270 pages. 1972. $10.00

(continued from back cover)

97042. Experiments in Medical Communications via the ATS-1 Satellite. 136 pages. 1972. $7.50

97043. Specifications for a Vertical Temperature and Moisture Sounder for the Synchronous Meteorological Satellites. 82 pages. 1972. $5.00

97044. Scientific Requirements of Sea Surface Measurements for the GARP Tropical Experiment. 18 pages. 1972. $2.50

97045. Studies of the Atmosphere Using Aerospace Probings: Annual Report, 1971, Vol. II: Application Studies. 104 pages. 1972. $5.00

97046. Multidisciplinary Studies of the Social, Economic and Political Impact Resulting from Recent Advances in Satellite Meteorology: An Interim Report, Vol. 3. 252 pages. 1972. $10.00

97047. Multidisciplinary Studies of the Social, Economic and Political Impact Resulting from Recent Advances in Satellite Meteorology: An Interim Report, Vol. 4. 199 pages. 1972. $10.00

97048. Satellite Teleconferencing: An Annotated Bibliography. 130 pages. 1972. $7.50

97049. Measurements from Satellite Platforms: Annual Scientific Report on NAS5-11542, 1971-72. 228 pages. 1972. $7.50

97050. Synchronous Meteorological Satellite Sounder Specification: Final Report under NASA Contract NAS5-21607. 73 pages. $5.00

97051. Multidisciplinary Studies of the Social, Economic and Political Impact Resulting from Recent Advances in Satellite Meteorology: An Interim Report, Vol. 5. 290 pages. 1973. $10.00

97052. Measurements from Satellite Platforms: Annual Scientific Report on NAS5-21798, 1972-73. 331 pages. 1974. $10.00

97053. Visual Channel Data Analysis for Synchronous Meteorological Satellite: Scientific Report on NOAA/NESS Grant NG-26-72. 252 pages. 1974. $7.50

97054. Studies of the Atmosphere Using Aerospace Probes. Annual Report, 1973. 272 pages. 1974. $7.50

97055. Meteorological Measurements from Satellite Platforms: Annual Scientific Report on NAS5-21798, 1973-74. 97 pages. 1975. $5.00

97056. Studies of the Atmosphere Using Aerospace Probes. Annual Report, 1974. 154 pages. 1975. $5.00

97057. Multidisciplinary Studies of the Social, Economic and Political Impact Resulting from Recent Advances in Satellite Meteorology: Final Report, Vol. 6. 100 pages. $10.00

97058. Studies of the Atmosphere Using Aerospace Probes. Annual Report, 1975. 91 pages. $7.50

97059. Studies of Soundings and Imaging Measurements. Final Scientific Report on NAS5-21798, 1974-1976. 273 pages. 1977. $10.00